

Universitat Politècnica de Catalunya

**A numerical formulation to solve the ALE Navier-Stokes
equations applied to the withdrawal of magma chambers**

Doctoral Thesis presented by

ARNAU FOLCH DURAN

Supervisors:

Dr. Ramon Codina Rovira

Departament de Resistència de Materials i Estructures a l'Enginyeria (UPC)

Dr. Joan Martí Molist

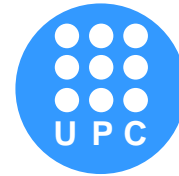
Institut de Ciències de la Terra "Jaume Almera" (CSIC)

Barcelona

April, 2000



Institut de Ciències de la Terra
"Jaume Almera", CSIC



Departament de Matemàtica
Aplicada III, UPC

A numerical formulation to solve the ALE Navier-Stokes equations applied to the withdrawal of magma chambers

Doctoral Thesis presented by

ARNAU FOLCH DURAN

Supervisors:

Dr. Ramon Codina Rovira

Departament de Resistència de Materials i Estructures a l'Enginyeria (UPC)

Dr. Joan Martí Molist

Institut de Ciències de la Terra "Jaume Almera" (CSIC)

Barcelona

April, 2000

A la memòria de
Josep Duran i Barba

AGRAÏMENTS

Primerament vull expressar la meva gratitud als meus directors de tesi: Ramon Codina, del Departament de Resistència de Materials i Estructures a l'Enginyeria (UPC) i Joan Martí, de l'Institut de Ciències de la Terra "Jaume Almera" (CSIC). D'en Joan Martí he après tot el que sé de vulcanologia i bastantes finances. El seu suport incondicional, la seva confiança en mi i les seves constants idees productives han estat fonamentals. Ramon Codina, enorme matemàtic i excel·lent persona, m'ha transmès no només molts coneixements de matemàtiques i mecànica de fluids, sinó també el rigor i l'apreci per la feina ben feta. Ha estat un autèntic plaer, i una gran sort, treballar amb ell. També vull donar les gràcies a Antonio Huerta, tutor d'aquesta tesi al Departament de Matemàtica Aplicada III i "culpable" que conegués en Ramon.

Estic agraït amb els meus companys de "viatge" durant aquests anys. Sílvia Zafrilla és la responsable que tot això hagi passat. Moltes gràcies també a Carles Soriano, Marcel Hürlimann, Elisenda Turón, Fernando Resta, Josep Mitjavila, Ignasi Queralt, Giray Ablay, François Legros i a tot el col·lectiu "Almeja Suckers" del CSIC i a Mariano Vázquez, Guillaume Houzeaux i Eduardo Car de la UPC. Molta més gent ha ensenyat coses importants i m'ha ajudat, d'una o altra manera, durant la realització d'aquesta tesi. Vull destacar a José Fernández (UCM) i a la seva dona Loli; a José Viramonte, Chino, Ana i Berta (Universidad de Salta); a Mayra i Marta (INETER); a August Gudmundsson (Nordic Volcanological Institute) i a Donald Dingwell (Bayreuth University).

També voldria expressar la meva gratitud als meus pares i, en general, a tota la meua família pel seu suport moral i, quan ha calgut, econòmic; i a la Sílvia pel seu amor incondicional. Finalment, gràcies a tots aquells que, malgrat que no han intervingut d'una manera directa en aquesta tesi, han compartit amb mi molt bons moments: Eva, Sonia, Joan, Hector i Jenny, Xavi, tots els "barrufets", els "físics per la botifarra" (control!), Celina, Chukri, Juanjo, Vicenç i "Antoni". Us estimo a tots. Ah!, i a Radio Gladys Palmera...

Aquesta tesi ha estat finançada per una beca de la Direcció General de Recerca de la Generalitat de Catalunya (1998FI 00019 CSIC APMARN).

ABSTRACT

This thesis presents a numerical formulation to solve the Navier-Stokes equations with mechanical coupling in the context of a Finite Element Method. The solution of the ALE Navier-Stokes equations is based on a fractional step method combined with a pressure gradient projection technique that produces the required stabilisation of the pressure field when implicit versions of the algorithm are considered. The algorithm deals simultaneously with both compressible and incompressible flows using the same interpolation spaces for the pressure and the velocity fields. Fluid-structure interaction problems are solved by means of a staggered procedure in which the fluid and the structural equations are alternatively integrated in time by using separate solvers. A remeshing strategy with a conservative interpolation of nodal variables is also developed. Particular applications are addressed concerning the modelling of the dynamics of magma withdrawal from crustal reservoirs. A physical model for the most common types of (explosive) volcanic eruptions is proposed. Several simulations of eruptive events, ranging from volatile oversaturation driven eruptions to caldera-forming eruptions, are presented. On the other hand, a numerical procedure to compute viscoelastic ground deformations in volcanic areas is also proposed. This procedure is based on the correspondence principle combined with the Laplace transform inversion by means of the Prony series method. It allows to constrain the domain of applicability of the analytical procedures used nowadays and, simultaneously, allows to contemplate a wider spectrum of possibilities such as, for instance, extended sources, topographic effects or anisotropies of the crust.

CONTENTS

List of Figures	iv
List of Tables	ix
Chapter 1. Foreword	
1.1 Introduction	1-1
1.2 Objectives	1-3
1.3 Structure of the Thesis	1-4
1.4 Notation	1-6
Chapter 2. Volcanic Processes: An Overview	
2.1 Magma Genesis	2-3
2.1.1 The Melting Process	2-3
2.1.2 Types of Magmas	2-7
2.2 Physical Properties of Magmas	2-9
2.2.1 Density and Temperature	2-9
2.2.2 Viscosity	2-11
2.2.3 Volatiles and Solubility Laws	2-12
2.2.4 Thermal Diffusivity	2-17
2.3 The Eruptive Process	2-19
2.3.1 Triggering Mechanisms	2-21
2.3.2 Explosive Volcanism. Exsolution and Fragmentation Levels	2-24
2.3.3 Caldera Forming Eruptions	2-26
2.4 Modelling in Physical Volcanology: State-of-the-Art	2-30
2.4.1 Eruptive Models	2-30
2.4.1.1 Conduit Models	2-31
2.4.1.2 Chamber Withdrawal Models	2-43
2.4.2 Ground Deformation Models	2-46
2.5 References	2-48
Chapter 3. Governing Equations	
3.1 Assumptions and Requirements	3-3
3.2 A State Law for the Magmatic Mixture	3-5
3.3 ALE Governing Equations	3-14
3.3.1 Introduction to the ALE Formulation	3-15
3.3.2 ALE Continuity Equation	3-21
3.3.3 ALE Momentum Equation	3-22
3.3.4 ALE Energy Equation	3-23
3.4 Flow Equations	3-25
3.4.1 Newtonian Fluids	3-25

3.4.2	ALE Navier-Stokes Equations	3-26
3.5	Structural Equations	3-28
3.5.1	Linear Elastic Materials	3-28
3.5.2	Linear Viscoelastic Materials	3-30
3.6	References	3-33
	Appendix 3A. Deduction of the ALE Governing Equations	3-36
Chapter 4. Numerical Methods		
4.1	The Navier-Stokes Equations	4-3
4.1.1	Time Discretisation	4-4
4.1.2	Pressure Gradient Projection	4-6
4.1.3	Splitting of the Momentum Equation	4-7
4.1.4	Weak Forms and Boundary Conditions	4-9
4.1.4.1	Fractional Momentum Equation.	4-10
4.1.4.2	Continuity Equation	4-17
4.1.4.3	Pressure Gradient Projection Equation	4-19
4.1.4.4	Momentum Equation	4-20
4.1.4.5	Energy Equation	4-20
4.1.5	Space Discretisation	4-21
4.1.6	Methods of Stabilisation	4-21
4.1.7	Time Step and Stability	4-26
4.2	The Convective Transport Equation	4-29
4.3	Fluid-Structure Interaction	4-32
4.3.1	Introduction and General Procedure	4-32
4.3.2	A Structural Integrator for the Rigid Solid.	4-35
4.3.3	The Quasi-Laplacian Method	4-38
4.3.4	Mesh Velocity and Boundary Conditions	4-42
4.3.5	Mesh Distortion and Remeshing	4-45
4.4	Numerical Examples	4-51
4.4.1	The Driven Cavity Flow	4-51
4.4.2	Flow Past a Circular Cylinder	4-63
4.4.3	Fluid in a Heated Cavity	4-72
4.4.4	Perfect Gas Flowing over a NACA Profile.	4-79
4.4.5	The Stokes Problem	4-83
4.4.6	Missile Launched From a Submarine	4-87
4.4.7	Mould Filling Simulation	4-98
4.5	The Mechanical Equations	4-104
4.5.1	Elastic Problem	4-104
4.5.1.1	Weak Form and Boundary Conditions	4-105

4.5.1.2	Space Discretisation	4-106
4.5.1.3	The Newmark method	4-107
4.5.2	Viscoelastic Problem. The Prony Series Method	4-109
4.6	References	4-114
Appendix 4A.	Weak Forms	4-119
Appendix 4B.	Discretised Algebraic Systems	4-122
Appendix 4C.	Programming Notes	4-132
Chapter 5. Numerical Simulations of Volcanic Eruptions		
5.1	Previous Considerations	5-3
5.1.1	Objectives	5-3
5.1.2	Geometry and Boundary Conditions	5-4
5.1.3	A Relation between W and ΔP	5-9
5.1.4	A Remark on the Time Step Size	5-12
5.2	Withdrawal from Closed Magma Chambers	5-14
5.2.1	Constant Volatile Content	5-14
5.2.1.1	General Overview	5-14
5.2.1.2	A Parametrical Study	5-20
5.2.2	Variable Volatile Content	5-30
5.3	Withdrawal from Open Magma Chambers	5-34
5.3.1	Chemically Homogeneous Chambers	5-34
5.3.2	Chemically Heterogeneous Chambers	5-40
5.4	Caldera-Forming Eruptions	5-47
5.4.1	Non-Vesiculated Magma	5-49
5.4.2	Partially Vesiculated Magma	5-68
5.5	References	5-73
Chapter 6. Ground Deformation		
6.1	The Axisymmetrical Problem	6-3
6.2	A Comparison between Point and Extended Sources. Constrains on the Analytical Solutions	6-10
6.2.1	Influence of the Size to Depth Ratio	6-11
6.2.2	Influence of the Topography	6-19
6.2.3	Influence of the Chamber Shape	6-22
6.3	The 1982-1984 Campi Flegrei Uplift.	6-26
6.4	A 3D Application to Tenerife Island	6-30
6.5	References	6-54
Chapter 7. Conclusion		
7.1	Summary and Conclusions	7-1
7.2	Future Lines of Research	7-7

LIST OF FIGURES

Chapter 2. Volcanic Processes: An Overview

Figure 2.1.1	Schematic phase diagram	2-3
Figure 2.1.2	Global tectonic map	2-4
Figure 2.1.3	Diagram of a mid-oceanic divergent plate margin	2-5
Figure 2.1.4	Diagram of a subduction zone	2-5
Figure 2.1.5	Original version of the TAS diagram	2-8
Figure 2.2.1	Magma properties in terms of its composition	2-9
Figure 2.2.2	Magma density plotted versus temperature	2-10
Figure 2.2.3	Experimental melt viscosities of hydrous melts	2-12
Figure 2.2.4	Water solubility plotted versus temperature	2-13
Figure 2.2.5	Water solubility plotted versus pressure	2-17
Figure 2.2.6	Experimental data of thermal diffusivity	2-18
Figure 2.3.1	Schematic cartoon showing the relation between volcanic processes	2-20
Figure 2.3.2	Main morphological features of a typical volcano	2-21
Figure 2.3.3	Cartoon showing main features of explosive volcanism	2-25
Figure 2.3.4	Cartoon showing processes leading to caldera collapse formation	2-29
Figure 2.4.1	Results of the Wilson's model	2-34
Figure 2.4.2	Results of the Wilson's model	2-34
Figure 2.4.3	Geometry of the Dobran's model	2-37
Figure 2.4.4	Results of the Dobran's model	2-39
Figure 2.4.5	Results of the Dobran and co-workers model	2-41
Figure 2.4.6	Results of the Spera's model	2-44
Figure 2.4.7	Results of the Spera's model	2-45

Chapter 3. Governing Equations

Figure 3.2.1	State law for rhyolitic magmas	3-8
Figure 3.2.2	Gas volume fraction versus density for rhyolitic magmas	3-9
Figure 3.2.3	State law for mafic magmas	3-10
Figure 3.2.4	Effect of the compressibility modulus on the state law	3-11
Figure 3.2.5	Effect of volatile content and temperature on the state law	3-13
Figure 3.3.1	Relation between spatial, material and computational frames	3-17

Chapter 4. Numerical Methods

Figure 4.3.1	Cartoon showing the general procedure of the staggered algorithm	4-36
Figure 4.3.2	Definition of the fluid-structure interface	4-39
Figure 4.3.3	Differences between the Laplacian and the Quasi-Laplacian methods	4-41
Figure 4.3.4	Illustration of the diffusivity associated to the Lagrange interpolation	4-47
Figure 4.4.1	Driven cavity flow. Boundary conditions	4-52

Figure 4.4.2	Driven cavity flow. Spatial discretisations	4-53
Figure 4.4.3	Driven cavity flow. Results at $R_e=0.01$	4-54
Figure 4.4.4	Driven cavity flow. Results at $R_e=100$	4-55
Figure 4.4.5	Driven cavity flow. Results at $R_e=1000$	4-56
Figure 4.4.6	Driven cavity flow. Results at $R_e=5000$	4-57
Figure 4.4.7	Driven cavity flow. Results at $R_e=10000$	4-58
Figure 4.4.8	Driven cavity flow. Detailed results at $R_e=1000$	4-59
Figure 4.4.9	Driven cavity flow. Detailed results at $R_e=5000$	4-60
Figure 4.4.10	Driven cavity flow. Detailed results at $R_e=10000$	4-61
Figure 4.4.11	Driven cavity flow. Velocity profiles	4-62
Figure 4.4.12	Flow past a cylinder. Boundary conditions	4-64
Figure 4.4.13	Flow past a cylinder. Spatial discretisation	4-64
Figure 4.4.14	Flow past a cylinder. Results at $R_e=100$	4-65
Figure 4.4.15	Flow past a cylinder. Detailed results at $R_e=100$	4-65
Figure 4.4.16	Flow past a cylinder. L^2 norms plotted versus time	4-66
Figure 4.4.17	Flow past a cylinder. Results at $R_e=100$ and $t = t_{ref}$	4-67
Figure 4.4.18	Flow past a cylinder. Illustration of the vortex shedding	4-67
Figure 4.4.19	Flow past a cylinder. Detailed view of the vortex shedding	4-68
Figure 4.4.20	Flow past a cylinder. Detailed view of the vortex shedding	4-69
Figure 4.4.21	Flow past a cylinder. Results at $R_e=200$	4-70
Figure 4.4.22	Flow past a cylinder. Detailed results at $R_e=200$	4-71
Figure 4.4.23	Fluid in a heated cavity. Boundary conditions	4-73
Figure 4.4.24	Fluid in a heated cavity. Spatial discretisation	4-74
Figure 4.4.25	Fluid in a heated cavity. Results for example A	4-75
Figure 4.4.26	Fluid in a heated cavity. Results for example A	4-76
Figure 4.4.27	Fluid in a heated cavity. Results for example B	4-77
Figure 4.4.28	Fluid in a heated cavity. Evolution of the Nusselt number	4-78
Figure 4.4.29	Perfect gas over a NACA profile. Boundary conditions	4-79
Figure 4.4.30	Perfect gas over a NACA profile. Spatial discretisation	4-80
Figure 4.4.31	Perfect gas over a NACA profile. Pressure contours	4-81
Figure 4.4.32	Perfect gas over a NACA profile. Results around the wing	4-82
Figure 4.4.33	Stokes problem. Sketch of the problem	4-83
Figure 4.4.34	Stokes problem. Spatial discretisation	4-85
Figure 4.4.35	Stokes problem. Fall velocity	4-85
Figure 4.4.36	Stokes problem. Numerical results around the sphere	4-86
Figure 4.4.37	Missile launched from a submarine. Boundary conditions	4-87
Figure 4.4.38	Missile launched from a submarine. Initial spatial discretisation	4-89
Figure 4.4.39	Missile launched from a submarine. Initial spatial discretisation	4-90

Figure 4.4.40	Missile launched from a submarine. Views of different meshes	4-91
Figure 4.4.41	Missile launched from a submarine. Results at $t = 0.2s$	4-92
Figure 4.4.42	Missile launched from a submarine. Results at $t = 0.5s$	4-93
Figure 4.4.43	Missile launched from a submarine. Results at $t = 0.8s$	4-94
Figure 4.4.44	Missile launched from a submarine. Results at $t = 1.0s$	4-95
Figure 4.4.45	Missile launched from a submarine. Results at $t = 1.5s$	4-96
Figure 4.4.46	Missile launched from a submarine. Results at $t = 2.0s$	4-97
Figure 4.4.47	Mould Filling Simulation. Geometry and space discretisation	4-98
Figure 4.4.48	Mould Filling Simulation. Position of the front at different time instants	4-100
Figure 4.4.49	Mould Filling Simulation. Position of the front at different time instants	4-101
Figure 4.4.50	Mould Filling Simulation. Results at $t = 0.1s$	4-102
Figure 4.4.51	Mould Filling Simulation. Results at $t = 0.25s$	4-102
Figure 4.4.52	Mould Filling Simulation. Results at $t = 0.7s$	4-103
Figure 4.4.53	Mould Filling Simulation. Results at $t = 1.0s$	4-103
Figure 4C.1	Flow diagram of Rigel	4-133
Figure 4C.2	Flow diagram of Sirius	4-134

Chapter 5. Numerical Simulation of Volcanic Eruptions

Figure 5.1.1	Classification of different possible simulations	5-3
Figure 5.1.2	Geometry for generic central vent and caldera-forming eruptions	5-5
Figure 5.1.3	Boundary and initial conditions	5-7
Figure 5.1.4	Schematic illustration of the fractional crystallisation process	5-9
Figure 5.1.5	Overpressure in terms of the volatile mass fraction	5-11
Figure 5.2.1	Geometry and space discretisation for a cylindrical chamber	5-15
Figure 5.2.2	Results for a cylindrical closed chamber. Pressure and exsolution level	5-16
Figure 5.2.3	Results for a cylindrical closed chamber. Density and pressure	5-17
Figure 5.2.4	Results for a cylindrical closed chamber. Eruption rate and velocity	5-18
Figure 5.2.5	Results for a cylindrical closed chamber. Erupted mass	5-19
Figure 5.2.6	Different geometries contemplated and its space discretisations	5-21
Figure 5.2.7	Results for closed chambers. Influence of geometry	5-22
Figure 5.2.8	Results for closed chambers. Influence of geometry	5-23
Figure 5.2.9	Results for a sill-like chamber. Influence of viscosity	5-25
Figure 5.2.10	Results for a sill-like chamber. Influence of viscosity	5-26
Figure 5.2.11	Results for a sill-like chamber. Influence of volatile content	5-27
Figure 5.2.12	Results for a sill-like chamber. Influence of volatile content	5-28
Figure 5.2.13	Examples with variable volatile content. Initial distribution of volatiles	5-30
Figure 5.2.14	Examples with variable volatile content. Pressure evolution	5-31
Figure 5.2.15	Examples with variable volatile content. Density distributions	5-32
Figure 5.2.16	Examples with variable volatile content. Erupted mass	5-33

Figure 5.3.1	Results for a cylindrical open chamber. Exsolution level	5-35
Figure 5.3.2	Results for a cylindrical open chamber. Density and streamlines	5-36
Figure 5.3.3	Results for a cylindrical open chamber. Eruption rate	5-37
Figure 5.3.4	Results for a cylindrical open chamber. Erupted mass	5-38
Figure 5.3.5	Results for a cylindrical open chamber. Influence of volatile content	5-39
Figure 5.3.6	Chemically heterogeneous chambers. Boundary conditions	5-41
Figure 5.3.7	Chemically heterogeneous chambers. Position of the interface	5-42
Figure 5.3.8	Chemically heterogeneous chambers. Averaged outlet composition	5-43
Figure 5.3.9	Chemically heterogeneous chambers. Different initial compositions	5-44
Figure 5.3.10	Chemically heterogeneous chambers. Averaged outlet compositions	5-45
Figure 5.3.11	Chemically heterogeneous chambers. Composition inside the chamber	5-46
Figure 5.4.1	Caldera forming eruptions. Geometries	5-47
Figure 5.4.2	Caldera forming eruptions. Discretisations for the elliptical chamber	5-50
Figure 5.4.3	Caldera forming eruptions. Discretisations for the elliptical chamber	5-51
Figure 5.4.4	Caldera forming eruptions. Elliptical chamber: results at $t = 2\text{min}$	5-52
Figure 5.4.5	Caldera forming eruptions. Elliptical chamber: results at $t = 9\text{min}$	5-53
Figure 5.4.6	Caldera forming eruptions. Elliptical chamber: results at $t = 16\text{min}$	5-54
Figure 5.4.7	Caldera forming eruptions. Elliptical chamber: zoom of the streamlines	5-55
Figure 5.4.8	Caldera forming eruptions. Discretisations for cylindrical chamber	5-56
Figure 5.4.9	Caldera forming eruptions. Discretisations for cylindrical chamber	5-57
Figure 5.4.10	Caldera forming eruptions. Cylindrical chamber: results at $t = 2\text{min}$	5-58
Figure 5.4.11	Caldera forming eruptions. Cylindrical chamber: results at $t = 15\text{min}$	5-59
Figure 5.4.12	Caldera forming eruptions. Cylindrical chamber: results at $t = 24\text{min}$	5-60
Figure 5.4.13	Caldera forming eruptions. Cylindrical chamber: streamlines	5-61
Figure 5.4.14	Caldera forming eruptions. Subsidence and eruption rate	5-62
Figure 5.4.15	Caldera forming eruptions. Erupted mass	5-64
Figure 5.4.16	Caldera forming eruptions. Influence of viscosity	5-65
Figure 5.4.17	Caldera forming eruptions. Influence of viscosity	5-66
Figure 5.4.18	Caldera forming eruptions. Influence of viscosity	5-67
Figure 5.4.19	Caldera forming eruptions. Case A. Results at $t = 15\text{min}$	5-69
Figure 5.4.20	Caldera forming eruptions. Case A. Results at $t = 30\text{min}$	5-69
Figure 5.4.21	Caldera forming eruptions. Case B. Results at $t = 10\text{min}$	5-70
Figure 5.4.22	Caldera forming eruptions. Case B. Results at $t = 22.5\text{min}$	5-70
Figure 5.4.23	Caldera forming eruptions. Results for cases A and B	5-71
Figure 5.4.24	Caldera forming eruptions. Results for cases A and B	5-72
Chapter 6. Ground Deformation		
Figure 6.1.1	Schematic illustration of a general axisymmetrical problem	6-3
Figure 6.1.2	Spatial discretisation	6-4

List of Figures

Figure 6.1.3	Displacement at different characteristic times	6-6
Figure 6.1.4	Displacements at the Earth's surface	6-7
Figure 6.1.5	Components of the Cauchy stress tensor	6-8
Figure 6.1.6	Radial stress component at the Earth's surface	6-9
Figure 6.2.1	Analytical/Numerical comparison. Influence of the chamber radius	6-13
Figure 6.2.2	Analytical/Numerical comparison. Influence of the chamber radius	6-14
Figure 6.2.3	Analytical/Numerical comparison. Influence of the chamber depth	6-15
Figure 6.2.4	Analytical/Numerical comparison. Influence of the chamber depth	6-16
Figure 6.2.5	Analytical/Numerical comparison. Influence of the chamber radius	6-17
Figure 6.2.6	Analytical/Numerical comparison. Influence of the chamber depth	6-18
Figure 6.2.7	Analytical/Numerical comparison. Influence of the topography	6-20
Figure 6.2.8	Analytical/Numerical comparison. Influence of the topography	6-21
Figure 6.2.9	Analytical/Numerical comparison. Influence of the chamber shape	6-23
Figure 6.2.10	Analytical/Numerical comparison. Influence of the chamber shape	6-24
Figure 6.2.11	Analytical/Numerical comparison. Influence of the chamber shape	6-25
Figure 6.3.1	General view of the Campi Flegrei area	6-26
Figure 6.3.2	Measured vertical displacements during the 1982-1984 uplift episode	6-27
Figure 6.3.3	Campi Flegrei. Numerical results considering a relaxation type 2	6-29
Figure 6.4.1	Location map for Tenerife island	6-31
Figure 6.4.2	Schematic illustration of the crustal model for Tenerife	6-32
Figure 6.4.3	Map showing the topography of the area selected for computations	6-33
Figure 6.4.4	View of the upper face of the mesh for Tenerife island	6-34
Figure 6.4.5	Lateral views of the mesh for Tenerife island	6-35
Figure 6.4.6	Close up views of the mesh for Tenerife island around LCC	6-36
Figure 6.4.7	Internal view of the mesh for Tenerife island around the chamber	6-37
Figure 6.4.8	Numerical results. Vertical displacements at surface	6-39
Figure 6.4.9	Numerical results. Horizontal displacements at surface	6-43
Figure 6.4.10	Numerical results. Horizontal displacements at surface	6-47
Figure 6.4.11	3D representation of the vertical displacement at surface	6-51
Figure 6.4.12	Results using the 2D axisymmetrical approximation	6-53

LIST OF TABLES

Chapter 1. Forward

Table 1.4.1	List of scalar variables designed by Greek alphabet	1-7
Table 1.4.2	List of scalar variables designed by Latin alphabet	1-8
Table 1.4.3	List of tensorial variables	1-9
Table 1.4.4	List of vectorial variables	1-10

Chapter 2. Volcanic Processes: An Overview

Table 2.1.1	Relationship between tectonic setting, volcanic feature and magma type.	2-6
Table 2.2.1	Densities and temperatures of magmas	2-11
Table 2.2.2	Standard values for the Henry law	2-14
Table 2.4.1	Characteristics of most relevant conduit models.	2-42

Chapter 4. Numerical Methods

Table 4.1.1	Treatment of the convective, viscous and energy terms according to q^i	4-5
Table 4.1.2	Values of A and B for different state laws	4-19
Table 4.1.3	Operators for different stabilisation methods	4-26
Table 4.1.4	Properties of the algorithm	4-28
Table 4.4.1	Fluid in a heated cavity. Compared results	4-76
Table 4.4.2	Perfect gas over a NACA profile. Compared results	4-81
Table 4.5.1	Summary of viscoelastic rheologies assumed for the crust	4-113
Table 4C.1	Summary of elements implemented in the programs	4-132

Chapter 5. Numerical Simulations of Volcanic Eruptions

Table 5.2.1	Summary of the parametrical study	5-29
-------------	---	------

Chapter 6. Ground Deformation

Table 6.2.1	Standard values used in the tests	6-10
Table 6.3.1	Values used in the analysis	6-28
Table 6.3.2	1982-1984 Campi Flegrei uplift. Compared results	6-29

Chapter 1

Foreword

1.1 Introduction

This thesis presents an algorithm for compressible and incompressible Newtonian flows with mechanical coupling. In addition, a procedure to solve structural problems considering some simple viscoelastic rheologies is also proposed. Applications focus on numerical simulation of some volcanic phenomena. Volcanic eruptions represent one of Nature's most violent environmental hazards. While the constructive power of volcanoes provides attractive conditions for human settlement in the form of rich soils or geothermal energy, their destructive power has the potential for instantaneous and total destruction of life and property in their vicinity. Moreover, volcanic eruptions can cause significant change on Earth's climate as they can inject large volumes of volatile components and fine-grained solid particles into the atmosphere. All these aspects can become significantly worse when volcanic eruptions are related to caldera collapse events. The reasons to advance into a better knowledge of such a fascinating natural phenomena are, in consequence, self-evident.

Volcanic eruptions are the culmination of long and complex geological and physical processes which involve the generation of magmas in the mantle or in the lower crust, its ascent to shallower levels, its storage and differentiation in shallow crustal chambers, and, finally, its eruption at the Earth's surface. The study of all these processes has been traditionally carried out through different geological disciplines, such as petrology, structural geology, geochemistry or sedimentology. Nevertheless, during the last two decades, the development of physical volcanology as well as the introduction of new powerful numerical techniques has progressively converted volcanology into a multidisciplinary science. Nowadays, scientists with very different backgrounds and expertises such as geologists, physicists, chemists, mathematicians or engineers work on volcanology. As any multidisciplinary field, volcanology has been largely benefited from these collaborations. The different ways and procedures to face the study of volcanic phenomena do not exclude each other and should be regarded as complementary.

Despite the present knowledge of volcanic phenomena has increased notably during the last two decades it is still far from being satisfactory. Deficiencies in knowledge can be attributed, partially, to the enormous complexity and multiple manifestations of a phenomena which involves many different physical processes (some of which are not well constrained yet) and hundreds/thousands of variables. A second important limitation is the obtention of data because only some aspects of the phenomena can be directly observed or measured. In consequence, many important properties must be inferred from indirect measurements, extrapolated from laboratory experiments or simply assumed. Clearly, these drawbacks suppose serious difficulties to test and validate the physical models.

Observation It is important to distinguish between a physical model and a numerical simulation because, sometimes, confusion between these two concepts can lead to misunderstandings. A *physical model* is a simplified abstraction to imitate or emulate a given observed phenomena. A physical model is acceptable when is able to reproduce not only the experimental data available but also when its predictions are confirmed by further measurements. Any physical model is characterised by a set of governing equations which describe the physics of the problem using the mathematical language. Very often, the solution of these governing equations cannot be obtained analytically and one must employ numerical techniques. A *numerical simulation* is the obtention of a particular solution of the physical model under a given set of “ambient” conditions (e.g. boundary and initial conditions for the most common case of governing equations which are time-dependent differential equations). A numerical simulation obtained using certain numerical techniques can be contrasted against other numerical procedures, that is, one can legitimately check whether two or more different numerical procedures proportionate similar results when applied to solve the same problem. However, it is important to remark that what must be contrasted against “reality” (against experimental/observed data) are the predictions of the physical model (i.e. the physical model itself) which, in many cases, will be obtained by means of numerical simulations. This subtle difference, which should be obvious to those scientists used to work in modelling is, in some cases, a source of misunderstandings and may cause a false controversy. Notwithstanding this, the term “numerical simulation” will be used here, by abuse of language, as a synonym of “solution of a given physical model obtained by means of numerical procedures”.

Nowadays, numerical modelling in volcanology covers different pre-eruptive, eruptive and post-eruptive aspects of the general “volcanic phenomena”. Among these aspects, the eruptive process itself is, by obvious reasons, of special interest. However, and due to its complexity, numerical simulations of eruptive related processes have been traditionally considered in separate domains (magma chamber, volcanic conduit and Earth’s surface). While most of the studies available focus on conduit and subaerial processes, the question of “what occurs within a magma chamber during the course of an eruption” has received little attention. Part of the applications of this thesis aim to fill this “hole” in order to advance into a global comprehension of the eruptive process.

1.2 Objectives

❶ This thesis presents a numerical formulation to solve the Navier-Stokes equations for both compressible and incompressible flows considering mechanical coupling. Generally speaking, the algorithm can be applied to solve a wide spectrum of problems which commonly appear in several scientific disciplines such as engineering, physics or geology, and, in consequence, its development constitutes an interesting objective by itself. Nevertheless, the particular applications will be addressed to solve an important question of physical volcanology which is still poorly understood: the dynamics of magma withdrawal from crustal reservoirs. The aim is to develop a physical model able to explain the most relevant physical processes that occur inside the magma chamber during the course of any kind of volcanic eruption. Particular objectives are:

❶.❶ To model the process of withdrawal from closed magma chambers (eruptions driven by oversaturation of volatiles) in order to obtain the temporal evolution of pressure, position of the exsolution level, eruptive rate and amount of erupted material for both chemically homogeneous and chemically heterogeneous magma chambers.

❶.❷ To model the process of withdrawal from open magma chambers (eruptions driven by injection of fresh magma into the chamber) in order to obtain the same temporal variations as in ❶.❶ and considering also chemically homogeneous and chemically heterogeneous chambers.

❶.❸ To model the process of withdrawal during the course of caldera-forming eruptions.

Cases ❶.❶ and ❶.❷ require the solution of the Navier-Stokes equations with an state law suitable for the magmatic mixture. In addition, the solution of a convective transport equation is also required for non-homogeneous chambers. Case ❶.❸ involves fluid-structure coupling. In the context of this thesis, this set of problems will be referred as the “*flow problem*”.

❷ A secondary objective is to propose an algorithm to solve structural problems considering some simple viscoelastic rheologies. Particular applications are focussed to model ground deformation in volcanic areas considering topographic effects and a chamber of arbitrary geometry buried within a heterogeneous viscoelastic crust. In the context of this thesis, this problem will be referred as the “*structural problem*”.

1.3 Structure of the Thesis

This is an interdisciplinary thesis and, therefore, deals with topics that are commonly treated within different scientific disciplines. I have tried to write a thesis as modular as possible avoiding unnecessary crossed references between chapters. The idea is that every chapter could be read as an independent self-consistent unit so that if any reader is interested only in some particular aspects such as, for instance, continuum mechanics, numerical procedures or the implications of the obtained results on volcanology, he/she can read only his/her particular part of interest. The work is organised as follows:

- **Chapter 2.** *“Volcanic Processes. An overview”*

This chapter reviews some fundamental concepts of volcanology. The purpose is to provide a basis for those readers without any volcanological background. The overview is shallow and non-exhaustive but, nevertheless, should be sufficient to follow the work that will be developed in further chapters. Its lecture is strongly recommended to readers without any previous knowledge on volcanology. The state-of-the-art of numerical simulations within the frame of physical volcanology is also presented in order to contextualize the contributions of this thesis within its framework.

- **Chapter 3.** *“Governing Equations”*

This chapter develops the physical model and its governing equations. A state law for the magmatic mixture under the homogeneous approach is presented. Governing equations for the “flow problem” (simulation of volcanic eruptions) are the Navier-Stokes equations. Navier-Stokes equations are formulated using an Arbitrary Lagrangian-Eulerian (ALE) formulation in order to face properly caldera forming eruptions, in which the coupling fluid-structure must be taken into account. Governing equations for the “structural problem” are the standard of linear viscoelastic materials. Part of this chapter may seem superfluous to readers with a background on continuum mechanics.

- **Chapter 4.** *“Numerical Methods”*

This chapter presents the numerical methodology and the algorithms which are implemented in the context of a Finite Element Method (FEM). The ALE Navier-Stokes equations are solved using a fractional step method which allows to deal simultaneously with compressible and incompressible flows. The fluid-structure interaction is solved using an staggered procedure with a conservative remeshing strategy. Finally, a method to solve the “structural problem” is presented for the case of some particular viscoelastic rheologies which are commonly assumed to model ground deformation in volcanic areas. Some standard

numerical benchmarks are also presented in order to test the validity and the implementation of the algorithms.

- **Chapter 5.** *“Numerical Simulations of Volcanic Eruptions”*

This chapter presents some numerical simulations of magma chamber withdrawal for three different types of volcanic eruptions: volatile oversaturation driven (closed magma chambers), injection of fresh magma driven (open magma chambers) and caldera-forming. Despite the limitations and simplifications of the physical model some interesting results and qualitative dependencies can be envisaged from these numerical simulations.

- **Chapter 6.** *“Ground Deformation”*

This chapter presents some numerical simulations of ground deformation in volcanic areas. A comparison between analytical approaches and numerical solutions is performed. The comparison allows to quantify the error implicit in the analytical solutions and constrains the range of applicability of these widely used procedures. Some natural examples are also considered.

- **Chapter 7.** *“Conclusion”*

The last chapter points out which are the original contributions of this thesis, summarises the conclusions, and indicates which should be the future lines of research.

1.4 Notation

The notation used along this present work is the following. Latin alphabet using Times New Roman in *italics* (e.g. a , b , F , etc.) and Greek alphabet (e.g. \mathbf{r} , \mathbf{m} , \mathbf{y} , etc.) are used to designate scalar quantities. Latin alphabet using Times New Roman in **bold** (e.g. \mathbf{F} , \mathbf{u} , $\hat{\mathbf{x}}$, etc.) is, with few exceptions, used to indicate vectorial quantities. Finally, Latin alphabet using Algerian is reserved to tensorial¹ quantities (e.g. \mathbf{A} , \mathbf{F} , \mathbf{T} , etc). Vectorial and tensorial components are, obviously, treated as scalar entities. If not indicated, the International System of Units (SI) is always assumed for dimensional quantities. Tables 1.4.1 to 1.4.4 compile all the variables that appear all along the thesis. Vectorial and tensorial indexes run from 1 to n , being n the space dimension (2 or 3). The standard Einstein criteria for summation of dummy indexes is also assumed. If not indicated, tensorial/vectorial expressions are considered using an orthonormal frame of reference (Cartesian coordinates), in which the metric tensor is the identity. In consequence no distinction is made between covariant and contravariant components of any tensorial/vectorial quantity. In Cartesian coordinates the following definitions apply:

- Tensorial product of two vectors $[\mathbf{a} \otimes \mathbf{b}]_{ij} = a_i b_j$ (1.4.1)

- Tensor-Vector product $[\mathbf{A} \cdot \mathbf{b}]_i = A_{ik} b_k$ (1.4.2)
 $[\mathbf{b} \cdot \mathbf{A}]_i = b_k A_{ki}$

- Divergence of a vector $[\nabla \cdot \mathbf{a}] = \frac{\partial a_i}{\partial x_i}$ (1.4.3)

- Divergence of a tensor $[\nabla \cdot \mathbf{T}]_i = \frac{\partial T_{ki}}{\partial x_k}$ (1.4.4)
 $[\mathbf{T} \cdot \nabla]_i = \frac{\partial T_{ik}}{\partial x_k}$

- Product of two tensors $[\mathbf{A} \cdot \mathbf{B}]_{ij} = A_{ik} B_{kj}$ (1.4.5)

¹ The “word” tensor means, in the context of this thesis, tensor of rank two or greater and, in consequence, does not include neither tensors of rank zero (scalars) nor tensors of rank one (vectors).

• Double tensorial contraction $\mathbf{A} : \mathbf{B} = A_{ij} B_{ij}$

$\mathbf{A} \cdot \cdot \mathbf{B} = A_{ij} B_{ji}$ (1.4.6)

Variable	Meaning(s)	Units (SI)
a	Coefficient of thermal expansion	$^{\circ}\text{K}^{-1}$
	Volumetric fraction of gas	—
	Parameter of stabilisation [eq. 4.1.16]	s
	Upwind function	$^{\circ}$
	Average slope of the volcanic flanks	—
b	Isothermal compressibility modulus	Pa
ΔP	Overpressure/Underpressure	Pa
Δt	Time step	s
Δt_c	Critical time step	s
Γ	Generic boundary	$\text{m} (\text{m}^2)$
Γ_0	Complement of Γ_{FS}	$\text{m} (\text{m}^2)$
Γ_D	Dirichlet part of the boundary	$\text{m} (\text{m}^2)$
Γ_{FS}	Fluid-structure interface	$\text{m} (\text{m}^2)$
Γ_N	Neumann part of the boundary	$\text{m} (\text{m}^2)$
g	Parameter of the algorithm	—
	State law coefficient [barotropic flow]	—
	Adiabatic exponent [perfect gas]	—
e	Size to depth magma chamber ratio	—
c	Solubility [mass fraction of dissolved volatiles]	—
h	Coefficient of viscosity [viscoelasticity]	Pa . s
k	Thermal diffusivity	$\text{m}^2 \cdot \text{s}$
l	Bulk viscosity	Pa . s
	Lamé parameter	Pa
	Viscosity	Pa . s
m	Lamé parameter	Pa
	Relaxation function [viscoelasticity]	Pa
	Parameter of the algorithm [convective transport equation]	—
q_c	Parameter of the algorithm [convective transport equation]	—
r	Density	$\text{Kg} \cdot \text{m}^{-3}$
r_g	Gas density	$\text{Kg} \cdot \text{m}^{-3}$
r_l	Liquid density [without dissolved volatiles]	$\text{Kg} \cdot \text{m}^{-3}$
r_r	Mean density of the crustal rocks	$\text{Kg} \cdot \text{m}^{-3}$
r_s	Melt density [with dissolved volatiles]	$\text{Kg} \cdot \text{m}^{-3}$
t	Characteristic time [viscoelasticity]	s^{-1}
	Upwind parameter [intrinsic time]	s
u	Poisson coefficient	—
	Cinematic viscosity	$\text{m}^2 \cdot \text{s}$
Ω	Generic spatial domain	$\text{m}^2 (\text{m}^3)$
x	Function for the quasi-Laplacian method [eq. 4.3.10]	—

Table 1.4.1. List of scalar variables designated with Greek alphabet.

1.4 Notation

Variable	Meaning(s)	Units (SI)
A	Parameter of the algorithm [table 4.1.2]	
	Parameter for the critical time step [eq. 4.1.81]	—
A^e	Elemental area	m ²
a	Half horizontal extension of the magma chamber	m
a_c	Radius of the collapse caldera	m
B	Parameter of the algorithm [table 4.1.2]	
b	Half vertical extension of the magma chamber	m
C	Scalar function [convective transport equation]	
	Composition field [volume fraction]	—
\bar{C}	Averaged magma composition	—
c	Speed of the sound	m · s ⁻¹
c_v	Specific heat at constant volume	J · Kg ⁻¹ · °K ⁻¹
d	Characteristic length	m
E	Total energy per unit of volume	J · m ⁻³
	Young modulus	Pa
e	Specific total energy	J · Kg ⁻¹
e_o	Specific internal energy	J · Kg ⁻¹
F	Determinant of \mathbf{F}	—
\hat{F}	Determinant of $\hat{\mathbf{F}}$	—
F_s	Factor of safety	—
f	Fugacity	Pa
Gr	Grashof number	—
H_c	Height of the volcanic conduit cut off	m
H_{cha}	Depth of the magma chamber	m
H_{con}	Height of the volcanic edifice	m
h	Element size	m
k	Thermal conductivity	J · s ⁻¹ · °K ⁻¹ · m ⁻¹
	Effective permeability	m ² · s · kg ⁻¹
L	Length of the volcanic conduit	m
M	Mass	Kg
M_c	Mach number	—
M_e	Total erupted mass	Kg
m_d	Mass of dissolved gas	Kg
m_g	Mass of exsolved gas	Kg
m_l	Mass of liquid	Kg
m_s	Mass of melt [$m_s = m_l + m_d$]	Kg
m_v	Mass of volatiles [$m_v = m_d + m_g$]	Kg
N	Shape function	
N_u	Nusselt number	—
n	Constant of solubility [Henry law]	—
n_e	Number of elements of the FEM mesh	—
n_g	Mass fraction of exsolved gas	—
P_e	Péclet number	—
P_r	Prandtl number	—
p	Pressure	Pa
p_c	Critical [exsolution] pressure	Pa
p_l	Lithostatic pressure	Pa

p_m	Molecular weight	Kg . mol ⁻¹
Q	Mass flow rate	Kg . s ⁻¹
	Gas constant [$Q = R / p_m$]	J . °K ⁻¹ . Kg ⁻¹
q_g	Mass flux of gas [Darcy's law]	Kg . m ⁻² . s ⁻¹
R	Perfect gas constant	J . mol ⁻¹ . °K ⁻¹
R_e	Reynolds number	—
r_c	Radius of the volcanic conduit	m
S_c	Section of the volcanic conduit	m ²
s	Constant of solubility [Henry law]	Pa ⁻ⁿ
T	Temperature	°K
t	Time	s
V	Volume	m ³
V_c	Volume of the magma chamber	m ³
W	Mass fraction of volatiles	—
W_C	Test function [convective transport equation]	
W_p	Test function [continuity equation]	
W_T	Test function [energy equation]	

Table 1.4.2. List of scalar variables designated with Latin alphabet.

Variable	Meaning	Units (SI)
D	Strain rate tensor [components D_{ij}]	s ⁻¹
E	Strain tensor [components E_{ij}]	—
F	Strain gradient tensor [components F_{ij}]	—
$\hat{\mathbf{F}}$	Mesh strain gradient tensor [components \hat{F}_{ij}]	—
G	Relaxation tensor [components G_{ijkl}]	Pa
I	Identity tensor	—
J	Creep tensor [components J_{ijkl}]	Pa ⁻¹
S	Cauchy stress tensor [components S_{ij}]	Pa
S^P	Piola-Kirchhoff tensor [components S_{ij}^P]	Pa
T	Viscous stress tensor [components T_{ij}]	Pa

Table 1.4.3. List of tensorial variables. Units refer to components.

Variable	Meaning(s)	Units (SI)
\mathbf{b}	Body forces per unit of mass [components b_i]	$\text{m} \cdot \text{s}^{-2}$
\mathbf{c}	Convective velocity [components c_i]	$\text{m} \cdot \text{s}^{-1}$
\mathbf{d}	Structural displacement or position [components d_i]	m
\mathbf{F}^C	Vector of convective fluxes [see eq. 4.1.2 for components]	
\mathbf{F}^D	Vector of diffusive fluxes [see eq. 4.1.2 for components]	
\mathbf{f}^{int}	Internal forces in the structure [components f_i^{int}]	N
\mathbf{f}^{ext}	External forces in the structure [components f_i^{ext}]	N
$\mathbf{f}_{\text{FS}}^{\text{ext}}$	External forces in the structure at Γ_{FS}	N
\mathbf{g}	Gravity acceleration [components g_i]	$\text{m} \cdot \text{s}^{-2}$
\mathbf{n}	Outwards unit normal [components n_i]	
\mathbf{q}	Heat flux [components q_i]	$\text{J} \cdot \text{s}^{-1}$
\mathbf{S}	Vector of source terms [see eq. 4.1.2 for components]	
\mathbf{U}	Momentum [components U_i]	$\text{Kg} \cdot \text{m} \cdot \text{s}^{-1}$
$\tilde{\mathbf{U}}$	Fractional momentum [components \tilde{U}_i]	$\text{Kg} \cdot \text{m} \cdot \text{s}^{-1}$
\mathbf{u}	Velocity [spatial frame] [components u_i]	$\text{m} \cdot \text{s}^{-1}$
	Displacement [components u_i]	m
\mathbf{u}_b	Velocity of collapse caldera subsidence	$\text{m} \cdot \text{s}^{-1}$
\mathbf{u}_g	Velocity of the gas	$\text{m} \cdot \text{s}^{-1}$
\mathbf{u}_i	Inflow velocity	$\text{m} \cdot \text{s}^{-1}$
\mathbf{u}_l	Velocity of the liquid	$\text{m} \cdot \text{s}^{-1}$
$\hat{\mathbf{u}}$	Mesh velocity [spatial frame] [components \hat{u}_i]	$\text{m} \cdot \text{s}^{-1}$
\mathbf{t}	Traction [components t_i]	Pa
\mathbf{V}	Fluid state vector [see eq. 4.1.2 for components]	
\mathbf{X}	Material coordinates [components X_i]	m
\mathbf{x}	Spatial coordinates [components x_i]	m
$\hat{\mathbf{x}}$	Mesh displacement [components \hat{x}_i]	m
\mathbf{W}	Test function [momentum] [components W_i]	
$\tilde{\mathbf{W}}$	Test function [fractional momentum] [components \tilde{W}_i]	
	Test function [mechanical equation] [components \tilde{W}_i]	
\mathbf{W}_G	Test function [pressure gradient projection]	
\mathbf{W}_L	Test function [mesh displacement equation]	
\mathbf{W}_X	Test function [quasi-Laplacian method]	
\mathbf{w}	Velocity [computational frame] [components w_i]	$\text{m} \cdot \text{s}^{-1}$
\mathbf{c}	Computational coordinates [components c_i]	m
\bar{q}_1	Parameter of the algorithm [components q_1^i]	—
\bar{q}_2	Parameter of the algorithm [components q_2^i]	—
\bar{q}_3	Parameter of the algorithm [components q_3^i]	—
ξ	Gradient of pressure [components x_i]	$\text{N} \cdot \text{m}^{-3}$

Table 1.4.4. List of vectorial variables. Units refer to components.

Chapter 2

Volcanic Processes:

An Overview

Chapter Contents

2.1 Magma Genesis

2.1.1 The Melting Process

2.1.2 Types of Magmas

2.2 Physical Properties of Magmas

2.2.1 Density and Temperature

2.2.2 Viscosity

2.2.3 Volatiles and Solubility Laws

2.2.4 Thermal Diffusivity

2.3 The Eruptive Process

2.3.1 Triggering Mechanisms

2.3.2 Explosive Volcanism. Exsolution and Fragmentation Levels

2.3.3 Caldera Forming Eruptions

2.4 Modelling in Physical Volcanology: State-of-the-Art

2.4.1 Eruptive Models

2.4.1.1 Conduit Models

2.4.1.2 Chamber Withdrawal Models

2.4.2 Ground Deformation Models

2.5 References

Abstract

This chapter has a double objective. Firstly, some elemental concepts of volcanology are explained. Rather than an exhaustive exposition, the aim is to provide a basis necessary to follow properly part of the work that will be developed during the subsequent chapters of this thesis. This part is mainly designed to those readers without any volcanological background. Secondly, the state-of-the-art of the numerical simulations within the frame of physical volcanology is considered. This is done in order to contextualize the contributions of this thesis within its own framework.

2.1 Magma Genesis

2.1.1 The Melting Process

Magmas are silicate melts originated in the upper mantle or at the base of the lower crust, where the existing physical conditions favour partial melting of rocks. Figure 2.1.1 reflects how magma genesis can be triggered by different factors that, in general, can act together or separately. Among them, the most important are decompression, increase of temperature and chemical composition changes (basically those related to water assimilation). Thus, magmas can be generated when a considerable increase of temperature is applied to an initially solid rock, when a solid rock initially at high pressures and temperatures is decompressed, or by the assimilation of water that significantly reduces the melting point of some mineral components.

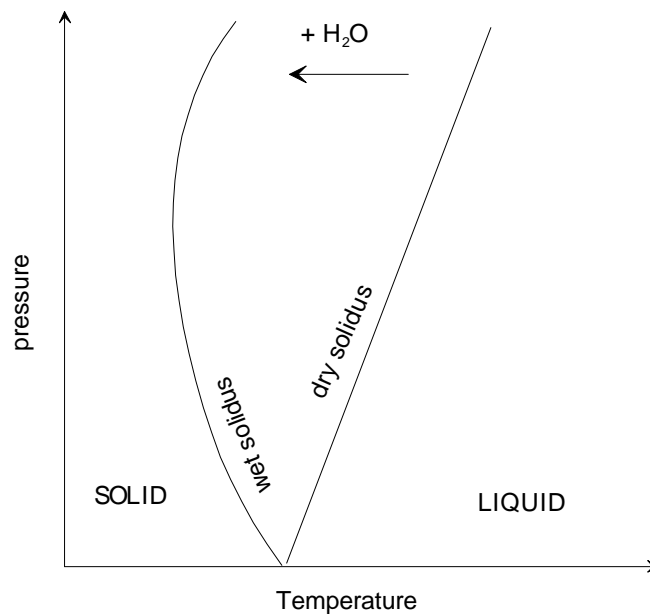


Figure 2.1.1. Schematic phase diagram. Melting can be produced increasing temperature or water content or decreasing pressure.

The processes related to the formation and subsequent evolution of magmas are known as *petrogenic processes*. Nowadays, petrogenic processes are well explained within the frame of the plate tectonics theory. In this theory, the rigid lithospheric plates constituted by the crust and the uppermost part of the mantle move above a plastic asthenosphere located in the upper mantle, at depths currently ranging from 150 to 400 Km. The association between most of the active volcanoes and the present margins of the lithospheric plates reflects that significant melting occurs at the neighbourhood of the plates junctions, that is, at the divergent plate

2.1 Magma Genesis

boundaries or mid-oceanic ridges and at the convergent plate boundaries or subduction zones (see figure 2.1.2). However, the existence of intraplate volcanoes shows that more located melting generated away from the plate boundaries is also possible.

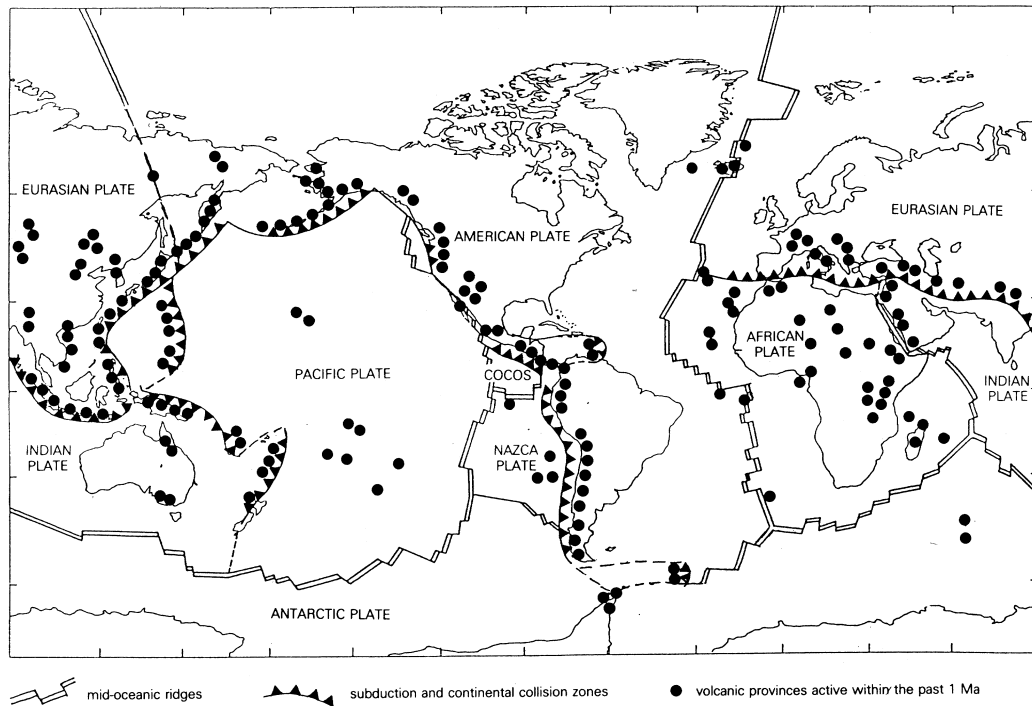


Figure 2.1.2. Global tectonic map showing the distribution of present-day volcanic activity. Extracted from [Wilson, 1989].

At the mid-oceanic ridges (at the divergent plate boundaries), the separation of lithospheric plates allows a continuous ascension of hot asthenospheric material through the axis of the ridge. This ascension induces an adiabatic decompression and a subsequent melting of great volumes of mantle material to form basaltic magmas that are either erupted or intruded into the oceanic crustal layer (see figure 2.1.3). At the subduction zones, cold lithospheric plates (continental or oceanic) containing sediments and metamorphosed oceanic crust sink into the mantle. The increase in temperature produced during the subduction dehydrate the subducted materials producing an appreciable entry of hydrous fluids into the mantle mineral system. This phenomena considerably reduces the melting point of the minerals and partial melting can take place even at relatively low ambient temperatures (see figure 2.1.4). The resultant hydrous magmas normally differentiate in magma chambers to form a range of more silica-rich magma types. Volcanism associated to this environment can be highly explosive due to the high volatile contents (mainly water) of the magmas. Finally, at the interior of the lithospheric plates, melting is generated by an anomalous increase of the upper mantle temperature. This phenomena is related to the convective dynamics of the asthenosphere which induces the existence of areas where hot currents of mantle material move upwards (hot spots) and areas where cold material

sinks downwards. In general, those magmas generated in the mantle have a high density and a low viscosity while, in contrast, magmas generated by melting of the crust are of low density and high viscosity. Table 2.1.1 summarises the different magma types associated with specific tectonic settings.

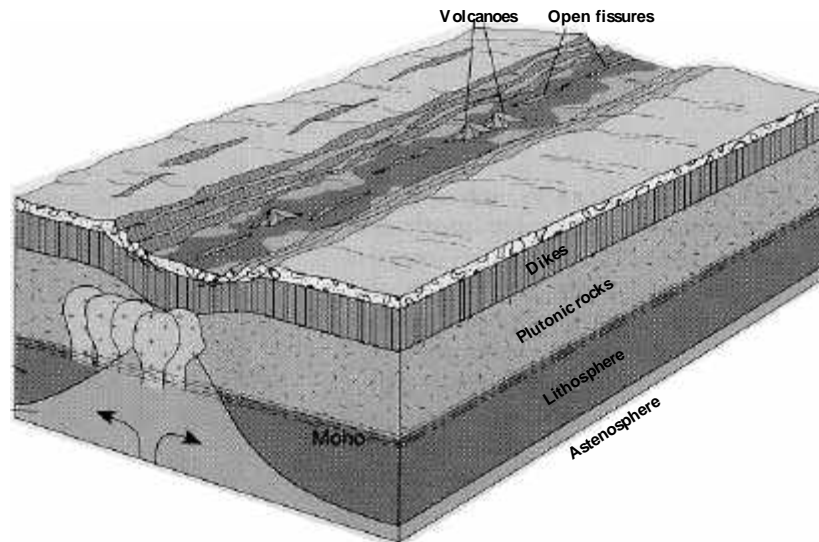


Figure 2.1.3. Schematic diagram illustrating a mid-oceanic divergent plate margin. Modified from [Moore and Twiss, 1995].

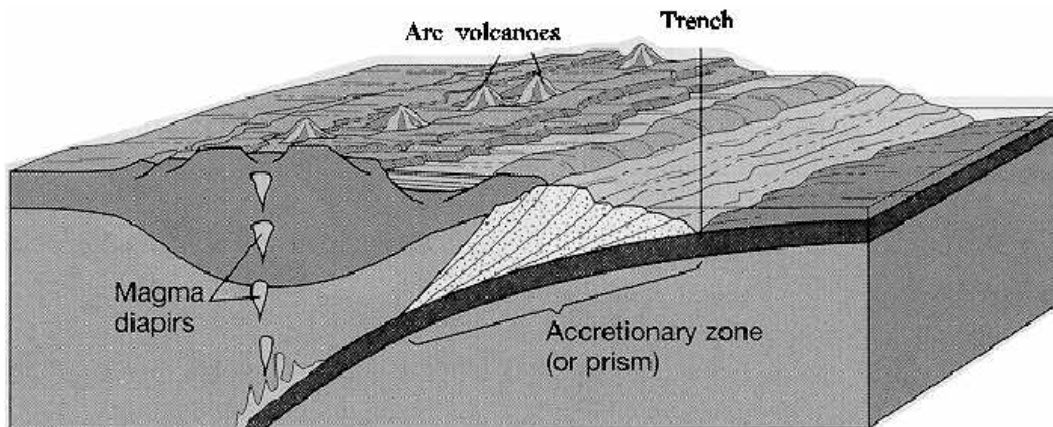


Figure 2.1.4. Schematic diagram illustrating a subduction zone. Modified from [Moore and Twiss, 1995].

Rocks are constituted by several minerals, each one with its own melting temperature at a given pressure. In consequence, and whichever the tectonic framework considered, magma genesis starts with the melting of those minerals with a lower melting point and, as cooling progresses, it gradually affects other minerals producing thus a melt formed by partial melting of the rocks. In general, liquids generated by partial melting are of lower density than the

2.1 Magma Genesis

surrounding material and, in consequence, experiment an upwards buoyancy force. As melting progresses and due to the gravity forces, the increasing volume of liquid tends to storage at the roof of the melting zone while the residual solid components tend to compact downwards giving rise to a more effective separation between solid and liquid phases. When the volume of liquid reaches a critical value it leaves the melting zone and ascends towards shallower zones forming a diapir (if the surrounding rocks admit plastic deformation) or flowing through fractures (if the host rock is fragile and exist fractures that intersect the melting zone). In many cases, magma ascends initially as a diapir due to the plastic behaviour of the environment and then, once it reaches shallower parts of the crust in which rocks can not stand plastic deformation, ascends through swarms of sills and dikes. During this process magma cools, changes its composition and, finally, stores in shallow reservoirs (magma chambers). Lithostatic pressure, local tectonic forces and the presence or absence of mechanical discontinuities such as pre-existing fractures or interfaces between different layers of rocks will determine where magma is stored. The accumulation of magmas in places different from the original melting zone will thus give rise to formation of magma chambers, the evolution of which will strongly influence the dynamics of the volcanic system. Magma chambers are far from steady systems. On the contrary, once in a reservoir, magmas continue its chemical evolution (mainly by means of fractional crystallisation processes) and, in addition, chambers are normally refilled with inflows of new material. Different factors during this evolutionary process can overpressurize the chamber and, eventually, trigger a (or a series of) volcanic eruption.

Tectonic setting	Convergent plate margin	Divergent plate margin	Within intra-oceanic plate	Within intra-continental plate
Volcanic feature	island arcs, active continental margins	mid-oceanic ridges	oceanic islands	continental rift zones
Magma type	basalts and differentiates	basalts	basalts and differentiates	basalts and differentiates

Table 2.1.1. Summary of the relationship between tectonic setting, volcanic feature and magma type.

2.1.2 Types of Magmas

A common procedure to classify magmas is the TAS (Total Alkalis-Silica) diagram¹, introduced by [Cox *et al.*, 1979]. This diagram plots the alkalis content (Na₂O+K₂O in wt. %) versus the silica content (SiO₂ in wt. %). Depending on the silica content, the TAS diagram divides magmas into ultrabasic, basic, intermediate and acid (see figure 2.1.5). Ultrabasic and basic magmas have a silica content lower than approximately 50% in wt., whereas a magma is considered to be acid if its silica content is greater than 65% in wt. Moreover, depending on its alkali content a magma is said to be alkali (with a high alkali content) or sub-alkali (with a low alkali content).

Observation The term silicic magma is also commonly used as a synonymous of acid magma. On the other hand, a visual classification (depending on the colour) divides magmas into mafic and felsic. With few exceptions, mafic magmas are basic and felsic magmas are acid (silicic).

The great variety of existing magmas as well as their different properties is explained not only by its different origin but also by the enormous variety of complex processes that they undergo during their evolution. Magmas originated by partial melting within the mantle are basic and ultrabasic. However, during migration to the surface they can suffer contamination, mixing and partial or fractional crystallisation processes that will change its initial composition and properties. Once placed in a magma chamber, magmas cool by losing heat through the walls of the reservoir and, as temperature decreases, different minerals begin to crystallise (each one when temperature falls below its liquidus). The density contrast between the newly formed crystals and the remainder liquid removes crystals from the melt. This process is known as *fractional crystallisation*. Fractional crystallisation processes are rather complex and are not under the scope of this work. For our purposes, it is sufficient to know that, as minerals with a higher temperature of crystallisation do not contain silica, the result of the process is that the residual liquid becomes richer in silica and, in consequence, magma progressively evolves from basic to acid (silicic). For this reason, the terms primitive magma and evolved magma (chemically evolved magma) are sometimes used as synonyms of basic magma and acid magma. Another important issue concerns to volatile species. Many volatile species (such as H₂O, CO₂, SO₂, F₂, S₂, etc.) may be present in the melt. Similarly, these volatiles are not retained by the formed crystals so that their proportion with respect to the residual melt will tend to increase. This has a dramatic effect on the possible eruptions since volatiles play a major role in determining whether a eruption is effusive or explosive. Once all the minerals have crystallised, the magma chamber quenches and becomes a plutonic rock. The duration of the whole process depends on

¹ Strictly speaking, the TAS diagram classifies volcanic rocks rather than magmas. However, this distinction is not important for our purposes.

2.1 Magma Genesis

the cooling velocity and, in general, can last thousands of years. However, the conditions to extrude magma out of the chamber can be eventually achieved at any time instant during the process. If they do so, a volcanic eruption is triggered providing, of course, that fractures are able to reach the surface of the Earth.

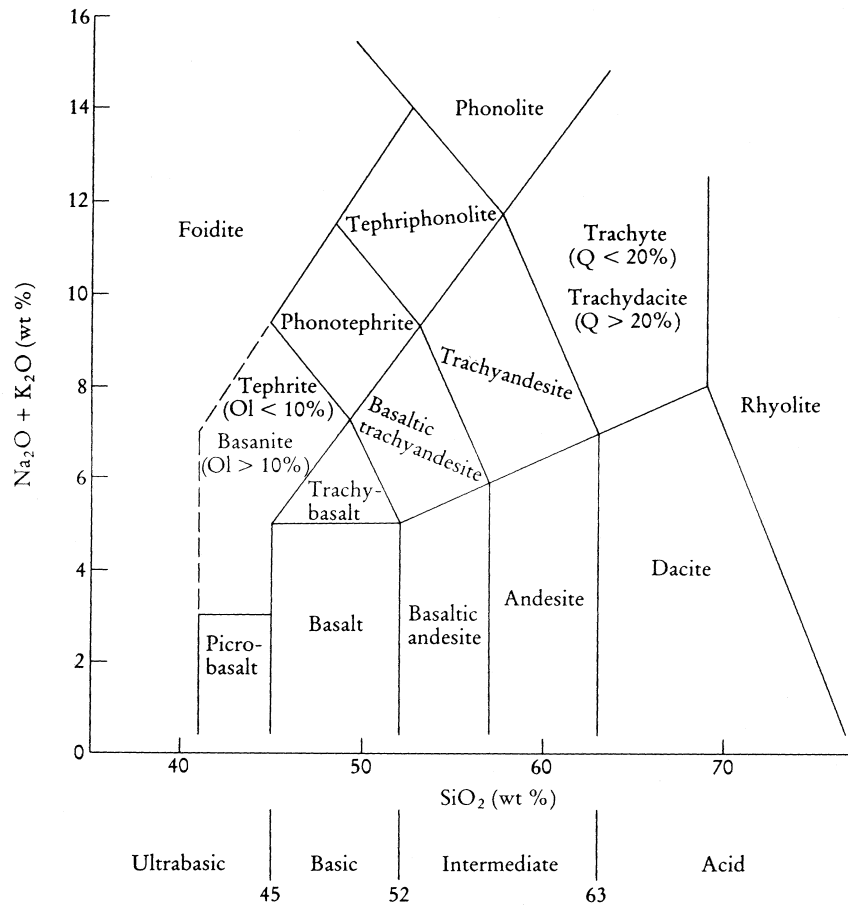


Figure 2.1.5. Chemical classification of volcanic rocks according to the original version of the total alkalis versus silica (TAS) diagram. Extracted from [Rollinson, 1993].

2.2 Physical Properties of Magmas

Generally speaking, physical properties of magma are strongly dependent on magma composition and, in consequence, susceptible to vary notably as magma evolves from basic to acid. This is schematically illustrated in figure 2.2.1. The lack of experimental data under magmatic conditions had been traditionally one of the major drawbacks in the comprehension and modelling of volcanic processes. However, during the last decades, the amount of experimental data available in literature has grown spectacularly in parallel with (and partially stimulated by) the development of physical volcanology. This section outlines briefly the present knowledge concerning to some physical properties of magmas that will be relevant in the context of the present work. The reader is referred to [McBirney and Murase, 1984], [Wilson, 1989] or [Dingwell, 1998] for a more extensive description.

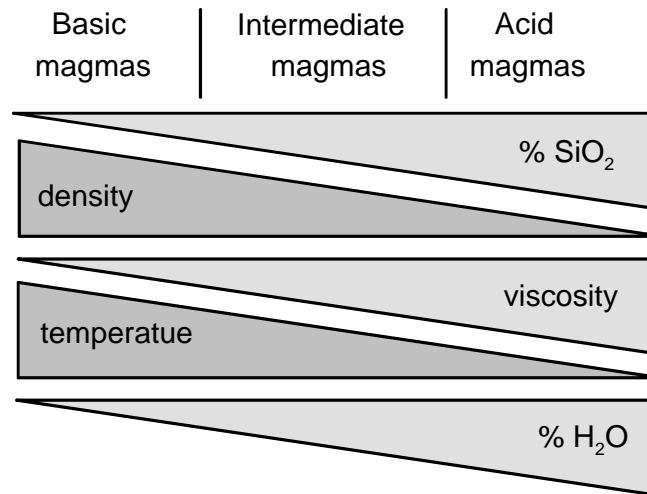


Figure 2.2.1. Schematic cartoon showing the qualitative dependence of important magma properties in terms magma composition.

2.2.1 Density and Temperature

Properties that govern magma density are composition, temperature, pressure, crystal content and, finally, the presence of volatile species. As previously explained, chemical evolution of magmas by means of fractional crystallisation processes leads to a progressive silica enrichment since it removes the heavier components of the initial melt by means of crystal segregation. This fact accounts for density dependence on chemical composition, that is, explains why the more evolved is a magma the lower is its density. Concerning to pressure and temperature dependencies, one can assume, as is usual in many liquids, that the density ρ is given by

$$r(T, p) = r_o \left[1 + \frac{p - p_o}{b} - a(T - T_o) \right] \quad (2.2.1)$$

where r_o is a reference density (that of the liquid at pressure p_o and temperature T_o), b is the isothermal compressibility modulus and a is the thermal expansion coefficient. Typical values for b in magmas are 10-100GPa, while a is commonly $10^{-5} \text{ }^\circ\text{K}^{-1}$ [Touloukian *et al.*, 1981]. It implies that density changes induced by those pressure and temperature variations which typically occur in volcanic processes are, in general, a second order effect and, whichever the case, are lower than those induced by compositional variations. This is illustrated in figure 2.2.2. Density is also sensible to the presence of volatile species. If these volatiles are dissolved within the magma its influence on the density can be (as a first approximation) neglected. However, when the melt is oversaturated in volatiles it becomes a two-phase flow which can be highly compressible. All in all, and for the purpose of the work, density of undersaturated magmas will be considered as a constant while a state law for the gas-magma mixture suitable under oversaturated magmatic conditions [Folch *et al.*, 1998a] will be proposed and widely discussed in section 3.2 of this present work.

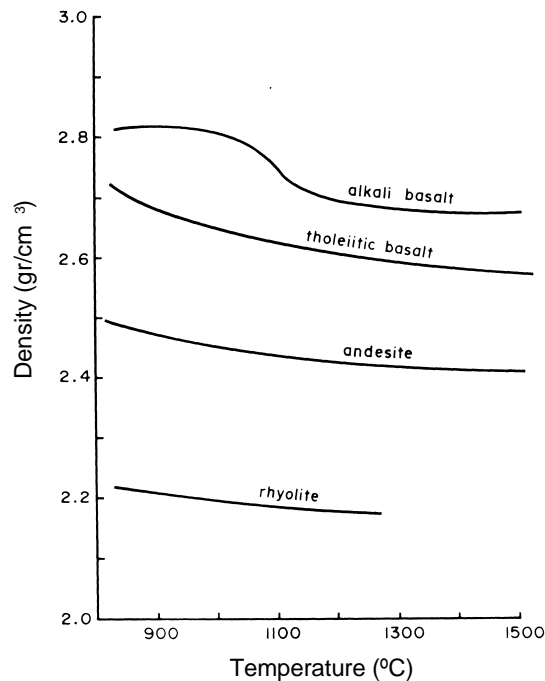


Figure 2.2.2. Magma density (at atmospheric pressure) versus temperature for different magma compositions. Extracted from [Cas and Wright, 1988] after [McBirney, 1973]. Note how density variations due to compositional changes are much more important than those induced by temperature variations.

Temperatures of magmas can be evaluated in a variety of ways such as, for instance, direct measurements on lavas. In the case of the acid magmas, there are fewer directly obtained data available not only because few eruptions have been observed in this century but also because the eruption of acid magmas is commonly associated with explosive volcanism which makes impossible an in situ measurement. Temperatures of magmas vary as it evolves due to cooling related processes. Thus, the general tendency is that the more evolved is a magma the lower is its temperature. Table 2.2.1 gives typical values of magma densities and temperatures.

Magma type	Density (kg/m ³)	Temperature (°C)
basalt	2600-2900	1000-1200
andesite	2400-2600	950-1200
dacite	2400-2600	800-1100
rhyolite	2200-2400	700-900

Table 2.2.1. Summary of typical density and temperature magma values. Values of density assume a non-vesiculated magma.

2.2.2 Viscosity

Magma rheology is a key factor to explain many volcanic processes. In particular, a good knowledge of the viscosity dependencies is vital in order to assess successfully many processes related to explosive volcanism such as, for instance, magma fragmentation. Viscosity of silicate melts is sensitive to several factors such as volatile content, temperature, composition, pressure or crystal content and is, by far, the property of silicate melts that may vary within a wider range of values. Two of these parameters have a major importance: temperature and, specially, volatile content (water in the case of acid magmas). In general, the lower are temperature and water content, the higher is the magma viscosity. The influence of other volatile species (such as CO₂) may be important in basic magmas, but its influence has not been well quantified yet.

Unfortunately the experimental measure of the viscosity of water-bearing melts is not an easy task because, in order to dissolve significant amounts of volatiles, high pressures (i.e. expensive apparatus) are required. Two methods proposed by [Shaw, 1972] and [Bottinga and Weill, 1972] have been traditionally used to compute viscosities of crystal-free magmas. These methods agree with experimental data, but only for low pressures and water contents. In general, the experimental data available is yet insufficient under natural conditions. However, [Hess and Dingwell, 1996] have recently obtained experimental values for viscosities of rhyolitic

(acid) melts that effectively cover the entire range of natural conditions. Despite these data should not be extrapolated to other compositions, they will be sufficient for our purposes.

Figure 2.2.3 shows the experimental data of [Hess and Dingwell, 1996]. For a given water content and at high temperatures, the \log_{10} of the viscosity is inversely proportional to the temperature. This relationship is known as the *Arrhenian behaviour*. As temperature decreases, the melts become significantly non-linear versus reciprocal temperature, that is, tend to show a non-Arrhenian behaviour. On the other hand, viscosity dependence on water presents a smooth slope at high to moderate water contents (equal or greater than 1-2 wt.%) but, in contrast, is strongly non-linear at low water content.

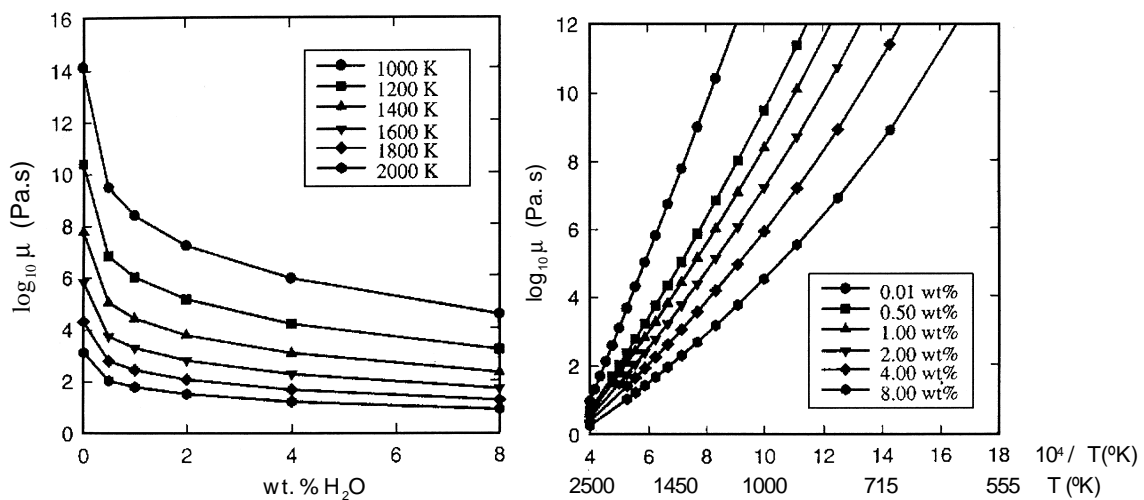


Figure 2.2.3. Experimental melt viscosities of hydrous melts extracted from [Hess and Dingwell, 1996]. Left: viscosity versus water content in wt.% for different temperatures. Right: viscosity versus temperature for different water contents. Note how the Arrhenian relationship ($\log_{10} \mu \propto 1/T$) is verified only at high temperatures.

2.2.3 Volatiles and Solubility Laws

As previously stated, magmas usually contain significant amounts of dissolved volatile species. Dissolved volatiles not only affect magma properties (such viscosity) but also play a major role in determining the nature of volcanic eruptions in terms of whether they might be explosive or non-explosive. In consequence, the solubility c of a given volatile specie, defined as the maximum mass fraction of the volatile that can be dissolved within the melt, is a key parameter to explain many important volcanic processes. When the amount of volatiles that a magma contains effectively is less than its solubility, the melt is *undersaturated*. On the contrary, when the amount of volatiles is greater than the maximum amount that can be dissolved for a given ambient conditions, the melt is *oversaturated*, the remainder volatiles are exsolved and

magma becomes a two-phase flow composed by oversaturated liquid plus gas bubbles. Gas exsolution may lead to explosive volcanism (see section 2.3).

Many volatile species can be, in general, present in magmas. Among them, the most important are water and carbon dioxide. In basic magmas both species can be important whereas in acid magmas water is more important due to its higher abundance. The variety in the water content is explained not only by the different origins, genesis and chemical composition of the resulting magmas but also because fractional crystallisation has the effect of concentrating the dissolved volatile components in the remainder liquid. Hence, and generally speaking, the more evolved is a magma the greater is its water content.

Solubility of volatiles in silicate melts mainly depends on chemical composition, pressure and temperature. In general, temperature dependence is the less important, and evolves from a slight negative dependence at low pressures through temperature invariance at intermediate pressures to a positive dependence at high pressures (see figure 2.2.4).

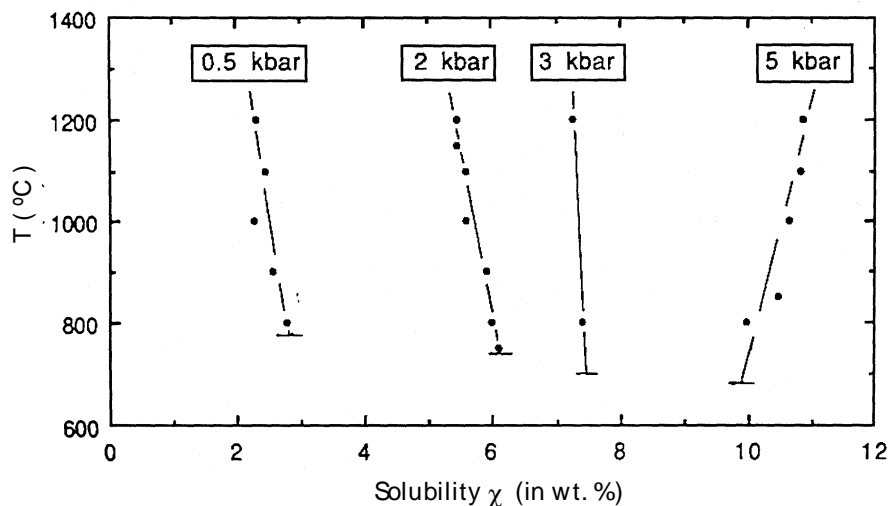


Figure 2.2.4. Temperature dependence of water solubility for an acid melt. Results at different pressures. Extracted from [Holtz *et al.*, 1995].

Pressure dependence is the most important and allows to explain some important processes related to explosive volcanism. The obtain of experimental data on volatile solubility has been a subject of increasing interest during the last decade. A compilation of the results available is not relevant here, and the reader is referred to [Carroll and Holloway, 1994] or [Dingwell, 1998] where extensive reviews can be found. However, and despite the relative abundance of data, the disposal of theoretical models that satisfactorily fit the experimental

2.2 Physical Properties of Magmas

results is still very constrained. The simplest analytical approach is a *Henry law* type equation, in which solubility is given by

$$c = s p^n \quad (2.2.2)$$

where p is pressure and s and n are constants that depend on the volatile specie considered and on magma composition. Table 2.2.2 gives some values for these parameters that will be relevant in this work.

Volatile	s	n
H ₂ O in rhyolite (acid magma) ^[1]	4.11×10^{-6}	0.5
H ₂ O in basalt ^[2]	6.8×10^{-8}	0.7
CO ₂ in basalt ^[3]	4.4×10^{-12}	1.0

Table 2.2.2. Standard values for the Henry law approach (see eq. 2.2.2). Values extracted from :[1] [Burnham and Jahns, 1962], [2] [Hamilton et al., 1964] and [3] [Stolper and Holloway, 1988]. Values are in SI.

After the early introduction of the Henry law dependence, different methods of successive complexity to estimate solubilities (specially that of water) have been proposed in order to fit the increasing amount of experimental data. Among them, the Burnham and the Stolper methods should be mentioned. The *Burnham method* [Burnham and Jahns, 1962; Burnham and Davis, 1971; Burnham and Davis, 1974; Burnham, 1994] computes water solubility in silicate melts in terms of 8-oxygen normative components for any pressure and temperature. The *Stolper method* [Silver and Stolper, 1988] fits thermodynamic parameters to available solubility data for individual magma compositions. The Stolper model is less versatile than the Burnham model but, in contrast, is likely to be more accurate for those compositions to which it has been applied. The description of both methods is not under the scope of this work. Nevertheless, its practical implementation is outlined in boxes 2.2.1 and 2.2.2. For our proposes, it will be sufficient to consider only the Henry law type dependence not only because the computation of solubilities by means of these methods can be tedious but also because the differences between the simple Henry law and these more elaborated models are relatively small, at least at low to moderate pressures. This fact is illustrated in figure 2.2.5.

Box 2.2.1. Calculation of water solubility in a silicate melt using a simplified version of the Burnham model. See [Burnham, 1994] or [Holloway and Blank, 1994] for major explanation.

1. Given the pressure p (in bars) and the temperature T (in °K) compute

$$k(p, T) = 5.0 + K + (\ln p) (4.481 \times 10^{-8} \cdot T^2 - 1.51 \times 10^{-4} \cdot T - 1.137) + (\ln p)^2 (1.831 \times 10^{-8} \cdot T^2 - 4.882 \times 10^{-5} \cdot T + 4.656 \times 10^{-2}) + (\ln p)^3 (7.8 \times 10^{-3}) - (\ln p)^4 (5.012 \times 10^{-4}) + T (4.754 \times 10^{-3} - 1.621 \times 10^{-6} \cdot T)$$

where K is a composition dependent factor (see below).

2. Compute the mole fraction of water X using

$$X = \frac{1}{\sqrt{k(p, T)}} \quad \text{or, if } X > 0.5, \text{ using}$$

$$X = 0.5 + \ln \left[\frac{4}{k(p, T)} \right] / \left[6.52 - \frac{2667}{T} \right]$$

3. Compute the solubility χ by means of

$$c = \frac{18.02 X}{18.02 X + (1 - X) \cdot W}$$

where W is a parameter. The parameters K and W for the most common compositions are

	W	K
basanite	297	0.14
alkalic basalt	296	0.19
tholeiitic basalt	292	0.24
andesite	276	0.17
dacite	265	0.15
rhyolite	261	0.19

Box 2.2.2. Computation of water solubility in a silicate melt using a version of the Stolper model. See [Silver and Stolper, 1988] or [Holloway and Blank, 1994] for major explanation. Let p_o (in bars) and T_o (in °K) be a reference pressure and a reference temperature (usually, $p_o = 1\text{bar}$ and $T_o = 1200^\circ\text{K}$).

1. Compute water fugacity f_{H_2O} at the required pressure p and temperature T by means of

$$f_{H_2O} = p_o e^{\frac{1}{RT} \int_{p_o}^p V(p) dp}$$

where R is the perfect gas constant ($R = 83.14 \text{ bar cm}^3 \text{ mol}^{-1} \text{ }^\circ\text{K}^{-1}$) and V is the molar volume, computed using the modified Redlich-Kwong equation [Holloway, 1977]

$$p = \frac{RT}{V-b} - \frac{a(T)}{V(V+b)\sqrt{T}}$$

with $b = 14.6$ and $a(T) = 166.8 \times 10^6 - 193080T + 186.4T^2 - 0.071288T^3$ (here, T is in °C).

2. Compute the activity of water X_{H_2O} in the melt at pressure p and temperature T using

$$X_{H_2O} = X_{H_2O}^o \frac{f_{H_2O}}{f_{H_2O}^o} e^{-\frac{V_o}{RT_o}(p-p_o)}$$

where $X_{H_2O}^o$, $f_{H_2O}^o$ and V_o are, respectively, the activity of water, its fugacity and its molar volume at the reference conditions.

3. Compute the activity of the hydroxyl group X_{OH} solving iteratively

$$-\ln \left(\frac{X_{OH}^2}{X_{H_2O} (1 - X_{OH} - X_{H_2O})} \right) = 0.403 + 15.333X_{OH} + 10.894X_{H_2O}$$

4. Calculate the total mole fraction of water in the melt $X = X_{H_2O} + 0.5 X_{OH}$

5. Compute the solubility χ by means of

$$c = \frac{18.02 X}{18.02 X + (1 - X) \cdot W}$$

where W is 36.6 in basic magmas and 32.5 in acid magmas (rhyolite).

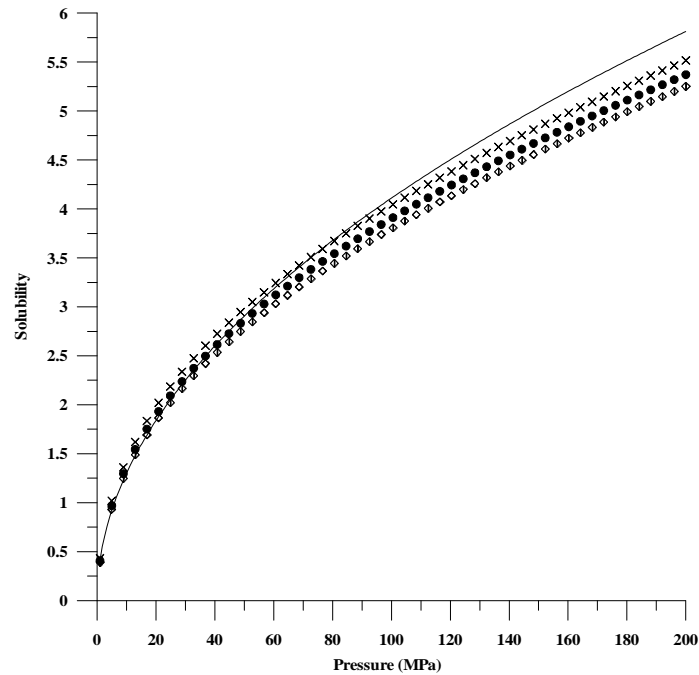


Figure 2.2.5. Water solubility in a rhyolitic melt as a function of pressure. Comparison between the Henry law (continuous curve) and the version of the Burnham model described in box 2.2.1 (symbols) for different temperatures: \times at 750°C, \bullet at 850°C, and \diamond at 950°C. Despite its simplicity, the Henry law works well at low to moderate pressures.

2.2.4 Thermal Diffusivity

Thermal diffusivity \mathbf{k} is defined as

$$\mathbf{k} = \frac{k}{c_v \mathbf{r}} \quad (2.2.3)$$

where k is the thermal conductivity, \mathbf{r} is density and c_v is the specific heat at constant volume. From a physical point of view, its value dictates whether heat is more likely to be transported by diffusion or by convection. The dependence of thermal diffusivity on temperature for a rhyolitic melt was measured by [Bagdassarov and Dingwell, 1994]. Experimental results are shown in figure 2.2.6, and reflect that thermal diffusivity is weakly dependent on temperature and has a typical value of 10^{-6} m²/s.

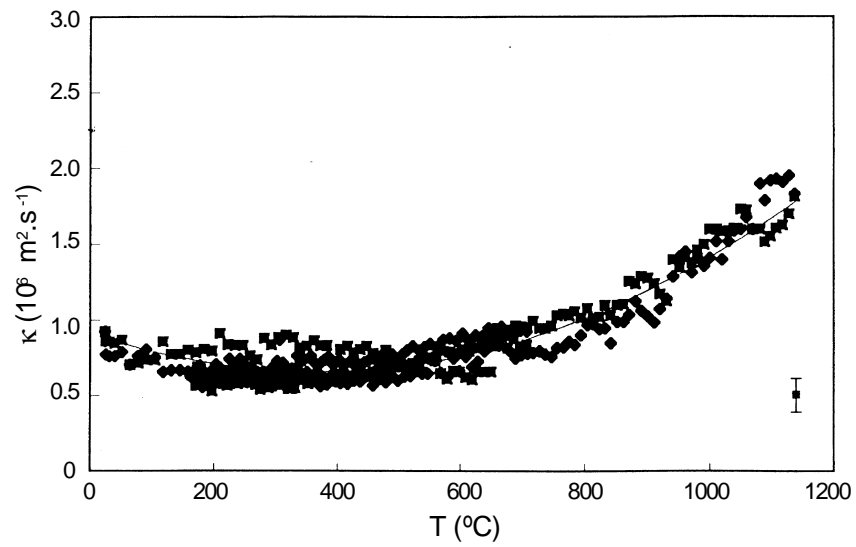


Figure 2.2.6. Experimental data of thermal diffusivity κ as a function of temperature. Extracted from [Bagdassarov and Dingwell, 1994].

2.3 The Eruptive Process

Volcanic eruptions are the culmination of a series of processes that start with magma genesis and end when it is erupted at the surface of the Earth. Figure 2.3.1 shows schematically the relation between such processes for the most typical (but the only one) situation. Commonly, a volcanic cycle starts with the formation of a magma chamber by emplacement within the lower crust, at a level of approximately neutral buoyancy, of basic magmas generated in the mantle and partially differentiated and contaminated during its ascent. Upper crust chamber depths range typically from 2 to 8 Km, while chamber volumes may vary from 0.01 to thousands of Km³. Once in a chamber, magma slowly cools by losing heat through the chamber walls. Progressive cooling allows fractional crystallisation processes to take place and changes gradually magma from basic to more acidic compositions. Crystal segregation together with possible assimilation of volatiles from the environment contributes to increase the mass fraction of volatiles dissolved within the magma. Despite the initial melt may be relatively homogeneous, different processes such as magma mixing or double diffusive convection will tend to convert the chamber into a stratified (chemically heterogeneous) system. If the conditions for magma to leave the chamber are not achieved, the natural conclusion is to quench the chamber and form a plutonic rock. However, the chamber may become overpressurized at any instant along its existence. The increase of pressure can be produced by two main reasons: volatile oversaturation and injection of fresh magma into the chamber. Whichever the case, magma chamber tries to restore the mechanical equilibrium with its surroundings injecting dykes or deforming the media. If the excess of pressure cannot be released, a fracture may propagate from the chamber to the surface and trigger a volcanic eruption. Figure 2.3.2 shows schematically the main morphological features of a volcano. Normally, a volcanic eruption ends once the equilibrium conditions have been restored and withdraws only a few per cent of the stored magma. When finished, the remainder magma continues its cooling and evolution, and a new eruptive event can be produced if the critical conditions are reached again. The period between two consecutive eruptions is known as the *response period*, and may vary from few to hundreds/thousands of years. In consequence, it is a common situation for a silicic magma chamber to produce a cycle of eruptions rather than a single event. The products extruded in such eruptions contribute to construct the volcanic edifice. In some cases, volcanic eruptions may evolve into caldera forming eruptions. Collapse calderas are probably the most violent, destructive and impressive event that can be observed in nature, and produce the partial (or even total) destruction of the chamber due to the collapse of the volcanic edifice. Such caldera collapse are generally associated with very large eruptions in which large amounts of magma (usually more than 1Km³) may erupt [Smith, 1979].

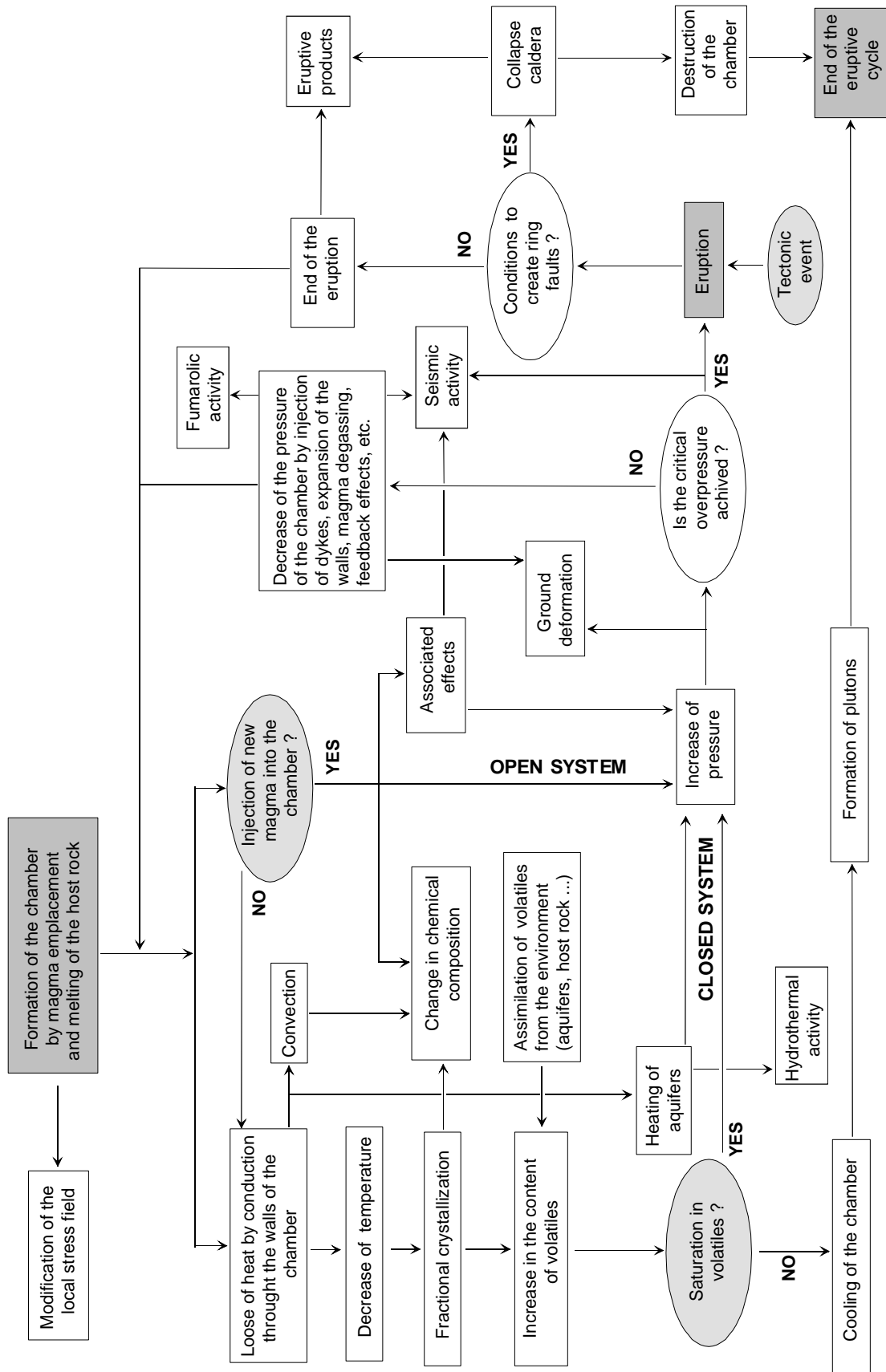


Figure 2.3.1. Schematic cartoon showing the relationship between volcanic processes.

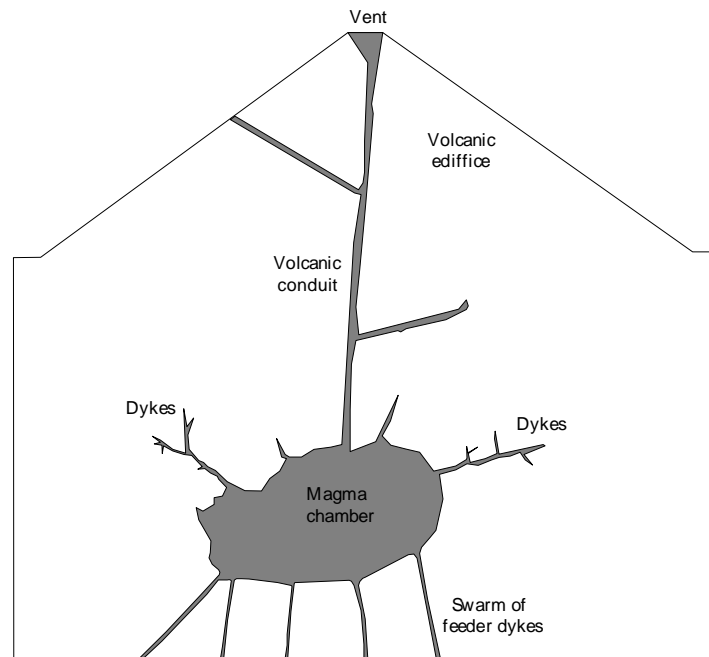


Figure 2.3.2. Main morphological features of a typical volcano.

2.3.1 Triggering Mechanisms

Volcanic eruptions are produced when the build-up of chamber pressure is sufficient to induce mechanical failure of the surrounding rocks. Fracture propagation will initiate as soon as magmatic overpressure exceeds the strength of the rocks. In practical cases, the evaluation of this critical overpressure as well as the estimation of the theoretical fracture paths is not an easy task because it depends on several not well known factors such as the rheological behaviour of the media or the stress field around the magma chamber which, in turn, is closely related not only to the ambient properties but also to the chamber geometry. Nevertheless, overpressures between 5 and 25 MPa are believed to be sufficient to rupture most chambers under tensile regime. Nowadays, it is widely accepted that two main mechanisms can account for this chamber pressurisation: volatile exsolution related to fractional crystallisation processes and the inflow of fresh magma into the chamber. Other much less common mechanisms such as external seismic excitation of entrapped bubbles [Sturtevant *et al.*, 1996] or local tectonic events have been also recognised as plausible.

Observation In some eruptions, magma is erupted without being previously stored within a shallow magma reservoir. A typical case can be the eruptions produced in tectonic frames such the mid-oceanic ridges, where basic and ultrabasic magmas are sometimes erupted directly from the mantle or the lower crust. These eruptions will be not considered here.

Observation The terms *open system* and *closed system* will be used in the context of this work as synonymous of eruption triggered by injection of fresh magma and eruption triggered by volatile saturation respectively. Thus, the terms open/closed refer to the situation of the chamber when the eruption is produced but do not say anything about its previous history. In other words, eruption from a closed system does not necessarily imply that the chamber has been an isolated system along its history.

The correlation usually observed between the lengthened of the volcanic repose periods and the increase of the eruption explosivity (associated with the increase in water content) early pointed out that the exsolution of volatiles within the chamber could produce sufficiently high overpressures to trigger an eruptive event [Morey, 1922; Smith and Bailey, 1968; Smith, 1979]. This hypothesis was also supported by multiple petrological evidences that showed that magmatic water content increased during the response periods. Effectively, the enrichment in volatiles as consequence of fractional crystallisation can, in some cases, produce an oversaturation of the melt resulting a two-phase flow mixture in which the exsolved gas bubbles tend to increase the ambient pressure. [Blake, 1984] was the first to develop a simple analytical model to quantify this processes. Despite the model was constrained to the effect of water in rhyolitic magmas, its general procedure can be applied to other volatile and magma compositions. This model allowed to quantify the water contents required to generate a critical overpressure equal to the tensile strength of the rock in terms of some parameters such chamber depth, magma compressibility or structural response. According to this model, water contents in the range of 3-6 wt.% are, in most cases, sufficient to rupture a chamber. Another important conclusion he came up with is that fractionated magmas evolving at shallow depth cannot attain water contents much above 6 or 7 in wt. %, because, if they do so, the chamber becomes critically overpressurized and a volcanic eruption is triggered. Generally speaking, predictions of the model are in good agreement with petrological evidences. More elaborated models have been proposed after that of Blake and, among them, the one of [Tait *et al.*, 1989] should be mentioned. [Tait *et al.*, 1989] calculated the overpressure in the chamber as a function of the amount of crystallisation, the solubility law (depending on the volatile specie present) and the presence of some initial mass of gas. They showed that the more soluble is a given volatile specie the more important is for the development of overpressure within the chamber. Thus, only a few per cent fractional crystallisation is required to cause overpressures equal to the fracture criteria for a pure H₂O gas phase, whereas a pure CO₂ is unlikely to overpressurize the chamber because is much less soluble.

Injection of new magma (usually basic) into the chamber is the second, and probably the most common, mechanism able to trigger volcanic eruptions [Blake, 1981]. The idea is that

the amount of material intruded within a magma chamber cannot be arbitrarily large because is constrained by the compression of the resident magma and by the expansion of the chamber walls. If this critical volume is exceeded, either a volcanic eruption or the injection of magma through dykes occurs. Evidences that magma chamber are open systems are numerous. Thus, the inflation of volcanoes (ground deformation), often accompanied by seismic activity, is attributable to the influx of magma. Active periods separated by periods of repose of few years are also regarded as being associated with the uprise of magma at rates of several cubic metres per second [Blake, 1981]. On the other hand, petrological studies reflect that, in many cases, *mixing* or *mingling*¹ between two magmas of contrasting physical and chemical properties occurs prior to an eruption.

In some cases, the period of repose occurring between the injection of magma and the eruption suggests that the volume of injected (basic) magma is not in itself sufficient to immediately trigger the eruption, and that some secondary effect(s) associated with the injection produces the critical overpressure necessary to rupture the magma chamber and permit the subsequent volcanic eruption. This idea was introduced to explain the 1875 Plinian eruption of Askja (Iceland) [Sparks *et al.*, 1977] and since then it has been used to explain many other eruptions such as the 1991 Pinatubo (Philippines) eruption [Pallister *et al.*, 1992]. When basic magma is injected into the base of a chamber containing a more evolved (acid) magma, any mixing will initially be strongly inhibited by the contrasts in density, temperature and viscosity between both magmas [Huppert *et al.*, 1982b; Sparks and Marshall, 1986; Turner and Campbell, 1986; Snyder and Tait, 1995]. Thermal equilibration will then result in cooling of the hotter, more basic magma which begins to crystallise, and heating of the acid magma which will tend to cause convection. Cooling of the newly injected magma can cause oversaturation and subsequent exsolution of volatiles [Huppert *et al.*, 1982a; Tait *et al.*, 1989; Pallister *et al.*, 1992] (mainly CO₂ because it is the most abundant volatile species in basic magmas). Superheating and decompression of parts of the acid magma due to convection may also lead to oversaturation in volatile phases, exsolution and bubble vesiculation [Sparks *et al.*, 1977]. Viscous coupling between the both magmas can then cause entrapment of basic magma within the convecting acid magma cells, thus bringing basic magma to the top of the chamber [Snyder and Tait, 1996] where it will decompress and may become oversaturated. As cooling of the acid magma progresses, crystallisation and the subsequent exsolution of volatiles can significantly

¹ Despite the terms mixing and mingling should not be confused, their incorrect use has often left to misunderstandings. The term magma mingling is used when the erupted products contain simultaneously two (or more) unmixed magmas of different compositions (like a mixture of water and oil). The term magma mixing refers to the mixture of two different magmas, say A and B, to form a third intermediate magma C. Normally, the mixture of magmas produces an initial mingling which evolves to mixing if the time of coexistence is large enough (chemical diffusion of magmas is very low).

reduce its density, permitting overturning and large scale mixing between the two magmas [Huppert *et al.*, 1982a; Turner and Campbell, 1986]. Eruption may occur at any time during this sequence of events related to the mixing process if the additional overpressure necessary to rupture the magma chamber is attained. In summary, the exsolution of volatiles from the acid magma due to its increase in temperature or due to convection, or the exsolution of volatiles from the basic magma during its cooling and subsequent crystallisation, have all been proposed as possible mechanisms related to the injection and subsequent mixing events which could contribute to overpressurize the chamber. For a quantification of the relative importance of the above mentioned processes in causing overpressure of the chamber see [Folch and Marti, 1998b].

2.3.2 Explosive Volcanism. Exsolution and Fragmentation Levels

The physics of explosive volcanism began to be understood during the late seventies, after the important contributions of G. Walker, L. Wilson and S. Sparks (e.g. [Walker, 1973; Wilson, 1976; Wilson *et al.*, 1980]). The study of processes related to explosive volcanism has become a subject of major interest during the last two decades due to its high potential hazard on human life and to its environmental risks. References in literature are more than abundant. Only the main ideas are briefly exposed here and the reader is referred to the original references or to any of the many existing reviews (e.g. [Papale, 1994a; Gilbert and Sparks, 1998]) for major descriptions.

Observation Volatiles (basically water) play a major role in determining whether volcanism is explosive or not. Since the abundance of water is, generally speaking, a characteristic feature of acid magmas, *explosive volcanism* is associated to the these evolved compositions. When the volcanism is not explosive is said to be effusive. *Effusive volcanism* is a phenomena related (but not restricted) to more basic magmas. Its characteristics will not reviewed in this thesis.

Solubility of volatile species is highly dependent on pressure (see section 2.2.3). Normally, a level is reached where magmatic pressure equals the *saturation pressure* of the dissolved gas species and magma begins to exsolve part of its dissolved gas forming vesicles and bubbles. This level is known as the *exsolution level* (see figure 2.3.3). Note that, in general, the exsolution level can be located either inside the magma chamber or within the volcanic conduit. Thus, in those eruptions triggered by volatile saturation, the exsolution level must be located inside the chamber (at least during the initial stages) because the presence of exsolved gas prior to the eruption is a necessary requirement. On the contrary, if the eruption is triggered by injection of new magma, the chamber may be previously vesiculated or not. If not, the exsolution level is placed within the conduit during the eruption, that is, magma leaves the

chamber undersaturated and, as it ascends and the ambient pressure decreases, eventually becomes oversaturated somewhere in the conduit.

Observation During magma ascent, one should distinct between the level where the melt becomes saturated (the saturation level) and the level where gas bubbles begin to nucleate and grow (the exsolution or nucleation level). If the characteristic time required for a gas bubble to nucleate is not negligible with respect to the transit time of magma both levels do not coincide. However, this distinction is not relevant to our purposes.

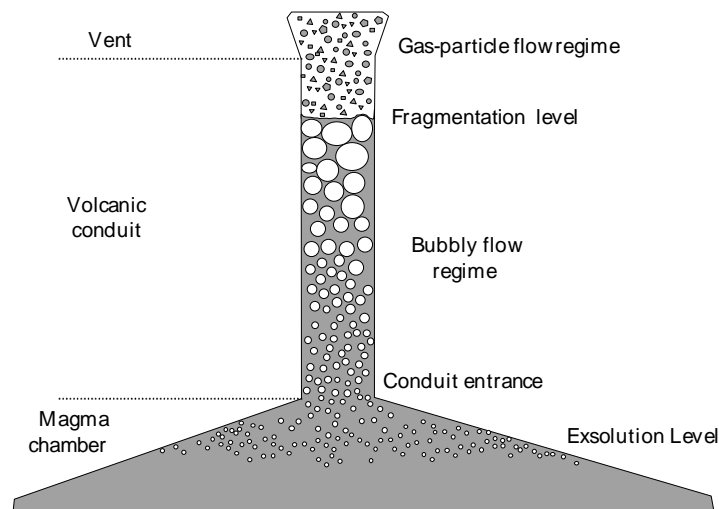


Figure 2.3.3. Schematic diagram showing the principal features associated to explosive volcanism. The exsolution level can be located inside the chamber (as in the figure) or within the conduit. In this case, however, other mechanism different from volatile exsolution must be responsible for triggering the eruption.

Above the exsolution level magma becomes a two-phase flow composed by a saturated continuum liquid with dispersed gas bubbles within. In this region the magma flows under the bubbly flow regime (see figure 2.3.3). Once nucleated, gas bubbles continue to grow by several mechanisms [Sparks, 1978; Toramaru, 1989; Prousevitch et al., 1993] such as diffusion (as more exsolved gas migrates into the bubbles), decompression (as the ascension of the mixture into shallower levels of lower pressure expands the bubbles) or coalescence (small gas bubbles joint to form larger ones). However, bubble size can not be arbitrarily large, that is, bubbly flow can not be maintained indefinitely. Normally, a level is reached where magma fragments and becomes a gas continuum with dispersed liquid particles called pyroclasts. This level is known as the *fragmentation level*, and above it the mixture flows under the gas-particle flow regime. Once fragmented, the viscosity of the mixture decreases by several orders of magnitude and magma is violently accelerated to sonic velocities.

Magma fragmentation is the defining feature of explosive volcanism. Despite its consequences on local, regional and global scales, the mechanism of fragmentation is still not well understood and controversial [Dingwell, 1996]. The debate on fragmentation is mainly contemplated within two different scenarios. The traditional explanation, initially proposed by [Sparks, 1978], is basically focussed on a strain criteria. According to it, magma disrupts when its vesicularity¹ reaches a critical value. The basic idea is that, during its ascension and subsequent lost of dissolved volatiles, magma increases its viscosity by several orders of magnitude (at low volatile content, viscosity varies dramatically. See figure 2.2.3 for a major comprehension). The increase in the viscosity of the mixture prevents further bubble growth and allows bubbles to accumulate sufficient energy to disrupt magma. This hypothesis is partially supported by the observation that vesicularity of pumice² clasts is usually in the range 0.70-0.75, which represents the value of a maximum spherical bubble packing. The second scenario is focussed on a strain-rate criteria. According to it, the kinematics of the mixture in uppermost parts of the conduit may produce strain-rates that generate a viscoelastic response of the melt and subsequent fragmentation if the stresses exceed the magma tensile strength. The question is still under debate.

2.3.3 Caldera Forming Eruptions

Calderas are large collapse depressions circular or elliptical in shape with a characteristic size ranging from few hundreds of meters up to tens of kilometres. The varying sizes and geometries are explained in terms of the diverse collapse processes, subsidence geometries and regional tectonic influences. The reader is referred to [Lipman, 1997] for an extensive structural and morphological descriptions of collapse calderas. The importance of calderas has been long recognised not only due to its potential volcanic hazards but also because they play a major role on many of the Earth's ore deposits and geothermal energy sources. In addition, its study provides key insights into the generation and evolution of large volume magma bodies.

Most calderas are associated with explosive volcanism in the sense that they typically initiate during the course of Plinian³ eruptions. Effectively, the common sequence of a caldera

¹ The vesicularity of a gas-liquid mixture is, by definition, the volume fraction of gas. It is usually designed by α and, obviously, is constrained to range within the interval [0,1].

² Pumice are a characteristic product of explosive eruptions. They are highly vesicular, may contain crystals and usually have a density lower than that of the water.

³ Plinian eruptions are variety of explosive eruptions. The name comes after Plinius, a roman chronicist who described the A. D. 79 Vesuvius eruption.

forming process starts with a Plinian central vent eruption which, under certain (not well known yet) conditions, evolves into a caldera forming eruption characterised by the extrusion of magma through a set of ring faults (see figure 2.3.4). During this stage part of the volcanic edifice collapses into the underlying magma chamber causing its partial (or even total) destruction and the extrusion of huge volumes of magma. The catastrophic impact of such process on the environment is obvious.

Estimations of the variation of mass discharge rate during caldera forming eruptions based on field observations indicate that the total volume of magma erupted during the Plinian phase does not exceed a few km³ to a few tens of km³, while the total erupted volume during the caldera phase in the same eruption may represent several hundreds or even thousands of km³. The intensity of an explosive eruption is largely a function of the conduit radius [Wilson *et al.*, 1980] and chamber size [Carey and Sigurdsson, 1989], but it also depends on the pressure variations inside the chamber [Scandone, 1996; Bower and Woods, 1998; Folch and Marti, 1998b]. Intensity during the Plinian phase increases progressively over a few hours and then it decreases gradually again over a few hours. Transition from the Plinian phase to the caldera collapse phase is marked by a new increase of the eruption intensity. Finally, at the end of the caldera collapse phase, when most of volatile rich magma has already been erupted, the intensity experiences a rapid decrease normally associated with the emplacement of lava domes along the ring fault and representing the cessation of the caldera subsidence.

Physical processes leading to caldera-forming eruptions of silicic magmas are still not well constrained. The mechanics and thermodynamics of magma chambers immediately before and during caldera collapse have not yet been studied in detail. The most detailed information on collapse calderas is concerned to the products of caldera-forming eruptions and to the resulting caldera structure [Williams, 1941; Williams and McBirney, 1979; Walker, 1984; Martí *et al.*, 1994; Branney, 1995; Lipman, 1997]. Field studies on silicic calderas show that caldera-forming eruptions are commonly preceded by a Plinian eruption from a central vent originally located either inside the caldera area [Heiken and McCoy, 1984; Self *et al.*, 1989; Suzuki-Kamata *et al.*, 1993], close to (or on) the ring fault [Hildreth and Mahood, 1986], or even outside, far from the perimeter of the subsided sector [Hildreth, 1991]. This constitutes a good evidence for caldera-forming eruptions being preceded by a significant decompression of the magma chamber and has led to the generally accepted idea that collapse calderas are the consequence of large volume ignimbritic¹ eruptions, thus implying removal of magma from the chamber. [Druitt and Sparks, 1984] gave the first analysis of the chamber pressure variations during an eruption and

¹ Ignimbrites are a typical product of explosive eruptions. Its origin is a pyroclastic flow originated during the collapse of the eruptive column (see figure 2.3.4).

concluded that collapse calderas initiate during the eruption of substantial volumes of magma (between 0.01 and 0.1 of the initial mass of the chamber according to the authors), when the chamber pressure has decreased well below the lithostatic pressure. In this model, the authors consider two stages: a first stage in which a central vent Plinian eruption starts to progressively decompress the initially overpressurized magma chamber; and a second stage in which caldera collapse results from a further decrease in magma pressure. [Bower and Woods, 1997] have recently refined this analysis reaching similar results. These analytical models only consider the decompression caused by the initial Plinian phase but they do not investigate pressure variations after caldera collapse has initiated. This is, however, a crucial aspect to understand the dynamics of caldera collapse processes and to better estimate the volume of the erupted products and that of the associated magma chamber.

A source of controversy is that the comparison between the estimated magma chamber volumes and those of the erupted products in some recent Plinian eruptions such as Pinatubo (Philippines), Mt St. Helens (USA) or Vesuvius (Italy), shows that these eruptions have emptied a volume fraction of the chamber large enough to theoretically initiate caldera collapse. In addition, some caldera-forming eruptions immediately develop into massive proportions without any preceding Plinian phase [Lipman, 1984; Sparks *et al.*, 1985; Fridrich and Mahood, 1987], thus suggesting that, at least in some cases, decompression is not a necessary condition to initiate a caldera-forming eruption. Recently, [Gudmundsson *et al.*, 1997] and [Gudmundsson, 1998] have investigated the stress field generating ring faults in volcanoes. They concluded that overpressure or underpressure in the chamber as the only loading is unlikely to initiate ring faults and proposed that a sill-like magma chambers subject to doming offers the most suitable stress configuration for the initiation of ring faults. Actually, many volcanic fields are subject to pressure at their base. This pressure normally results from magma accumulation and commonly leads to doming of an area much larger than that of the shallow magma chamber and the subsequently formed collapse caldera [Williams, 1941; Williams and McBirney, 1979; Lipman, 1984; Newhall and Dzurisin, 1988].

In summary, caldera-forming eruptions result from the complex coupling between mechanic and thermodynamic processes which control the behaviour of a particular volcanic system and in particular that of the associated magma chamber. Field and theoretical studies conclude, however, that silicic collapse calderas are always associated with large volume ignimbritic eruptions and that the formation of the ring faults (required to produce the collapse) is not a necessary consequence of the previous eruption of a critical volume of magma.

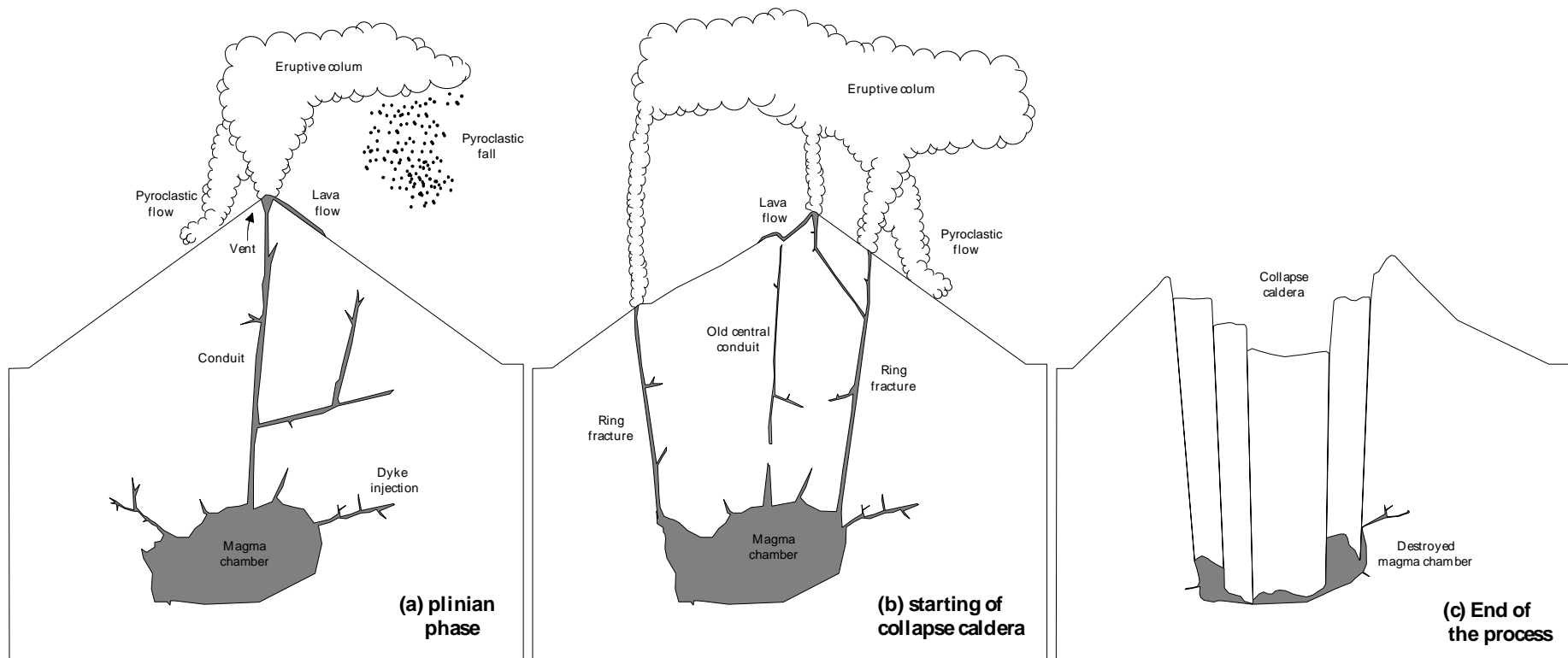


Figure 2.3.4. Cartoon showing the typical (but not the only possible) processes leading to caldera collapse formation. (a) Ordinary central vent Plinian eruption. Features of the eruption are lava flows (not often) and the eruptive column composed by gas and fragmented magma particles (pyroclasts). Collapse of the eruptive column leads to pyroclastic flows and subsequent formation of ignimbrites. Pyroclasts may also fall from the column due to gravitational effects producing a pyroclastic fall. (b) Under certain conditions, ring fractures connect the chamber with the surface and a collapse caldera begins to form. During this stage, part of the volcanic edifice collapses into the chamber and produces large volume explosive eruptions. (c) The final result is the destruction of the chamber and the formation of a caldera with a characteristic size proportional to that of the ancient chamber.

2.4 Modelling in Physical Volcanology : State-of-the Art

The study of volcanic phenomena has been traditionally considered within the frame of geology and geophysics. Nevertheless, during the last decades, the development of physical volcanology together with the disposal of more powerful numerical techniques has progressively lead to the introduction of numerical modelling to a wide variety of volcanic processes, becoming thus, a useful tool to complement the traditional geological and geophysical studies. Nowadays, numerical simulations are applied to many different volcanic processes such as, for instance, convection inside magma chambers, ground deformation of volcanic areas, dynamics of volcanic eruptions or transport and subsequent emplacement of eruptive products. This section reviews the most relevant models -together with its results, predictions and some implications- concerning to volcanic eruptions and ground deformation processes in order to situate the contributions of this present thesis within its framework.

2.4.1 Eruptive Models

Numerical simulation of volcanic eruptions is a complex problem. Its proper solution should include the coupling between different physical processes that occur inside the magma chamber, within the volcanic conduit and at the Earth's surface, because the processes which occur in each of these domains affects the dynamics of the others. Moreover, one should also take into account the coupling with the mechanical response of the medium (deformation, fracture propagation, etc.). Clearly, a successful solution of such global problem is, at least by now, unachievable not only because its associated numerical difficulties, but mainly due to the fact that many of the involved processes are not well constrained or are simply unknown. To simplify the problem, the simulation of the eruption related processes has been traditionally considered in three separate domains: chamber, conduit and surface.

This section reviews the present stage of models concerning to magma chamber withdrawal and volcanic conduits. Modelling of subaerial processes¹ is not reviewed because will be not considered in this work. The reader is referred to the abundant literature (e.g.

¹ The term subaerial processes refers to all the eruptive processes which take place at the Earth's surface and at the atmosphere, that is, refers to the dynamics and emplacement of the erupted materials. Modelling of such processes has been one of the most active topics in volcanology during the last two decades due to its obvious importance in terms of volcanic hazard, risk to population and environmental influence.

[*Valentine and Wohletz, 1989; Dobran et al., 1993; Woods, 1995; Neri and Macedonio, 1996; Sparks, 1997; Neri et al., 1998*] among many others).

2.4.1.1 Conduit Models

The appropriate modelling of magma ascent along volcanic conduits should be performed solving a three-dimensional, unsteady, three-phase (liquid, gas and solid crystals) and non-homogeneous flow problem. Moreover, effects such as crack formation and propagation, erosion of the conduit walls and the existence of a multicomponent gas phase should be also considered. Clearly, the proper solution of such a complex problem is not an easy task not only due to its associated numerical difficulties, but mainly because the knowledge of the involved variables as well as its interrelations is far from being satisfactory. In consequence, many simplifying hypothesis which involve the neglect or simplification of some processes must be necessarily done. Thus, most of the conduit models available in literature are one-dimensional and steady. Obviously, steady models do not contemplate time-dependent boundary conditions (that is, they do not consider the coupling with neither the magma chamber dynamics nor the subaerial processes) and, for this reason, its application is constrained to those phases of an eruption during which no significant variation of the flow parameters occurs. The main difference between the existing models concerns to the homogeneity hypothesis. Homogeneous models assume thermal and mechanical equilibrium between phases while, in contrast, non-homogeneous models take into account mechanical disequilibrium (different velocities between gas and liquid). The homogeneous approach can be justified for viscous magmas in the bubbly flow regime¹. However, once these magmas are fragmented its viscosity decreases dramatically allowing the relative motion. In summary, the homogeneous hypothesis may introduce appreciable errors when used to model low viscosity magmas or high viscosity magmas above the fragmentation level.

This section briefly reviews the characteristics and results of the most important conduit models developed up to date. A summary of its properties is given in table 2.4.1.

- **The model of Wilson and co-workers.** [*Wilson et al., 1980; Wilson and Head, 1981; Gilberti and Wilson, 1990*]. Despite its simplicity, this model gave the first insight into the modelling of magma ascent along volcanic conduits. The model is one-dimensional, steady, homogeneous and considers a variable conduit radius. The equations to solve are

¹ In these magmas, the high viscosity impedes the relative motion between bubbles and liquid. In contrast, low viscosity magmas (basalts) usually show characteristics of separated flows.

$$\frac{dr}{r} + \frac{du}{u} + 2\frac{dr_c}{r_c} = 0 \quad (2.4.1)$$

$$\frac{1}{r} \frac{dp}{dz} + u \frac{du}{dz} + g + f \frac{u^2}{4r_c} = 0 \quad (2.4.2)$$

$$\frac{1}{r} = \frac{n_g RT}{p} + \frac{1-n_g}{r_l} \quad (2.4.3)$$

where z is the vertical coordinate (positive upwards, origin at the conduit entrance), r is the mixture density, u is the mixture velocity, r_c is the (variable) conduit radius, p is the pressure, g is the acceleration due to gravity, f is a dimensionless coefficient related to the drag of the wall, r_l is the liquid density, n_g is the mass fraction of exsolved gas, R is a gas constant and T is the (constant) temperature. The above equations are nothing but the continuity equation, the momentum equation and the definition of the mixture density under the homogeneous approach. Note that in equation (2.4.3) the perfect gas equation is implicitly used as a state law. In the momentum equation (2.4.2) the general expression for f was taken to be

$$f = \frac{32m}{r r u} + 0.01 \quad (2.4.4)$$

where m is the viscosity of the mixture. In this model, viscosity is assumed to be constant but with a jump once magma fragments. Thus, the authors consider a constant value in the range $10^4 - 10^7$ Pa.s below the fragmentation level and a constant value of 2×10^{-5} Pa.s once magma has fragmented, being the criteria for magma fragmentation a maximum value of the gas volume fraction. Finally, the mass fraction of gas n_g is related to the volatile (dissolved plus exsolved) mass fraction W by means of

$$W = n_g + (1 - n_g) c \quad (2.4.5)$$

where c is the solubility. Wilson and co-workers assumed a Henry-law type equation (see equation 2.2.2) for the solubility, being water the only present volatile specie.

The aim of the model is to find density $r(z)$, velocity $u(z)$, pressure $p(z)$ and conduit radius $r_c(z)$ solving equations (2.4.1), (2.4.2) and (2.4.3). Since this system is not complete, the

authors solved numerically¹ for mixture velocity and conduit radius (by assuming a lithostatic pressure profile) and for the mixture velocity and pressure (by assuming a given conduit geometry). Boundary conditions are given in terms of the exit pressure and the mass eruption rate². This choice is justified because mass eruption rate is a useful quantity to characterise an eruption since it can be inferred from the spatial dispersal of pyroclasts near the vent, that is, is one of the (few) observables that can be inferred *a posteriori*.

Despite its simplicity, this model allowed to examine the influence of volatiles, viscosity of the magma and shape of the conduit on the outflow conditions (see figures 2.4.1 and 2.4.2). Since the conditions in the vent are closely related to the style of the activity (e.g. [Sparks and Wilson, 1976; Wilson, 1976]), the model explained the different explosive regimes in terms of the properties of the ascending magma. Thus, for instance, a result of the model is that either a decrease in the magma water content (associated to the extrusion of deeper layers in a stratified magma chamber) or an increase in the radius of the vent (associated to erosion) produce a lower exit velocity which could explain the transition from plinian air-fall to collapsing column. An other important prediction of the model is that if some geometrical conditions are verified the flow can experiment a transition from subsonic to supersonic and reach the vent with velocities of several hundreds of meters per second.

- **The model of Buresti and Casarosa.** [Buresti and Casarosa, 1989]. This model is one-dimensional, steady and mechanically homogeneous. Despite it is limited to the gas-particle flow region (that is, above the fragmentation level), the model contemplates thermal disequilibrium between gas and liquid. The equations are basically the same that those of the Wilson's model but adding, obviously, the energy equation. For a near-uniform flow cross-sectional area and adiabatic conduit the model predicts that temperature changes within the two-phase flow are, in general, negligible.

- **The model of Turcotte and co-workers.** [Turcotte et al., 1990]. This model is one-dimensional, homogeneous, without gravitational nor frictional effects and transient. In fact, the authors modelled the initial phase of an explosive eruption by analogy with the one-dimensional shock tube problem and found the analytical solution for an expansion wave in a magma-gas mixture.

¹ The authors do not specify the numerical integration scheme. Some analytical solutions are also found under certain hypothesis.

² The authors also derive expressions to relate the mass eruption rate to the conduit radius and mixture velocity at the conduit entrance. In other words, the prescription of the mass eruption rate is equivalent to the standard Dirichlet inflow boundary condition on the velocity.

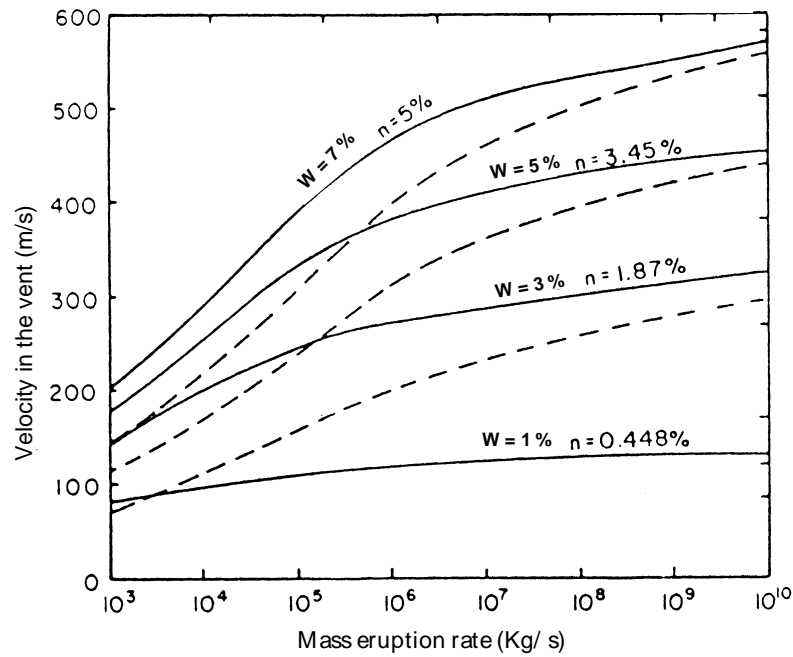


Figure 2.4.1. Velocity in the vent as a function of the mass eruption rate for different values of the magma water content W according to the Wilson's model. The conduit pressure profile is lithostatic and the exit pressure is atmospheric. The mass fraction of gas n_g is also shown. Broken lines show the same result but assuming that the pressure at the fragmentation level is lower than lithostatic by 300 bars. Extracted from [Wilson et al., 1980].

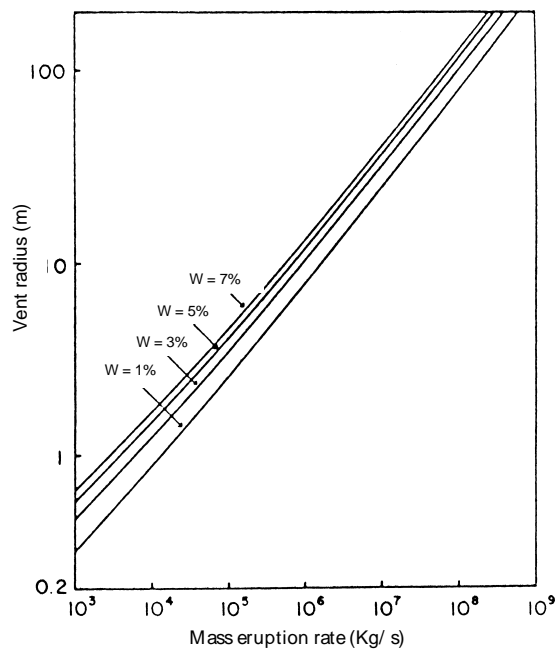


Figure 2.4.2. Vent radius as a function of the mass eruption rate for different values of the magma water content W according to the Wilson's model. The conduit pressure profile is lithostatic and the exit pressure is atmospheric. Extracted from [Wilson et al., 1980].

The authors showed that, during this initial stage, the sudden pressure decrease (associated to the opening of the conduit) produces an exsolution front which moves downwards and a fragmentation front with a shock wave ahead which propagates upwards.

- **The model of Jaupart and Allègre.** [*Jaupart and Allègre, 1991*]. This model is a variation of the Wilson and co-workers model (one-dimensional, steady, homogeneous and with a constant conduit radius) which incorporates the loss of gas through permeable conduit walls¹ and a variable viscosity. The mass flux of gas (per unit of area) through the conduit walls q_g is assumed to follow Darcy's law

$$q_g = r_g \mathbf{a} k \Delta p \quad (2.4.6)$$

where r_g is the gas density (given by the perfect gas law), \mathbf{a} is the volume fraction of gas, k is an effective permeability ($k = 10^{-7} - 10^{-14} \text{ m}^2 \text{ s kg}^{-1}$ according to the authors) and Δp is the pressure difference between the conduit and the ambient. For viscosity, both the presence of bubbles and the effect of the dissolved volatiles are taken into account by means of

$$\mathbf{m} = \mathbf{m}_l (1 - \mathbf{a})^{-5/2} = \mathbf{m}_l e^{-b(c - c_i)} (1 - \mathbf{a})^{-5/2} \quad (2.4.7)$$

where c is solubility (given by the Henry law), \mathbf{m}_l is the viscosity at a reference pressure (in which the solubility is c_i and $\mathbf{a} = 0$) and b is a dimensionless parameter ($b = 100$ according to the authors). The first contribution in the right-hand-side (RHS) of the above equation reflects how the viscosity of the liquid increases when the amount of dissolved volatiles decreases, while the second reflects how the mixture viscosity increases as volume fraction of gas increases. This viscosity law (and subsequent variations of it) is based on the work of [*Shaw, 1972*]. The equations to solve are the momentum equation (2.4.2) (with the factor f given by equation (2.4.4)) completed with the definition of the mixture density under the homogeneous approach²

$$\mathbf{r} = \mathbf{a} \frac{RT}{p} + (1 - \mathbf{a}) \mathbf{r}_l \quad (2.4.8)$$

¹ The physical motivation was the increase in fumarolic activity commonly observed in many volcanic events.

² This equation is in fact equal to (2.4.3) but using the gas volume fraction rather than its mass fraction.

and the continuity equation which, in this model, contemplates a mass balance for both the liquid and the gas phase

$$\frac{d}{dz} [\mathbf{r}_g \mathbf{a} u + \mathbf{c} \mathbf{r}_l (1 - \mathbf{a}) u] = - \frac{2q_g}{r_c} \quad (2.4.9)$$

$$\frac{d}{dz} [\mathbf{r}_l (1 - \mathbf{a}) u] = 0$$

Numerical solution¹ allows to determine density $\mathbf{r}(z)$, velocity $u(z)$, pressure $p(z)$ and the gas volume fraction $\mathbf{a}(z)$ along the volcanic conduit. An important result of the model is that the amount of gas lost is inversely proportional to the eruption rate. Since the eruption rate decreases with time as the chamber empties, the amount of gas lost will tend to increase producing thus a reduction of the gas content of the erupted material as the eruption proceeds. This provides an alternative explanation for the transition from plinian air-fall to collapsing column². [Woods and Koyaguchi, 1994] considered also a model with permeable walls to explain transitions in the eruptive regime. Their model is basically the same that the Jaupart and Allègre's but considers also that the magma chamber is supplied with magma during the course of an eruption.

- **The model of Dobran and co-workers.** [Dobran, 1987][Dobran, 1992]. This model is one-dimensional, steady and non-homogeneous, that is, the multiphase system is treated considering separate systems of equations for the different phases which are in mechanical disequilibrium³. A characteristic feature of this model is that distinguishes three zones within the volcanic conduit: one below the exsolution level, another between the exsolution and the fragmentation levels and a third above the fragmentation level (see figure 2.4.3). Below the exsolution level, the flow is considered homogeneous (a single liquid phase), incompressible and with a mean density and viscosity that account for the dissolved gas and crystals in the liquid. In this region, the flow is governed by the Bernoulli equation with friction. In contrast,

¹ Again, the numerical procedure is not specified by the authors.

² In the Wilson's model this transition is attributed to the presence of a gradient in the chamber which causes a decrease in the gas content. On the other hand, some petrological and geochemical studies [Eichelberger *et al.*, 1986] seem to support this second mechanism to explain the decrease in the gas content. In fact, both possibilities are plausible and, moreover, susceptible to act together.

³ The first non-homogeneous model was proposed by Vergnolle and Jaupart [Vergnolle and Jaupart, 1986]. However, this first model is restricted to the case of low-viscosity basaltic magmas and, in consequence, does not take into account the gas-particle flow regime. This model is not reviewed because its results can be recuperated as particular solutions of the Dobran's model.

above this level, the flow is modelled as a separate two-phase flow governed by (subscripts l and g refer to liquid and gas respectively)

$$r_l (1-a) u_l S_c = (1-n_g) Q \quad (2.4.10)$$

$$r_g a u_g S_c = n_g Q \quad (2.4.11)$$

$$r_l (1-a) u_l \frac{du_l}{dz} = -(1-a) \frac{dp}{dz} - r_l (1-a) g - F_{wl} + F_{lg} \quad (2.4.12)$$

$$r_g a u_g \frac{du_g}{dz} = -a \frac{dp}{dz} - r_g a g - F_{wg} - F_{lg} \quad (2.4.13)$$

where S_c is the area of the volcanic conduit and Q is the mass flow rate. Equations (2.4.10) and (2.4.11) are nothing but the continuity equation for the liquid and gas phase respectively applied to a conduit of constant section S_c and considering mass transfer from the liquid to the gas. Equations (2.4.12) and (2.4.13) are the one-dimensional momentum equation for the liquid and the gas phase respectively, where F_{lg} accounts for the drag between phases whereas F_{wl} and F_{wg} account for the frictional effects between the walls and the liquid and between the walls and the gas respectively.

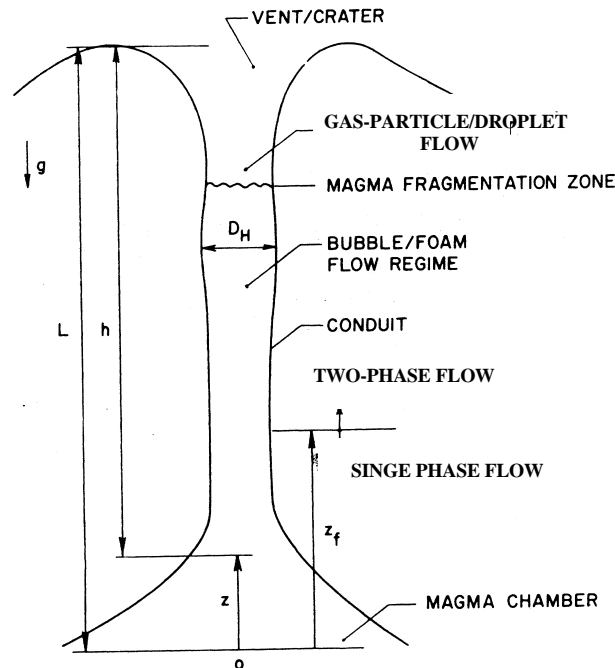


Figure 2.4.3. Geometry considered in the Dobran's model. Magma accelerates from the stagnation state o and begins to exsolve gas at $z=z_f$. Extracted from [Dobran, 1992].

Equations (2.4.10) to (2.4.13) are used to simulate both the bubbly flow before magma fragmentation and the gas-particle droplet flow after magma fragmentation, being the definitions of the functions F the only difference between the governing equations in these two regions. In the original version of the model

$$\begin{aligned}
 F_{lg} &= F_{lg}(u_l - u_g) \\
 F_{wl} &\neq 0 \text{ in the bubbly flow regime} \\
 F_{wl} &= 0 \text{ in the gas-particle regime} \\
 F_{wg} &= 0 \text{ in the bubbly flow regime} \\
 F_{wg} &\neq 0 \text{ in the gas-particle regime}
 \end{aligned}
 \tag{2.4.14}$$

where the values of the above constitutive relations are rather complex, highly non-linear and depend on several parameters (such as drag coefficients) and variables (such as viscosity or gas volume fraction). These relationships are based on the experimental work of [Ishii and Zuber, 1979]. With these constitutive relations, an exsolution law (the Henry law), state laws for the gas (perfect gas) and the mixture and a relation for the viscosity¹ the set of equations (2.4.10) to (2.4.13) can be numerically solved to find pressure $p(z)$, volume fraction of gas $\alpha(z)$ and velocities of the phases $u_l(z)$ and $u_g(z)$. Although results are much dependent on the choice of the “free” parameters, non-homogeneous models predict results which can be appreciably different from those of the homogeneous models. In general, non-homogeneous models predict a higher pressure gradient and larger volume fractions of gas and exit velocities than the homogeneous models (see figure 2.4.4). However, it should be remarked that this results can not be generalised because they are strongly dependent on parameters which are subject to uncertainties. A discussion between these differences can be found in [Papale, 1994].

A variation of this model was introduced by [Macedonio et al., 1994]. This variation contemplates the possibility of conduit erosion due to the impact of particles on the conduit wall (only above the fragmentation level) and due to the fluid shear stresses². The model predicts that erosion due to the impact of particles is important near the vent (where the velocities are greatest) and that erosion produced by shear stresses is constrained to a narrow

¹ This model uses three different relations for the viscosity, one for each domain. In the bubbly flow and the gas-particle droplet flow regimes viscosity depends on the gas volume fraction and on the solubility law. These dependencies (which are similar to that of equation (2.4.7)) are based on experimental results.

² The inclusion of erosion affects the continuity and the momentum equations of the liquid phase (equations (2.4.10) and (2.4.12)), which must include the mass erosion rate per unit of volume.

region in the vicinity of the fragmentation level, where viscosity and velocity gradients become very large.

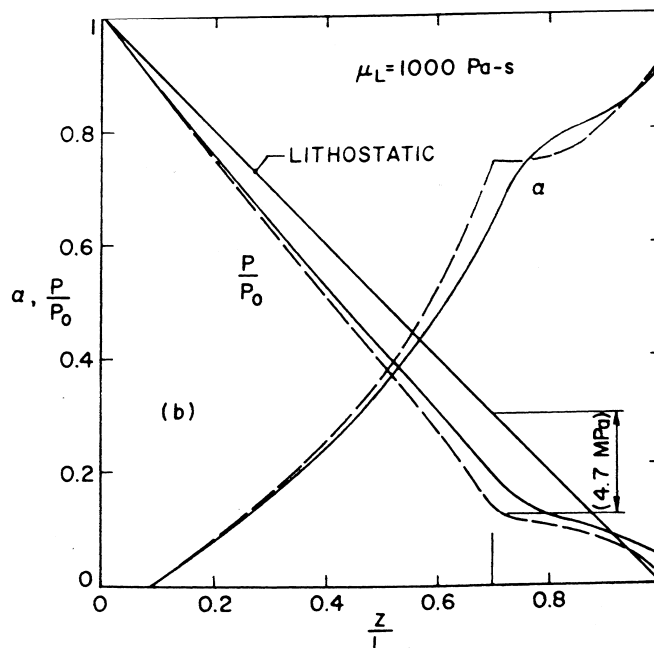


Figure 2.4.4. An illustrative result of the Dobran's model. Gas volumetric fraction α and dimensionless pressure inside the conduit. The distance is also dimensionless (L is the length of the conduit), and the origin is at the stagnation point (see figure 2.4.3). Solid lines: homogeneous approach. Dashed lines: non-homogeneous solution. Note how appreciable differences arise only in the uppermost part of the conduit. The exact parameters of this simulation are not relevant here, but the shape of the curves may vary notably depending on magmatic and geometrical properties. Extracted from [Dobran, 1992].

Dobran's model has been improved and refined in [Papale and Dobran, 1993; Papale and Dobran, 1994b; Papale et al., 1998]. These changes concern mainly the introduction of more precise magma properties and, despite they produce sensible changes in the predictions of the model, do not affect its main structure. The last version [Papale et al., 1998] is, doubtless, one of the most complex and realistic model for the prediction of flow properties in volcanic conduits available up to date. The authors investigated the roles of magma composition, water content and crystal content on the volcanic conduit dynamics in explosive eruptions. Some results are shown in figure 2.4.5. This figure shows pressure, gas volume fraction and gas velocity along the conduit for three different magma compositions (rhyolite, rhyodacite and dacite) and for different water contents. Note how pressure and gas volume fraction experiment high variations immediately before fragmentation due, partly, to the increase in the viscosity of the mixture. After fragmentation, viscosity dramatically decreases and the mixture is highly accelerated to sonic velocities. The relative velocity between phases is negligible except in a region close to the conduit exit, where the authors found, in some cases, relative velocities of up

to 35 m/s (results not shown here). Note also how depending on specific conditions (magma composition and volatile content) the pressure inside the conduit can be different (greater or lower) than the lithostatic one by several MPa. This is important since overpressures can lead to conduit failure and loss of gas while underpressures can lead to conduit closure or to phreatomagmatic eruptions¹ [Barberi *et al.*, 1988]. Finally, another relevant result of the model is that the position of the exsolution level depends mainly on water content (as expected) but, in contrast, the fragmentation level depth is governed by magma composition and is essentially independent of the water content.

- **The model of Ramos.** [Ramos, 1995]. This model is one-dimensional, homogeneous and transient. In fact, the governing equations and the constitutive relations are practically the same than those used in the initial versions of the Dobran's model (considering the homogeneous approach), being the only difference the addition of the temporal dependence in both the continuity and the momentum equations². The model allows to reproduce the propagation of the exsolution and fragmentation fronts during the initial stages of an eruption and recuperates the analytical results of [Turcotte *et al.*, 1990] as a particular case in which neither friction nor gravity are considered. According to it, the transient decompression stage is very short. Moreover, and as expected, the steady solutions coincide with those of the Dobran's model in the homogeneous limit.

¹ Phreatomagmatic eruptions are produced when water from the underground aquifers flows into the volcanic conduit.

² It should be noted that, in the context of conduit models, the term transient refers to the initial phase of an eruption, just after the sudden opening of the conduit. Thus, transient models ([Turcotte *et al.*, 1990] and [Ramos, 1995]) consider the temporal evolution starting from an initial non-equilibrium state but assuming always constant boundary conditions. However, in real systems, boundary conditions are time-dependent and functions of both the chamber withdrawal dynamics (inlet) and the subaerial processes (outlet). Obviously, the proper solution would require the coupling between these different regions, an objective which has not been achieved up to date.

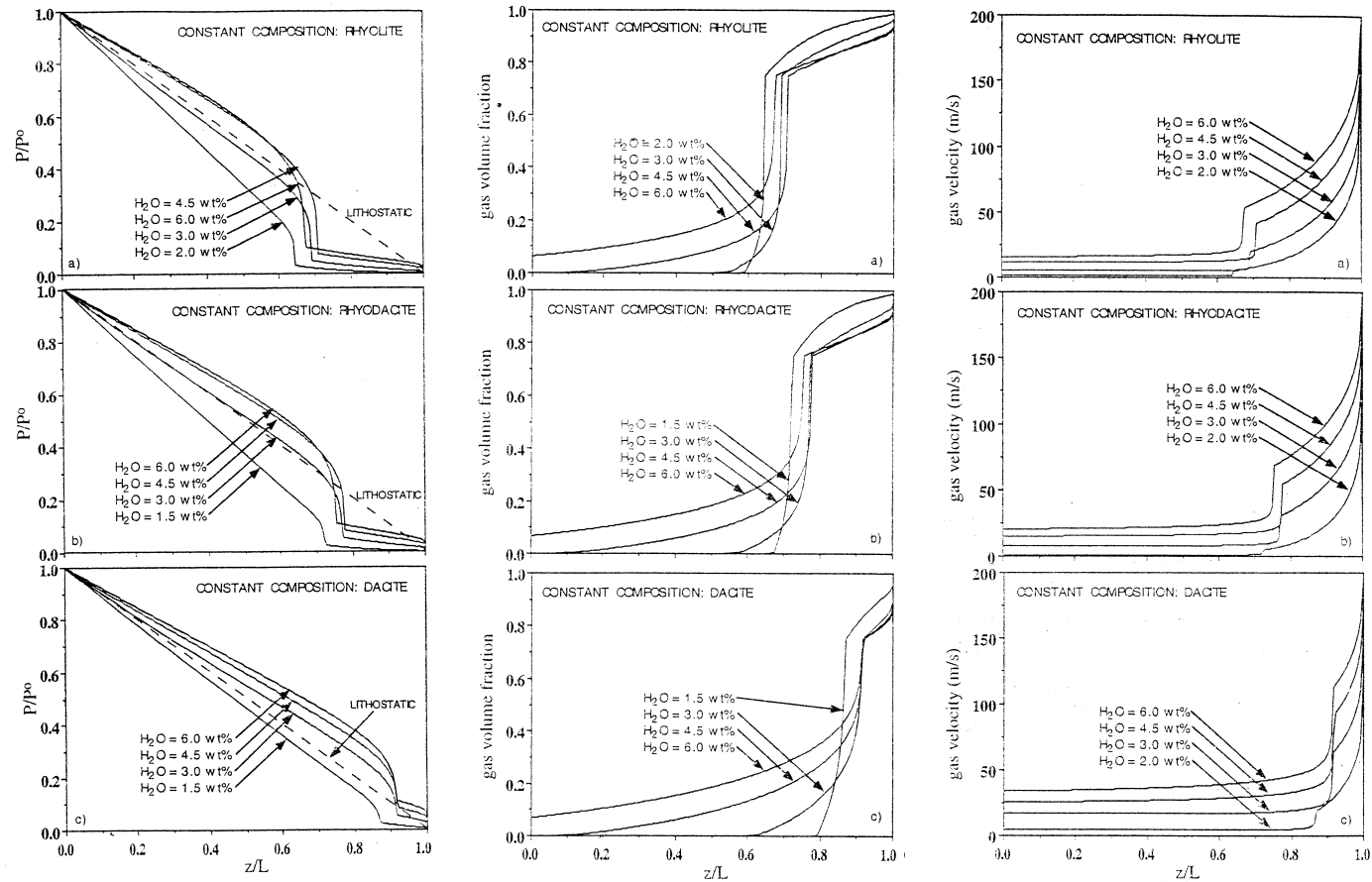


Figure 2.4.5. Dimensionless pressure (left column), gas volume fraction (central column) and gas velocity (right column) versus dimensionless depth. L is the length of the conduit and the origin ($z=0$) is at the conduit entrance. Results for three different compositions: (a) rhyolite (b) rhyodacite (c) dacite and for different constant water contents. In these particular simulations, L is 7Km and the mass flow rate at the conduit entrance is $4 \cdot 10^8$ Kg/s. Lithostatic pressure is computed assuming a constant crustal density of 2800 Kg/m³. Extracted from [Papale, 1998].

Model	Year (1 st version)	Space dimension	Homogeneity	Thermal coupling	Volatile species	Variable conduit size	Domain of applicability
Wilson & co-workers	1980	1D	homogeneous	No	One	Yes	All the conduit
Vergnolle & Jaupart	1986	1D	non-homogeneous	No	One	No	Only basaltic magmas
Buresti & Casarosa	1989	1D	homogeneous	Yes	One	Yes	Above fragmentation level
Turcotte & co-workers	1990	1D	homogeneous	No	One	No	All the conduit
Jaupart & Allègre	1991	1D	homogeneous	No	One	No	All the conduit
Dobran & co-workers	1992	1D	non-homogeneous	No	One	No	All the conduit
Ramos	1995	1D	homogeneous	No	One	No	All the conduit

Table 2.4.1. Summary of characteristics of the most relevant conduit models available.

2.4.1.2 Chamber Withdrawal Models

The study of the dynamics of magma withdrawal from crustal reservoirs is one of the main objectives of this thesis. Previous studies on the subject are basically analytical approaches (e.g. [Blake, 1981; Ivey and Blake, 1985; Blake and Ivey, 1986; Lister, 1989; Bower and Woods, 1997]) or experimental results (e.g. [Freund and Tait, 1986; Blake and Fink, 1987]). Numerical simulations of this topic are restricted to a couple of works.

[Spera, 1984] solved the two-dimensional Navier-Stokes equations within the magma chamber assuming that magma behaves as an incompressible fluid with constant viscosity. The solution was found in terms of vorticity and streamfunction and using a finite difference method. The geometry of the problem was constrained to squared and rectangular magma chambers. As boundary conditions, two different velocity profiles (uniform and parabolic) were imposed at the bottom of the chamber while the non-slip condition was assumed at the rest of the walls. In consequence, the model is only applicable to open chambers in which the eruption is triggered by means of the injection of fresh magma. Note that this limitation is a necessary physical requirement because the flow is incompressible and there is not mechanical coupling (the chamber has a constant volume). The aim of this work was mainly to study the transient history of the evacuation process at arbitrary Reynolds numbers within the laminar regime ($Re \leq 10^3$) and for different aspect ratios of the reservoir by considering the evacuation isochrons. An example of a characteristic simulation is shown in figure 2.4.6. According to this model, the maximum depth of withdrawal increases monotonically as the eruption proceeds and, as intuitively expected, significant portions of magma initially located near the roof but at certain lateral distance from the conduit are not erupted.

[Spera et al., 1986] and [Trial et al., 1992] improved the model by adding the possibility of compositional gradients within the chamber. For this purpose, both density (ρ) and viscosity (μ) were considered to be functions of composition (C) according to

$$\rho = (1 - C) \rho_1 + C \rho_2 \quad (2.4.15)$$

$$\frac{1}{\mu} = \frac{1 - C}{\mu_1} + \frac{C}{\mu_2} \quad (2.4.16)$$

where $C (\in [0,1])$ represents the volume fraction of the component 2. The idea is to reproduce any initial compositional profile (continuous or discontinuous) between two extreme members named 1 (with properties ρ_1 and μ_1) and 2 (with properties ρ_2 and μ_2). Clearly, the physical motivation for this is to improve the previous simulation [Spera, 1984] of chamber withdrawal

during eruptions triggered by injection of basic magmas into chambers initially filled with more compositionally evolved melts (i.e. with lower density and higher viscosity). Since chemical diffusion can be neglected during the course of an eruption, the composition field is only governed by the convective transport equation

$$\frac{\partial C}{\partial t} + \mathbf{u} \cdot \nabla C = 0 \quad (2.4.17)$$

where \mathbf{u} is the velocity.

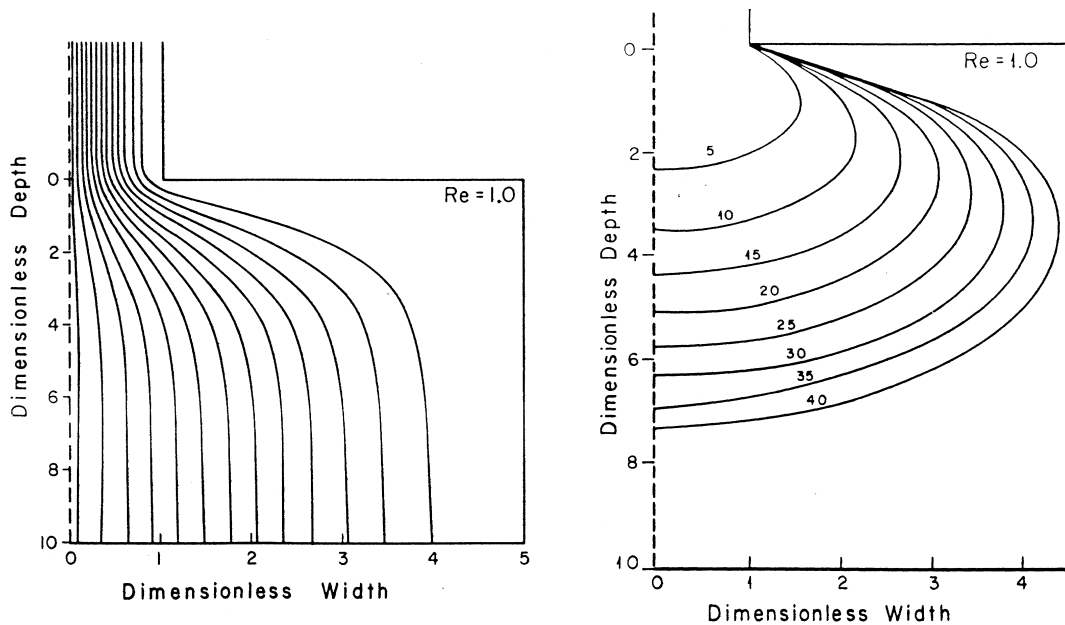


Figure 2.4.6. Typical result of the Spera's model. Streamlines (left) and evacuation isochrons (right, small numbers indicate dimensionless time) at Reynolds number equal to 1.0. Extracted from [Spera, 1984].

The governing equations were solved using the standard Galerkin Finite Element Method with a penalty formulation and using spatial discretisations which range from 400 to 3200 triangular elements (quadratic interpolation for velocity, linear for pressure). Geometry and boundary conditions were analogous to those of the previous version but with the inclusion of sloped roof chambers. From a petrological point of view, one of the most relevant conclusion of this model is that the diversity of the erupted products is not necessarily an indication of the previous diversity of compositions in the magma chamber¹. In other words, the presence of compositional mingling in the deposits may be a consequence of the withdrawal

¹ Commonly, the stratigraphic sequences of the erupted products show compositional variations. Traditionally, these sequences had been interpreted to inversely reflect the initial chamber composition.

dynamics and does not necessarily reflect the existence of pre-eruptive mixtures. Numerical simulations also showed that significant fraction of evolved magma, initially located at the chamber top, may remain trapped depending on the chamber/conduit width and indicated the possibility of distinguishing between continuously and discontinuously (layered) zoned chambers by inspection of the compositional curves derived from geochemical sampling (see figure 2.4.7).

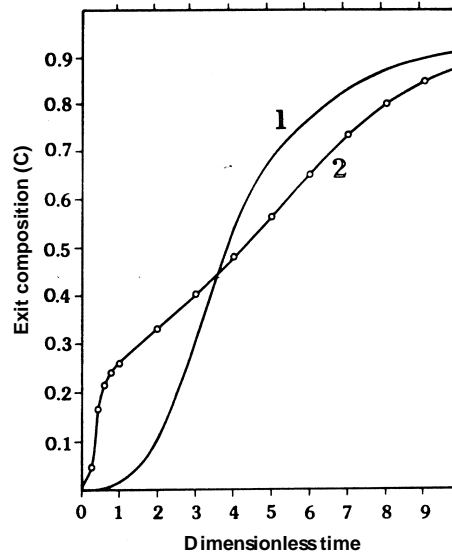


Figure 2.4.7. Averaged exit composition versus dimensionless time for a rectangular flat-topped reservoir. Values of C equal to 0 correspond to a pure acid magma (rhyolite in this simulation) while values equal to 1 correspond to a pure basic magma. Curve 1 is for a chamber initially layered with two layers (rhyolite overlaying basalt) of equal thickness, that is, considering that C is initially a step function. Curve 2 is for a system linearly layered. Note the different behaviour. Providing that the intensity of the eruption is known *a posteriori* by using some indirect measurement, the adequate geochemical sampling of the resulting deposit can indicate the pre-eruptive zonation of the chamber. Extracted from [Spera *et al.*, 1986].

As observed, the few available studies on chamber withdrawal are related to open systems. This work constitutes the first attempt to include also the modelling of volatile oversaturation driven eruptions. Some previous results have been already published [Folch *et al.*, 1998a; Folch *et al.*, 1999].

2.4.2 Ground Deformation Models

Ground deformation inside active volcanic areas is a usual phenomena. Commonly, this deformation is attributed to the pressure increase of the chamber and/or to the heating of the shallow system of aquifers which produces a subsequent increase on the vapour pressure. The importance of a correct monitoring and interpretation of the observed deformation patterns is, in consequence, a key aspect in order to predict volcanic eruptions. The study of ground deformation inside active volcanic areas has been one of the most active topics in volcanology during the last decades. [Mogi, 1958] was the first to apply a point source of pressure in a elastic half-space to interpret ground deformation in areas of volcanic activity. The physical meaning generally ascribed to this model is that of a spherical buried magma chamber with a certain overpressure. Notwithstanding this analytical model has been extensively and sometimes successfully employed, its intrinsic limitations demanded for more elaborated models. Thus, within the frame of the elastic models, [McTigue, 1987] derived an approximate analytical solution for the displacement and the stress fields that includes higher-order terms to represent the finite size of a spherical cavity. [Davis, 1986] developed solutions for ellipsoidal magma chambers. [Bianchi *et al.*, 1987] considered various spatial distributions of the elastic properties and [McTigue and Stein, 1984] and [McTigue and Segall, 1988] introduced the effect of topography. On the other hand, many numerical models of successive complexity have been considered since the early work of [Dieterich and Decker, 1975]. In this first numerical work, the authors solved the equations of linear elasticity using a Finite Element Method and considering chambers of different geometries in order to constrain the validity of the point source hypothesis. Numerical solutions of the elastic problem have allowed to compute surface displacements and stresses considering several effects such as, for instance, extended sources, gravity, far-field stresses (e.g. [Sartoris *et al.*, 1990]), structural discontinuities (e.g. [De Natale and Pingue, 1993; De Natale *et al.*, 1997]) or topography (e.g. [Cayol and Cornet, 1998; Williams and Wadge, 1998]).

The solution of the mechanical problem considering an elastic rheology for the crust has allowed to explain the measured geodetic data in many volcanic areas with certain success. However, in many cases, the elastic models seem to be unable to reproduce the observed uplifts unless unrealistic overpressures are considered (e.g. [Berrino *et al.*, 1984]). [Bonafede *et al.*, 1986] pointed out that, in volcanic areas, the presence of incoherent materials and higher temperatures can produce a lower effective viscosity of the Earth's crust that makes necessary to consider its anelastic properties. The authors worked out analytical solutions for the displacements and associated stress fields induced by a point source of pressure in a viscoelastic half-space and showed that a viscoelastic response may reproduce the observed uplifts with plausible overpressures.

Several analytical models with *anelastic*¹ properties have been proposed after this work². Thus, for instance, [Dragonì and Magnanensi, 1989] derived the analytical solution for a spherical magma chamber surrounded by a viscoelastic shell and reproduced the order of magnitude of the ground uplift observed at Campi Flegrei (Italy). [Bonafede, 1990] re-derived the analytical solution for a point-like spherical magma chamber and found a solution that provides a maximum uplift which is a 1.8 times greater than the value obtained from Maruyama's strain nuclei given by [Bonafede et al., 1986]. On the other hand, [Rundle, 1980], [Rundle, 1982], [Fernández and Rundle, 1994] and [Fernández et al., 1997] derived the solution for a centre of expansion and a point mass in a multilayered medium allowing both elastic and viscoelastic properties for the layers and bottom half-space. [Hofton et al., 1995] extended part of these works considering the existence of a gravitational field in a layered system with a viscoelastic half-space underlying an elastic layer with a point source of pressure. All the models with anelastic properties considered so far are analytical and, generally, assume both a point source of pressure and a flat surface. The advantage of these assumptions are that they allow to derive the solution with a relative generality and simplicity but, in contrast, constrain the applicability of the model. It is well known from the elastic case that the assimilation of the magma chamber with a point of dilatation implicitly assumes that the dimension of the body is small compared to its depth. In volcanic applications, this approach is rather controversial since examples of magma chambers with rather large radius/depth ratio are common, making clear the necessity of obtaining (numerical) solutions for extended sources. This is a second objective of the present thesis. Some results which quantify the error produced on the viscoelastic solution by the point source assumption are already available in [Folch et al., 2000]. This work compares analytical (point source) and numerical (extended source) solutions considering different parameters such as size, shape and depth of the chamber, its overpressure or the type of relaxation. The influence of the topography is also investigated. Considering the above different models and the quantity of volcanic zones monitored, the existing list of bibliography on deformation modelling applied to volcanism is so large that it is not possible to include all these references here. For a major review on the applications of the above mentioned models, the reader is referred to the following list as well as to the references therein included: [Rundle, 1982; Tilling and Dvorak, 1993; Delaney and McTigue, 1994; Langbein et al., 1995; Rymer et al., 1995; Dvorak and Dzurisin, 1997; Bonafede and Mazzanti, 1998; Delaney et al., 1998; Fernández et al., 1999].

¹ The term *anelastic* is used, in the context of this thesis, as a synonym of non-elastic.

² In fact, two different lines of research have been developed in parallel during the last two decades in order to fit satisfactorily the huge increasing amount of experimental data. The first tendency has worked on improving the accuracy of the numerical models by adding successive effects (gravity, topography, mechanical discontinuities, etc.) but considering always elastic rheologies for the crust. In contrast, the second tendency has considered analytical approaches but using anelastic properties.

2.5 References

- Bagdassarov, N., and D. Dingwell, Thermal properties of vesicular rhyolite, *J. Volcanol. Geotherm. Res.*, 60, 179-191, 1994.
- Barberi, F., J. M. Navarro, M. Rosi, R. Santacroce, and A. Sbrana, Explosive interaction of magma with ground water: insights from xenoliths and geothermal drillings, *Rend. Soc. Ital. Mineral. Petrol.*, 43, 901-926, 1988.
- Berrino, G., G. Corrado, G. Luongo, and B. Toro, Ground deformation and gravity changes accompanying the 1982 Pozzuoli uplift, *Bull. Volcanol.*, 44, 187-200, 1984.
- Bianchi, R., A. Coradini, C. Federico, G. Giberti, P. Lancian, J. P. Pozzi, G. Sartoris, and R. Scandone, Modeling of surface deformation in volcanic areas: The 1970-1972 and 1982-1984 crises of Campi Flegrei, Italy, *J. Geophys. Res.*, 92, 14139-14150, 1987.
- Blake, S., Volcanism and the dynamics of open magma chambers, *Nature*, 289, 783-785, 1981.
- Blake, S., Volatile oversaturation during the evolution of silicic magma chambers as an eruption trigger, *J. Geophys. Res.*, 89, 8237-8244, 1984.
- Blake, S., and G. N. Ivey, Density and viscosity gradients in zoned magma chambers, and their influence on withdrawal dynamics, *J. Volcanol. Geotherm. Res.*, 30, 201-230, 1986.
- Blake, S., and J. H. Fink, The dynamics of magma withdrawal from a density stratified dyke, *Earth Planet. Sci. Lett.*, 85, 516-524, 1987.
- Bonafede, M., M. Dragoni, and M. Quarenì, Displacement and stress fields produced by a centre of dilation and by a pressure source in a viscoelastic half-space: application to the study of ground deformation and seismic activity at Campi Flegrei, Italy, *Geophys. J. Royal Astr. Soc.*, 87, 455-485, 1986.
- Bonafede, M., Axisymmetric deformation of a thermo-poro-elastic half-space: inflation of a magma chamber, *Geophys. J. Int.*, 103, 1990.
- Bonafede, M., and M. Mazzanti, Modelling gravity variations consistent with ground deformation in the Campi Flegrei caldera (Italy), *J. Volcanol. Geotherm. Res.*, 81, 137-157, 1998.
- Bottinga, Y., and D. F. Weill, The viscosity of magmatic silicate liquids: a model for calculation, *Am. J. Sci.*, 272, 438-475, 1972.
- Bower, S., and A. W. Woods, Control of magma volatile content and chamber depth on the mass erupted during explosive volcanic eruptions, *J. Geophys. Res.*, 102, 10273-10290, 1997.
- Bower, S., and A. W. Woods, On the influence of magma chambers in controlling the evolution of explosive volcanic eruptions, *J. Volcanol. Geotherm. Res.*, 1998.
- Branney, M. J., Downsag and extension at calderas: new perspectives on collapse geometries from ice-melt, mining and volcanic subsidence, *Bull. Volcanol.*, 57, 303-318, 1995.

- Buresti, G., and C. Casarosa, One-dimensional adiabatic flow of equilibrium gas-particle mixture in long vertical ducts with friction, *J. Fluid Mech.*, 203, 251-272, 1989.
- Burnham, C. W., and R. H. Jahns, A method for determining the solubility of water in silicate melts, *Am. J. Sci.*, 260, 721-745, 1962.
- Burnham, C. W., and N. F. Davis, The role of water in silicate melts: I. P-V-T relations in the system NaAlSi₃O₈-H₂O to 10 kilobars, 700°C-1000°C, *Am. J. Sci.*, 270, 49-54, 1971.
- Burnham, C. W., and N. F. Davis, The role of water in silicate melts: II. Thermodynamic and phase relations in the system NaAlSi₃O₈-H₂O to 10 kilobars, 700°C-1000°C, *Am. J. Sci.*, 274, 902-940, 1974.
- Burnham, C. W., Development of the Burnham model for prediction of water solubility in magmas, in Carroll, M. and Holloway, J. R. eds., Volatiles in magmas, Mineralogical Society of America, *Reviews in Mineralogy*, 30, 123-129, 1994.
- Carey, S., and H. Sigurdsson, The intensity of plinian eruptions, *Bull. Volcanol.*, 51, 28-40, 1989.
- Carroll, M. C., and J. R. Holloway, Volatiles in magmas, Mineralogical society of America, *Reviews in mineralogy*, 30, 1994.
- Cas, R. A. F., and J. V. Wright, Volcanic successions, *Chapman & Hall*, London, 1988.
- Cayol, V., and F. H. Cornet, Effects of topography on the interpretation of the deformation field of prominent volcanoes. Application to Etna, *Geophys. Res. Lett.*, 25, 1979-1982, 1998.
- Cox, K. G., J. D. Bell, and R. J. Pankhurst, Interpretation of igneous rocks, *Allen and Unwind*, London, 1979.
- Davis, P. M., Surface deformation due to inflation of an arbitrarily oriented triaxial ellipsoidal cavity in an elastic half-space, with reference to Kilauea volcano, Hawaii, *J. Geophys. Res.*, 91, 7429-7438, 1986.
- De Natale, G., and F. Pingue, Ground deformations in collapsed caldera structures, *J. Volcanol. Geotherm. Res.*, 57, 19-38, 1993.
- De Natale, G., S. M. Petrazzuoli, and F. Pingue, The effect of collapse structure on ground deformations in calderas, *Geophys. Res. Lett.*, 24, 1555-1558, 1997.
- Delaney, P. T., and D. F. McTigue, Volume of magma accumulation or withdrawal estimated from surface uplift or subsidence, with application to the 1960 collapse of Kilauea volcano, *Bull. Volcanol.*, 56, 417-424, 1994.
- Delaney, P., R. Denlinger, M. Lisowski, A. Miklius, P. G. Okubo, T. Okamura, and M. Sako, Volcanic spreading at Kilauea, 1976-1996, *J. Geophys. Res.*, 103, 18003-18023, 1998.
- Dieterich, J. H., and R. W. Decker, Finite element modeling of surface deformation associated with volcanism, *J. Geophys. Res.*, 80, 4094-4102, 1975.
- Dingwell, D., Volcanic dilemma: flow or blow ?, *Science*, 273, 1054-1055, 1996.
- Dingwell, D., Recent experimental progress in the physical description of silicic magma relevant to explosive volcanism, in eds. J. S. Gilbert and R. S. J. Sparks, The physics of explosive volcanic eruptions, *Geological society special publication*, 145, London, 1998.

2.5 References

- Dobran, F., Nonequilibrium modeling of two-phase critical flows in tubes, *J. Heat Transfer*, 109, 731-738, 1987.
- Dobran, F., Nonequilibrium flow in volcanic conduits and application to the eruptions of Mt. St. Helens on May 18, 1980, and Vesuvius in AD 79, *J. Volcanol. Geotherm. Res.*, 49, 285-311, 1992.
- Dobran, F., A. Neri, and G. Macedonio, Numerical simulation of collapsing volcanic columns, *J. Geophys. Res.*, 98, 4231-4259, 1993.
- Dragoni, M., and C. Magnanensi, Displacement and stress produced by a pressurized, spherical magma chamber, surrounded by a viscoelastic shell, *Phys. Earth Plan. Interiors*, 56, 316-328, 1989.
- Druitt, T. H., and R. S. J. Sparks, On the formation of calderas during ignimbrite eruptions, *Nature*, 310, 679-681, 1984.
- Dvorak, J. J., and D. Dzurisin, Volcano geodesy: the search for magma reservoirs and the formation of eruptive vents, *Rev. Geophys.*, 35, 343-384, 1997.
- Eichelberger, J. C., C. R. Carrigan, H. R. Westrich, and R. H. Price, Non-explosive silicic volcanism, *Nature*, 323, 598-602, 1986.
- Fernández, J., and J.B. Rundle, Gravity changes and deformation due to a magmatic intrusion in a two-layered crustal model, *J. Geophys. Res.*, 99, 2737-2746, 1994.
- Fernández, J., J. B. Rundle, R. Granell, and T.-T. Yu, Programs to compute deformation due magma intrusion in a elastic-gravitational layered Earth model, *Computers & Geosciences*, 23, 231-249, 1997.
- Fernández, J., J. M. Carrasco, J. B. Rundle, and V. Araña, Geodetic methods for detecting volcanic unrest. A theoretical approach, *Bull. Volcanol.*, 60, 534-544, 1999.
- Folch, A., J. Martí, R. Codina, and M. Vázquez, A numerical model for temporal variations during explosive central vent eruptions, *J. Geophys. Res.*, 103, 20883-20899, 1998a.
- Folch, A., and J. Martí, The generation of overpressure in felsic magma chambers by replenishment, *Earth Planet. Sci. Lett.*, 163, 310-314, 1998b.
- Folch, A., M. Vázquez, R. Codina, and J. Martí, A fractional-step finite-element method for the Navier-Stokes equations applied to magma chamber withdrawal, *Computers & Geosciences*, 25, 263-275, 1999.
- Folch, A., J. Fernández, J. B. Rundle, and J. Martí, Ground deformation in a viscoelastic medium composed of a layer overlaying a half-space. A comparison between point and extended sources, *Geophys. J. Int.*, 140, 37-50, 2000.
- Freund, A., and S. R. Tait, The entrainment of high-viscosity magma in eruption conduit, *Bull. Volcanol.*, 48, 325-339, 1986.
- Fridrich, C. J., and G. A. Mahood, Compositional layers in the zoned magma chamber of the Grizzly Peak Tuff, *Geology*, 15, 299-303, 1987.

-
- Gilbert, J. S., and R. S. J. Sparks, The physics of explosive volcanism, *Geological society special publication*, 145, London, 1998.
- Gilberti, G., and L. Wilson, The influence of geometry on the ascent of magma in open fissures, *Bull. Volcanol.*, 52, 515-521, 1990.
- Gudmundsson, A., J. Martí, and E. Turón, Stress fields generating ring faults in volcanoes, *Geophys. Res. Lett.*, 24, 1559-1562, 1997.
- Gudmundsson, A., Formation and development of normal-fault calderas and the initiation of large explosive eruptions, *Bull. Volcanol.*, 60, 160-171, 1998.
- Hamilton, D. L., C. W. Burnham, and E. F. Osborn, The solubility of water and effects of oxygen fugacity and water content on crystallization in mafic magmas, *J. Petrol.*, 5, 21-39, 1964.
- Heiken, G., and F. McCoy, Caldera development during the Minoan eruption, Thira, Cyclades, Greece, *J. Geophys. Res.*, 89, 8441-8462, 1984.
- Hess, K.U., and D. Dingwell, Viscosities of hydrous leucogranitic melts: a non-Arrhenian model, *Am. Mineral.*, 80, 94-108, 1996.
- Hildreth, W., and G. A. Mahood, Ring-fracture eruption of the Bishop Tuff, *Geol. Soc. Am. Bull.*, 97, 396-403, 1986.
- Hildreth, W., The timing of caldera collapse at Mount Katmai in response to magma withdrawal toward Novarupta, *Geophys. Res. Lett.*, 18, 1541-1544, 1991.
- Hofton, M. A., J. B. Rundle, and G. R. Foulger, Horizontal surface deformation due to dike emplacement in an elastic-gravitational layer overlying a viscoelastic-gravitational half-space, *J. Geophys. Res.*, 100, 6329-6338, 1995.
- Holloway, J. R., Fugacity and activity of molecular species in supercritical fluids, *Thermodynamics in Geology*, ed. D. G. Fraser, Holland, 1977.
- Holloway, J. R., and J. G. Blank, Application of experimental results to C-O-H species in natural melts, in Carroll, M. and Holloway, J. R. eds., *Volatiles in magmas*, Mineralogical Society of America, *Reviews in Mineralogy*, 30, 187-230, 1994.
- Holtz, F., H. Behrens, and D. Dingwell, Water solubility in haplogranitic melts: compositional, pressure and temperature dependence, *Am. Mineral.*, 80, 94-108, 1995.
- Huppert, H. E., R. S. J. Sparks, and J. S. Turner, Effects of volatiles on mixing in calc-alkaline magma systems, *Nature*, 297, 554-557, 1982a.
- Huppert, H. E., J. S. Turner, and R. S. J. Sparks, Replenished magma chambers: effects of compositional zonation and input rates, *Earth Planet. Sci. Lett.*, 57, 345-357, 1982b.
- Ishii, M., and N. Zuber, Drag coefficient and relative velocity in bubbly, droplet and particulate flows, *Am. Inst. Chem. Engrg. J.*, 25, 843-855, 1979.
- Ivey, G. N., and S. Blake, Axisymmetric withdrawal and inflow in a density stratified container, *J. Fluid Mech.*, 161, 115-137, 1985.
- Jaupart, C., and C. J. Allègre, Gas content, eruption rate and instabilities of eruption regime in silicic volcanoes, *Earth Planet. Sci. Lett.*, 102, 413-429, 1991.

2.5 References

- Langbein, J., D. Dzurisin, G. Marshall, R. Stein, and J. B. Rundle, Shallow and peripheral volcanic sources of inflation revealed by modeling two-colour geodimeter and leveling data from Long Valley caldera, California, 1988-1992, *J. Geophys. Res.*, *100*, 12487-12495, 1995.
- Lister, J. R., Selective withdrawal from a viscous two-layer system, *J. Fluid Mech.*, *198*, 231-254, 1989.
- Lipman, P. W., The roots of ash flow calderas in western north America: windows into tops of granitic batholiths, *J. Geophys. Res.*, *89*, 8801-8841, 1984.
- Lipman, P. W., Subsidence of ash-flow calderas: relation to caldera size and magma-chamber geometry, *Bull. Volcanol.*, *59*, 198-218, 1997.
- Macedonio, G., F. Dobran, and A. Neri, Erosion processes in volcanic conduits and application to the AD 79 eruption of Vesuvius, *Earth Planet. Sci. Lett.*, *121*, 137-152, 1994.
- Martí, J., G. Ablay, L. T. Redshaw, and R. S. J. Sparks, Experimental studies of collapse calderas, *J. Geol. Soc. London*, *151*, 919-929, 1994.
- McBirney, A. R., Factors governing the intensity of explosive volcanic eruptions, *Bull. Volcanol.*, *37*, 443-453, 1973.
- McBirney, A. R., and T. Murase, Rheological properties of magmas, *Ann. Rev. Earth Planet. Sci.*, *12*, 337-357, 1984.
- McTigue, D. F., and R. S. Stein, Topographic amplification of tectonic displacement: implications for geodetic measurement of strain changes, *J. Geophys. Res.*, *89*, 1123-1131, 1984.
- McTigue, D. F., Elastic stress and deformation near a finite spherical magma body: resolution of the point source paradox, *J. Geophys. Res.*, *92*, 12931-12940, 1987.
- McTigue, D. F., and P. Segall, Displacements and tilts from dip-slip faults and magma chambers beneath irregular surface topography, *Geophys. Res. Lett.*, *15*, 601-604, 1988.
- Mogi, K., Relations of the eruptions of various volcanoes and the deformations of the ground surface around them, *Bull. Earthq. Res. Inst.*, *36*, 99-134, 1958.
- Moores, M., and R. J. Twiss, *Tectonics*, W.H. Freeman and Company, New York, 1995.
- Morey, G. W., The development of pressure in magmas as a result of crystallization, *J. Wash. Acad. Sci.*, *12*, 219-230, 1922.
- Neri, A., and G. Macedonio, Numerical simulation of collapsing volcanic columns with particles of two sizes, *J. Geophys. Res.*, *101*, 8153-8174, 1996.
- Neri, A., P. Papale, and G. Macedonio, The role of magma composition and water content in explosive eruptions: 2. Pyroclastic dispersion dynamics, *J. Volcanol. Geotherm. Res.*, *87*, 95-115, 1998.
- Newhall, C. G., and D. Dzurisin, Historical unrest at large calderas of the world, *US Geol. Surv. Bull.*, *1855*, 1-1108, 1988.

-
- Pallister, J. S., R. P. Hoblitt, and A. G. Reyes, A basalt trigger for the 1991 eruptions of Pinatubo volcano, *Nature*, 356, 426-428, 1992.
- Papale, P., and F. Dobran, Modeling of the ascent of magma during the plinian eruption of Vesuvius in AD 79, *J. Volcanol. Geotherm. Res.*, 58, 101-132, 1993.
- Papale, P., Modeling of magma ascent along volcanic conduits: a review, Environment and climate programme. In: The mitigation of volcanic hazards, *ECC Report*, 5-40, 1994a.
- Papale, P., and F. Dobran, Magma flow along volcanic conduit during the plinian and pyroclastic flow phases of the May 18, 1980, Mount St. Helens eruption, *J. Geophys. Res.*, 99, 4355-4373, 1994b.
- Papale, P., A. Neri, and G. Macedonio, The role of magma composition and water content in explosive eruptions. 1- Conduit ascent dynamics, *J. Volcanol. Geotherm. Res.*, 87, 75-93, 1998.
- Prousevitch, A. A., D. L. Shagian, and A. T. Anderson, Dynamics of diffusive bubble growth in magmas: Isothermal case, *J. Geophys. Res.*, 98, 22283-22307, 1993.
- Ramos, J. I., One-dimensional, time-dependent, homogeneous, two-phase flow in volcanic conduits, *Int. J. Numer. Meth. Fluids*, 21, 253-278, 1995.
- Rollinson, H., Using geochemical data: evaluation, presentation, interpretation, *Longman Scientific&Technical*, New York, 1993.
- Rundle, J. B., Static elastic-gravitational deformation of a layered half space by point couple sources, *J. Geophys. Res.*, 85, 5355-5363, 1980.
- Rundle, J. B., Deformation, gravity, and potential changes due to volcanic loading of the crust, *J. Geophys. Res.*, 87, 10729-10744, 1982.
- Rymer, H., J. Cassidy, C. A. Locke, and J. B. Murray, Magma movements in Etna volcano associated with the major 1991-1993 lava eruption: evidence from gravity and deformation, *Bull. Volcanol.*, 57, 451-461, 1995.
- Sartoris, G., J. P. Pozzi, C. Philippe, and J. L. Moüel, Mechanical stability of shallow magma chambers, *J. Geophys. Res.*, 95, 5141-5151, 1990.
- Scandone, R., Factors controlling the temporal evolution of explosive eruptions, *J. Volcanol. Geotherm. Res.*, 72, 71-83, 1996.
- Self, S., F. Goff, J. N. Gardner, J. V. Wright, and W. M. Kite, Explosive rhyolitic volcanism in the Jemez Mountains: vent location, caldera development and relation to regional structure, *J. Geophys. Res.*, 91, 1770-1798, 1989.
- Shaw, H. R., Viscosities of magmatic silicate liquids: an empirical method of prediction, *Am. J. Sci.*, 272, 870-893, 1972.
- Silver, L., and E. Stolper, Water in albitic glasses, *J. Petrol.*, 30, 667-709, 1988.
- Smith, R.L., and R. A. Bailey, Resurgent cauldrons, *Geol. Soc. Am. Mem.*, 116, 613-622, 1968.
- Smith, R. L., Ash flow magmatism, *Spec. Pap. Geol. Soc. Am.*, 180, 5-27, 1979.

2.5 References

- Snyder, D., and S. Tait, Replenishment of magma chambers: comparison of fluid-mechanic experiments with field relations, *Contrib. Mineral. Petrol.*, 122, 230-240, 1995.
- Snyder, D., and S. Tait, Magma mixing by convective entrainment, *Nature*, 379, 529-531, 1996.
- Sparks, R.S.J., and L. Wilson, A model for the formation of ignimbrite by gravitational column collapse, *J. Geol. Soc. London.*, 132, 441-451, 1976.
- Sparks, R. S. J., H. Sigurdsson, and L. Wilson, Magma mixing: a mechanism for triggering acid explosive eruptions, *Nature*, 267, 315-318, 1977.
- Sparks, R. S. J., The dynamics of bubble formation and growth in magmas, a review and analysis, *J. Volcanol. Geotherm. Res.*, 3, 1-37, 1978.
- Sparks, R. S. J., P. W. Francis, R. D. Hamer, R. J. Pankhurst, L. O. O'Callaghan, R. S. Thorpe, and R. Page, Ignimbrites of the Cerro Galan caldera, NW Argentina, *J. Volcanol. Geotherm. Res.*, 24, 205-248, 1985.
- Sparks, R. S. J., and L. A. Marshall, Thermal and mechanical constraints between mafic and silicic magmas, *J. Volcanol. Geotherm. Res.*, 29, 99-124, 1986.
- Sparks, R.S.J., *Volcanic plumes*, 1997.
- Spera, F., Some numerical experiments on the withdrawal of magma from crustal reservoirs, *J. Geophys. Res.*, 89, 8222-8236, 1984.
- Spera, F., D. A. Yuen, J. C. Greer, and G. Sewell, Dynamics of magma withdrawal from stratified magma chambers, *Geology*, 14, 723-726, 1986.
- Stolper, E., and J. R. Holloway, Experimental determination of the solubility of carbon dioxide in molten basalt at low pressure, *Earth Planet. Sci. Lett.*, 87, 397-408, 1988.
- Sturtevant, B., B. Kanamori, and E. E. Brodsky, Seismic triggering by rectified diffusion in geothermal systems, *J. Geophys. Res.*, 101, 25269-25282, 1996.
- Suzuki-Kamata, K., H. Kamata, and C. R. Bacon, Evolution of the caldera-forming eruption at Crater Lake, Oregon, indicated by component analysis of lithic fragments, *J. Geophys. Res.*, 98, 14059-14074, 1993.
- Tait, S., C. Jaupart, and S. Vergnolle, Pressure, gas content and eruption periodicity of a shallow crystallizing magma chamber, *Earth Planet. Sci. Lett.*, 92, 107-123, 1989.
- Tilling, R. I., and J. J. Dvorak, Anatomy of a basaltic volcano, *Nature*, 363, 125-133, 1993.
- Toramaru, A., Vesiculation processes and bubble size distributions in ascending magmas with constant velocities, *J. Geophys. Res.*, 43, 17523-17542, 1989.
- Touloukian, Y. S., W. R. Judd, and R. F. Roy, Physical properties of rocks and minerals, vol. 1, *McGraw-Hill*, New York, 1981.
- Trial, A. F., F. Spera, J. Greer, and D. Yuen, Simulations of magma withdrawal from compositionally zoned bodies, *J. Geophys. Res.*, 97, 6713-6733, 1992.
- Turcotte, D. L., H. Ockendon, J. R. Ockendon, and S. J. Cowley, A mathematical model of vulcanian eruptions, *Geophys. J. Int.*, 103, 211-217, 1990.

-
- Turner, J. S., and I. H. Campbell, Convection and mixing in magma chambers, *Earth Sci. Rev.*, 23, 255-352, 1986.
- Valentine, G. A., and K. H. Wohletz, Numerical models of Plinian eruption columns and pyroclastic flows, *J. Geophys. Res.*, 94, 1867-1887, 1989.
- Vergnolle, S., and C. Jaupart, Separated two-phase flow and basaltic eruptions, *J. Geophys. Res.*, 91, 12842-12860, 1986.
- Walker, G. P., Explosive volcanic eruptions; a new classification scheme, *Geol. Rundschau*, 62, 431-446, 1973.
- Walker, G. P., Downsag calderas, ring faults, caldera sizes, and incremental growth, *J. Geophys. Res.*, 89, 8407-8416., 1984.
- Williams, H., Calderas and their origin, *Univ. California Dept. Geol. Sci. Bull.*, 25, 239-346, 1941.
- Williams, H., and A. R. McBirney, *Volcanology*, California, 1979.
- Williams, C.A., and G. Wadge, The effects of topography on magma chamber deformation models: Applications to Mt. Etna and radar interferometry, *Geophys. Res. Lett.*, 25, 1549-1552, 1998.
- Wilson, L., Explosive volcanic eruptions. III. Plinian eruption columns, *Geophys. J. Royal. Astr. Soc.*, 45, 543-556, 1976.
- Wilson, L., R. S. J. Sparks, and G. Walker, Explosive volcanic eruptions- IV. The control of magma properties and conduit geometry on eruption column behaviour, *Geophys. J. Royal. Astr. Soc.*, 63, 117-148, 1980.
- Wilson, L., and J. W. Head, Ascent and eruption of basaltic magma on the earth and moon, *J. Geophys. Res.*, 86, 2971-3001, 1981.
- Wilson, M., *Igneous petrogenesis*, Chapman & Hall, U.K., 1989.
- Woods, A., The dynamics of explosive volcanic eruptions, *Rev. of Geophys.*, 33, 495-530, 1995.
- Woods, A., and T. Koyaguchi, Transitions between explosive and effusive eruptions of silicic magmas, *Nature*, 370, 641-644, 1999.

Chapter 3

Governing Equations

Chapter Contents

- 3.1. Assumptions and Requirements
 - 3.2. A State Law for the Magmatic Mixture
 - 3.3. ALE Governing Equations
 - 3.3.1. Introduction to the ALE Formulation
 - 3.3.2. ALE Continuity Equation
 - 3.3.3. ALE Momentum Equation
 - 3.3.4. ALE Energy Equation
 - 3.4. Flow Equations
 - 3.4.1. Newtonian Fluids
 - 3.4.2. ALE Navier-Stokes Equations
 - 3.5. Structural Equations
 - 3.5.1. Linear Elastic Materials
 - 3.5.2. Linear Viscoelastic Materials
 - 3.6. References
- Appendix 3A. Deduction of the ALE Governing Equations

Abstract

Most of this chapter has been designed for those readers without a basis on continuum mechanics. The chapter presents all the governing equations required to solve both the “flow problem” and the “structural problem”. Firstly, some necessary hypothesis and simplifications of the physical model are briefly exposed and an original state law for the magmatic mixture under the homogeneous approach is presented. An important characteristic of the proposed state law is that magma can be either compressible or incompressible depending on a critical pressure. This property justifies the choice of the numerical formulation that will be developed further. Secondly, a review of the principles of the Arbitrary Lagrangian Eulerian (ALE) formulation as well as the governing equations of any continuous medium considering an ALE formulation are presented. The use of an ALE formulation is required in order to face properly the problem of caldera-forming eruptions, for which the coupling fluid-structure must be considered. Finally, these equations are particularised to the cases of interest: Newtonian fluids and linear viscoelastic materials.

3.1 Assumptions and Requirements

This work focuses on the modelling some of particular volcanic processes. The main objective is to model the chamber withdrawal process (for both open and closed systems) as well as caldera forming eruptions. These are basically “flow problems”, in which the following assumptions are done

- Magma is a continuous medium.
- Magma behaves as a Newtonian fluid. Laboratory experiments have demonstrated that a Newtonian behaviour is a good approximation to the rheology of silicate melts at low strain rates [Webb and Dingwell, 1990; Dingwell *et al.*, 1993]. However, it should be noted that this is just a first approach to reality since when the strain rate increases or when the melt contains vesicles and/or crystals a wide variety of non-Newtonian effects may appear. Newtonian hypothesis does not imply any supposition on viscosity dependencies. Any dependence on dissolved volatiles, crystal content, temperature, pressure, etc. can be considered in the model.
- Most volcanic eruptions (specially explosive) involve conduit erosion. On the other hand, both conduit and chamber geometries are susceptible to vary during the course of an eruption in response to the pressure changes. It implies that a complete modelling of volcanic eruptions should be performed considering not only the flow problem but also the response of the environment to the pressure changes. To have into account this coupling one has to face two major drawbacks. Firstly, the rheology of the host rock is not well known in general and, in many cases, the simplest rheological model (linear elastic) is insufficient. Secondly, and whichever the rheology considered, one should know both the depth-dependent properties of the environment and the particularities (faults, local tectonics, etc.) that affect the stress field around a given volcanic system. In practise, this knowledge is difficult, if not impossible. Due to these limitations and in order to simplify the problem (to avoid the coupling with the mechanical problem) rigid walls are assumed during the course of an eruption. It applies also to the modelling of caldera forming eruptions, where the falling block is considered to be a rigid solid. Despite these assumptions should not affect the results qualitatively, they impede the determination of the beginning /ending of the eruptive process (opening/closure of fractures). In other words, initial and final conditions can not be a result of the model but must be imposed.
- The model contemplates the possibility of chemically heterogeneous magma chambers. When heterogeneous, it is assumed that heterogeneities (e.g. variations of density, viscosity, volatile

3.1 Assumptions and Requirements

content, etc.) are transported by means of a purely convective transport equation during the eruptive process. This assumption is justified because chemical diffusion operates in a time scale orders of magnitude longer than the duration of an eruption. As discussed later, some effects induced by density variations are neglected in the numerical solution of the problem.

Under these assumptions, the only requirement for the “flow problems” is the solution of the Navier-Stokes equations complemented with a suitable state law for the magmatic mixture (developed in section 3.2). An additional convective transport equation is also required in non-homogeneous systems. Moreover, in the case of caldera collapse, one must consider also the coupling between the fluid and the motion of the rigid solid (the block that subsides). For this purpose, it is very advantageous from a numerical point of view to consider the flow governing equations in the frame of an ALE formulation (see sections 3.3 and 3.4).

On the other hand, a secondary objective is to model ground deformations in active volcanic areas considering both elastic and viscoelastic rheologies for the crust. For this “structural problem” the only requirement is to solve the classical elastic/viscoelastic governing equations of a solid material.

3.2 A State Law for the Magmatic Mixture

Magmas are silicate melts with crystals and dissolved volatile species within. Processes leading to magma genesis, its subsequent chemical evolution and its physical properties have been already exposed in chapter 2. In general, its composition (i.e. its physical properties) as well as its thermodynamic conditions can vary notably from one magma to another. This very wide spectrum of possibilities makes almost impossible to characterise its behaviour using a single state law to cover all the compositional and thermodynamic ranges. In this section, a relatively simple state law, already proposed in [Folch *et al.*, 1998], is presented. The hypothesis implicitly assumed to deduce this state law constrain its validity to the bubbly flow regime and, in consequence, to the magma chamber and to the lowermost parts of the volcanic conduit.

When high viscosity magmas (chemically evolved) are located above the exsolution level and prior to its fragmentation (i.e. when they are below the fragmentation level), magmatic mixture can be regarded as a bubbly flow characterised by a liquid continuum with dispersed gas bubbles and crystals in thermal and mechanical equilibrium [Papale, 1994]. In this bubbly flow regime, pressure differences between liquid and gas bubbles can be ignored [Sparks, 1978] and both phases can be considered to move with the same velocity even for centimetric bubble sizes¹. Then, the mixture is a continuous medium with density

$$\mathbf{r} = \mathbf{a} \mathbf{r}_g + (1 - \mathbf{a}) \mathbf{r}_s \cong \mathbf{a} \mathbf{r}_g + (1 - \mathbf{a}) \mathbf{r}_l \quad (3.2.1)$$

where \mathbf{a} is the gas volume fraction, \mathbf{r}_g is the gas density, \mathbf{r}_s is the density of the melt (containing dissolved volatiles) and \mathbf{r}_l is the density of the liquid (without considering the volatiles dissolved within). This homogeneous approximation for the mixture is commonly assumed in the literature [Wilson *et al.*, 1980; Gilberti and Wilson, 1990], at least in the lowermost parts of the conduit and for high viscosity magmas. Note that the above equation considers that dissolved volatiles do not change the bulk density of the liquid. Gas phase will be assumed to behave as a perfect gas [Vergnolle and Jaupart, 1986], so that one can relate gas density \mathbf{r}_g and pressure p by means of

$$p = \mathbf{r}_g Q T \quad (3.2.2)$$

¹ Notwithstanding this, the formation of large bubbles in high-viscosity magmas is unlikely because growth by coalescence is impeded.

3.2 A State Law for the Magmatic Mixture

where T is temperature and Q is the perfect gas constant $R = 8.31 \text{ J/}^\circ\text{K mol}$ divided by the molecular weight¹.

Let m_d be the mass of dissolved gas, m_g the mass of exsolved gas, m_v the total mass of volatiles (dissolved plus exsolved, that is $m_v = m_g + m_d$), m_l the mass of the liquid, m_s the mass of the melt (liquid plus dissolved gas within, that is $m_s = m_l + m_d$) and M the total mass ($M = m_l + m_v = m_s + m_g$). Then, the gas mass fraction of volatiles dissolved in the melt c , the volatile mass fraction (dissolved plus exsolved) W and the gas mass fraction n_g are respectively given by

$$c = \frac{m_d}{m_d + m_l} = \frac{m_d}{m_s} \quad (3.2.3)$$

$$W = \frac{m_v}{M} = \frac{m_v}{m_v + m_l} \quad (3.2.4)$$

$$n_g = \frac{m_g}{M} = \frac{m_g}{m_g + m_s} \quad (3.2.5)$$

$$W = n_g + (1 - n_g)c \quad (3.2.6)$$

In order to find the state law, one should consider that volatile species can be either dissolved within the melt or, if the magma is above the exsolution level, exsolved as a gas phase. Therefore, a solubility law is also needed to determine the mass fraction of volatiles dissolved in the melt at given thermodynamic conditions. In general, many volatile species (such as H_2O , CO_2 , H_2S , HF , etc.) are susceptible to be present in magmas but, in order to simplify the problem, only one is considered here (H_2O for chemically evolved magmas and CO_2 for mafic magmas). The simplest relationship under magmatic conditions is a Henry law equation, where the solubility² c depends only on a pressure power

$$c = s p^n \quad (3.2.7)$$

¹ In the most typical cases of H_2O and CO_2 one has $Q=461.66 \text{ J/}^\circ\text{K Kg}$ and $Q=188.86 \text{ J/}^\circ\text{K Kg}$ respectively.

² Solubility is, by definition, the maximum amount of volatiles that can be dissolved under certain ambient conditions. If the amount of existing volatiles is lower than this critical value the melt is undersaturated and all the volatiles are dissolved. On the contrary, the melt is oversaturated and the remainder volatiles are exsolved as a gas phase.

s and n being constants that depend on both magma and volatile compositions. Values for these solubility constants are experimentally determined for the most common volatile species [Tait *et al.*, 1989]. Gas exsolution takes place when $c = W$. It occurs at a critical pressure p_c which, for the Henry law, depends only on the volatile content W

$$p_c = \left(\frac{W}{s} \right)^{\frac{1}{n}} \quad (3.2.8)$$

It is also assumed that exsolution occurs instantaneously when pressure descends below this critical value, and no energetic contributions are considered during the vesiculation process. Considering the solubility law (3.2.7), the following relationships are verified

$$\left. \begin{aligned} s p^n = c = \frac{m_d}{m_d + m_l} < W = \frac{m_v}{m_v + m_l} \\ n_g > 0 \end{aligned} \right\} \text{above exsolution level (oversaturated)} \quad (3.2.9)$$

$$\left. \begin{aligned} s p^n = c > \frac{m_d}{m_d + m_l} = W = \frac{m_v}{m_v + m_l} \\ n_g = 0 \end{aligned} \right\} \text{below exsolution level (undersaturated)}$$

Finally, using equations (3.2.1) to (3.2.9) and after some algebra, one gets the searched expression for the state law

$$\mathbf{r} = \frac{\mathbf{r}_l}{1 + \left(\frac{\mathbf{r}_l}{\mathbf{r}_g} - 1 \right) \left(\frac{W - s p^n}{1 - s p^n} \right) \mathbf{q}(p_c - p)} \cong \frac{\mathbf{r}_l}{1 + \left(\frac{\mathbf{r}_l Q T}{p} \right) \left(\frac{W - s p^n}{1 - s p^n} \right) \mathbf{q}(p_c - p)} \quad (3.2.10)$$

where \mathbf{q} is the Heaviside step function ($\mathbf{q} = 0$ for $p \geq p_c$ and $\mathbf{q} = 1$ for $p \leq p_c$). Note that (3.2.10) is a general state law applicable not only to vesiculated magmas but also to any two phase system in the bubbly flow regime. In general, the critical pressure p_c at which gas exsolution begins will be attained or not inside the magma chamber depending on chamber depth (lithostatic pressure) and volatile content. If this critical pressure is not attained, that is, if magma is not vesiculated, one has $\mathbf{q} = 0$ in (3.2.10) and the density of the mixture is that of the liquid.

Once the state law has been obtained, it is possible to determine the gas volume fraction \mathbf{a} . Substituting (3.2.2) and (3.2.10) into the homogeneous approach (3.2.1) one obtains

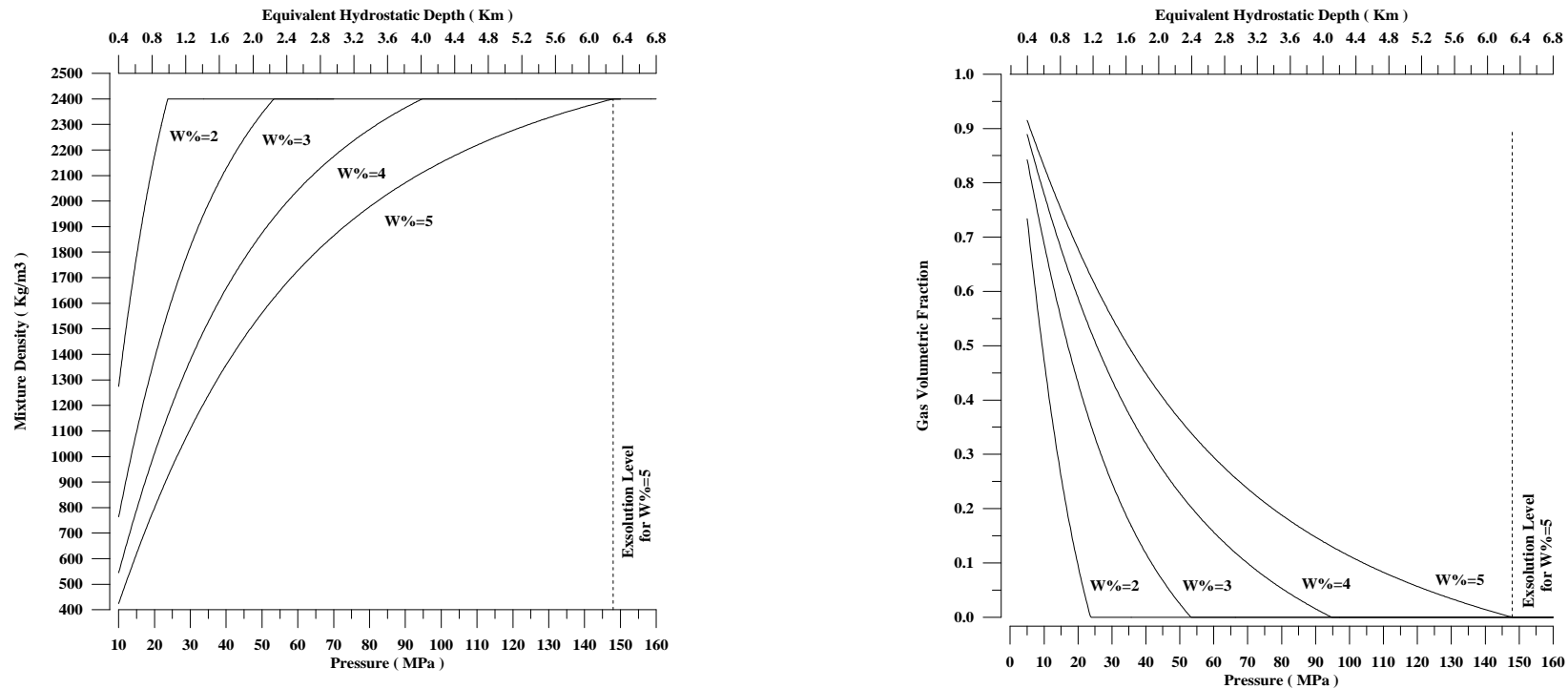


Figure 3.2.1. Results for a rhyolitic magma with $\rho_l=2400 \text{ Kg/m}^3$ at $T=850^\circ\text{C}$ and considering water as the only volatile specie. Results for water contents of 2, 3, 4, and 5% in weight (for W values of 0.02, 0.03, 0.04, and 0.05 respectively). Solubility constants are, in this case, $s=4.11 \cdot 10^{-6} \text{ Pa}^{-1/2}$ and $n=0.5$ [Tait *et al.*, 1989]. Left: mixture density versus pressure predicted by the state law. The equivalent hydrostatic depth for every pressure is also shown. This equivalent hydrostatic depth is, by definition, the depth at which the pressure produced by a liquid with constant density ρ_l at rest would be equal to the thermodynamic pressure p . It approximately indicates the depth at which a given process (such, for instance, volatile exsolution) may take place. Note how the exsolution level depends on water content. Below the exsolution level (for $p > p_c$) magma has a constant density $\rho = \rho_l$, but above this level (for $p < p_c$) mixture density is presents non-linearity and depends on pressure. As pressure descends, bubbles grow reducing thus the density of the mixture. Right: gas volume fraction versus pressure using the same water contents. Note how, whichever the water content, high volume gas fractions ($\alpha > 0.7$) that are commonly observed when magma fragments are only achieved at low pressure values (i.e. at the uppermost parts of the volcanic conduit).

$$\mathbf{a} = \frac{\mathbf{r}_l}{(\mathbf{r}_l - \mathbf{r}_g)} \frac{\mathbf{a}}{1 + \mathbf{a}} \quad \text{where} \quad \mathbf{a} = \frac{\mathbf{r}_l Q T (W - s p^n)}{p (1 - s p^n)} \mathbf{q} (p - p_c) \quad (3.2.11)$$

Figure 3.2.1 shows the density predicted by (3.2.10) as well as the gas volume fraction predicted by (3.2.11) as a function of pressure and for a rhyolitic magma considering several water contents. Note how high volumetric gas fractions ($\mathbf{a} \geq 0.7$) that impede bubbly flow regime, lead magma to fragment¹, and constrain the application of the state law, are only achieved at low pressure values (i.e. at the uppermost parts of the conduit). The behaviour of the state law at this critical region has been checked comparing its predictions with some experimental data. As illustrated in figure 3.2.2, even in this region where the assumptions of the law are clearly not verified, its predictions are, surprisingly, reasonable. Figure 3.2.3 shows results similar to those of figure 3.2.1 but when a mafic magma with different contents on carbon dioxide is considered.

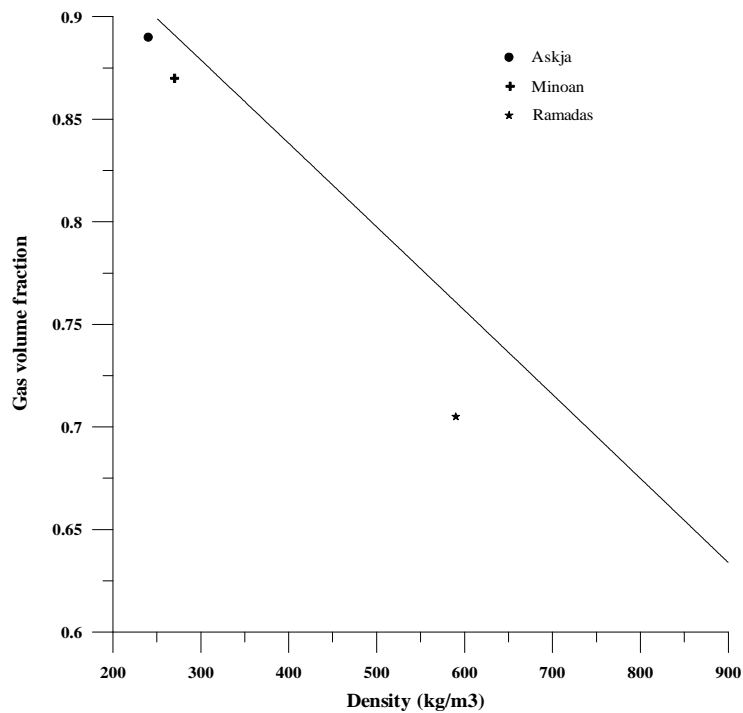


Figure 3.2.2. Gas volume fraction versus density for rhyolitic magmas at the uppermost parts of the conduit and according to the state law. Symbols represent averaged data of pumices from the 1875 Askja (Iceland) eruption [Whitham and Sparks, 1986], the Minoan (Santorini) eruption [Whitham and Sparks, 1986] and the Ramadas (Argentina) eruption [Martí et al., 1999]. Despite the assumptions used to derive the state law are not accomplished in this region, results are not unreasonable.

¹ This fact is controversial. See section 2.3.2 for major comprehension.

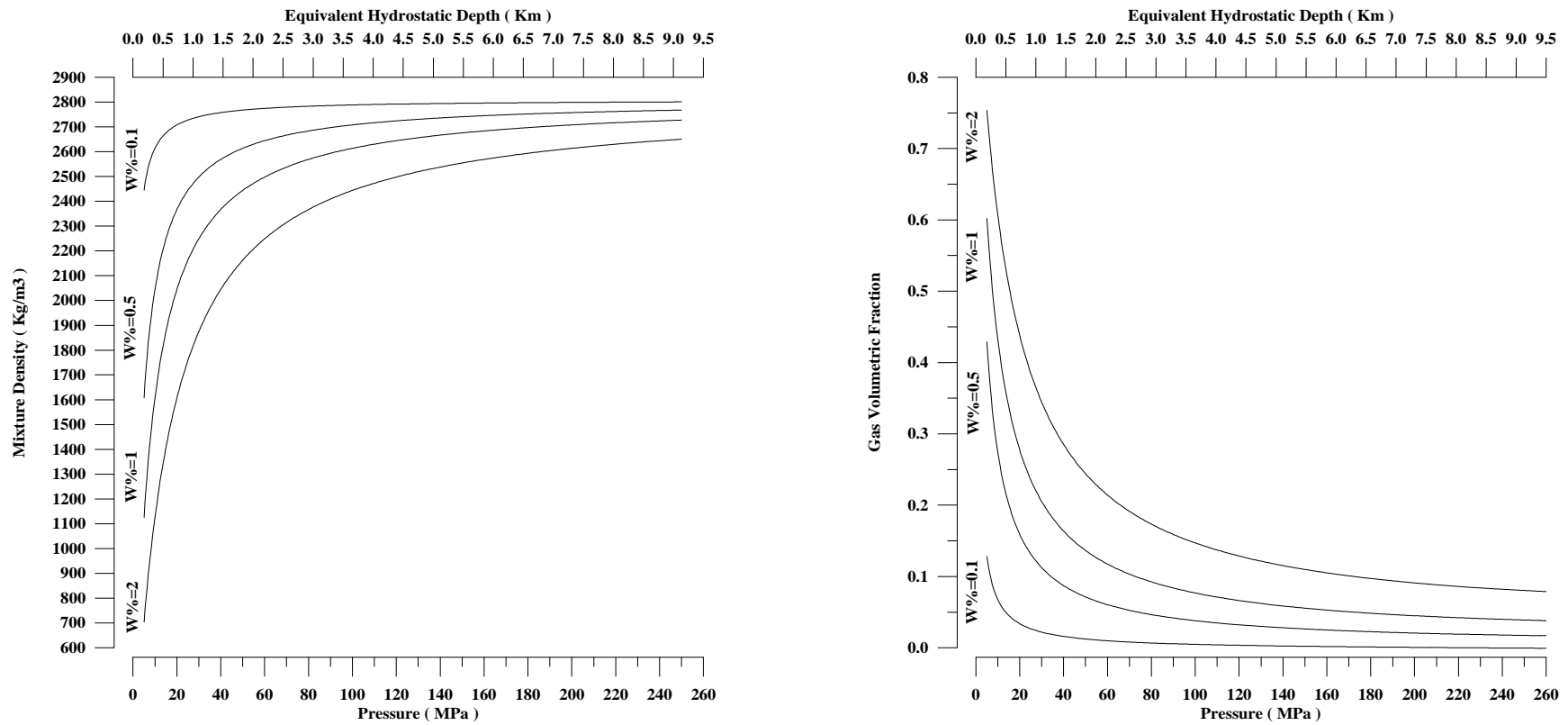


Figure 3.2.3. Results for a mafic magma with $\rho_i=2800 \text{ kg/m}^3$ at $T=1200^\circ\text{C}$ considering carbon dioxide as the only volatile specie. Results for CO_2 contents of 0.1, 0.5, 1, and 2% in weight (for W values of 0.001, 0.005, 0.01, and 0.02 respectively). Solubility constants are, in this case, $s=4.4 \cdot 10^{-12} \text{ Pa}$ and $n=1.0$ [Tait *et al.*, 1989]. Left: mixture density versus pressure predicted by the state law. Right: gas volume fraction versus pressure using the same CO_2 contents. Despite the different solubility laws produce very different behaviours, similar conclusions that in the case of rhyolitic magmas with water can be drawn (see figure 3.2.1).

A couple of comments should be done before concluding this section.

❶ The state law (3.2.10) depends on liquid density r_l which, in general, could be considered either as constant or pressure dependent. In this case, one could assume that [Blake, 1984]

$$r_l = r_0 \exp\left(\frac{p-p_0}{b}\right) \quad (3.2.12)$$

where b is the compressibility modulus and r_0 is the density at a pressure reference p_0 . Typical magma values for compressibility modulus b are 10-100 GPa [Touloukian *et al.*, 1981]. Figure 3.2.4 shows how the differences in the state law when both possibilities are considered (that is, $r_l = \text{cte}$ or r_l given by (3.2.12)) are negligible.

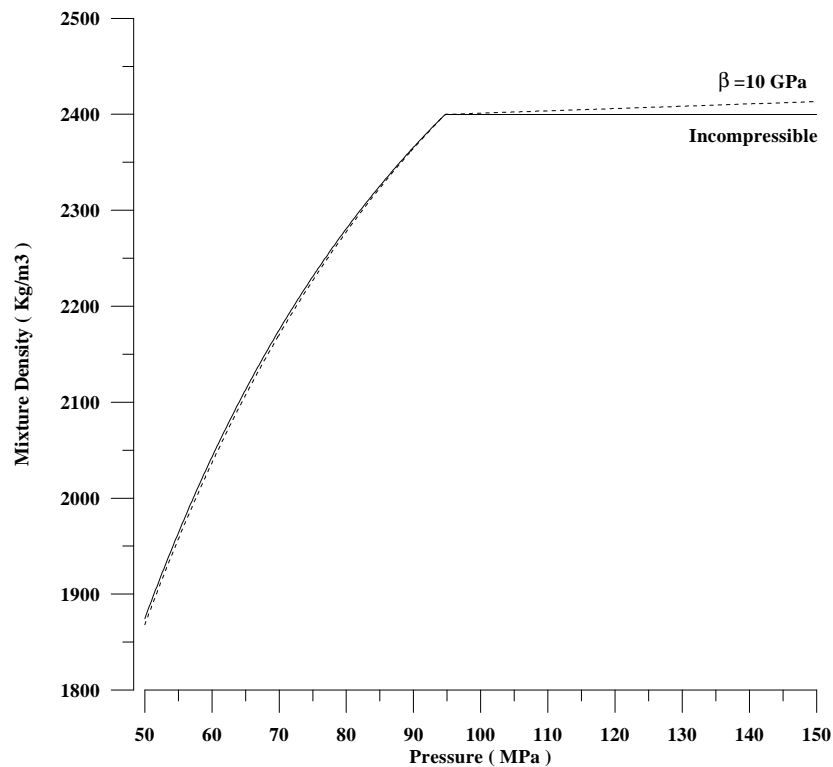


Figure 3.2.4. Mixture density versus pressure for rhyolitic magmas with $\rho_l = 2400 \text{ Kg/m}^3$, $T=850^\circ\text{C}$ and water content of 4% in weight ($W=0.04$). Results for $\beta=\infty$ (incompressible) and $\beta=10 \text{ GPa}$ (magma has values of the compressibility modulus β ranging from 10 to 100 GPa). Note that, even for low values of the compressibility modulus β , its influence is a second order effect. It implies that magma can be considered to be an incompressible flow below the exsolution level.

3.2 A State Law for the Magmatic Mixture

In consequence, it can be concluded that, due to the high values of b , non-vesiculated magmas can be safely considered to be incompressible flows. Hence, liquid density r_l is set as constant and the state law becomes finally

$$r = \left\{ \begin{array}{ll} r_l = \text{constant} & \text{Below the exsolution level (if } p \geq p_c) \\ \frac{r_l}{1 + \left(\frac{r_l QT}{p} \right) \left(\frac{W - s p^m}{1 - s p^m} \right)} & \text{Above the exsolution level (if } p < p_c) \end{array} \right\} \quad (3.2.13)$$

Observation The use of (3.2.13) implies that, depending on pressure, the flow is either compressible or incompressible. In consequence, the numerical solution of the flow problem will require an algorithm able to deal simultaneously well with both kind of flows.

❷ The state law depends also on temperature. It means that, theoretically, mechanical and thermal equations are coupled. Figure 3.2.5 illustrates the influence of temperature on the state law considering two extreme values for temperature. As observed from this figure, the effect of temperature is small near the exsolution level but, in contrast, produces appreciable differences at low pressures (i.e. at the uppermost parts of the conduit). It means that depending on the domain of interest, the coupling between thermal and mechanical equations should be considered or not. In other words, below or close the exsolution level the mixture is incompressible or barotropic, temperature can be considered constant, and the thermal problem is not needed. In contrast, at the uppermost part of the conduit, both pressure and temperature have influence on the state law and, in consequence, both thermal and mechanical equations should be solved simultaneously.

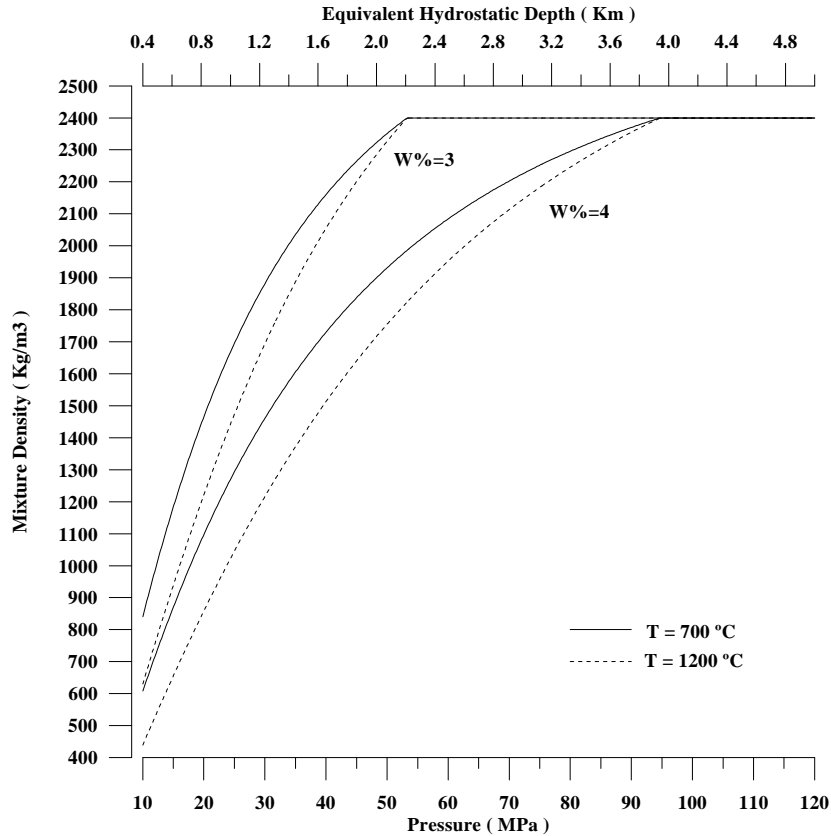


Figure 3.2.5. Mixture density versus pressure for rhyolitic magmas with $\rho_1 = 2400 \text{ Kg/m}^3$, considering water contents of 3 and 4% in weight (W values of 0.03, and 0.04 respectively) and at two different temperatures. These temperatures are two extreme values (physically unrealistic for rhyolites) but allow to illustrate the influence of the temperature on the state law. Close to the exsolution level temperature has not much influence on the state law and the problem can be considered thermally uncoupled. In contrast, at the uppermost parts of the conduit (i.e. at low pressure values) coupling between thermal and mechanical problems should be considered since temperature influence becomes appreciable.

3.3 ALE Governing Equations

This section presents the equations that govern the behaviour of any continuous medium. These equations reflect three fundamental physical principles: mass conservation, Newton's second law (momentum balance) and the first law of the thermodynamics, and are deduced considering an Arbitrary Lagrangian-Eulerian (ALE) formulation which generalises the usual Lagrangian and Eulerian descriptions. The equations need to be complemented with additional constitutive equations and state laws in order to fully describe the physics of any particular continuous medium.

Two different formulations have been traditionally considered to describe the physics of a continuous medium. One is the material or *Lagrangian formulation*, in which the frame of reference, known as the *material frame of reference*, coincides with the particles of the medium. Thus, in a Lagrangian description, any physical property of the material is determined over the particles of the medium. The second is the spatial or *Eulerian formulation*, in which the frame of reference, known as the *spatial frame of reference*, is fixed with respect to the laboratory frame.

When the equations that govern a continuous medium are numerically solved using any method available such as, for instance, a finite element method, they must be discretised in order to compute the properties of the medium in a finite number of points. This discretisation of the equations can be also regarded as a discretisation of the frame of reference in the sense that, once discretised, the physical properties are only known in a discrete number of mesh points. Thus, in a discrete Lagrangian description, nodal points coincide with particles of the medium. This coincidence allows us to describe with accuracy the movement of the medium boundaries and avoids convective effects. However, if the medium presents distortion, as in the case of fluids or solids with large deformations, the Lagrangian description requires a computationally expensive continuous mesh rezoning in order to deal properly with elemental distortion or entanglement [Ramaswamy, 1990; Okamoto and Kawahara, 1992]. In contrast, in a discretised Eulerian description, nodal points are fixed with respect to the laboratory. It allows to deal properly with the distortions of the medium without need of any mesh rezoning and makes this description specially suitable to treat fluids. Nevertheless, two inconveniences arise when an Eulerian description is considered. Firstly, convective terms appear due to the relative movement between the medium and the frame of reference (between the particles and the mesh). These convective terms are susceptible to introduce numerical difficulties such as oscillations and non-linearity. In the context of finite element methods, many different numerical techniques have been developed during the last two decades in order to deal correctly with the convective term [Christie et al., 1976; Heinrich et al., 1977; Hughes and Brooks,

1979; Kelly et al., 1980; Douglas and Russell, 1982; Hughes and Brooks, 1982; Pironneau, 1982; Donéa, 1984; Hughes and Tezduyar, 1984; Hughes et al., 1989; Franca and Stenberg, 1991; Hughes, 1995]. The second drawback of the Eulerian formulation is that the description of moveable boundaries requires specific techniques such a space-time finite element formulation [e.g. Masud, 1993; Hansbo, 1995; Masud and Hughes, 1997].

In order to avoid the shortcomings that Lagrangian and Eulerian descriptions present, an arbitrary Lagrangian-Eulerian (ALE) formulation was developed in both finite differences [Noh, 1964; Hirt et al., 1974] and finite elements [Donéa et al., 1977; Belytschko et al., 1980; Hughes et al., 1981; Huerta and Liu, 1988; Donéa and Giuliani, 1989; Soulaïmani et al., 1991; Huerta and Casadei, 1994]. In the ALE description the frame of reference, known as the *computational frame of reference*, moves with an arbitrary velocity with respect to the laboratory system. It allows to use a purely Lagrangian description at the boundaries and, simultaneously, maintain a regular element shape in the rest of the domain. In consequence, the ALE formulation incorporates advantages from both Lagrangian (accuracy in the description of moving boundaries) and Eulerian (treatment of distortion) formulations. Convective terms are, however, still present in the ALE equations.

3.3.1 Introduction to the ALE Formulation

Consider a continuous medium Ω in the space \mathbf{R}^n and let $t \in [0, \infty) \subset \mathbf{R}$ be the time variable. Let \mathbf{x} , \mathbf{X} and \mathbf{c} denote, respectively, spatial, material, and computational coordinates, that is, the coordinates of a certain particle in the Eulerian, the Lagrangian, and the ALE descriptions respectively. Let also denote the material region by $\Omega_{\mathbf{x}}$, $\Omega_{\mathbf{X}}$, and $\Omega_{\mathbf{c}}$. Although the position of the computational frame is, in general, totally arbitrary, it is very useful from a computational point of view to consider that this frame of reference coincides with the mesh.

The kinematics of the continuum can be described by a application \mathbf{j} which, at any given instant t , gives the spatial coordinates of the material particle \mathbf{X}

$$\begin{array}{ccc} \Omega_{\mathbf{x}} \times [0, \infty) & \rightarrow & \Omega_{\mathbf{X}} \times [0, \infty) \\ t & \mapsto & t \\ \mathbf{X} & \mapsto & \mathbf{x} = \mathbf{j}(\mathbf{X}, t) \end{array} \quad (3.3.1)$$

In fact, the above expression is nothing but a change of coordinates and, in consequence, must verify that

$$F \equiv \det \begin{pmatrix} \mathcal{J} \mathbf{x} \\ \mathcal{J} \mathbf{X} \end{pmatrix} = \det(\mathbf{F}) \neq 0 \quad (3.3.2)$$

in order to have an invertible change of coordinates (at $t=0$, $F > 0$). The tensor $\mathbf{F} \equiv \mathbf{x} \otimes \nabla_{\mathbf{X}}$ is known as the *strain gradient tensor*, and has components

$$F_{ij} \equiv \frac{\mathcal{J} x_i}{\mathcal{J} X_j} \quad (3.3.3)$$

Analogously, spatial and computational coordinates are related by an application \mathbf{y} , which, at any particular time instant t , gives the spatial coordinates in terms of the computational coordinates

$$\begin{array}{ccc} \Omega_{\mathbf{c}} \times [0, \infty) & \rightarrow & \Omega_{\mathbf{x}} \times [0, \infty) \\ t & \mapsto & t \\ \mathbf{c} & \mapsto & \mathbf{x} = \mathbf{y}(\mathbf{c}, t) \end{array} \quad (3.3.4)$$

where, again, it must be verified that

$$\hat{F} \equiv \det \begin{pmatrix} \mathcal{J} \mathbf{x} \\ \mathcal{J} \mathbf{c} \end{pmatrix} = \det(\hat{\mathbf{F}}) \neq 0 \quad (3.3.5)$$

where the tensor $\hat{\mathbf{F}} \equiv \mathbf{x} \otimes \nabla_{\mathbf{c}}$ is known as the *mesh strain gradient tensor* and has components

$$\hat{F}_{ij} \equiv \frac{\mathcal{J} x_i}{\mathcal{J} c_j} \quad (3.3.6)$$

Finally, the relation between material and computational frames is automatically defined by composition of mappings because both \mathbf{j} and \mathbf{y} are invertible (see figure 3.3.1)

$$\mathbf{X} = \mathbf{j}^{-1} \circ \mathbf{y}(\mathbf{c}, t) \quad (3.3.7)$$

$$\mathbf{c} = \mathbf{y}^{-1} \circ \mathbf{j}(\mathbf{X}, t) \quad (3.3.8)$$

Note that, in particular, when $\mathbf{y} = \mathbf{j}$ the computational and the material frames are identical, so that mesh points coincide with particles of the medium and the ALE description recovers the

Lagrangian one. On the contrary, when \mathbf{y} is the identity, the computational and the spatial frames are identical, so that mesh points are fixed with respect to the laboratory frame and the ALE description coincides with the Eulerian one. Once the applications \mathbf{j} and \mathbf{y} are determined, it is possible to express any arbitrary property \mathbf{G} of the continuous medium in any frame of reference because

$$\begin{aligned}\mathbf{G} &\equiv f(\mathbf{x}, t) \\ &= f(\mathbf{y}(\mathbf{c}, t), t) \equiv f^*(\mathbf{c}, t) \\ &= f(\mathbf{j}(\mathbf{X}, t), t) \equiv f^{**}(\mathbf{X}, t)\end{aligned}\quad (3.3.9)$$

where, following [Huerta and Liu, 1988] the symbols * and ** are used to denote “with respect to \mathbf{c} and \mathbf{X} ”, respectively. In order to derive the conservation equations in the ALE formulation it is necessary to express the material derivative as well as the Reynolds transport theorem in the computational frame of reference.

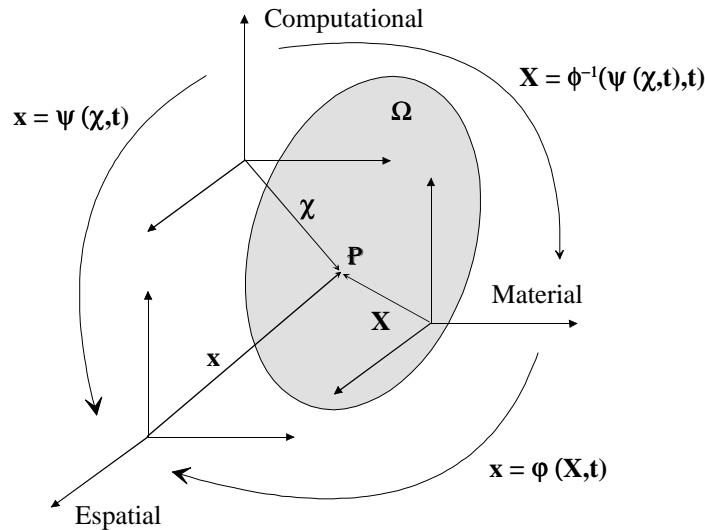


Figure 3.3.1. Schematic illustration to show the relation between spatial, material and computational frames of reference in the ALE formulation.

The *material derivative* $\dot{\mathbf{G}}$ of a property \mathbf{G} is, by definition, the temporal variation of \mathbf{G} evaluated in the material frame of reference (that is, holding \mathbf{X} fixed). Applying the chain rule to (3.3.9), the material derivative can be expressed in the spatial frame of reference

$$\dot{\mathbf{G}} \equiv \left. \frac{\mathcal{D} f^{**}}{\mathcal{D} t} \right|_{\mathbf{X}} = \left. \frac{\mathcal{D} f}{\mathcal{D} t} \right|_{\mathbf{X}} = \left. \frac{\mathcal{D} f}{\mathcal{D} t} \right|_{\mathbf{x}} + \mathbf{u} \cdot \nabla_{\mathbf{x}} f \quad (3.3.10)$$

3.3 ALE Governing Equations

where $\nabla_x \equiv \frac{\partial}{\partial \mathbf{x}}$ and

$$\mathbf{u} \equiv \left. \frac{\partial \mathbf{x}}{\partial t} \right|_x \quad (3.3.11)$$

can be interpreted as the velocity of the particles evaluated in the spatial frame of reference. Equation (3.3.10) states that the material derivative of a property \mathbf{g} is its the temporal variation evaluated in the spatial frame (that is, evaluated at a point fixed with respect to the laboratory) plus a convective term that appears due to the relative movement between particles and spatial frame (laboratory). Analogously, the material derivative can be also expressed in the computational frame of reference

$$\dot{\mathbf{g}} \equiv \left. \frac{\partial f^{**}}{\partial t} \right|_x = \left. \frac{\partial f^*}{\partial t} \right|_x = \left. \frac{\partial f^*}{\partial t} \right|_c + \mathbf{w} \cdot \nabla_c f^* \quad (3.3.12)$$

where $\nabla_c \equiv \frac{\partial}{\partial \mathbf{c}}$ and

$$\mathbf{w} \equiv \left. \frac{\partial \mathbf{c}}{\partial t} \right|_x \quad (3.3.13)$$

can be interpreted as the velocity of the particles evaluated in the computational frame of reference. Equation (3.3.12) states that the material derivative of a property \mathbf{g} is its the temporal variation evaluated in the computational frame (that is, evaluated at a nodal point) plus a convective term that appears due to the relative movement between particles and computational frame (mesh). In particular, when \mathbf{g} represents the spatial coordinates of a particle, (3.3.12) becomes

$$\left. \frac{\partial \mathbf{x}^{**}}{\partial t} \right|_x = \left. \frac{\partial \mathbf{x}^*}{\partial t} \right|_c + \mathbf{w} \cdot \nabla_c \mathbf{x}^* \quad (3.3.14)$$

or

$$\mathbf{c} \equiv \mathbf{u} - \hat{\mathbf{u}} = \mathbf{w} \cdot \hat{\mathbf{F}} \quad (3.3.15)$$

where $\mathbf{c} = \mathbf{u} - \hat{\mathbf{u}}$ is the convective velocity and

$$\hat{\mathbf{u}} \equiv \left. \frac{\mathcal{D} \mathbf{x}^*}{\mathcal{D} t} \right|_c \quad (3.3.16)$$

can be interpreted as the velocity of the computational frame (evaluated in the spatial frame of reference). Equation (3.3.15) was originally developed by [Hughes *et al.*, 1981] and states that the difference between the velocity of the particles and the velocity of the mesh evaluated in the spatial frame (the convective velocity) is the velocity of the particles respect to the mesh multiplied by the mesh strain gradient tensor. In particular, if there is not relative movement between particles and mesh one has $\mathbf{w} = \mathbf{0}$ and (3.3.15) becomes $\mathbf{u} = \hat{\mathbf{u}}$, that is, the ALE formulation recovers the Lagrangian one. On the contrary, if the velocity of the mesh in the spatial frame vanishes one has $\hat{\mathbf{u}} = \mathbf{0}$, $\hat{\mathbf{F}} = \mathbf{I}$ (since $\mathbf{x} = \mathbf{c}$) and (3.3.15) becomes $\mathbf{u} = \mathbf{w}$, so that the velocity of the particles in the spatial and in the computational frames is the same and the ALE formulation coincides with the Eulerian one. It is interesting to express the material derivative (3.3.12) in terms of the convective velocity using (3.3.15) and the chain rule. It yields

$$\dot{\mathbf{g}} \equiv \left. \frac{\mathcal{D} f^{**}}{\mathcal{D} t} \right|_x = \left. \frac{\mathcal{D} f^*}{\mathcal{D} t} \right|_x = \left. \frac{\mathcal{D} f^*}{\mathcal{D} t} \right|_c + \mathbf{c} \cdot \nabla_x f \quad (3.3.17)$$

which, using (3.3.10), can be expressed also as

$$\left. \frac{\mathcal{D} f}{\mathcal{D} t} \right|_x = \left. \frac{\mathcal{D} f^*}{\mathcal{D} t} \right|_c - \hat{\mathbf{u}} \cdot \nabla_x f \quad (3.3.18)$$

Equation (3.3.18) is very interesting form a computational point of view because is the basis to develop the “quasi-Eulerian” formulation.

Let now $G(t)$ be an scalar property defined by the volume integral

$$G(t) = \int_{V_c} f^*(\mathbf{c}, t) dV_c \quad (3.3.19)$$

where V_c is a control volume (that is, a volume held fixed in the referential frame). Then, the Reynolds transport theorem expressed in its referential form is [e.g. Huerta and Liu, 1988]

$$\frac{\mathcal{J}}{\mathcal{J}t} \int_{V_c} f^* dV_c = \int_{V_c} \left(\left. \frac{\mathcal{J} f^*}{\mathcal{J}t} \right|_c + \nabla_c \cdot (f^* \mathbf{w}) \right) dV_c \quad (3.3.20)$$

The above equation express that the rate of change of $G(t)$ is the amount created-destroyed within the control volume plus its flux through the surface induced by the relative movement between the particles and the volume of control (between the particles and the frame). In particular, when the referential frame coincides with the material, i.e. when $\mathbf{c} = \mathbf{X}$ and $\mathbf{w} = \mathbf{0}$, the Reynolds transport theorem (3.3.20) becomes

$$\frac{\mathcal{J}}{\mathcal{J}t} \int_{V_x} f^{**} dV_x = \int_{V_x} \left. \frac{\mathcal{J} f^{**}}{\mathcal{J}t} \right|_x dV_x \quad (3.3.21)$$

Note that, in this case, the control volume is a material volume and, in consequence, the rate of change of $G(t)$ within the volume is directly the amount instantaneously created-destroyed (there is not flux of particles through a material surface). On the other hand, when the referential frame coincides with the spatial one, i.e. when $\mathbf{c} = \mathbf{x}$ and $\mathbf{w} = \mathbf{u}$, (3.3.20) reduces to the usual Eulerian version of the Reynolds transport theorem

$$\frac{\mathcal{J}}{\mathcal{J}t} \int_{V_x} f dV_x = \int_{V_x} \left(\left. \frac{\mathcal{J} f}{\mathcal{J}t} \right|_x + \nabla_x \cdot (f \mathbf{u}) \right) dV_x \quad (3.3.22)$$

In the general case, two main drawbacks appear when the transport equations are formulated using the referential frame. Firstly, numerical difficulties appear in the momentum equation because it is expressed in terms of the non-symmetric Piola-Kirchhoff stress tensor. On the other hand, constitutive equations are usually written in terms of the Cauchy stress tensor instead of in terms of the Piola-Kirchhoff tensor. These inconveniences can be solved considering a “quasi-Eulerian” formulation, originally introduced by [Hughes et al., 1981]. The “quasi-Eulerian” formulation can be viewed as a particular case of the general ALE formulation in which governing equations are deduced by integration over the spatial domain (as in the Eulerian description) but time derivatives are kept in the referential frame. It allows to express the equations in terms of the Cauchy stress tensor and, simultaneously, keep the rest of advantages of the general ALE formulation (that is, no element distortion or entanglement, correct treatment of the moving boundaries, etc.). After [Hughes et al., 1981], most of the authors made distinctions between ALE and “quasi-Eulerian” formulations in order to emphasise that the “quasi-Eulerian” formulation is nothing but a particular case of a more general ALE description. However, the wide use of the “quasi-Eulerian” formulation has progressively led to

the elimination of this distinction. In fact, the terms “quasi-Eulerian” and “ALE” are, nowadays, used as synonymous. The “quasi-Eulerian” (from now on synonymous of ALE) governing equations are obtained substituting (3.3.18) into its usual Eulerian strong form (Appendix 3A contains a deduction of the ALE governing equations and its particularisation)

$$\frac{\mathcal{I} \mathbf{r}}{\mathcal{I} t} \Big|_{\mathbf{x}} + \nabla_{\mathbf{x}} \cdot (\mathbf{r} \mathbf{u}) = 0 \quad (\text{Continuity}) \quad (3.3.23)$$

$$\mathbf{r} \frac{\mathcal{I} \mathbf{u}}{\mathcal{I} t} \Big|_{\mathbf{x}} + \mathbf{r} \mathbf{u} \cdot \nabla_{\mathbf{x}} \mathbf{u} = \nabla_{\mathbf{x}} \cdot \mathbf{S} + \mathbf{r} \mathbf{g} \quad (\text{Momentum}) \quad (3.3.24)$$

$$\mathbf{r} \frac{\mathcal{I} e_o}{\mathcal{I} t} \Big|_{\mathbf{x}} + \mathbf{r} \mathbf{u} \cdot \nabla_{\mathbf{x}} e_o = \nabla_{\mathbf{x}} \cdot (k \nabla_{\mathbf{x}} T) + \mathbf{S} \cdot \nabla_{\mathbf{x}} \mathbf{u} + \mathbf{r} \mathbf{g} \cdot \mathbf{u} \quad (\text{Energy}) \quad (3.3.25)$$

where t is time, \mathbf{r} is density, \mathbf{S} is the Cauchy stress tensor, \mathbf{g} is the gravity vector, e_o is the specific internal energy, k is the thermal conductivity and T is the temperature. The above equations assume that gravity is the only body force, that thermal conductivity is isotropic, and that there is not internal generation of heat.

3.3.2 ALE Continuity Equation

The introduction of (3.3.18) into the Eulerian continuity equation (3.3.23) yields

$$\frac{\mathcal{I} \mathbf{r}^*}{\mathcal{I} t} \Big|_{\mathbf{c}} + \nabla_{\mathbf{x}} \cdot (\mathbf{r} \mathbf{u}) - \hat{\mathbf{u}} \cdot \nabla_{\mathbf{x}} \mathbf{r} = 0 \quad (3.3.26)$$

or, in terms of the momentum $\mathbf{U} = \mathbf{r} \mathbf{u}$

$$\frac{\mathcal{I} \mathbf{r}^*}{\mathcal{I} t} \Big|_{\mathbf{c}} + \nabla_{\mathbf{x}} \cdot \mathbf{U} - \hat{\mathbf{u}} \cdot \nabla_{\mathbf{x}} \mathbf{r} = 0 \quad (3.3.27)$$

Equation (3.3.26) presents two differences with respect to its Eulerian version (3.3.23). Firstly, a new term appears due to the relative movement between the computational frame (the mesh) and the laboratory. Secondly, the time derivative is now considered in the referential frame instead of in the spatial frame. In the Eulerian description, this time derivative is the difference of densities in the same fixed spatial point at two different time instants divided by the time increment, while, in the ALE description, this difference is considered at two different time instants but also at two different spatial points due to the relative movement between the mesh

and the laboratory. However, from a computational point of view, these derivatives are equivalent because in both cases are computed using the difference of densities in a point of the mesh (that coincides or not with the same spatial point) at two different time instants. For this reason subindexes can be dropped for computational purposes and the equation can be expressed as

$$\boxed{\frac{\rho}{\rho} \frac{\mathbf{r}}{t} + \nabla \cdot \mathbf{U} - \hat{\mathbf{u}} \cdot \nabla \mathbf{r} = 0} \quad (3.3.28)$$

Observation Notwithstanding that *from a computational point of view* spatial and referential time derivatives are equivalent, the dependency will be omitted from now on and, in consequence, the indexes will be dropped. However, it should be kept in mind that, despite not explicitly indicated, these two time derivatives are *conceptually* different.

3.3.3 ALE Momentum Equation

The introduction of (3.3.18) into the Eulerian momentum equation (3.3.24) yields

$$\mathbf{r} \frac{\rho \mathbf{u}^*}{\rho t} \Big|_c + \mathbf{r} (\mathbf{u} - \hat{\mathbf{u}}) \cdot \nabla \mathbf{u} = \nabla \cdot \mathbf{S} + \mathbf{r} \mathbf{g} \quad (3.3.29)$$

or dropping indexes (see observation above)

$$\mathbf{r} \frac{\rho \mathbf{u}}{\rho t} + \mathbf{r} (\mathbf{u} - \hat{\mathbf{u}}) \cdot \nabla \mathbf{u} = \nabla \cdot \mathbf{S} + \mathbf{r} \mathbf{g} \quad (3.3.30)$$

The above equation can be expressed also in a conservative way (i.e. writing the time derivative in terms of the momentum instead of in terms of the velocity) using the following identities

$$\frac{\rho \mathbf{U}}{\rho t} = \mathbf{r} \frac{\rho \mathbf{u}}{\rho t} + \mathbf{u} \frac{\rho \mathbf{r}}{\rho t} \quad (3.3.31)$$

$$\nabla \cdot (\mathbf{u} \otimes \mathbf{U}) = \mathbf{U} \cdot \nabla \mathbf{u} + \mathbf{u} \nabla \cdot \mathbf{U} \quad (3.3.32)$$

$$\hat{\mathbf{u}} \cdot \nabla \mathbf{U} = \mathbf{u} [\hat{\mathbf{u}} \cdot \nabla \mathbf{r}] + \mathbf{r} \hat{\mathbf{u}} \cdot \nabla \mathbf{u} \quad (3.3.33)$$

Substituting these identities into (3.3.30) and using the continuity equation (3.3.28) yields

$$\frac{\mathcal{I} \mathbf{U}}{\mathcal{I} t} + \nabla \cdot (\mathbf{u} \otimes \mathbf{U}) - \hat{\mathbf{u}} \cdot \nabla \mathbf{U} = \nabla \cdot \mathbf{S} + \mathbf{r} \mathbf{g} \quad (3.3.34)$$

3.3.4 ALE Energy Equation

Finally, the introduction of (3.3.18) into the Eulerian energy equation (3.3.25) yields

$$\mathbf{r} \frac{\mathcal{I} e_o^*}{\mathcal{I} t} \Big|_c + \mathbf{r} (\mathbf{u} - \hat{\mathbf{u}}) \cdot \nabla e_o = \nabla \cdot (k \nabla T) + \mathbf{S} \cdot \nabla \mathbf{u} + \mathbf{r} \mathbf{g} \cdot \mathbf{u} \quad (3.3.35)$$

or dropping indexes

$$\mathbf{r} \frac{\mathcal{I} e_o}{\mathcal{I} t} + \mathbf{r} (\mathbf{u} - \hat{\mathbf{u}}) \cdot \nabla e_o = \nabla \cdot (k \nabla T) + \mathbf{S} \cdot \nabla \mathbf{u} + \mathbf{r} \mathbf{g} \cdot \mathbf{u} \quad (3.3.36)$$

The above energy equation is sometimes written in terms of the temperature. To relate specific internal energy and temperature a caloric state law is required. A common procedure is to assume a proportional dependence between specific internal energy e_o and temperature (being the constant of proportionality the specific heat at constant volume c_v)

$$e_o = c_v T \quad (3.3.37)$$

Using the above expression the energy equation becomes

$$\frac{\mathcal{I} T}{\mathcal{I} t} + (\mathbf{u} - \hat{\mathbf{u}}) \cdot \nabla T = \frac{1}{\mathbf{r} c_v} [\nabla \cdot (k \nabla T) + \mathbf{S} \cdot \nabla \mathbf{u}] + \frac{1}{c_v} \mathbf{g} \cdot \mathbf{u} \quad (3.3.38)$$

The above form of the energy equation is known as the *heat transport equation*. Equation (3.3.36) can be also expressed in a conservative way (i.e. writing the time derivative in terms of the total energy instead of in terms of the internal energy per unit of mass). The total energy per unit of mass e is the internal energy per unit of mass plus the kinetic energy per unit of mass

$$e = e_o + \frac{1}{2} |\mathbf{u}|^2 \quad (3.3.39)$$

so that

$$\mathbf{r} \frac{\mathcal{I} e_o}{\mathcal{I} t} + \mathbf{r} (\mathbf{u} - \hat{\mathbf{u}}) \cdot \nabla e_o = \mathbf{r} \frac{\mathcal{I} e}{\mathcal{I} t} + \mathbf{r} (\mathbf{u} - \hat{\mathbf{u}}) \cdot \nabla e - \frac{1}{2} \mathbf{r} \frac{\mathcal{I} |\mathbf{u}|^2}{\mathcal{I} t} - \frac{1}{2} \mathbf{r} (\mathbf{u} - \hat{\mathbf{u}}) \cdot \nabla |\mathbf{u}|^2 \quad (3.3.40)$$

Substituting the identities

$$\frac{1}{2} \mathbf{r} \frac{\mathcal{I} |\mathbf{u}|^2}{\mathcal{I} t} = \mathbf{r} \mathbf{u} \cdot \frac{\mathcal{I} \mathbf{u}}{\mathcal{I} t} \quad (3.3.41)$$

$$\frac{1}{2} \mathbf{r} (\mathbf{u} - \hat{\mathbf{u}}) \cdot \nabla |\mathbf{u}|^2 = \mathbf{r} \mathbf{u} \cdot [(\mathbf{u} - \hat{\mathbf{u}}) \cdot \nabla \mathbf{u}] \quad (3.3.42)$$

into (3.3.40), equation (3.3.36) can be rewritten as

$$\mathbf{r} \left(\frac{\mathcal{I} e}{\mathcal{I} t} + (\mathbf{u} - \hat{\mathbf{u}}) \cdot \nabla e \right) - \mathbf{u} \cdot \left(\mathbf{r} \frac{\mathcal{I} \mathbf{u}}{\mathcal{I} t} + \mathbf{r} (\mathbf{u} - \hat{\mathbf{u}}) \cdot \nabla \mathbf{u} \right) = \nabla \cdot (k \nabla T) + \mathbf{S} \cdot \nabla \mathbf{u} + \mathbf{r} \mathbf{g} \cdot \mathbf{u} \quad (3.3.43)$$

and, using the momentum equation (3.3.30) and the identity

$$\nabla \cdot (\mathbf{S} \cdot \mathbf{u}) = \mathbf{u} \cdot (\nabla \cdot \mathbf{S}) + \mathbf{S} \cdot \nabla \mathbf{u} \quad (3.3.44)$$

one gets

$$\mathbf{r} \left(\frac{\mathcal{I} e}{\mathcal{I} t} + (\mathbf{u} - \hat{\mathbf{u}}) \cdot \nabla e \right) = \nabla \cdot (\mathbf{S} \cdot \mathbf{u}) + \nabla \cdot (k \nabla T) + \mathbf{r} \mathbf{u} \cdot \mathbf{g} \quad (3.3.45)$$

The above equation can be finally expressed in terms of the total energy $E = \mathbf{r} e$ considering

$$\frac{\mathcal{I} E}{\mathcal{I} t} = \mathbf{r} \frac{\mathcal{I} e}{\mathcal{I} t} + e \frac{\mathcal{I} \mathbf{r}}{\mathcal{I} t} \quad (3.3.46)$$

$$\nabla \cdot (E \mathbf{u}) = \mathbf{r} \mathbf{u} \cdot \nabla e + e \nabla \cdot (\mathbf{r} \mathbf{u}) \quad (3.3.47)$$

$$\hat{\mathbf{u}} \cdot \nabla (\mathbf{r} e) = \mathbf{r} \hat{\mathbf{u}} \cdot \nabla e + e \hat{\mathbf{u}} \cdot \nabla \mathbf{r} \quad (3.3.48)$$

and making use of the continuity equation (3.3.28). It finally yields

$$\frac{\mathcal{I} E}{\mathcal{I} t} + \nabla \cdot (E \mathbf{u}) - \hat{\mathbf{u}} \cdot \nabla E = \nabla \cdot (\mathbf{S} \cdot \mathbf{u}) + \nabla \cdot (k \nabla T) + \mathbf{r} \mathbf{u} \cdot \mathbf{g} \quad (3.3.49)$$

3.4 Flow Equations

3.4.1 Newtonian Fluids

A constitutive equation for the fluid is required in order to close the flow equations. Whichever the choice, any constitutive equation must reflect the fact that fluids can not hold shear stresses when they are at rest or moving with uniform velocity (the state of stress is, in this case, purely hydrostatic). If one considers that the difference between any tensional state and the purely hydrostatic state depends only on the strain rate tensor, the most general constitutive equation for a fluid is then

$$\mathbf{S} = -p \mathbf{I} + \Theta(\mathbf{D}) \quad (3.4.1)$$

where \mathbf{S} is the Cauchy stress tensor, p is the thermodynamic pressure (given by the state law), Θ is an arbitrary tensorial function and \mathbf{D} is the *strain rate tensor* defined as

$$\mathbf{D} \equiv \frac{1}{2}(\nabla \mathbf{u} + \mathbf{u} \nabla) \quad (3.4.2)$$

A *Newtonian fluid* is, by definition, a fluid in which the function Θ is linear, that is, is a fluid in which the deviatoric stress tensor is directly proportional to the strain rate tensor. Only Newtonian fluids will be considered in the frame of this work. Under these circumstances, equation (3.4.1) reduces to

$$\mathbf{S} = -p \mathbf{I} + \mathbf{C} : \mathbf{D} \quad (3.4.3)$$

where \mathbf{C} is a fourth order constitutive tensor (in a 3D space has 81 components). It can be shown that, under isotropic conditions, its components are given by

$$C_{ijkl} = l d_{ij} d_{kl} + m (d_{ik} d_{jl} + d_{il} d_{jk}) \quad (3.4.4)$$

The substitution of the above expression into (3.4.3) yields

$$\mathbf{S} = -p \mathbf{I} + l (\nabla \cdot \mathbf{u}) \mathbf{I} + 2m \mathbf{D} \quad (3.4.5)$$

where \mathbf{m} and \mathbf{l} are, respectively, the viscosity and the bulk viscosity. This constitutive equation can also be expressed in terms of the *deviatoric stress tensor* (or *viscous stress tensor*) \mathbf{T} which, by definition, is

$$\mathbf{T} \equiv \mathbf{S} - \frac{1}{3} \text{Tr}(\mathbf{S}) \mathbf{l} \quad (3.4.6)$$

Finally, inserting (3.4.6) into (3.4.5) and having into account the *Stokes hypothesis* ($3\mathbf{l} + 2\mathbf{m} = 0$) one gets the final expression for the constitutive equation of an isotropic Newtonian fluid

$$\mathbf{T} = \mathbf{S} + p\mathbf{l} = \mathbf{m} \left(\nabla \mathbf{u} + \mathbf{u} \nabla - \frac{2}{3} (\nabla \cdot \mathbf{u}) \mathbf{l} \right) \quad (3.4.7)$$

3.4.2 ALE Navier-Stokes Equations

Navier-Stokes equations are the governing equations of Newtonian fluids. Considering an ALE formulation, the physics of these fluids is characterised by the continuity equation (3.3.28), the momentum equation (3.3.34), the energy equation (3.3.49) (the heat equation (3.3.38) can be also alternatively considered), the constitutive equation (3.4.7) and an additional state law $\mathbf{j}(\mathbf{r}, T, p) = 0$. In summary, the equations to solve are

$$\begin{aligned} \frac{\mathcal{J} \mathbf{r}}{\mathcal{J} t} &= -\nabla \cdot \mathbf{U} + \hat{\mathbf{u}} \cdot \nabla \mathbf{r} \\ \frac{\mathcal{J} \mathbf{U}}{\mathcal{J} t} &= -\nabla \cdot (\mathbf{u} \otimes \mathbf{U}) + \hat{\mathbf{u}} \cdot \nabla \mathbf{U} - \nabla p + \nabla \cdot \mathbf{T} + \mathbf{r} \mathbf{g} \\ \frac{\mathcal{J} E}{\mathcal{J} t} + \nabla \cdot (E \mathbf{u}) - \hat{\mathbf{u}} \cdot \nabla E &= \nabla \cdot (\mathbf{S} \cdot \mathbf{u}) + \nabla \cdot (k \nabla T) + \mathbf{r} \mathbf{u} \cdot \mathbf{g} \\ \mathbf{S} &= -p\mathbf{l} + \mathbf{T} = -p\mathbf{l} + \mathbf{m} \left(\nabla \mathbf{u} + \mathbf{u} \nabla - \frac{2}{3} (\nabla \cdot \mathbf{u}) \mathbf{l} \right) \\ \mathbf{j}(\mathbf{r}, T, p) &= 0 \end{aligned}$$

completed with a mesh motion equation. An algorithm to solve numerically the above set of equations is presented in chapter 4.

Observation When neither the state law nor the viscosity depend on temperature, the thermal and the mechanical problems are uncoupled, i.e. they can be considered as independent

problems. This is the case, for instance, of those incompressible or barotropic flows for which viscosity is temperature independent.

Apart from magmas, other different kinds of Newtonian fluids such as, for instance, incompressible, slightly compressible or perfect gas will be considered here. A state law for magmatic mixtures has been already proposed and widely discussed in section 3.2. The rest of state laws are well known and need no presentation. Incompressible flows ($\mathbf{r} = \text{cte}$) constitute a case of special interest. In this case, provided that viscosity is temperature independent, the thermal and the mechanical problems are uncoupled and the ALE Navier-Stokes equations reduce to

$$\nabla \cdot \mathbf{u} = 0 \quad (3.4.8)$$

$$\mathbf{r} \frac{\mathcal{D} \mathbf{u}}{\mathcal{D} t} + \mathbf{r} (\mathbf{u} - \hat{\mathbf{u}}) \cdot \nabla \mathbf{u} = -\nabla p + \mathbf{m} \nabla^2 \mathbf{u} + \mathbf{r} \mathbf{g} \quad (3.4.9)$$

• **Boundary and Initial Conditions.** Boundary and initial conditions are a necessary requirement in order to set the problem correctly. Proper boundary conditions for the Navier-Stokes equations in the most general case are still an open question [Hirsch, 1991]. However, it is well established that the problem is well posed if an extrapolation of the 1D Euler equations (non-viscous flow equations) is considered. In this case, boundary conditions for the Navier-Stokes equations are chosen, depending on the Match number, as

❶ *Subsonic regime:* two conditions at the inlets (velocity \mathbf{u} and temperature T) and one condition at the outlet (pressure p or, alternatively, density \mathbf{r} in the case of compressible flows).

❷ *Supersonic regime:* three conditions at the inlets (\mathbf{u} , T and p or \mathbf{r}) and none at the outlets.

Whichever the case, both the non-slip condition (i.e. $\mathbf{u} = \mathbf{0}$) or the prescription of the normal component of the velocity to zero can be considered at the walls. Finally, initial conditions are set on velocity, temperature and pressure (or, alternatively, density when the flow is compressible) fields.

3.5 Structural Equations

As in the case of fluids, a constitutive equation for solids is required in order to complete the governing equations. To describe the behaviour of solids within the range of small deformations it is usual to employ a Lagrangian description of the continuous medium. In this case, the governing equations for the mechanical problem are¹ (see appendix 3A)

$$\frac{\rho}{\rho_0} (F \mathbf{r}) \Big|_{\mathbf{x}} = 0 \quad (\text{Continuity equation}) \quad (3.5.1)$$

$$\rho^* \frac{\rho^* \mathbf{u}^*}{\rho^{*2}} \Big|_{\mathbf{x}} = \nabla_{\mathbf{x}} \cdot \mathbf{S}^P + \rho^* \mathbf{g} \quad (\text{Momentum equation}) \quad (3.5.2)$$

When neither the density of the material nor the constitutive equation depend on temperature, the energy equation becomes uncoupled from the mechanical ones and, in consequence, is not required. Moreover, if the strain is small, material and spatial descriptions are very similar, i.e. one has $\mathbf{x} \cong \mathbf{X}$, $\mathbf{F} \cong \mathbf{I}$, $F \cong 1$, $\mathbf{r} \cong \mathbf{r}^*$ and $\mathbf{S}^P \cong \mathbf{S}$. This approach is widely used in structural mechanics and presents two main advantages. Firstly, continuity equation (3.5.1) is not required because the density of the material is approximately time independent. Secondly, momentum equation can be expressed in terms of the Cauchy stress tensor \mathbf{S} as

$$\rho \frac{\rho \mathbf{u}}{\rho^2} \Big|_{\mathbf{x}} = \nabla_{\mathbf{x}} \cdot \mathbf{S} + \rho \mathbf{g} \quad (3.5.3)$$

Under these circumstances, the above equation completed with the constitutive relationship is sufficient to describe the physics of the solid material. Obviously, the specific constitutive equation depends on the rheology of the solid. Only two types of solids are treated here: linear elastic and linear viscoelastic.

3.5.1 Linear Elastic Materials

A linear elastic material is, by definition, a material in which the (Cauchy) stress tensor is proportional to the *strain tensor* \mathbf{E}

¹ In structural mechanics, displacement is normally designed by \mathbf{u} , the same symbol used for velocity in the flow equations. These two meanings should not be confused.

$$\mathbf{S} = \mathbf{C} : \mathbf{E} \quad (3.5.4)$$

where \mathbf{C} is a fourth order constitutive tensor (in a 3D space has 81 components) and

$$\mathbf{E} = \frac{1}{2}(\nabla \mathbf{u} + \mathbf{u} \nabla) \quad (3.5.5)$$

It can be shown that, under isotropic conditions, the constitutive equation reduces to the *Lamé equation*¹

$$\mathbf{S} = I (\nabla \cdot \mathbf{u}) \mathbf{I} + 2m \mathbf{E} \quad (3.5.6)$$

where I and m are the Lamé parameters. In many cases the Lamé equation is also expressed alternatively as

$$\mathbf{S} = \frac{n E}{(1+n)(1-2n)} (\nabla \cdot \mathbf{u}) \mathbf{I} + \frac{E}{(1+n)} \mathbf{E} \quad (3.5.7)$$

where E is the Young modulus and n the Poisson coefficient. Substituting (3.5.6) into (3.5.3) one finally obtains the *Navier equation*

$$\nabla \cdot [m(\nabla \mathbf{u} + \mathbf{u} \nabla)] + \nabla [I (\nabla \cdot \mathbf{u})] + \mathbf{r} \mathbf{g} = \mathbf{r} \frac{\rho^2 \mathbf{u}}{\rho t^2} \quad (3.5.8)$$

The Navier equation is well posed when displacement is prescribed at the Dirichlet part of the boundary Γ_D and the traction vector $\mathbf{t} = \mathbf{S} \cdot \mathbf{n}$ (being \mathbf{n} the outward unit normal) is prescribed at the Neumann part of the boundary Γ_N . Moreover, initial conditions for displacement and velocity within the whole domain Ω are also needed. In summary the conditions required are

$$\left. \begin{array}{l} \mathbf{u} = \bar{\mathbf{u}} \quad \text{in } \Gamma_D, t > 0 \\ \mathbf{S} \cdot \mathbf{n} = \bar{\mathbf{t}} \quad \text{in } \Gamma_N, t > 0 \end{array} \right\} \quad \left. \begin{array}{l} \mathbf{u} = \mathbf{u}^0 \quad \text{at } t = 0 \text{ in } \Omega \\ \dot{\mathbf{u}} = \dot{\mathbf{u}}^0 \quad \text{at } t = 0 \text{ in } \Omega \end{array} \right\} \quad (3.5.9)$$

¹ Note the similarity with (3.4.5), the constitutive equation of an isotropic Newtonian fluid.

3.5.2 Linear Viscoelastic Materials

Viscoelastic materials possess both some of the characteristics of elastic solids and some of the characteristics of viscous fluids. These materials present the phenomenon of *creep* (strain increases when stresses are held constant) and *relaxation* (stresses relax when strain is held constant). A viscoelastic material is linear when shows a time-dependent linearity between stress and strain. This time dependence implies that these materials have memory in the sense that the present state of deformation cannot be determined completely unless the entire history of the material is known. The general constitutive equation for a linear viscoelastic material is (in components)

$$S_{ij}(t) = \int_{-\infty}^t G_{ijkl}(t-t) \frac{dE_{kl}(t)}{dt} dt \quad (3.5.10)$$

where G_{ijkl} are called the relaxation functions and are components of a 4th order tensor \mathbf{G} known as *relaxation tensor*. If one assumes that the motion starts at $t = 0$ ($S_{ij} = E_{ij} = 0$ for $t < 0$) the above expression can also be written as

$$S_{ij}(t) = G_{ijkl}(t) E_{kl}(0) + \int_0^t G_{ijkl}(t-t) \frac{dE_{kl}}{dt} dt \equiv (\mathbf{G} * \dot{\mathbf{E}})_{ij} \quad (3.5.11)$$

where the first term gives the effect of an initial (elastic) disturbance and the second takes into account the stress relaxation. The symbol $*$ denotes convolution product. If \mathbf{G} is twice differentiable and $G_{ijkl}(0) \neq 0$ the inverse of (3.5.10) exists and can be expressed as

$$E_{ij}(t) = \int_{-\infty}^t J_{ijkl}(t-t) \frac{dS_{kl}(t)}{dt} dt \quad (3.5.12)$$

where J_{ijkl} are called the creep functions and are components of a 4th order tensor \mathbf{J} known as *creep tensor*. Analogously

$$E_{ij}(t) = J_{ijkl}(t) S_{kl}(0) + \int_0^t J_{ijkl}(t-t) \frac{dS_{kl}}{dt} dt \equiv (\mathbf{J} * \dot{\mathbf{S}})_{ij} \quad (3.5.13)$$

where the first term gives the effect of an initial (elastic) disturbance and the second takes into account the strain increase (creep).

A linear viscoelastic material is defined once the tensor \mathbf{G} (or \mathbf{J}) is given¹. A case of particular interest is that of isotropic materials in which the required symmetries of the tensors allow to simplify (3.5.10) to

$$S_{ij}(t) = \int_{-\infty}^t \left[\mathbf{I}(t-t) \frac{dE_{kk}(t)}{dt} \mathbf{d}_{ij} + 2\mathbf{m}(t-t) \frac{dE_{kl}(t)}{dt} \right] dt \quad (3.5.14)$$

where $\mathbf{I}(t)$ and $\mathbf{m}(t)$ are two *relaxation functions* that define the material (note that for isotropic materials only two functions are required instead of the 81 functions $G_{ijkl}(t)$ of the general case). Again, assuming that the motion starts at $t = 0$, the constitutive equation simplifies to

$$S_{ij}(t) = \mathbf{I}(t) E_{kk}(0) \mathbf{d}_{ij} + 2\mathbf{m}(t) E_{ij}(0) + \int_0^t \left[\mathbf{I}(t-t) \frac{dE_{kk}(t)}{dt} \mathbf{d}_{ij} + 2\mathbf{m}(t-t) \frac{dE_{kl}(t)}{dt} \right] dt \quad (3.5.15)$$

Observation Linear elasticity can be regarded as a limiting case of linear viscoelasticity in which the relaxation functions are time independent. In this case, (3.5.15) reduces to

$$\begin{aligned} S_{ij}(t) &= \mathbf{I} E_{kk}(0) \mathbf{d}_{ij} + 2\mathbf{m} E_{ij}(0) + \mathbf{I} [E_{kk}(t) - E_{kk}(0)] \mathbf{d}_{ij} + 2\mathbf{m} [E_{ij}(t) - E_{ij}(0)] \\ &= \mathbf{I} E_{kk}(t) \mathbf{d}_{ij} + 2\mathbf{m} E_{ij}(t) \end{aligned} \quad (3.5.16)$$

which is the constitutive equation of an isotropic linear elastic material (3.5.6). Analogously, if the relaxation functions are given by $\mathbf{I}(t) = \mathbf{I} \delta(t)$, $\mathbf{m}(t) = \mathbf{m} \delta(t)$, being $\delta(t)$ the delta of Dirac, and the initial disturbance is not considered one has

$$S_{ij}(t) = \mathbf{I} \dot{E}_{kk}(t) \mathbf{d}_{ij} + 2\mathbf{m} \dot{E}_{ij}(t) \quad (3.5.17)$$

which is nothing but the constitutive equation of an isotropic Newtonian fluid (except for the hydrostatic contribution).

Only the simplest viscoelastic rheologies will be considered here. These rheologies are simple extrapolations of 1D mechanical models composed of combinations of linear springs with spring constant \mathbf{m} and dashpots with coefficient of viscosity \mathbf{h} . A linear spring is supposed to produce an instantaneous deformation proportional to the load, whereas a dashpot

¹ These tensors are not independent. Given one of them, the other is unequivocally determined.

3.5 Structural Equations

produces, at any instant, a velocity proportional to the load. A case of particular interest is the *Maxwell model*, composed by a spring and a dashpot. In the 1D version, the relaxation function is

$$\mathbf{m}(t) = \mathbf{m} e^{-\frac{m}{2h}t} = \mathbf{m} e^{-\frac{t}{t_{cha}}} \quad (3.5.18)$$

where t_{cha} is the characteristic time of the Maxwell model. The 3D model is obtained by taking both relaxation functions as in (3.5.18). Then

$$S_{ij}(t) = \mathbf{I}(t)E_{kk}(0)d_{ij} + 2\mathbf{m}(t)E_{ij}(0) + \int_0^t \left[\mathbf{I} e^{-\frac{t-t}{t_{cha}}} \frac{dE_{kk}(t)}{dt} d_{ij} + 2\mathbf{m} e^{-\frac{t-t}{t_{cha}}} \frac{dE_{kl}(t)}{dt} \right] dt \quad (3.5.19)$$

is the constitutive equation of a Maxwell viscoelastic material. It can be seen from the above expression how the Maxwell model produces an initial linear elastic response (at $t = 0$ equation (3.5.6) is recovered) followed by an exponential relaxation of the stresses. It can also be shown that the creep functions are proportional to time. Thus, during a creep test, the Maxwell solid deforms initially as in the elastic case and, as time increases, the strain increases linearly.

A final remark. Linear elastic and linear viscoelastic constitutive equations can be formally written as

$\mathbf{S} = \mathbf{C} : \mathbf{E}$ (linear elastic)	$\mathbf{S} = \mathbf{G} * \dot{\mathbf{E}}$ (linear viscoelastic)
$\mathbf{S} = \mathbf{I} \text{Tr}(\mathbf{E})\mathbf{I} + 2\mathbf{m}\mathbf{E}$ (isotropic linear elastic)	$\mathbf{S} = \mathbf{I} * \text{Tr}(\dot{\mathbf{E}})\mathbf{I} + 2\mathbf{m} * \dot{\mathbf{E}}$ (isotropic linear viscoelastic)

that is, the governing equations of the linear viscoelastic problem are exactly the same than those of the linear elasticity but changing $\mathbf{I} E_{kk} \rightarrow \mathbf{I} * \dot{E}_{kk}$ and $\mathbf{m}\mathbf{E} \rightarrow \mathbf{m} * \dot{\mathbf{E}}$. This analogy is known as the *principle of correspondence* and is the basis of the methodology presented in section 4.5 in order to solve the viscoelastic problem numerically.

3.6 References

- Belytschko, T., J.M. Kennedy, and D.F. Schoeberie, Quasi-Eulerian finite element formulation for fluid structure interaction, *J. Pressure Vessel Tech*, 102, 62-69, 1980.
- Blake, S., Volatile oversaturation during the evolution of silicic magma chambers as an eruption trigger, *J. Geophys. Res.*, 89, 8237-8244, 1984.
- Christie, I., D.F. Griffiths, A.R. Mitchell, and O.C. Zienkiewicz, Finite element methods for second order differential equations with first order derivatives, *Int. J. Numer. Meth. Engrg.*, 10, 1389-1396, 1976.
- Dingwell, D.B., N.S. Bagdassarov, G.Y. Bussod, and S.L. Webb, Magma rheology, *Mineral. Assoc. Canada*, 21, 131-196, 1993.
- Donéa, J., P. Fasoli-Stella, and S. Giuliani, Lagrangian and Eulerian finite element techniques for transient fluid structure interaction problems, in: *Transactions of the 4th International Conference of Structural Mechanics in Reactor Techonlogy*, B1/2, 1977.
- Donéa, J., A Taylor-Galerkin method for convection transport equations, *Int. J. Numer. Meth. Fluids*, 20, 101-119, 1984.
- Donéa, J., and S. Giuliani, An explicit ALE finite element formulation for 3D transient dynamic fluid-structure interaction problems, *Comission of the European Communities. Report EUR 11936 EN*, 1989.
- Douglas, J., and T.F. Russell, Numerical methods for convection dominated problems based on combining the method of characteristics with finite element or finite differences procedures, *J. Numer. Analysis*, 19, 871-885, 1982.
- Folch, A., J. Marti, R. Codina, and M. Vázquez, A numerical model for temporal variations during explosive central vent eruptions, *J. Geophys. Res.*, 103, 20883-20899, 1998.
- Franca, L.P., and R. Stenberg, Error analysis of some Galerkin least-squares methods for the elasticity equations, *J. Numer. Analysis*, 28, 1680-1697, 1991.
- Gilberti, G., and L. Wilson, The influence of geometry on the ascent of magma in open fissures, *Bull. Volcanol.*, 52, 515-521, 1990.
- Hansbo, P., Lagrangian incompressible flow computations in three dimensions by use of space-time finite elements, *Int. J. Numer. Meth. Fluids*, 20, 989-1001, 1995.
- Heinrich, J.C., P.S. Huyakron, and O.C. Zienkiewicz, An upwind finite element scheme for two-dimensional convective transport equation, *Int. J. Numer. Meth. Engrg.*, 11, 131-143, 1977.
- Hirsch, C., Numerical Computation of Internal and External Flows, *John Wiley&Sons*, 1991.
- Hirt, C.W., A.A. Amsden, and J.L. Cook, An arbitrary Lagrangian Eulerian computing method for all flow speeds, *J. Comput. Phys.*, 14, 227-253, 1974.
- Huerta, A., and W.K. Liu, Viscous flow with large free surface motion, *Comput. Meth. Appl. Mech. Engrg.*, 69, 277-324, 1988.

-
- Huerta, A., and F. Casadei, New ALE applications in non-linear fast-transient solid dynamics, *Engrg. Comput.*, 11, 317-345, 1994.
- Hughes, T.J.R., and A. Brooks, A multi-dimensional upwind scheme with no crosswind diffusion, *ASME, New York*, 1979.
- Hughes, T.J.R., W.K. Liu, and T.K. Zimmerman, Lagrangian-Eulerian finite element formulation for incompressible viscous flows, *Comput. Meth. Appl. Mech. Engrg.*, 29, 329-349, 1981.
- Hughes, T.J.R., and A. Brooks, A theoretical framework for Petrov-Galerkin methods, with discontinuous weighting functions: applications to the streamline procedure, *Finite Elements in Fluids*, *Wiley & Sons*, London, 1982.
- Hughes, T.J.R., and T.E. Tezduyar, Finite element methods for first-order hyperbolic systems with particular emphasis on the compressible Euler equations, *Comput. Meth. Appl. Mech. Engrg.*, 45, 217-284, 1984.
- Hughes, T.J.R., L.P. Franca, and G.M. Hulbert, A new finite element formulation for computational fluid dynamics: VIII. The Galerkin/least-squares method for advective-diffusion equations, *Comput. Methods Appl. Mech. Engrg.*, 73, 173-198, 1989.
- Hughes, T.J.R., Multiscale phenomena: Green's function, the Dirichlet to Neumann formulation, subgrid scale models, bubbles and the origins of stabilized formulations, *Comput. Methods Appl. Mech. Engrg.*, 127, 387-401, 1995.
- Kelly, D.W., S. Nakazawa, O.C. Zienkiewicz, and J.C. Heinrich, A note on upwinding and anisotropic balancing dissipation in finite element approximations to convective diffusion problems, *Inter. J. Numer. Methods Engrg.*, 15, 1705-1711, 1980.
- Martí, J., C. Soriano, and D. Dingwell, Tube pumices: strain markers of a ductile-brittle transition in explosive eruptions, *Nature*, 402, 650-653, 1999.
- Masud, A., A space-time finite element method for fluid structure interaction, *Ph. D. Thesis*, Stanford University, 1993.
- Masud, A., and T.J.R. Hughes, A space-time Galerkin/least-squares finite element formulation of the Navier-Stokes equations for moving domain problems, *Comput. Methods Appl. Mech. Engrg.*, 146, 91-126, 1997.
- Noh, W.F., CEL: A time-dependent two-space-dimensional coupled Eulerian-Lagrangian code, *Meth. Comput. Phys.*, 3, 1964.
- Okamoto, T., and M. Kawahara, Three dimensional sloshing analysis by arbitrary Lagrangian-Eulerian finite element method, *First World Conference in Appl. Comput. Fluid Dynamics*, 1-6, 1992.
- Papale, P., Modeling of magma ascent along volcanic conduits: a review, *Environment and climate programme. In: The mitigation of volcanic hazards*, ECC Report, 5-40, 1994.
- Pironneau, O., On the transport-diffusion algorithm and its applications to the Navier-Stokes equations, *Numer. Math.*, 38, 309-332, 1982.

-
- Ramaswamy, B., Numerical simulation on steady viscous free surface flow, *J. Comput. Phys.*, 32, 396-430, 1990.
- Soulaimani, A., M. Fortin, D. Dhatt, and Y. Ouellet, Finite element simulation of two and three dimensional free surface flows, *Comput. Meth. Appl. Mech. Engrg.*, 89, 265-296, 1991.
- Sparks, R.S.J., The dynamics of bubble formation and growth in magmas, a review and analysis, *J. Volcanol. Geotherm. Res.*, 3, 1-37, 1978.
- Tait, S., C. Jaupart, and S. Vergnolle, Pressure, gas content and eruption periodicity of a shallow crystallizing magma chamber, *Earth Planet. Sci. Lett.*, 92, 107-123, 1989.
- Touloukian, Y.S., W.R. Judd, and R.F. Roy, Physical properties of rocks and minerals, v. 1, *McGraw-Hill*, New York, 1981.
- Vergnolle, S., and C. Jaupart, Separated two-phase flow and basaltic eruptions, *J. Geophys. Res.*, 91, 12842-12860, 1986.
- Webb, S.L., and D.B. Dingwell, Non-Newtonian rheology of igneous melts at high stresses and strain-rates: experimental results for rhyolite, andesite, basalt and nephelinite, *J. Geophys. Res.*, 95, 15695-15701, 1990.
- Wilson, L., R.S.J. Sparks, and G. Walker, Explosive volcanic eruptions- IV. The control of magma properties and conduit geometry on eruption column behaviour, *Geophys. J. Royal Astr. Soc.*, 63, 117-148, 1980.
- Whitham, A.G., and R.S.J. Sparks, Pumice, *Bull. Volcanol.*, 48, 209-223, 1986.

Appendix 3A. Deduction of the ALE Governing Equations

This appendix contents the deduction of the ALE governing equations. The standard Lagrangian and Eulerian formulations can be recovered as a particular case. The notation employed is that of [Huerta and Liu, 1988], in which the symbols $*$ and $**$ are used to denote, respectively, dependencies with respect to computational coordinates \mathbf{c} and to material coordinates \mathbf{X} .

Continuity Equation

Let V_c be a control volume in the computational frame of reference (i.e. a volume fixed with respect to the computational frame) and S_c its surface with outward unit normal \mathbf{n}_c . The principle of mass conservation states that the temporal variation of mass within the control volume must be equal to the mass flux through its surface, i.e.

$$\int_{V_c} \left. \frac{\rho \mathbf{r}^*}{\rho t} \right|_c dV_c = - \int_{S_c} \mathbf{r}^* \mathbf{w}^* \cdot \mathbf{n}_c dS_c \quad (3A.1)$$

where \mathbf{r}^* is the density and \mathbf{w}^* is the velocity of the particles in the referential frame as defined in (3.3.13). The application of the Gauss theorem to the above expression yields

$$\int_{V_c} \left[\left. \frac{\rho \mathbf{r}^*}{\rho t} \right|_c + \nabla_c \cdot (\mathbf{r}^* \mathbf{w}^*) \right] dV_c = 0 \quad (3A.2)$$

or, using the arbitrariness of V_c

$$\left. \frac{\rho \mathbf{r}^*}{\rho t} \right|_c + \nabla_c \cdot (\mathbf{r}^* \mathbf{w}^*) = 0 \quad (3A.3)$$

Observation When the computational and the spatial frames coincide (i.e. when the mesh is fixed with respect to the laboratory), the Eulerian formulation is recovered. In this case, $\mathbf{x} = \mathbf{c}$, $\mathbf{r}^* = \mathbf{r}$, $\hat{\mathbf{u}} = \mathbf{0}$ (see 3.3.16), $\hat{\mathbf{F}} = \mathbf{I}$ (see 3.3.6), $\mathbf{w} = \mathbf{u}$ (see 3.3.15) and (3A.3) becomes

$$\left. \frac{\rho \mathbf{r}}{\rho t} \right|_x + \nabla_x \cdot (\mathbf{r} \mathbf{u}) = 0 \quad (3A.4)$$

On the other hand, the Lagrangian formulation is recovered when the computational and the material frames coincide (i.e. when the points of the mesh coincide with particles). In this case, $\mathbf{X} = \mathbf{c}$, $\mathbf{r}^* = \mathbf{r}^{**}$, $\mathbf{w} = \mathbf{0}$ (see 3.3.13) and (3A.3) becomes

$$\left. \frac{\mathcal{I} \mathbf{r}^{**}}{\mathcal{I} t} \right|_{\mathbf{x}} = 0 \quad (3A.5)$$

The above equation states that the mass of a material volume (or in particular, the mass of a particle) is constant. Alternatively, it can also be expressed as

$$\left. \frac{\mathcal{I}(\mathbf{r} F)}{\mathcal{I} t} \right|_{\mathbf{x}} = 0 \quad (3A.6)$$

Momentum Equation

Let V_c be a control volume in the computational frame of reference and S_c its surface with outward unit normal \mathbf{n}_c . The second Newton's law states that the rate of change of the total momentum $\mathbf{r} \mathbf{u}$ within the control volume V_c is equal to the net force acting on the medium, that is

$$\left. \frac{\mathcal{I}}{\mathcal{I} t} \left(\int_{V_c} \mathbf{r}^* \mathbf{u}^* dV_c \right) \right|_{\mathbf{x}} = \int_{V_c} \mathbf{r}^* \mathbf{g} dV_c + \int_{S_c} \mathbf{t}^* dS_c \quad (3A.7)$$

where \mathbf{g} is gravity acceleration (gravity is, for simplicity, considered as the only contribution to the body forces) and \mathbf{t}^* is force per unit of area acting over the surface S_c . This force can be written in terms of the Piola-Kirchhoff stress tensor (in the referential sense) as $\mathbf{t}^* = \hat{\mathbf{S}}^P \cdot \mathbf{n}_c$. Applying the Gauss theorem to the above equation and using the vectorial version of Reynolds transport theorem (3.3.20) one gets

$$\int_{V_c} \left\{ \left. \frac{\mathcal{I}}{\mathcal{I} t} [\mathbf{r}^* \mathbf{u}^*] \right|_{\mathbf{c}} + \nabla_c \cdot [\mathbf{w}^* \otimes (\mathbf{r}^* \mathbf{u}^*)] \right\} dV_c = \int_{V_c} [\nabla_c \cdot \hat{\mathbf{S}}^P + \mathbf{r}^* \mathbf{g}] dV_c \quad (3A.8)$$

This equation can be simplified by means of the continuity equation (3A.3) as

$$\int_{V_c} \left(\mathbf{r}^* \frac{\mathcal{I} \mathbf{u}^*}{\mathcal{I} t} \Big|_c + \mathbf{r}^* \mathbf{w}^* \cdot \nabla_c \mathbf{u}^* \right) dV_c = \int_{V_c} (\nabla_c \cdot \hat{\mathbf{S}}^P + \mathbf{r}^* \mathbf{g}) dV_c \quad (3A.9)$$

or, using that V_c is arbitrary

$$\mathbf{r}^* \frac{\mathcal{I} \mathbf{u}^*}{\mathcal{I} t} \Big|_c + \mathbf{r}^* \mathbf{w}^* \cdot \nabla_c \mathbf{u}^* = \nabla_c \cdot \hat{\mathbf{S}}^P + \mathbf{r}^* \mathbf{g} \quad (3A.10)$$

Observation When the computational and the spatial frames coincide one has $\mathbf{x} = \mathbf{c}$, $\mathbf{r}^* = \mathbf{r}$, $\hat{\mathbf{u}} = \mathbf{0}$ (see 3.3.16), $\hat{\mathbf{F}} = \mathbf{I}$ (see 3.3.6), $\mathbf{w} = \mathbf{u}$ (see 3.3.15), $\hat{\mathbf{S}}^P = \mathbf{S}$ (\mathbf{S} is the Cauchy stress tensor) and (3A.10) becomes

$$\mathbf{r} \frac{\mathcal{I} \mathbf{u}}{\mathcal{I} t} \Big|_x + \mathbf{r} \mathbf{u} \cdot \nabla_x \mathbf{u} = \nabla_x \cdot \mathbf{S} + \mathbf{r} \mathbf{g} \quad (3A.11)$$

On the other hand, if the computational frame coincides with the material, one has $\mathbf{X} = \mathbf{c}$, $\mathbf{r}^* = \mathbf{r}^{**}$, $\mathbf{w} = \mathbf{0}$ (see 3.3.13), $\hat{\mathbf{S}}^P = \mathbf{S}^P$ (\mathbf{S}^P is the Piola-Kirchhoff stress tensor defined as usual) and (3A.10) becomes

$$\mathbf{r}^{**} \frac{\mathcal{I} \mathbf{u}^{**}}{\mathcal{I} t} \Big|_x = \nabla_x \cdot \mathbf{S}^P + \mathbf{r}^{**} \mathbf{g} \quad (3A.12)$$

Energy Equation

Let V_c be a control volume in the computational frame of reference and S_c its surface with outward unit normal \mathbf{n}_c . The first principle of the thermodynamics states that the temporal variation of the internal energy within the control volume V_c is equal to tensional work (internal work) plus the flux of heat through the surface S_c , that is

$$\frac{\mathcal{I}}{\mathcal{I} t} \left(\int_{V_c} \mathbf{r}^* e_o^* dV_c \right) \Big|_x = \int_{V_c} \hat{\mathbf{S}}^P : \nabla \mathbf{w}^* dV_c - \int_{S_c} \mathbf{q} \cdot \mathbf{n}_c dS_c \quad (3A.13)$$

where e_o^* is the specific internal energy and \mathbf{q} is the heat flux vector. Note that it has been assumed that there is not internal generation-destruction of heat. If one considers that the flux of heat is isotropic and given by the *Fourier law*, the flux vector is

$$\mathbf{q} = -k \nabla T \quad (3A.14)$$

where k is the thermal conductivity and T is temperature. Using (3A.14), the Reynolds transport theorem (3.3.20) and the continuity equation (3A.3), equation (3A.13) becomes finally

$$\int_{V_c} \left(\mathbf{r}^* \frac{\mathcal{I} e_o^*}{\mathcal{I} t} \Big|_c + \mathbf{r}^* \mathbf{w}^* \cdot \nabla_c e_o^* \right) dV_c = \int_{V_c} [\hat{\mathbf{S}}^P : \nabla_c \mathbf{w}^* + \nabla_c \cdot (k \nabla_c T)] dV_c \quad (3A.15)$$

or, using that V_c is arbitrary

$$\mathbf{r}^* \frac{\mathcal{I} e_o^*}{\mathcal{I} t} \Big|_c + \mathbf{r}^* \mathbf{w}^* \cdot \nabla_c e_o^* = \hat{\mathbf{S}}^P : \nabla_c \mathbf{w}^* + \nabla_c \cdot (k \nabla_c T) \quad (3A.16)$$

Observation When the computational and the spatial frames coincide, one has $\mathbf{x} = \mathbf{c}$, $\mathbf{r}^* = \mathbf{r}$, $\hat{\mathbf{u}} = \mathbf{0}$ (see 3.3.16), $\hat{\mathbf{F}} = \mathbf{I}$ (see 3.3.6), $\mathbf{w} = \mathbf{u}$ (see 3.3.15), $\hat{\mathbf{S}}^P = \mathbf{S}$ and (3A.16) becomes

$$\mathbf{r} \frac{\mathcal{I} e_o}{\mathcal{I} t} \Big|_x + \mathbf{r} \mathbf{u} \cdot \nabla_x e_o = \mathbf{S} \cdot \nabla_x \mathbf{u} + \nabla_x \cdot (k \nabla_x T) \quad (3A.17)$$

Note that due to the symmetry of the Cauchy stress tensor the identity $\mathbf{S} : \nabla \mathbf{u} = \mathbf{S} \cdot \nabla \mathbf{u}$ is verified. On the other hand, when the computational frame coincides with the material, one has

$\mathbf{X} = \mathbf{c}$, $\mathbf{r}^* = \mathbf{r}^{**}$, $\mathbf{w} = \mathbf{0}$ (see 3.3.13) and (3A.16) becomes

$$\mathbf{r}^{**} \frac{\mathcal{I} e_o^{**}}{\mathcal{I} t} \Big|_x = \nabla_x \cdot (k \nabla_x T) \quad (3A.18)$$

Chapter 4

Numerical Methods

Chapter Contents

- 4.1 The Navier-Stokes Equations
 - 4.1.1 Time Discretisation
 - 4.1.2 Pressure Gradient Projection
 - 4.1.3 Splitting of the Momentum Equation
 - 4.1.4 Weak Forms and Boundary Conditions
 - 4.1.4.1 Fractional Momentum Equation
 - 4.1.4.2 Continuity Equation
 - 4.1.4.3 Pressure Gradient Projection Equation
 - 4.1.4.4 Momentum Equation
 - 4.1.4.5 Energy Equation
 - 4.1.5 Space Discretisation
 - 4.1.6 Methods of Stabilisation
 - 4.1.7 Time Step and Stability
- 4.2 The Convective Transport Equation
- 4.3 Fluid-Structure Interaction
 - 4.3.1 Introduction and General Procedure
 - 4.3.2 A Structural Integrator for the Solid Rigid
 - 4.3.3 The Quasi-Laplacian Method
 - 4.3.4 Mesh Velocity and Boundary Conditions
 - 4.3.5 Mesh Distortion and Remeshing
- 4.4 Numerical Examples
 - 4.4.1 The Driven Cavity Flow
 - 4.4.2 Flow Past a Circular Cylinder
 - 4.4.3 Fluid in a Heated Cavity
 - 4.4.4 Perfect Gas Flowing over a NACA Profile
 - 4.4.5 The Stokes Problem
 - 4.4.6 Missile Launched from a Submarine
 - 4.4.7 Mould Filling Simulation
- 4.5 The Mechanical Equations
 - 4.5.1 Elastic Problem
 - 4.5.1.1 Weak Form and Boundary Conditions
 - 4.5.1.2 Space Discretisation
 - 4.5.1.3 The Newmark Method
 - 4.5.2 Viscoelastic Problem. The Prony Series Method
- 4.6 References
- Appendix 4A. Weak Forms
- Appendix 4B. Discretised Algebraic Systems
- Appendix 4C. Programming Notes

Abstract

This chapter outlines all the numerical methodology employed along this work in order to solve the Navier-Stokes equations, the fluid-structure interaction and the mechanical problem. All these problems are solved using a Finite Element Method. Firstly, an algorithm to solve the ALE Navier-Stokes equations is presented. A remarkable contribution is that the algorithm uses a fractional step method combined with a pressure gradient projection technique which provides a stabilisation effect on the pressure field. The algorithm allows the use of equal interpolation spaces for the pressure and velocity fields, and can be applied to solve both compressible and incompressible flows. This last property is extremely important in order to model the problem of the magma withdrawal from a closed system because the state law proposed herein for the magmatic mixture presents two differentiated domains: the flow is incompressible below the exsolution level and compressible above it. Since the position of the exsolution level is time-dependent, parts of the flow change from incompressible to compressible while the withdrawal process evolves. Once the discrete version of the equations is obtained, different methods to stabilise the convective dominated flows and the general properties of the algorithm are examined. Secondly, the fluid-structure interaction problem is tackled. A new procedure to compute the ALE mesh velocity, based on the quasi-Laplacian method, is proposed and a new conservative remeshing strategy is discussed. Some numerical tests are also presented in order to test the validity and implementation of the algorithm. Finally, a method to solve the mechanical equations is considered for both the elastic and some particular viscoelastic rheologies which are commonly employed in volcanology for the modelling of ground deformation processes. The elastic problem is solved as standard. The correspondence principle together with the Prony series method is employed to obtain the viscoelastic solution in an cost-effective manner.

4.1 The Navier-Stokes Equations

The aim of this section is to present an algorithm to numerically solve the Navier-Stokes equations, which in its conservative form and using an ALE formulation are

$$\frac{\partial \mathbf{V}}{\partial t} - \hat{\mathbf{u}} \cdot \nabla \mathbf{V} + \nabla \cdot \mathbf{F}^C + \nabla \cdot \mathbf{F}^D + \mathbf{S} = 0 \quad (4.1.1)$$

where $\hat{\mathbf{u}}$ is the ALE mesh velocity, \mathbf{V} is the fluid state vector, \mathbf{F}^C and \mathbf{F}^D are the convective and the diffusive fluxes respectively, and \mathbf{S} stands for the source terms. For three-dimensional flows and considering Cartesian coordinates, \mathbf{V} , \mathbf{F}^C , \mathbf{F}^D and \mathbf{S} are given by

$$\mathbf{V} = \begin{bmatrix} \mathbf{r} \\ \mathbf{r} u_1 \\ \mathbf{r} u_2 \\ \mathbf{r} u_3 \\ E \end{bmatrix} \quad \mathbf{F}_i^C = \begin{bmatrix} \mathbf{r} u_i \\ \mathbf{r} u_i u_1 + \mathbf{d}_{1i} p \\ \mathbf{r} u_i u_2 + \mathbf{d}_{2i} p \\ \mathbf{r} u_i u_3 + \mathbf{d}_{3i} p \\ (E + p) u_i \end{bmatrix} \quad \mathbf{F}_i^D = \begin{bmatrix} 0 \\ -\mathbf{T}_{1i} \\ -\mathbf{T}_{2i} \\ -\mathbf{T}_{3i} \\ -k \frac{\partial T}{\partial x_i} - \mathbf{T}_{ij} u_j \end{bmatrix} \quad \mathbf{S} = \begin{bmatrix} 0 \\ -\mathbf{r} g_1 \\ -\mathbf{r} g_2 \\ -\mathbf{r} g_3 \\ -\mathbf{r} g_i u_i \end{bmatrix} \quad (4.1.2)$$

The meaning of each variable as well as an extensive deduction of the above equations can be found in chapter 3. These equations must be completed with a constitutive equation and with a state law. Since no shocks are expected, the ALE energy equation will be solved in terms of the temperature rather than in terms of the total energy (i.e. it will not be expressed in a conservative way). In summary, the system of equations is solved in the following form

$$\frac{\mathcal{J}}{\mathcal{J} t} \mathbf{U} = -\nabla \cdot (\mathbf{u} \otimes \mathbf{U}) + \hat{\mathbf{u}} \cdot \nabla \mathbf{U} - \nabla p + \nabla \cdot \mathbf{T} + \mathbf{r} \mathbf{g} \quad (\text{Momentum equation}) \quad (4.1.3)$$

$$\frac{\mathcal{J}}{\mathcal{J} t} \mathbf{r} = -\nabla \cdot \mathbf{U} + \hat{\mathbf{u}} \cdot \nabla \mathbf{r} \quad (\text{Continuity equation}) \quad (4.1.4)$$

$$\frac{\mathcal{J}}{\mathcal{J} t} T = (\hat{\mathbf{u}} - \mathbf{u}) \cdot \nabla T + \frac{k}{c_v \mathbf{r}} \nabla^2 T + \frac{1}{c_v \mathbf{r}} \mathbf{S} \cdot \nabla \mathbf{u} + \frac{1}{c_v} \mathbf{g} \cdot \mathbf{u} \quad (\text{Energy equation}) \quad (4.1.5)$$

$$\mathbf{S} = -p \mathbf{I} + \mathbf{T} = -p \mathbf{I} + \mathbf{m} \left(\nabla \mathbf{u} + \mathbf{u} \nabla - \frac{2}{3} (\nabla \cdot \mathbf{u}) \mathbf{I} \right) \quad (\text{Constitutive equation}) \quad (4.1.6)$$

$$\mathbf{j}(\mathbf{r}, T, p) = 0 \quad (\text{State law}) \quad (4.1.7)$$

and in $\Omega(t) \times (0, T]$ where t designates time, $\Omega(t) \subset \mathbb{R}^n$ ($n = 2, 3$) is the computational domain and $[0, T]$ is the time interval under consideration. Obviously it is assumed that the above equations satisfy a given suitable set of boundary and initial conditions.

Observation The set of equations (4.1.3) to (4.1.7) must be complemented with a mesh motion equation which provides the ALE mesh velocity $\hat{\mathbf{u}}$. Along this section, it will be assumed that this mesh velocity is known at any time instant and, in consequence, $\hat{\mathbf{u}}$ will be considered as a given function. The proper evaluation of $\hat{\mathbf{u}}$ for fluid-structure interaction problems (for those problems in which $\hat{\mathbf{u}} \neq \mathbf{0}$) will be discussed later, in section 4.3.

In this section, an algorithm to numerically solve the above equations using a Finite Element Method is presented. The algorithm uses a fractional step method that allows the use of equal interpolation spaces for the pressure and the velocity fields, and can be used to solve both compressible and incompressible flows simultaneously. It also uses a pressure gradient projection technique that contributes to stabilise the pressure field. The section is organised as follows. Firstly, the set of equations (4.1.3) to (4.1.7) is time discretised using the traditional trapezoidal rule. Once time discretised, both the pressure gradient projection and the splitting of the momentum equation are introduced and the weak form is obtained using the traditional Galerkin formulation. The proper implementation of boundary conditions as well as different methods to stabilise the convective term in convective dominated flows are also considered. Finally, the critical time step and the stability of the algorithm are tackled.

4.1.1 Time Discretisation

The conservation equations (4.1.3), (4.1.4) and (4.1.5) are firstly time discretised by means of a traditional finite difference scheme (the trapezoidal rule), in which a general problem

$$\frac{\partial u}{\partial t} = f(u, t) \quad (4.1.8)$$

is discretised as

$$\frac{\Delta u^n}{\Delta t} = f^{n+\bar{q}}(u, t) \quad (4.1.9)$$

Notation The superscripts denote time step level. Let $f(u, t)$ be an arbitrary function defined in $\Omega(t) \times [0, T]$. Then, by definition

$$\Delta f^n \equiv f^{n+1} - f^n \quad (4.1.10)$$

$$f^{n+\vec{q}} \equiv \mathbf{q}^1 f^{n+1} + \mathbf{q}^2 f^n + \mathbf{q}^3 f^{n-1} \quad (4.1.11)$$

where \vec{q} is a vector with components $\vec{q} = (\mathbf{q}^1, \mathbf{q}^2, \mathbf{q}^3)$, where $\mathbf{q}^i \in [0, 1] \forall i$ and $\mathbf{q}^1 + \mathbf{q}^2 + \mathbf{q}^3 = 1$. The notation introduced in (4.1.10) and (4.1.11) allows to express compactly any finite difference scheme up to second order depending on the values of \mathbf{q}^i . This is reflected in table 4.1.1.

θ^1	θ^2	θ^3	Scheme	Order
0	1	0	Explicit	1
0	3/2	-1/2	Explicit	2
1	0	0	Implicit	1
1/2	1/2	0	Implicit	2

Table 4.1.1. Characteristics of a finite difference scheme depending on the values of \mathbf{q}^i .

The conservation equations are discretised in time as follows

$$\frac{\Delta \mathbf{U}^n}{\Delta t} = -\nabla \cdot (\mathbf{u} \otimes \mathbf{U})^{n+\vec{q}_1} + \hat{\mathbf{u}} \cdot \nabla \mathbf{U}^{n+\vec{q}_1} - \nabla p^{n+1} + \nabla \cdot \mathbf{T}^{n+\vec{q}_2} + \mathbf{r}^n \mathbf{g} \quad (4.1.12)$$

$$\frac{\Delta \mathbf{r}^n}{\Delta t} = -\nabla \cdot \mathbf{U}^{n+1} + \hat{\mathbf{u}} \cdot \nabla \mathbf{r}^n \quad (4.1.13)$$

$$\frac{\Delta T^n}{\Delta t} = \left[(\hat{\mathbf{u}} - \mathbf{u}) \cdot \nabla T + \frac{k}{c_v \mathbf{r}} \nabla^2 T + \frac{1}{c_v \mathbf{r}} \mathbf{S} \cdot \nabla \mathbf{u} + \frac{1}{c_v} \mathbf{g} \cdot \mathbf{u} \right]^{n+\vec{q}_3} \quad (4.1.14)$$

Note that three different parameters \vec{q}_1 , \vec{q}_2 and \vec{q}_3 have been introduced. In the momentum equation (4.1.12) the convective, the moveable mesh and the viscous terms can be treated implicitly or explicitly depending on the values of \vec{q}_1 and \vec{q}_2 whereas the pressure gradient term is treated implicitly because the algorithm must be able to deal with incompressible flows. Note also how the whole scheme of the energy equation (4.1.14) may be also implicit or explicit depending on the values of \vec{q}_3 .

Observation In the momentum equation the body forces term is treated explicitly (\mathbf{r}^{n+1} is unknown when this equation is solved). A first order approach is assumed for simplicity. However, if one wishes to have a second order treatment in all the terms a trivial correction should be done (for compressible flows).

4.1.2 Pressure Gradient Projection

The pressure gradient projection technique [Codina and Blasco, 1997; Codina and Blasco, 2000] was originally developed for incompressible flows in the context of monolithic velocity-pressure formulations in order to inherit the stability properties of some fractional step methods that allow the use of the same interpolation spaces for the pressure and the velocity fields. The idea was to introduce a new unknown to the problem (the projection of the pressure gradient into the space of velocities) and add the difference between the laplacian of the pressure and the divergence of this new variable to the continuity equation. This concept can also be applied to the fractional step methods for compressible flows defining

$$\mathbf{x}^n \equiv \nabla p^n \quad (4.1.15)$$

and modifying the time discretised continuity equation (4.1.13)

$$\frac{\Delta \mathbf{r}^n}{\Delta t} = -\nabla \cdot \mathbf{U}^{n+1} + \hat{\mathbf{u}} \cdot \nabla \mathbf{r}^n + \mathbf{a} (\nabla^2 p^{n+1} - \nabla \cdot \mathbf{x}^n) \quad (4.1.16)$$

where \mathbf{x} is the *pressure gradient projection* and \mathbf{a} is a numerical parameter. Note that the term added in (4.1.16) vanishes in the continuous version of the continuity equation but not in its discrete version. Although in the case of some fractional step methods the pressure gradient projection is not required to use equal interpolation spaces, it will produce an additional stabilising effect on the pressure field. Note also that the parameter \mathbf{a} has units of time. For the steady case, it can be shown that this parameter is the critical time step of the one-dimensional diffusion-convection equation [Codina, 1993]. For transient problems, the value of \mathbf{a} is not established theoretically, but numerical experience shows that its best value is also the same critical time step.

4.1.3 Splitting of the Momentum Equation

The most significant feature of the numerical scheme here proposed is the splitting of the time discretised momentum equation (4.1.12) using a fractional step method, a technique first suggested for incompressible flows by [Chorin, 1967; Chorin, 1969] and [Temam, 1969]. The idea behind any fractional step method is to compute first the momentum equation without the implicit contribution of the gradient of pressure and add this subtracted term later, once the pressure has been calculated. Some versions of this technique avoid the need of different pressure and velocity interpolation spaces in order to satisfy the Babuska-Brezzi condition [Brezzi and Fortin, 1991]. However, the use of a fractional step method introduces both a new unknown to the system (the fractional momentum) as well as an error in the boundary conditions. When the concept of splitting is applied to compressible flows it is possible to have a single algorithm able to deal equally well with both compressible and incompressible regimes and using the same interpolation spaces for all of the unknowns. The fractional momentum $\tilde{\mathbf{U}}$ is defined as

$$\tilde{\mathbf{U}}^{n+1} \equiv \mathbf{U}^{n+1} + \Delta t \nabla (p^{n+1} - \mathbf{g} p^n) \quad (4.1.17)$$

so that

$$\Delta \tilde{\mathbf{U}}^n \equiv \tilde{\mathbf{U}}^{n+1} - \mathbf{U}^n = \Delta \mathbf{U}^n + \Delta t \nabla (p^{n+1} - \mathbf{g} p^n) \quad (4.1.18)$$

where \mathbf{g} is a parameter. Depending on its value, the fractional step method can be a *total fractional step method* (when $\mathbf{g}=0$) or an *incremental fractional step method* (when $\mathbf{g}=1$). The difference between both methods is that, in the first case, the whole gradient of pressure is extracted from the momentum equation to compute the fractional momentum, while in the second case, its explicit contribution remains¹. Using (4.1.18) the time discretised momentum equation (4.1.12) can be split as

¹ It will be shown later how the case $\mathbf{g}=1$ corrects automatically the splitting error that appears in the implicit versions of the algorithm up to second order of accuracy and, in consequence, allows implicit schemes of order $O(\Delta t^2)$. However, pressure stability is, in this case, very weak if the pressure gradient projection technique is not considered.

$$\frac{\Delta \tilde{\mathbf{U}}^n}{\Delta t} = -\nabla \cdot (\mathbf{u} \otimes \mathbf{U})^{n+q_1} + \hat{\mathbf{u}} \cdot \nabla \mathbf{U}^{n+q_1} - \mathbf{g} \nabla p^n + \nabla \cdot \mathbf{T}^{n+q_2} + \mathbf{r}^n \mathbf{g} \quad (4.1.19)$$

$$\frac{\Delta \mathbf{U}^n}{\Delta t} = \frac{\Delta \tilde{\mathbf{U}}^n}{\Delta t} - \nabla (p^{n+1} - \mathbf{g} p^n) \quad (4.1.20)$$

Observation It is also possible to introduce the fractional momentum as

$$\Delta \tilde{\mathbf{U}}^n \equiv \Delta \mathbf{U}^n + \Delta t \nabla (p^{n+1} - \mathbf{g} p^n) \quad (4.1.21)$$

$$\Delta \tilde{\mathbf{U}}^n = \tilde{\mathbf{U}}^{n+1} - \tilde{\mathbf{U}}^n \quad (4.1.22)$$

instead of the usual definition (4.1.17). This second option can be interpreted as a continuous splitting in which the splitting of the momentum equation is done before its time discretisation. This can be shown by splitting the continuous version of the momentum equation (4.1.3) as

$$\frac{\partial \tilde{\mathbf{U}}}{\partial t} + \nabla \cdot (\mathbf{u} \otimes \mathbf{U}) - \hat{\mathbf{u}} \cdot \nabla \mathbf{U} - \nabla \cdot \mathbf{T} - \mathbf{r} \mathbf{g} + \nabla \tilde{p} = \mathbf{0} \quad (4.1.23)$$

$$\frac{\partial \mathbf{U}}{\partial t} - \frac{\partial \tilde{\mathbf{U}}}{\partial t} + \nabla p - \nabla \tilde{p} = \mathbf{0} \quad (4.1.24)$$

Trivially, the above expressions are equivalent to (4.1.3). If time discretisation is now performed as in the “standard case” and the time discretised version of \tilde{p} is defined as

$$\tilde{p}^n = \begin{cases} p^n & \text{for } \mathbf{g} = 1 \\ 0 & \text{for } \mathbf{g} = 0 \end{cases} \quad (4.1.25)$$

the resulting equations are formally equal to (4.1.19) and (4.1.20). In consequence, the final discretised momentum equations are the same in both cases, but the schemes differ in the definition of $\Delta \tilde{\mathbf{U}}^n$. Obviously, both possibilities will give rise to very similar final algorithms but this second option is a little bit less effective from a computational point of view because requires the storage of $\tilde{\mathbf{U}}^n$.

From now on, equation (4.1.19) will be referred as the fractional momentum equation, while equation (4.1.20) will be referred as the momentum equation. The time discretised continuity equation (4.1.16) must also be expressed in terms of $\tilde{\mathbf{U}}^{n+1}$ because, due to the

splitting, the momentum \mathbf{U}^{n+1} is still an unknown when either pressure or density are computed by means of this equation. Applying the divergence operator to (4.1.17) one gets

$$\nabla^2(p^{n+1} - \mathbf{g} p^n) = \frac{1}{\Delta t} \nabla \cdot \tilde{\mathbf{U}}^{n+1} - \frac{1}{\Delta t} \nabla \cdot \mathbf{U}^{n+1} \quad (4.1.26)$$

and substituting the time discrete continuity equation (4.1.16) into the above expression one obtains

$$\begin{aligned} \frac{1}{\Delta t^2} \mathbf{r}^{n+1} - \left(1 + \frac{\mathbf{a}}{\Delta t}\right) \nabla^2 p^{n+1} &= \frac{1}{\Delta t^2} \mathbf{r}^n + \frac{1}{\Delta t} \hat{\mathbf{u}} \cdot \nabla \mathbf{r}^n - \mathbf{g} \nabla^2 p^n \\ &\quad - \frac{\mathbf{a}}{\Delta t} \nabla \cdot \mathbf{x}^n - \frac{1}{\Delta t} \nabla \cdot (\mathbf{U}^n + \Delta \tilde{\mathbf{U}}^n) \end{aligned} \quad (4.1.27)$$

This substitution at the continuous spatial level will lead to a stabilising pressure dissipation term in the final discrete finite element scheme that will allow the use of the same interpolation spaces for the velocity and the pressure. The effect of the parameter \mathbf{g} on the stability of the final resulting algorithm will be discussed later. Once the splitting has been introduced, each time step is solved as follows

- ❶ Solve the fractional momentum equation (4.1.19) to obtain $\tilde{\mathbf{U}}^{n+1}$.
- ❷ Solve the continuity equation (4.1.27) to obtain either pressure p^{n+1} or density \mathbf{r}^{n+1} . Obviously, once one of them is determined, the state law (4.1.7) automatically gives the other variable. Clearly (in thermally coupled problems) this is done in terms of T^n unless an iterative procedure is considered within each time step.
- ❸ Solve the gradient projection equation (4.1.15) to obtain \mathbf{x}^{n+1} .
- ❹ Solve the momentum equation (4.1.20) to obtain \mathbf{U}^{n+1} .
- ❺ If necessary, solve the energy equation (4.1.14) to obtain T^{n+1} .

4.1.4 Weak Forms and Boundary Conditions

Next step is to obtain the weak forms of the equations (4.1.19), (4.1.27), (4.1.15), (4.1.20), and (4.1.14) by projecting these time-discretised equations into the usual space of test functions and integrating then over the domain Ω .

Observation In fluid-structure interaction problems the spatial domain changes with time. It naturally rises the question of where the spatial integrals must be computed: at $\Omega(t^n)$, at $\Omega(t^{n+1})$ or at another instant in between these two spatial configurations. This question will be discussed further, in section 4.3. By now, and without loss of generality, the spatial domain Ω will be considered without temporal dependence. Note that, in particular, a constant spatial computational domain (i.e. time independent) is always the case of the problems without fluid-structure interaction.

4.1.4.1 Fractional Momentum Equation

Multiplying (4.1.19) by the test function $\tilde{\mathbf{W}}$, and integrating over the domain Ω one gets

$$\begin{aligned} \int_{\Omega} \tilde{\mathbf{W}} \cdot \tilde{\mathbf{U}}^{n+1} d\Omega &= \int_{\Omega} \tilde{\mathbf{W}} \cdot \mathbf{U}^n d\Omega - \Delta t \int_{\Omega} \tilde{\mathbf{W}} \cdot (\nabla \cdot (\mathbf{u} \otimes \mathbf{U})^{n+\bar{q}_1}) d\Omega + \\ &\Delta t \int_{\Omega} \tilde{\mathbf{W}} \cdot (\hat{\mathbf{u}} \cdot \nabla \mathbf{U}^{n+\bar{q}_1}) d\Omega - \mathbf{g} \Delta t \int_{\Omega} \tilde{\mathbf{W}} \cdot \nabla p^n d\Omega + \\ &\Delta t \int_{\Omega} \mathbf{r}^n \tilde{\mathbf{W}} \cdot \mathbf{g} d\Omega + \Delta t \int_{\Omega} \tilde{\mathbf{W}} \cdot (\nabla \cdot \mathbf{T}^{n+\bar{q}_2}) d\Omega \end{aligned} \quad (4.1.28)$$

If the viscous term of the above expression is integrated by parts using the identity

$$\tilde{\mathbf{W}} \cdot (\nabla \cdot \mathbf{T}) = \nabla \cdot (\tilde{\mathbf{W}} \cdot \mathbf{T}) - \nabla \tilde{\mathbf{W}} \cdot \mathbf{T} \quad (4.1.29)$$

and the Gauss theorem is applied to transform the volume integral into a surface integral, one obtains

$$\begin{aligned} \int_{\Omega} \tilde{\mathbf{W}} \cdot \tilde{\mathbf{U}}^{n+1} d\Omega &= \int_{\Omega} \tilde{\mathbf{W}} \cdot \mathbf{U}^n d\Omega - \Delta t \int_{\Omega} \tilde{\mathbf{W}} \cdot (\nabla \cdot (\mathbf{u} \otimes \mathbf{U})^{n+\bar{q}_1}) d\Omega + \Delta t \int_{\Omega} \tilde{\mathbf{W}} \cdot (\hat{\mathbf{u}} \cdot \nabla \mathbf{U}^{n+\bar{q}_1}) d\Omega \\ &- \mathbf{g} \Delta t \int_{\Omega} \tilde{\mathbf{W}} \cdot \nabla p^n d\Omega + \Delta t \int_{\Omega} \mathbf{r}^n \tilde{\mathbf{W}} \cdot \mathbf{g} d\Omega - \Delta t \int_{\Omega} \nabla \tilde{\mathbf{W}} \cdot \mathbf{T}^{n+\bar{q}_2} d\Omega + \\ &\Delta t \int_{\Gamma} \tilde{\mathbf{W}} \cdot \mathbf{T}^{n+\bar{q}_2} \cdot \mathbf{n} d\Gamma \end{aligned} \quad (4.1.30)$$

where \mathbf{n} is the unit outward normal to the boundary Γ . Note how the convective, the moveable mesh and the viscous terms of (4.1.30) can be treated implicit or explicitly depending on the values of \bar{q}_1 and \bar{q}_2 respectively. When these terms are fully developed they respectively become

$$\begin{aligned}
 \Delta t \int_{\Omega} \tilde{\mathbf{W}} \cdot (\nabla \cdot (\mathbf{u} \otimes \mathbf{U})^{n+q_1}) d\Omega &= \Delta t q_1^1 \int_{\Omega} \tilde{\mathbf{W}} \cdot \nabla \cdot (\mathbf{u}^{n+1} \otimes \mathbf{U}^{n+1}) d\Omega + \\
 &\quad \Delta t q_1^2 \int_{\Omega} \tilde{\mathbf{W}} \cdot \nabla \cdot (\mathbf{u}^n \otimes \mathbf{U}^n) d\Omega + \quad (\text{convective term}) \quad (4.1.31) \\
 &\quad \Delta t q_1^3 \int_{\Omega} \tilde{\mathbf{W}} \cdot \nabla \cdot (\mathbf{u}^{n-1} \otimes \mathbf{U}^{n-1}) d\Omega
 \end{aligned}$$

$$\begin{aligned}
 \Delta t \int_{\Omega} \tilde{\mathbf{W}} \cdot (\hat{\mathbf{u}} \cdot \nabla \mathbf{U}^{n+q_1}) d\Omega &= \Delta t q_1^1 \int_{\Omega} \tilde{\mathbf{W}} \cdot (\hat{\mathbf{u}} \cdot \nabla \mathbf{U}^{n+1}) d\Omega + \\
 &\quad \Delta t q_1^2 \int_{\Omega} \tilde{\mathbf{W}} \cdot (\hat{\mathbf{u}} \cdot \nabla \mathbf{U}^n) d\Omega + \quad (\text{moveable mesh term}) \quad (4.1.32) \\
 &\quad \Delta t q_1^3 \int_{\Omega} \tilde{\mathbf{W}} \cdot (\hat{\mathbf{u}} \cdot \nabla \mathbf{U}^{n-1}) d\Omega
 \end{aligned}$$

$$\begin{aligned}
 \Delta t \int_{\Omega} \nabla \tilde{\mathbf{W}} \cdot \cdot \mathbf{T}^{n+q_2} d\Omega &= \Delta t q_2^1 \int_{\Omega} \nabla \tilde{\mathbf{W}} \cdot \cdot \mathbf{T}^{n+1} d\Omega + \\
 &\quad \Delta t q_2^2 \int_{\Omega} \nabla \tilde{\mathbf{W}} \cdot \cdot \mathbf{T}^n d\Omega + \quad (\text{viscous term}) \quad (4.1.33) \\
 &\quad \Delta t q_2^3 \int_{\Omega} \nabla \tilde{\mathbf{W}} \cdot \cdot \mathbf{T}^{n-1} d\Omega
 \end{aligned}$$

$$\begin{aligned}
 \Delta t \int_{\Gamma} \tilde{\mathbf{W}} \cdot \mathbf{T}^{n+q_2} \cdot \mathbf{n} d\Gamma &= \Delta t q_2^1 \int_{\Gamma} \tilde{\mathbf{W}} \cdot \mathbf{T}^{n+1} \cdot \mathbf{n} d\Gamma + \\
 &\quad \Delta t q_2^2 \int_{\Gamma} \tilde{\mathbf{W}} \cdot \mathbf{T}^n \cdot \mathbf{n} d\Gamma + \quad (\text{boundary viscous term}) \quad (4.1.34) \\
 &\quad \Delta t q_2^3 \int_{\Gamma} \tilde{\mathbf{W}} \cdot \mathbf{T}^{n-1} \cdot \mathbf{n} d\Gamma
 \end{aligned}$$

All the terms above present some particularities that should be pointed out separately.

- **The Convective Term.** Two inconveniences arise when the convective term (4.1.31) is treated implicitly (i.e. with $q_1^1 > 0$) because neither \mathbf{u}^{n+1} nor \mathbf{U}^{n+1} are known when (4.1.30) is solved to obtain $\tilde{\mathbf{U}}^{n+1}$. This inconveniences are solved as follows.

- Firstly, in order to avoid the need to solve a non-linear problem within each time step, the convective velocity is evaluated at the previous time step, that is

$$\begin{aligned}
 \nabla \cdot (\mathbf{u} \otimes \mathbf{U})^{n+q_1} &\equiv q_1^1 \nabla \cdot (\mathbf{u} \otimes \mathbf{U})^{n+1} + q_1^2 \nabla \cdot (\mathbf{u} \otimes \mathbf{U})^n + q_1^3 \nabla \cdot (\mathbf{u} \otimes \mathbf{U})^{n-1} \\
 &\equiv q_1^1 \nabla \cdot (\mathbf{u}^n \otimes \mathbf{U}^{n+1}) + q_1^2 \nabla \cdot (\mathbf{u} \otimes \mathbf{U})^n + q_1^3 \nabla \cdot (\mathbf{u} \otimes \mathbf{U})^{n-1}
 \end{aligned} \quad (4.1.35)$$

4.1 The Navier-Stokes Equations

This is a common approach to linearise the convective term in incompressible flows for first order schemes [*Simo and Armero, 1994*].

Observation The substitution $\mathbf{u}^{n+1} \rightarrow \mathbf{u}^n$ implies that the scheme is of first order when $q_1^1 > 0$. This is correct is the case $q_1^1 = 1$. However, if $q_1^1 = 1/2$ and one wishes to keep the order of the scheme the substitution should be $\mathbf{u}^{n+1} \rightarrow 3/2 \mathbf{u}^n - 1/2 \mathbf{u}^{n-1}$. Notwithstanding this comment, the development will be done, for simplicity, only for the first order case.

❷ Secondly, the implicit term in the above expression is evaluated using $\tilde{\mathbf{U}}^{n+1}$ instead of \mathbf{U}^{n+1} . Obviously, this introduces an splitting error. Nevertheless, this splitting error can be partially corrected up to second order of accuracy. This can be shown using the definition of the fractional momentum (4.1.17), so that the linearised implicit term becomes

$$\begin{aligned} \nabla \cdot (\mathbf{u}^n \otimes \mathbf{U}^{n+1}) &= \nabla \cdot (\mathbf{u}^n \otimes \tilde{\mathbf{U}}^{n+1}) - \Delta t \nabla \cdot (\mathbf{u}^n \otimes \nabla p^{n+1}) + \mathbf{g} \Delta t \nabla \cdot (\mathbf{u}^n \otimes \nabla p^n) \\ &= \nabla \cdot (\mathbf{u}^n \otimes \tilde{\mathbf{U}}^{n+1}) - \Delta t (1 - \mathbf{g}) \nabla \cdot (\mathbf{u}^n \otimes \nabla p^n) + O(\Delta t^2) \end{aligned} \quad (4.1.36)$$

and

$$\begin{aligned} \nabla \cdot (\mathbf{u} \otimes \mathbf{U})^{n+\tilde{q}_1} &\cong q_1^1 \nabla \cdot (\mathbf{u}^n \otimes \tilde{\mathbf{U}}^{n+1}) + q_1^2 \nabla \cdot (\mathbf{u} \otimes \mathbf{U})^n + q_1^3 \nabla \cdot (\mathbf{u} \otimes \mathbf{U})^{n-1} \\ &\quad - q_1^1 \Delta t (1 - \mathbf{g}) \nabla \cdot (\mathbf{u}^n \otimes \nabla p^n) \end{aligned} \quad (4.1.37)$$

Inserting the above expression into equation (4.1.31), the convective term of the weak form (4.1.30) becomes finally

$$\begin{aligned} -\Delta t \int_{\Omega} \tilde{\mathbf{W}} \cdot (\nabla \cdot (\mathbf{u} \otimes \mathbf{U})^{n+\tilde{q}_1}) d\Omega &= -\Delta t q_1^1 \int_{\Omega} \tilde{\mathbf{W}} \cdot \nabla \cdot (\mathbf{u}^n \otimes \tilde{\mathbf{U}}^{n+1}) d\Omega \\ -\Delta t q_1^2 \int_{\Omega} \tilde{\mathbf{W}} \cdot \nabla \cdot (\mathbf{u}^n \otimes \mathbf{U}^n) d\Omega &- \Delta t q_1^3 \int_{\Omega} \tilde{\mathbf{W}} \cdot \nabla \cdot (\mathbf{u}^{n-1} \otimes \mathbf{U}^{n-1}) d\Omega \\ -\Delta t^2 q_1^1 (1 - \mathbf{g}) \int_{\Omega} \nabla \tilde{\mathbf{W}} : (\mathbf{u}^n \otimes \nabla p^n) d\Omega &+ \Delta t^2 q_1^1 (1 - \mathbf{g}) \int_{\Gamma} \tilde{\mathbf{W}} \cdot (\nabla p^n \otimes \mathbf{u}^n) \cdot \mathbf{n} d\Gamma \end{aligned} \quad (4.1.38)$$

where the term that corrects the splitting error has been integrated by parts. Note that when $\mathbf{g} = 1$ (i.e. when an incremental fractional step method is used) the last two terms of (4.1.38) vanish. In consequence, the use of an incremental fractional step method allows to reduce the splitting error up to second order in time without adding any additional corrective term in the weak form of the fractional momentum equation. In contrast, one additional term will appear in both the weak forms of the continuity and the momentum equations with respect to the

traditional total fractional step method (with $\mathbf{g} = 0$), as observed from (4.1.27) and (4.1.20). Whichever the case considered ($\mathbf{g} = 0$ or $\mathbf{g} = 1$), the use of (4.1.38) corrects the splitting error of the convective terms, so that the only splitting error will come from the viscous contribution.

- **The moveable mesh term.** When the moveable mesh term (4.1.32) is treated implicitly (i.e. with $q_1^1 > 0$) the implicit contribution is evaluated using $\tilde{\mathbf{U}}^{n+1}$ instead of \mathbf{U}^{n+1} . As in the case of the convective term, this will introduce an splitting error that, again, can be partially corrected up to second order of accuracy for the pressure term. Proceeding as in the previous case, the definition of the fractional momentum (4.1.17) leads to

$$\begin{aligned} \hat{\mathbf{u}} \cdot \nabla \mathbf{U}^{n+q_1^1} &= q_1^1 \hat{\mathbf{u}} \cdot \nabla \mathbf{U}^{n+1} + q_1^2 \hat{\mathbf{u}} \cdot \nabla \mathbf{U}^n + q_1^3 \hat{\mathbf{u}} \cdot \nabla \mathbf{U}^{n-1} \\ &= q_1^1 \hat{\mathbf{u}} \cdot \nabla \tilde{\mathbf{U}}^{n+1} + q_1^2 \hat{\mathbf{u}} \cdot \nabla \mathbf{U}^n + q_1^3 \hat{\mathbf{u}} \cdot \nabla \mathbf{U}^{n-1} \\ &\quad - q_1^1 \Delta t (1 - \mathbf{g}) \hat{\mathbf{u}} \cdot \nabla (\nabla p) + O(\Delta t^2) \end{aligned} \quad (4.1.39)$$

Inserting the above expression into equation (4.1.32), the moveable mesh term of the weak form (4.1.30) becomes finally

$$\begin{aligned} \Delta t \int_{\Omega} \tilde{\mathbf{W}} \cdot (\hat{\mathbf{u}} \cdot \nabla \mathbf{U})^{n+q_1^1} d\Omega &= \Delta t q_1^1 \int_{\Omega} \tilde{\mathbf{W}} \cdot (\hat{\mathbf{u}} \cdot (\nabla \tilde{\mathbf{U}})^{n+1}) d\Omega \\ &+ \Delta t q_1^2 \int_{\Omega} \tilde{\mathbf{W}} \cdot (\hat{\mathbf{u}} \cdot (\nabla \mathbf{U})^n) d\Omega + \Delta t q_1^3 \int_{\Omega} \tilde{\mathbf{W}} \cdot (\hat{\mathbf{u}} \cdot (\nabla \mathbf{U})^{n-1}) d\Omega \\ &+ \Delta t^2 q_1^1 (1 - \mathbf{g}) \int_{\Omega} \nabla \cdot (\tilde{\mathbf{W}} \otimes \hat{\mathbf{u}}) \cdot \nabla p d\Omega - \Delta t^2 q_1^1 (1 - \mathbf{g}) \int_{\Gamma} \tilde{\mathbf{W}} \cdot (\nabla p \otimes \hat{\mathbf{u}}) \cdot \mathbf{n} d\Gamma \end{aligned} \quad (4.1.40)$$

where, again, the term that corrects the splitting error has been integrated by parts. As in the convective term, when $\mathbf{g} = 1$ the last two terms of the above expression vanish.

- **The viscous term.** The same inconvenience that appears in the convective term rises if one considers the implicit contribution of the viscous term (4.1.33)

$$\Delta t q_2^1 \int_{\Omega} \nabla \tilde{\mathbf{W}} \cdot \cdot \mathbf{T}^{n+1} d\Omega = \Delta t q_2^1 \int_{\Omega} \mathbf{m} \left[\nabla \tilde{\mathbf{W}} : \nabla \mathbf{u} + \nabla \tilde{\mathbf{W}} \cdot \cdot \nabla \mathbf{u} - \frac{2}{3} (\nabla \cdot \tilde{\mathbf{W}}) (\nabla \cdot \mathbf{u}) \right]^{n+1} d\Omega \quad (4.1.41)$$

Note that the constitutive equation of a Newtonian fluid (4.1.6) has been introduced in the above expression. To express this equation in terms of $\tilde{\mathbf{U}}^{n+1}$ the following approach can be done

$$\begin{aligned}
 \nabla \mathbf{u}^{n+1} &= \nabla \left(\frac{\mathbf{U}^{n+1}}{\mathbf{r}} \right) = \frac{1}{\mathbf{r}^{n+1}} \nabla \mathbf{U}^{n+1} - \frac{1}{(\mathbf{r}^{n+1})^2} \nabla \mathbf{r}^{n+1} \otimes \mathbf{U}^{n+1} \\
 &\cong \frac{1}{\mathbf{r}^n} \nabla \tilde{\mathbf{U}}^{n+1} - \frac{1}{(\mathbf{r}^n)^2} \nabla \mathbf{r}^n \otimes \tilde{\mathbf{U}}^{n+1}
 \end{aligned} \tag{4.1.42}$$

It can be observed that some splitting error is introduced when this approach is used to compute the implicit contribution of the viscous term (4.1.41). This substitution (inherent to any fractional step method) must be necessarily done because \mathbf{U}^{n+1} is still an unknown when the weak form (4.1.30) is solved to obtain $\tilde{\mathbf{U}}^{n+1}$. Note also that, for the same reason, the density is evaluated explicitly (\mathbf{r}^{n+1} is also an unknown when the fractional momentum is computed).

Observation Using the definition of the fractional momentum (4.1.17) in the above equation it can be shown that, if $\mathbf{g}=1$, the splitting error in the viscous term is also $O(\Delta t^2)$. In consequence, the incremental fractional step method has an splitting error $O(\Delta t^2)$ whereas the total fractional step method has always an splitting error $O(\Delta t)$ in the viscous term. Note also that if $\mathbf{g}=1$, and for compressible flows, the substitution of \mathbf{r}^{n+1} in (4.1.42) should be $\mathbf{r}^{n+1} \rightarrow 3/2\mathbf{r}^n - 1/2\mathbf{r}^{n-1}$ if one wishes to keep the order of the scheme.

On the other hand, equation (4.1.41) couples all the components of the fractional momentum, that is, if it were space discretised in its present form it would lead to an algebraic system of 2 or 3 (spatial dimension) coupled scalar equations. Obviously, this would be an expensive procedure from a computational point of view. In order to avoid this coupling, only the first term of the RHS in (4.1.41) is evaluated implicitly, while the other terms, which cause the coupling, are explicitly evaluated using the same order of approximation that in the term implicitly treated. Taking this into account and substituting the approximation into equation (4.1.41) one finally obtains

$$\begin{aligned}
 \Delta t \int_{\Omega} \nabla \tilde{\mathbf{W}} \cdot \mathbf{T}^{n+1} d\Omega &\cong \\
 \Delta t \int_{\Omega} \left[\frac{\mathbf{m}}{\mathbf{r}^n} \nabla \tilde{\mathbf{W}} : \nabla \tilde{\mathbf{U}}^{n+1} - \frac{\mathbf{m}}{(\mathbf{r}^n)^2} \nabla \tilde{\mathbf{W}} : (\nabla \mathbf{r}^n \otimes \tilde{\mathbf{U}}^{n+1}) \right] d\Omega &+ \\
 \Delta t \int_{\Omega} \mathbf{m} \left[\nabla \tilde{\mathbf{W}} \cdot \nabla \mathbf{u}^n - \frac{2}{3} (\nabla \cdot \tilde{\mathbf{W}}) (\nabla \cdot \mathbf{u})^n \right] d\Omega &
 \end{aligned} \tag{4.1.43}$$

when $\mathbf{q}_2^1 = 1$ (that is, when a first order implicit treatment of the viscous term is considered) and

$$\begin{aligned}
 & \Delta t q_2^1 \int_{\Omega} \nabla \tilde{\mathbf{W}} \cdot \mathbf{T}^{n+1} d\Omega \cong \\
 & \Delta t q_2^1 \int_{\Omega} \left[\frac{\mathbf{m}}{\mathbf{r}^n} \nabla \tilde{\mathbf{W}} : \nabla \tilde{\mathbf{U}}^{n+1} - \frac{\mathbf{m}}{(\mathbf{r}^n)^2} \nabla \tilde{\mathbf{W}} : (\nabla \mathbf{r}^n \otimes \tilde{\mathbf{U}}^{n+1}) \right] d\Omega + \\
 & \frac{3}{4} \Delta t \int_{\Omega} \mathbf{m} \left[\nabla \tilde{\mathbf{W}} \cdot \nabla \mathbf{u}^n - \frac{2}{3} (\nabla \cdot \tilde{\mathbf{W}}) (\nabla \cdot \mathbf{u})^n \right] d\Omega - \\
 & \frac{1}{4} \Delta t \int_{\Omega} \mathbf{m} \left[\nabla \tilde{\mathbf{W}} \cdot \nabla \mathbf{u}^{n-1} - \frac{2}{3} (\nabla \cdot \tilde{\mathbf{W}}) (\nabla \cdot \mathbf{u})^{n-1} \right] d\Omega
 \end{aligned} \tag{4.1.44}$$

when $q_2^1 = 1/2$ (that is, when a second order implicit treatment of the viscous term is considered). The important point is that, whichever the case considered, when part of the implicit viscous term is treated explicitly as in (4.1.43) (or as in (4.1.44)), the spatial components in equation (4.1.41) can be uncoupled. Nevertheless, it should be pointed out that the contribution of the terms implicitly treated is the most important. Thus, for incompressible flows, the contribution of the terms which are treated explicitly is reduced to a boundary contribution. This can be shown applying the identity

$$\nabla \cdot (\tilde{\mathbf{W}} \cdot \nabla \mathbf{u}) = \nabla \tilde{\mathbf{W}} \cdot \nabla \mathbf{u} + \tilde{\mathbf{W}} \cdot \nabla (\nabla \cdot \mathbf{u}) \tag{4.1.45}$$

so that

$$\begin{aligned}
 & \Delta t q_2^1 \int_{\Omega} \mathbf{m} \left[\nabla \tilde{\mathbf{W}} \cdot \nabla \mathbf{u} - \frac{2}{3} (\nabla \cdot \tilde{\mathbf{W}}) (\nabla \cdot \mathbf{u}) \right] d\Omega = \\
 & - \Delta t q_2^1 \int_{\Omega} \mathbf{m} \left[\tilde{\mathbf{W}} \cdot \nabla (\nabla \cdot \mathbf{u}) + \frac{2}{3} (\nabla \cdot \tilde{\mathbf{W}}) (\nabla \cdot \mathbf{u}) \right] d\Omega \\
 & + \Delta t q_2^1 \int_{\Gamma} \mathbf{m} (\tilde{\mathbf{W}} \cdot \nabla \mathbf{u} \cdot \mathbf{n}) d\Gamma
 \end{aligned} \tag{4.1.46}$$

It can be easily seen from the above equation how, for incompressible flows (i.e. when $\nabla \cdot \mathbf{u} = 0$), the contribution of the terms that are explicitly treated in order to allow the uncoupling reduces to a boundary contribution.

• **The boundary viscous term.** Analogously, the implicit contribution of the boundary viscous term (4.1.34) is given by

$$\Delta t q_2^1 \int_{\Gamma} \tilde{\mathbf{W}} \cdot \mathbf{T}^{n+1} \cdot \mathbf{n} d\Gamma = \Delta t q_2^1 \int_{\Gamma} \mathbf{m} \left[\tilde{\mathbf{W}} \cdot (\mathbf{u} \nabla) \cdot \mathbf{n} + \tilde{\mathbf{W}} \cdot (\nabla \mathbf{u}) \cdot \mathbf{n} - \frac{2}{3} (\tilde{\mathbf{W}} \cdot \mathbf{n}) (\nabla \cdot \mathbf{u}) \right]^{n+1} d\Gamma \tag{4.1.47}$$

where the following approach can be done in order to express this equation in terms of $\tilde{\mathbf{U}}^{n+1}$

$$\begin{aligned} (\mathbf{u}\nabla)^{n+1} &= \left(\frac{\mathbf{U}^{n+1}}{\mathbf{r}^{n+1}} \right) \nabla = \frac{1}{\mathbf{r}^{n+1}} (\mathbf{U}\nabla)^{n+1} - \frac{1}{(\mathbf{r}^{n+1})^2} \mathbf{U}^{n+1} \otimes \nabla \mathbf{r}^{n+1} \\ &\cong \frac{1}{\mathbf{r}^n} (\tilde{\mathbf{U}}\nabla)^{n+1} - \frac{1}{(\mathbf{r}^n)^2} \tilde{\mathbf{U}}^{n+1} \otimes \nabla \mathbf{r}^n \end{aligned} \quad (4.1.48)$$

Again, some splitting error is introduced when the above approach is used to compute the implicit contribution of the boundary viscous term (4.1.47) and only the first term of the RHS allows the uncoupling between components¹. Using the same arguments that in the viscous term one gets

$$\begin{aligned} \Delta t \int_{\Gamma} \tilde{\mathbf{W}} \cdot \mathbf{T}^{n+1} \cdot \mathbf{n} \, d\Gamma &\cong \\ \Delta t \int_{\Gamma} \left[\frac{\mathbf{m}}{\mathbf{r}^n} \tilde{\mathbf{W}} \cdot (\tilde{\mathbf{U}}\nabla)^{n+1} \cdot \mathbf{n} - \frac{\mathbf{m}}{(\mathbf{r}^n)^2} \tilde{\mathbf{W}} \cdot (\tilde{\mathbf{U}}^{n+1} \otimes \nabla \mathbf{r}^n) \cdot \mathbf{n} \right] d\Gamma &+ \\ \Delta t \int_{\Gamma} \mathbf{m} \left[\tilde{\mathbf{W}} \cdot \nabla \mathbf{u}^n \cdot \mathbf{n} - \frac{2}{3} (\tilde{\mathbf{W}} \cdot \mathbf{n}) (\nabla \cdot \mathbf{u})^n \right] d\Gamma & \end{aligned} \quad (4.1.49)$$

when $\mathbf{q}_2^1 = 1$ (that is, when a first order implicit treatment of the boundary viscous term is considered) or

$$\begin{aligned} \Delta t \mathbf{q}_2^1 \int_{\Gamma} \tilde{\mathbf{W}} \cdot \mathbf{T}^{n+1} \cdot \mathbf{n} \, d\Gamma &\cong \\ \Delta t \mathbf{q}_2^1 \int_{\Gamma} \left[\frac{\mathbf{m}}{\mathbf{r}^n} \tilde{\mathbf{W}} \cdot (\tilde{\mathbf{U}}\nabla)^{n+1} \cdot \mathbf{n} - \frac{\mathbf{m}}{(\mathbf{r}^n)^2} \tilde{\mathbf{W}} \cdot (\tilde{\mathbf{U}}^{n+1} \otimes \nabla \mathbf{r}^n) \cdot \mathbf{n} \right] d\Gamma &+ \\ \frac{3}{4} \Delta t \int_{\Gamma} \mathbf{m} \left[\tilde{\mathbf{W}} \cdot \nabla \mathbf{u}^n \cdot \mathbf{n} - \frac{2}{3} (\tilde{\mathbf{W}} \cdot \mathbf{n}) (\nabla \cdot \mathbf{u})^n \right] d\Gamma &- \\ \frac{1}{4} \Delta t \int_{\Gamma} \mathbf{m} \left[\tilde{\mathbf{W}} \cdot \nabla \mathbf{u}^{n-1} \cdot \mathbf{n} - \frac{2}{3} (\tilde{\mathbf{W}} \cdot \mathbf{n}) (\nabla \cdot \mathbf{u})^{n-1} \right] d\Gamma & \end{aligned} \quad (4.1.50)$$

when $\mathbf{q}_2^1 = 1/2$ (that is, when a second order implicit treatment of the boundary viscous term is considered).

¹ As in the viscous term, when $\mathbf{g} = 1$ and the flow is compressible, the substitution of \mathbf{r}^{n+1} should be $\mathbf{r}^{n+1} \rightarrow 3/2\mathbf{r}^n - 1/2\mathbf{r}^{n-1}$ if one wishes to keep the order of the scheme.

• **Boundary Conditions.** The integration by parts in the weak form leads to a boundary integral in which the deviatoric stress tensor \mathbf{T} is contracted with the outward unit normal. In Newtonian fluids, the deviatoric stress tensor is, by definition, proportional to the velocity's first derivatives, so that imposing any value on the boundary integral can be considered as a Neumann boundary condition for the velocity. Usually, both the inflows and the walls are Dirichlet type boundaries for the velocity (momentum), while the outflows are Neumann type boundaries. In consequence, the boundary integral should be prescribed at the outflows. However, if the boundary integral is evaluated with no impositions on the fractional momentum (i.e. computed in all the boundary Γ with no prescriptions), the results are the correct ones [Codina *et al.*, 1998b]. Therefore, no boundary condition is imposed in the weak form of the fractional momentum.

The final expression for the fractional momentum weak form is obtained inserting equations (4.1.38), (4.1.40), (4.1.43) (or (4.1.44)), and (4.1.49) (or (4.1.50)) into (4.1.30). The result is given in the Appendix 4A.

4.1.4.2 Continuity Equation

Multiplying the time discretised continuity equation (4.1.27) by the test function W_p , and integrating over the domain Ω one gets

$$\begin{aligned}
 & \int_{\Omega} W_p \mathbf{r}^{n+1} d\Omega + \Delta t^2 \left(1 + \frac{\mathbf{a}}{\Delta t} \right) \int_{\Omega} \nabla W_p \cdot \nabla p^{n+1} d\Omega - \Delta t^2 \left(1 + \frac{\mathbf{a}}{\Delta t} \right) \int_{\Gamma} W_p \mathbf{n} \cdot \nabla p^{n+1} d\Gamma = \\
 & \int_{\Omega} W_p \mathbf{r}^n d\Omega + \Delta t \int_{\Omega} W_p \hat{\mathbf{u}} \cdot \nabla \mathbf{r}^n d\Omega - \Delta t \int_{\Omega} W_p \nabla \cdot \mathbf{U}^n d\Omega + \\
 & \Delta t \int_{\Omega} \nabla W_p \cdot \Delta \tilde{\mathbf{U}}^n d\Omega - \Delta t \int_{\Gamma} W_p \mathbf{n} \cdot \Delta \tilde{\mathbf{U}}^n d\Gamma + \\
 & \Delta t^2 \mathbf{g} \int_{\Omega} \nabla W_p \cdot \nabla p^n d\Omega - \Delta t^2 \mathbf{g} \int_{\Gamma} W_p \mathbf{n} \cdot \nabla p^n d\Gamma + \\
 & \mathbf{a} \Delta t \int_{\Omega} \nabla W_p \cdot \mathbf{x}^n d\Omega - \mathbf{a} \Delta t \int_{\Gamma} W_p \mathbf{n} \cdot \mathbf{x}^n d\Gamma
 \end{aligned} \tag{4.1.51}$$

where the terms containing second spatial derivatives and the last term of the RHS in equation (4.1.27) have been integrated by parts. If the normal component of the equations (4.1.15) and (4.1.18) is imposed to be verified on the boundary one has

$$\begin{aligned}
 \int_{\Gamma} \mathbf{n} \cdot \Delta \tilde{\mathbf{U}}^n d\Gamma &= \int_{\Gamma} \mathbf{n} \cdot \Delta \mathbf{U}^n d\Gamma + \Delta t \int_{\Gamma} \mathbf{n} \cdot \nabla p^{n+1} d\Gamma - \mathbf{g} \Delta t \int_{\Gamma} \mathbf{n} \cdot \nabla p^n d\Gamma \\
 \int_{\Gamma} \mathbf{n} \cdot \mathbf{x}^n d\Gamma &= \int_{\Gamma} \mathbf{n} \cdot \nabla p^n d\Gamma
 \end{aligned} \tag{4.1.52}$$

Using these identities, the weak form of the continuity equation becomes

$$\begin{aligned}
 & \int_{\Omega} W_p \mathbf{r}^{n+1} d\Omega + \Delta t^2 \left(1 + \frac{\mathbf{a}}{\Delta t} \right) \int_{\Omega} \nabla W_p \cdot \nabla p^{n+1} d\Omega = \\
 & \int_{\Omega} W_p \mathbf{r}^n d\Omega + \Delta t \int_{\Omega} W_p \hat{\mathbf{u}} \cdot \nabla \mathbf{r}^n d\Omega - \Delta t \int_{\Omega} W_p (\nabla \cdot \mathbf{U})^n d\Omega + \Delta t \int_{\Omega} \nabla W_p \cdot \Delta \tilde{\mathbf{U}}^n d\Omega + \\
 & \mathbf{g} \Delta t^2 \int_{\Omega} \nabla W_p \cdot \nabla p^n d\Omega + \mathbf{a} \Delta t \int_{\Omega} \nabla W_p \cdot \xi^n d\Omega - \Delta t \int_{\Gamma} W_p \mathbf{n} \cdot \Delta \mathbf{U}^n d\Gamma
 \end{aligned} \tag{4.1.53}$$

For compressible flows, either the pressure or the density can be considered as unknowns. On the contrary, for incompressible flows, only the pressure can be the unknown of the above equation. In order to have a single algorithm able to deal properly with both kinds of flows, the pressure must be chosen as the adequate unknown. It is important to remark that no shocks are expected and, in consequence, this non-conservative form of the continuity equation can be used. The relationship between pressure and density is then given by the state law and, in consequence, will depend on the kind of flow. To reflect this fact, this weak form can be also expressed as

$$\begin{aligned}
 & \int_{\Omega} W_p A p^{n+1} d\Omega + \Delta t^2 \left(1 + \frac{\mathbf{a}}{\Delta t} \right) \int_{\Omega} \nabla W_p \cdot \nabla p^{n+1} d\Omega = \\
 & \int_{\Omega} W_p B \mathbf{r}^n d\Omega + \Delta t \int_{\Omega} W_p \hat{\mathbf{u}} \cdot \nabla \mathbf{r}^n d\Omega - \Delta t \int_{\Omega} W_p (\nabla \cdot \mathbf{U})^n d\Omega + \Delta t \int_{\Omega} \nabla W_p \cdot \Delta \tilde{\mathbf{U}}^n d\Omega + \\
 & \mathbf{g} \Delta t^2 \int_{\Omega} \nabla W_p \cdot \nabla p^n d\Omega + \mathbf{a} \Delta t \int_{\Omega} \nabla W_p \cdot \xi^n d\Omega - \Delta t \int_{\Gamma} W_p \mathbf{n} \cdot \Delta \mathbf{U}^n d\Gamma
 \end{aligned} \tag{4.1.54}$$

where A and B depend on the state law. The values adopted for the most common flows of interest are reflected in table 4.1.2.

Observation When the state law depends on the temperature (as in the case, for instance, of a perfect gas), the continuity equation is also coupled with the energy equation. To uncouple the equations, the influence of the temperature on the continuity equation can be explicitly considered. The values of A and B assumed in table 4.1.2 reflect this fact. This assumption can be done in weakly coupled problems (or when a “sufficiently small” time step is used) as in the case, for instance, of a perfect gas in the subsonic regime. In strongly coupled problems, an iterative procedure should be used within each time step. This case will not be considered here. Note also that table 4.1.2 contains approximations of $O(\Delta t)$ in order to use pressure as a variable.

Type of flow	State law	A	B
Incompressible	$\mathbf{r} = \text{cte}$	0	0
Slightly incompressible	$\left(\frac{\partial p}{\partial \mathbf{r}}\right)_s = c^2$	$\frac{1}{c^2}$	$\frac{p^n}{c^2 \mathbf{r}^n}$
Barotropic	$p = A \mathbf{r}^g$	$\frac{\mathbf{r}^n}{\mathbf{g} p^n}$	$\frac{1}{\mathbf{g}}$
Perfect gas	$p = \mathbf{r} Q T$	$\frac{1}{Q(2T^n - T^{n-1})}$	1
Magma with volatiles	$\mathbf{r} = \frac{\mathbf{r}_l}{1 + \left(\frac{\mathbf{r}_l Q T}{p}\right) \left(\frac{W - s p^n}{1 - s p^n}\right) \mathbf{q}(p_c - p)}$	$\frac{\mathbf{r}^n}{p^n}$	1

 Table 4.1.2. Adopted values for A and B for the most common state laws.

• Boundary Conditions. In Dirichlet-type contours for the momentum, the boundary integral that appears in (4.1.54) vanishes when the boundary conditions are time independent. However, in the Neumann-type boundaries its contribution should be computed. In this case, the boundary integral couples the equations because involves \mathbf{U}^{n+1} which is not known yet when the continuity equation is solved. In order to avoid the coupling, the contribution of this boundary integral is neglected. It produces localised errors of order Δt during transient calculations or in time dependent stationary states; but, if the steady state is reached, gives the correct solution. The Dirichlet conditions for the pressure are implemented in a standard way in the weak form (4.1.54).

4.1.4.3 Pressure Gradient Projection Equation

Multiplying (4.1.15) by the test function \mathbf{W}_G and integrating over the domain Ω , one obtains

$$\int_{\Omega} \mathbf{W}_G \cdot \mathbf{x}^{n+1} d\Omega = \int_{\Omega} \mathbf{W}_G \cdot \nabla p^{n+1} d\Omega \quad (4.1.55)$$

The above equation allows to uncouple the components, that is, once space discretised leads to a 2 or 3 (space dimension) scalar algebraic systems of equations. No boundary conditions need to be imposed in the weak form (4.1.55).

4.1.4.4 Momentum Equation

Multiplying (4.1.20) by the test function \mathbf{W} , and integrating over the domain Ω leads to

$$\int_{\Omega} \mathbf{W} \cdot \mathbf{U}^{n+1} d\Omega = \int_{\Omega} \mathbf{W} \cdot \tilde{\mathbf{U}}^{n+1} d\Omega - \Delta t \int_{\Omega} \mathbf{W} \cdot \nabla p^{n+1} d\Omega + \mathbf{g} \Delta t \int_{\Omega} \mathbf{W} \cdot \nabla p^n d\Omega \quad (4.1.56)$$

which is also uncoupled. In (4.1.56), all the components of the momentum can be prescribed in a standard way on its Dirichlet-type boundaries.

4.1.4.5 Energy Equation

Multiplying (4.1.14) by the test function W_T , and integrating over the domain Ω leads to

$$\begin{aligned} \int_{\Omega} W_T T^{n+1} d\Omega &= \int_{\Omega} W_T T^n d\Omega + \Delta t \int_{\Omega} W_T [(\hat{\mathbf{u}} - \mathbf{u}) \cdot \nabla T]^{n+q_3} d\Omega - \\ &\Delta t \int_{\Omega} \frac{k}{c_v} \nabla W_T \cdot \left(\frac{1}{\mathbf{r}} \nabla T \right)^{n+q_3} d\Omega + \Delta t \int_{\Omega} \frac{k}{c_v} W_T \left(\frac{1}{\mathbf{r}^2} \nabla \mathbf{r} \cdot \nabla T \right)^{n+q_3} d\Omega + \\ &\Delta t \int_{\Gamma} \frac{k}{c_v} W_T \mathbf{n} \cdot \left(\frac{1}{\mathbf{r}} \nabla T \right)^{n+q_3} d\Gamma + \Delta t \int_{\Omega} \frac{1}{c_v} W_T \left[\frac{1}{\mathbf{r}} \mathbf{S} \cdot \nabla \mathbf{u} \right]^{n+q_3} d\Omega + \\ &\Delta t \int_{\Omega} \frac{1}{c_v} W_T \mathbf{g} \cdot \mathbf{u}^{n+q_3} d\Omega \end{aligned} \quad (4.1.57)$$

where the diffusive term has been integrated by parts. Obviously, if $q_3^1 > 0$ the terms that contain T^{n+1} are implicitly treated. The fully developed expression of the weak form (4.1.57) is also given in the Appendix 4A.

• **Boundary Conditions.** If one assumes that the conduction of heat is given by the Fourier's law, the flux of heat \mathbf{q} appears in the boundary integral of (4.1.57). It allows to impose the Neumann boundary conditions for the temperature by prescribing directly this flux on Γ_D . Dirichlet boundary conditions for temperature are implemented as usual.

4.1.5 Space Discretisation

Once the weak forms of the differential equations are established, one can proceed to discretise the space. In the standard Galerkin formulation, all the test functions $\tilde{\mathbf{W}}$, W_p , \mathbf{W}_G , \mathbf{W} , and W_T of the weak forms (4.1.30), (4.1.54), (4.1.55), (4.1.56) and (4.1.57) are taken to be equal to the shape functions. Once the spatial discretisation has been performed, the equations (now algebraic systems) can be written in a matrix form

$$\mathbf{F} \cdot \tilde{\mathbf{U}}_m^{n+1} = \bar{\mathbf{F}}_m \quad (\text{Fractional momentum equation}) \quad (4.1.58)$$

$$\mathbf{C} \cdot \bar{p}^{n+1} = \bar{\mathbf{C}} \quad (\text{Continuity equation}) \quad (4.1.59)$$

$$\mathbf{M} \cdot \bar{\mathbf{x}}_m^{n+1} = \bar{\mathbf{G}}_m \quad (\text{Pressure gradient projection equation}) \quad (4.1.60)$$

$$\mathbf{M} \cdot \bar{\mathbf{U}}_m^{n+1} = \bar{\mathbf{Q}}_m \quad (\text{Momentum equation}) \quad (4.1.61)$$

$$\mathbf{E} \cdot \bar{T}^{n+1} = \bar{\mathbf{E}} \quad (\text{Energy equation}) \quad (4.1.62)$$

where $\tilde{\mathbf{U}}$, \bar{p} , $\bar{\mathbf{x}}$, $\bar{\mathbf{U}}$ and \bar{T} are the vectors of nodal unknowns. The expressions for all these vectors as well as the matrixes that appear in the above expressions are given in the Appendix 4B.

4.1.6 Methods of Stabilisation

It is well known that the standard Galerkin formulation requires an additional term of stabilisation in convective dominated problems. In the particular case of the Navier-Stokes equations, both the momentum equation (4.1.3) and the energy equation (4.1.5) contain a convective term that could lead to numerical instabilities if the spatial discretisation is done using the standard Galerkin formulation. In consequence, some additional term of stabilisation must be added to the momentum (to the fractional momentum when a fractional step method is used) and to the energy weak forms.

The introduction of artificial numerical diffusion was initially proposed three decades ago in the context of finite difference methods. Since then, many different methods have been proposed. An exhaustive description of these methods is not under the scope of this work, but can be found in [Codina, 1998a]. Five different methods are briefly described in this section: the Streamline Upwind Petrov-Galerkin method (SUPG), the Characteristic Galerkin method (CG),

the Galerkin Leasted-Squares method (GLS), the Taylor-Galerkin method (TG), and the Subgrid Scale method (SGS). Whichever the method employed, the important point is that, when the Galerkin formulation is used in convective dominated flows, the convective term must be stabilised by adding numerical diffusion along the streamlines in a consistent manner.

Consider a general scalar diffusion-convection equation

$$\frac{\partial U}{\partial t} + \mathbf{u} \cdot \nabla U - \nabla \cdot (\mathbf{e} \nabla U) = f \quad \text{in } \Omega \quad (4.1.63)$$

where U is the unknown function, \mathbf{u} is the velocity, \mathbf{e} is the diffusion coefficient, and f is a source term. The diffusion-convection equation (4.1.63) requires both boundary and initial conditions in order to be solved. Although only an scalar equation with homogeneous Dirichlet boundary conditions (i.e. with $U = 0$ on Γ) is considered here for simplicity, the results obtained can be easily generalised to a vectorial case with non-homogeneous boundary conditions. Note that both the momentum equation (4.1.3) and the energy equation (4.1.5) resemble (4.1.63), so that the results drawn in this section can be extrapolated in a straightforward way to these equations by substituting the values of \mathbf{e} and f properly.

The solution of (4.1.63) must belong to the space $L^2(0, T; H_0^1(\Omega))$, where

$$H_0^1(\Omega) \equiv \{f : \Omega \rightarrow \mathbb{R} \mid f, Df \in L^2(\Omega) \text{ and } f = 0 \text{ on } \Gamma\} \quad (4.1.64)$$

that is, for a fixed time $t \in (0, T)$ the function U belongs to $H_0^1(\Omega)$ and its norm (in the space $H_0^1(\Omega)$) is square integrable in time. Equation (4.1.63) can be also expressed as

$$\frac{\partial U}{\partial t} + \mathcal{L}(U) = f \quad (4.1.65)$$

where \mathcal{L} is an operator that can be decomposed in its convective \mathcal{L}_c and diffusive \mathcal{L}_d contributions

$$\mathcal{L}(U) \equiv \mathbf{u} \cdot \nabla U - \nabla \cdot (\mathbf{e} \nabla U) = \mathcal{L}_c(U) + \mathcal{L}_d(U) \quad (4.1.66)$$

Defining the scalar product in the space of functions as usual, the following identities are verified $\forall U, W \in H_0^1(\Omega)$

$$\begin{aligned}
 (W, \mathcal{L}_c(U)) &\equiv \int_{\Omega} W (\mathbf{u} \cdot \nabla U) d\Omega = - \int_{\Omega} U \nabla \cdot (\mathbf{u} W) d\Omega = (U, \mathcal{L}_c^*(W)) \\
 &\Rightarrow \mathcal{L}_c^*(U) = -\nabla \cdot (\mathbf{u} U)
 \end{aligned} \tag{4.1.67}$$

$$\begin{aligned}
 (W, \mathcal{L}_d(U)) &\equiv - \int_{\Omega} W \nabla \cdot (\mathbf{e} \nabla U) d\Omega = - \int_{\Omega} U \nabla \cdot (\mathbf{e} \nabla W) d\Omega = (U, \mathcal{L}_d^*(W)) \\
 &\Rightarrow \mathcal{L}_d^*(U) = \mathcal{L}_d(U)
 \end{aligned} \tag{4.1.68}$$

where \mathcal{L}_c^* and \mathcal{L}_d^* are the adjoint operators of \mathcal{L}_c and \mathcal{L}_d respectively. Note that \mathcal{L}_d is self-adjoint for homogeneous boundary conditions. The adjoint operator of \mathcal{L} is then

$$\mathcal{L}^*(U) = \mathcal{L}_c^*(U) + \mathcal{L}_d^*(U) = -\nabla \cdot (\mathbf{u} U) - \nabla \cdot (\mathbf{e} \nabla U) \tag{4.1.69}$$

All the methods of stabilisation add to the LHS of the standard Galerkin weak form a term like [Codina, 1998a]

$$S(W, U_h) = \sum_{e=1}^{n_e} \int_{\Omega^e} \mathbf{P}(W) \mathbf{t} \mathbf{R}(U_h) d\Omega \tag{4.1.70}$$

where n_e is the number of elements of the finite element mesh, W is the test function, U_h is the approximation to the solution, \mathbf{P} is an operator, \mathbf{t} is an upwind parameter (the intrinsic time), and the operator \mathbf{R} is the residual of the equation, given by

$$\begin{aligned}
 \mathbf{R}_{\text{SUPG}}(U_h) &= \mathbf{R}_{\text{GLS}}(U_h) = \mathbf{R}_{\text{SGS}}(U_h) = \frac{\Delta U_h}{\Delta t} + \mathcal{L}(U_h) - f \\
 \mathbf{R}_{\text{CG}}(U_h) &= \mathbf{R}_{\text{TG}}(U_h) = \mathcal{L}(U_h) - f
 \end{aligned} \tag{4.1.71}$$

The different expressions for \mathbf{R} can be explained from the different starting points: the SUPG, the GLS and the SGS methods were originally proposed to stabilise stationary problems, while the CG and the TG methods were developed in the context of transient problems. Note how the contributions introduced by the CG and the TG methods into the final discretised system do not affect the mass matrix. However, the main differences between the methods as well as its properties come from the different expressions for \mathbf{P} and \mathbf{t} rather than from the above expressions.

Observation The integral of equation (4.1.70) must be understood in the elementwise sense, that is, it is a summation over all the elements of the elemental integrals.

• **The SUPG Method.** (Original idea in the context of the FEM by [Kelly *et al.*, 1980] and [Hughes and Brooks, 1979; Hughes and Brooks, 1982]). The SUPG was the first method of stabilisation applied in the finite element context and, originally, was inspired in the upwind methods used in centred finite differences [von Neumann and Richtmeyer, 1950]. In the modern version of this method, the operator \mathbf{P} is given by

$$\mathbf{P}_{\text{SUPG}}(W) = \mathcal{L}_c(W) \quad (4.1.72)$$

that is, $\mathbf{P}_{\text{SUPG}}(W)$ is the convective operator applied to the test function. Any method of stabilisation must contain, at least, the term \mathcal{L}_c in the operator \mathbf{P} in order to stabilise the convective term. In consequence, the SUPG is, in fact, the simplest method. The intrinsic time \mathbf{t} is usually obtained from the one-dimensional convection-diffusion equation. It can be shown that, in this case, the solution is nodally exact when

$$\mathbf{t}_{\text{SUPG}} = \frac{\mathbf{a} h}{2|\mathbf{u}|} \quad (4.1.73)$$

where h is the element size and \mathbf{a} is the upwind function, given by

$$\mathbf{a} = \coth(P_e) - \frac{1}{P_e} \quad P_e \equiv \frac{|\mathbf{u}|h}{2k} \quad (4.1.74)$$

where P_e is the Péclet number. In the general case, the straightforward extension of (4.1.73) has been traditionally considered, that is, the intrinsic time \mathbf{t}_{SUPG} which gives a one-dimensional nodal exact solution is used for all the cases.

• **The CG Method.** (Original idea in the context of the FEM by [Douglas and Russell, 1982; Pironneau, 1982] and [Lönher *et al.*, 1984]). In the explicit (modern) version of this method, the operator \mathbf{P} is given by

$$\mathbf{P}_{\text{CG}}(W) = -\mathcal{L}_c^*(W) \quad (4.1.75)$$

that is, $\mathbf{P}_{\text{CG}}(W)$ is minus the adjoint of the convective operator applied to the test function. Note from equation (4.1.67) how, in the case of incompressible flows (i.e. with $\nabla \cdot \mathbf{u} = 0$), the CG

method is very similar to the SUPG since then $\mathbf{P}_{\text{SUPG}}(W) = \mathbf{P}_{\text{CG}}(W)$. The main difference between both methods comes then from the different definitions of the intrinsic time \mathbf{t} . In contrast, for compressible flows, the CG method introduces an additional term proportional to $\nabla \cdot \mathbf{u}$. The intrinsic time in the CG method is given by

$$\mathbf{t}_{\text{CG}} = \frac{\Delta t}{2} \quad (4.1.76)$$

where Δt is the time step. Best results are obtained when it is close to the *internal time step* (the maximum time step that ensures the stability of the explicit scheme. See section 4.1.7).

• **The GLS Method.** ([Franca and Stenberg, 1991; Hughes and Franca, 1987; Hughes et al., 1989]). In this method, the operator \mathbf{P} is given by

$$\mathbf{P}_{\text{GLS}}(W) = \mathbf{L}(W) = \mathbf{L}_c(W) + \mathbf{L}_d(W) \quad (4.1.77)$$

that is, $\mathbf{P}_{\text{GLS}}(W)$ is the total operator (the convective plus the diffusive contributions) applied to the test function. The convergence analysis shows that, for the steady problem and using linear elements, the intrinsic time is given by

$$\mathbf{t}_{\text{GLS}} = \min\left(1, \frac{P_e}{3}\right) \frac{h}{2|\mathbf{u}|} \quad (4.1.78)$$

In fact, the above expression is the asymptotic approximation of (4.1.73), so that the intrinsic time in the GLS method is quite similar to that of the SUPG method.

• **The TG Method.** ([Donéa, 1984]). In the modern version of this method, the operator \mathbf{P} is

$$\mathbf{P}_{\text{TG}}(W) = -\mathbf{L}^*(W) \quad (4.1.79)$$

that is, $\mathbf{P}_{\text{TG}}(W)$ is minus the adjoint of the total operator. The intrinsic time \mathbf{t} is in this case the same that in the CG method (4.1.76). In consequence, the TG method can be considered as an extension of the CG method in which the a diffusive contribution has been added to the operator \mathbf{P} .

• **The SGS Method.** ([Hughes, 1995]). Although the departure point is very different, the SGS method resembles very closely to the TG method, being the only difference the expression of

the residual and the intrinsic time. The deduction of the intrinsic time in the SGS is not trivial and involves an integral of the Green's function of the operator \mathbf{L} . However, it is shown [Hughes, 1995] that the expression (4.1.73) is obtained in the one-dimensional case.

Table 4.1.3 summarises the expressions for the operators \mathbf{P} and \mathbf{R} as well as the different intrinsic times for the different stabilisation methods. The results for all the previous methods applied to the weak forms of the fractional momentum (4.1.30) and continuity (4.1.54) equations are shown in the Appendix 4B.

Method	Operator $\mathbf{R}(U_h)$	Operator $\mathbf{P}(W)$	Intrinsic time t
SUPG	$\frac{\Delta U_h}{\Delta t} + \mathbf{L}(U_h) - f$	$\mathbf{L}_c(W)$	$\frac{a h}{2 \mathbf{u} }$
CG	$\mathbf{L}(U_h) - f$	$-\mathbf{L}_c^*(W)$	$\frac{\Delta t}{2}$
GLS	$\frac{\Delta U_h}{\Delta t} + \mathbf{L}(U_h) - f$	$\mathbf{L}(W) = \mathbf{L}_c(W) + \mathbf{L}_d(W)$	$\min\left(1, \frac{P_c}{3}\right) \frac{h}{2 \mathbf{u} }$
TG	$\mathbf{L}(U_h) - f$	$-\mathbf{L}^*(W)$	$\frac{\Delta t}{2}$
SGS	$\frac{\Delta U_h}{\Delta t} + \mathbf{L}(U_h) - f$	$-\mathbf{L}^*(W)$	$\frac{a h}{2 \mathbf{u} }$

Table 4.1.3. Expressions of t , \mathbf{P} and \mathbf{R} for the different stabilisation methods.

4.1.7 Time Step and Stability

In the present algorithm, both the convective and the viscous terms of the momentum equation (4.1.3) and the whole energy equation (4.1.5) can be treated explicitly or implicitly up to second order time-accuracy depending on the values of \bar{q}_1, \bar{q}_2 and \bar{q}_3 respectively. The stability analysis in finite differences shows that any explicit scheme is conditionally stable, that is, there exists a maximum time step able to ensure the stability. In consequence, when any term in the equations is explicitly treated, the time step size can not be arbitrarily large. In the case of the Navier-Stokes equations there is a condition of stability even if a fully implicit scheme is considered because the equations are non-linear and strongly coupled. Moreover, in the algorithm here presented, part of the viscous term is treated explicitly even when $q_2^1 > 0$ in order to uncouple the components of the momentum equation. This uncoupling reduces enormously the computational cost but introduces a more restrictive condition of stability.

In the case of a one-dimensional diffusion-convection equation like (4.1.63), the critical time step Δt_c when linear elements of size h are considered is given by [Hindmarsh, 1984]

$$\Delta t_c = \frac{1}{\frac{4\mathbf{e}}{h^2} + \frac{2|\mathbf{u}|}{h}} \quad (4.1.80)$$

The above expression can be generalised to quadratic elements [Codina *et al.*, 1992a]

$$\Delta t_c = \frac{1}{A \left(\frac{4\mathbf{e}}{h^2} + \frac{2|\mathbf{u}|}{h} \right)} \quad (4.1.81)$$

where $A=1$ for linear elements. For quadratic elements $A=2$ and h is half of the elemental size.

Usually, an extension of the one-dimensional diffusion-convection equation is considered in order to compute the critical time step of the Navier-Stokes equations, that is, the terms of the Navier-Stokes equations are identified with the analogous terms of the one-dimensional diffusion-convection equation. The critical time step is then given by (4.1.81) but multiplied by a safety factor F_s . Thus, when the energy equation (4.1.5) is treated explicitly ($\mathbf{q}_3^1 = 0$) its stability condition is

$$\Delta t \leq \frac{F_s}{A \left(\frac{4k}{c_v \mathbf{r} h^2} + \frac{2|\mathbf{u}|}{h} \right)} \quad (4.1.82)$$

and, analogously, when the momentum equation (4.1.3) is treated explicitly (with $\mathbf{q}_1^1 = \mathbf{q}_2^1 = 0$) one has

$$\Delta t \leq \frac{F_s}{A \left(\frac{4\mathbf{m}}{\mathbf{r} h^2} + \frac{2|\mathbf{u}|}{h} \right)} \quad (4.1.83)$$

The maximum time step able to ensure the stability in the fully explicit case is then the minimum value between (4.1.82) and (4.1.83). In practise, the time step size is always computed as in the fully explicit case. However, safety factors greater than 1 can be used when some terms are implicitly treated. Table 4.1.4 summarises some properties of the algorithm depending on the values of $\bar{\mathbf{q}}_1, \bar{\mathbf{q}}_2, \bar{\mathbf{q}}_3, \mathbf{g}, \mathbf{a}, A$ and B .

Parameter	Effect	Possible values	Observations
\bar{q}_1	Controls the treatment of the convective and moveable mesh terms in the fractional momentum equation (4.1.30)	(0, 1, 0) Explicit $O(\Delta t)$. (0, 3/2, -1/2) Explicit $O(\Delta t^2)$. (1, 0, 0) Implicit $O(\Delta t)$. (1/2, 1/2, 0) Implicit $O(\Delta t^2)$.	<ul style="list-style-type: none"> • If $\theta_1^1 > 0$ (Implicit treatment of the convective term) : <ul style="list-style-type: none"> ↓ Non-linearity. Depending on the solution the error is $O(\Delta t)$ or $O(\Delta t^2)$. See (4.1.35) and observation. ↓ Splitting error. Can be corrected up to $O(\Delta t^2)$. See (4.1.38). ↑ More stability ($F_s > 1$). • If $\theta_1^1 = 0$ (Explicit treatment of the convective term) : <ul style="list-style-type: none"> ↑ Linearity. No splitting error. ↓ Less stability ($F_s < 1$).
\bar{q}_2	Controls the treatment of the viscous term in the fractional momentum equation (4.1.30)	(0, 1, 0) Explicit $O(\Delta t)$. (0, 3/2, -1/2) Explicit $O(\Delta t^2)$. (1, 0, 0) Implicit $O(\Delta t)$. (1/2, 1/2, 0) Implicit $O(\Delta t^2)$.	<ul style="list-style-type: none"> • If $\theta_2^1 > 0$ (Implicit treatment of the viscous term) : <ul style="list-style-type: none"> ↓ Splitting error. If $\gamma = 1$ the error is $O(\Delta t^2)$. If $\gamma = 0$ the error is $O(\Delta t)$. See (4.1.42) and observation. ↓ Coupling of components. Uncoupling does not affect the order of the scheme but reduces its stability since some terms are treated explicitly. For incompressible flows, these terms are just a boundary contribution. See (4.1.46). ↑ More stability ($F_s > 1$). • If $\theta_2^1 = 0$ (Explicit treatment of the viscous term) : <ul style="list-style-type: none"> ↑ No splitting error. No coupling of components. ↓ Less stability ($F_s < 1$).
\bar{q}_3	Controls the treatment of all the terms in the energy equation (4.1.57)	(0, 1, 0) Explicit $O(\Delta t)$. (0, 3/2, -1/2) Explicit $O(\Delta t^2)$. (1, 0, 0) Implicit $O(\Delta t)$. (1/2, 1/2, 0) Implicit $O(\Delta t^2)$.	<ul style="list-style-type: none"> • If $\theta_3^1 > 0$ (Implicit treatment) : <ul style="list-style-type: none"> ↓ Solution of an algebraic system. ↑ More stability ($F_s > 1$). • If $\theta_3^1 = 0$ (Explicit treatment) : <ul style="list-style-type: none"> ↑ If the lumped mass matrix is used it is not necessary to solve any algebraic system. ↓ Less stability ($F_s < 1$).
g	Treatment of the pressure gradient in the fractional momentum equation (4.1.30)	$\gamma = 0, 1$	<ul style="list-style-type: none"> • If $\gamma = 1$ (Incremental fractional step method) : <ul style="list-style-type: none"> ↑ If $\theta_1^1 > 0$ reduces the splitting error of the convective and viscous terms without adding any additional correction. ↓ Additional terms appear in the continuity and momentum equations. See (4.1.54) and (4.1.56). Poor stability if $\alpha = 0$ • If $\gamma = 0$ (Total fractional step method) : <ul style="list-style-type: none"> ↓ If $\theta_1^1 > 0$ additional terms must be added to correct the splitting error of the convective term. See (4.1.38). ↓ Splitting error of order $O(\Delta t)$ for pressure remains in the viscous term. ↑ No additional terms appear in continuity and momentum equations. See (4.1.54) and (4.1.56). More stability if $\alpha = 0$
a	Modification of the continuity equation (4.1.16)	$\alpha = 0$ $\alpha = \Delta t_c$ (Best value)	<ul style="list-style-type: none"> • If $\alpha \neq 0$ ($= \Delta t_c$) (With pressure gradient projection) <ul style="list-style-type: none"> ↓ Adds a new equation to the system. ↑ Additional stabilising effect of the pressure field. This is strongly recommended if $\gamma = 1$. • If $\alpha = 0$ (Without pressure gradient projection) <ul style="list-style-type: none"> ↑ No additional equation to the system. ↓ No additional stabilising effect. However, equal interpolation spaces for pressure and velocity fields can be also used.
A and B	Allow to solve continuity the equation (4.1.16) in terms of p	Depend on the state law. See table 4.1.2	<ul style="list-style-type: none"> ↑ The algorithm can be used to solve simultaneously compressible and incompressible flows. ↓ Depending on the state law approximations of $O(\Delta t)$ are required to solve in terms of pressure.

Table 4.1.4. Characteristics of the algorithm depending on the values of the parameters. The symbols \uparrow and \downarrow indicate, respectively, advantages and inconveniences.

4.2 The Convective Transport Equation

In some problems, the Navier-Stokes equations must be solved together with the convective transport equation. This is the case, for instance, of the mould filling simulations solved by means of the pseudo-concentration method. In the frame of the present work, the convective transport equation is required to simulate chemically heterogeneous magma chambers (with two different magmas) as well as magmas with a variable volatile content. Whichever the case, the important point is that, in all these problems, the state law depends on a property that is transported by means of convection, that is, the values of this variable depend on the velocity field. The consequence is that one must add a new equation which is coupled with the Navier-Stokes ones. In this section, an algorithm to numerically solve the ALE convective transport equation using a Finite Element Method is presented.

Consider the ALE convective transport equation

$$\frac{\partial C}{\partial t} + (\mathbf{u} - \hat{\mathbf{u}}) \cdot \nabla C = 0 \quad (4.2.1)$$

where \mathbf{u} and $\hat{\mathbf{u}}$ are, respectively, the velocity of the particles and the ALE mesh velocity and C is a scalar function. This equation, complemented with adequate boundary and initial conditions, is solved in $\Omega(t) \times (0, T)$ where t designates time and $\Omega(t) \subset \mathbb{R}^n$ ($n = 2, 3$). In the context of this work, the physical meaning of C will always be a mass fraction (a volatile mass fraction or a component mass fraction, depending on the simulation considered) and, in consequence, its values will be constrained to range in $[0, 1]$. However, the procedure herein developed to solve the equation is, obviously, of general applicability to any arbitrary function $f \in L^2(0, T; L^2(\Omega))$.

Firstly, equation (4.2.1) is discretised in time using the trapezoidal rule

$$\frac{\Delta C^n}{\Delta t} + (\mathbf{u}^{n+q_c} - \hat{\mathbf{u}}) \cdot \nabla C^{n+q_c} = 0 \quad (4.2.2)$$

where, as in the case of the Navier-Stokes equations, $\Delta C^n \equiv C^{n+1} - C^n$ and $q_c \in [0, 1]$. Depending on its value the resulting scheme will be of first/second order and implicit/explicit.

4.2 The Convective Transport Equation

Observation Again, it is assumed that the mesh velocity $\hat{\mathbf{u}}$ is a given function. Its time discretisation for those problems where $\hat{\mathbf{u}} \neq \mathbf{0}$ (for fluid-structure interaction problems) is discussed later, in section 4.3.

Once the equation is time discretised, the weak form is obtained projecting onto the usual space of test functions and integrating over the domain Ω

$$\int_{\Omega} W_c \left(\frac{\Delta C^n}{\Delta t} + (\mathbf{u}^{n+q_c} - \hat{\mathbf{u}}) \cdot \nabla C^{n+q_c} \right) d\Omega = 0 \quad (4.2.3)$$

or, more explicitly

$$\begin{aligned} \int_{\Omega} W_c C^{n+1} d\Omega + \Delta t \mathbf{q}_c \int_{\Omega} W_c (\mathbf{u}^{n+1} - \hat{\mathbf{u}}) \cdot \nabla C^{n+1} d\Omega = \\ \int_{\Omega} W_c C^n d\Omega - \Delta t (1 - \mathbf{q}_c) \int_{\Omega} W_c (\mathbf{u}^n - \hat{\mathbf{u}}) \cdot \nabla C^n d\Omega \end{aligned} \quad (4.2.4)$$

If the weak form is now space discretised (the standard Galerkin formulation is assumed) one obtains the final algebraic system

$$\mathbf{T} \cdot \bar{\mathbf{c}}^{n+1} = \bar{\mathbf{T}} \quad (4.2.5)$$

where $\bar{\mathbf{c}}$ is the vector of nodal unknowns. The resulting expressions for the matrix \mathbf{T} and the vector $\bar{\mathbf{T}}$ is given in the Appendix 4B.

Observation In fluid-structure interaction problems one has $\Omega = \Omega(t)$, that is, the spatial domain is time dependent. Section 4.3 discusses in which spatial configuration is “more adequate” to consider the weak form (to evaluate the resulting spatial integrals).

Since equation (4.2.1) contains a convective term, the use of the Galerkin formulation requires an additional stabilisation term in convective dominated flows. The different methods of stabilisation have been explained in section 4.1.6. The particularisation of these methods to the case of the convective transport equation is trivial and straightforward. The final result is also shown in Appendix 4B.

Observation In the convective transport equation one has $\mathbf{L}_d = 0$, so that $\mathbf{L} = \mathbf{L}_c = \mathbf{u} \cdot \nabla$. In consequence (see table 4.1.3) the SUPG method practically coincides with the GLS method (the

only -minimum- difference is the definition of the intrinsic time). Analogously, the CG and the TG methods are exactly the same.

Observation The explicit versions of the method are conditionally stable. The critical time step (extrapolated from the one-dimensional case) is

$$\Delta t_c = \frac{1}{A \frac{2|\mathbf{u}|}{h}} \quad (4.2.6)$$

where, for linear elements, h is the elemental size and $A = 1$ (for quadratic elements $A = 2$ and h is half the elemental size). This critical time step is always larger than that of the Navier-Stokes equations, so that the resolution of convective transport equation should not produce any stability problem to the final global scheme. However, in order to uncouple the effect of the convective transport equation on the Navier-Stokes equations, this equation is solved at the end of each time step (i.e. when \mathbf{u}^n and \mathbf{u}^{n+1} are already known). Obviously, this will produce a time lag because the evaluation of \mathbf{r}^{n+1} by means of the state law is done using C^n instead of the adequate value C^{n+1} . Note that the validity of this procedure (i.e. its influence on the stability and accuracy of the global scheme) depends on the time step size considered¹.

¹ In fact, other procedures such as the approximations to uncouple components in the fractional momentum equation or the evaluation of the state law in terms of T^{n+1} induce also a time lag in the Navier-Stokes equations.

4.3 Fluid-Structure Interaction

4.3.1 Introduction and General Procedure

In fluid-structure interaction problems, the position of the structure determines some boundaries of the fluid and, in turn, some properties of the flow (such as pressure or stress) act as boundary conditions that partially affect the structural response, thus resulting an intimately coupled problem. In many practical applications, some of the fluid boundaries undergo a motion with large amplitude making thus necessary to solve the flow equations on a deforming grid. As explained in the previous section, the flow equations have been written using an ALE formulation in order to account for this dynamic mesh. Other possibilities could be also considered in order to solve the flow equations on a deforming mesh, among which the co-rotational approach [Farhat and Lin, 1990; Farhat and Lin, 1993; Kandil and Chuang, 1988] or the space-time formulation [Tezduyar et al., 1992a; Masud, 1993; Masud and Hughes, 1997] (among many others) should be mentioned.

The general equations to solve are

$$\begin{aligned} \frac{\partial \mathbf{V}}{\partial t} + \nabla \cdot \mathbf{F}^C(\mathbf{V}) + \nabla \cdot \mathbf{F}^D(\mathbf{V}) - \hat{\mathbf{u}} \cdot \nabla \mathbf{V} &= 0 \\ M \ddot{\mathbf{d}} &= \mathbf{f}^{\text{int}}(\mathbf{d}, \dot{\mathbf{d}}) + \mathbf{f}^{\text{ext}}(\mathbf{V}) \end{aligned} \quad (4.3.1)$$

where t designates time, \mathbf{V} is the fluid state vector, $\hat{\mathbf{u}}$ is the dynamic mesh velocity, \mathbf{F}^C and \mathbf{F}^D are the vectors of convective and the diffusive ALE fluxes, \mathbf{d} is the vector of structural displacement, M is the mass of the structure and \mathbf{f}^{int} and \mathbf{f}^{ext} are, respectively, the internal and the external vectors of forces in the structure. The first of the above equations describes the behaviour of a fluid when is complemented with a constitutive equation, a state law and a criteria for the arbitrary ALE mesh velocity. Its properties and its solution via a FEM have been widely discussed in section 4.1. The second equation is that of a rigid solid. We will constrain the fluid-structure interaction problems to the case of a rigid solid but, nevertheless, the procedure herein exposed to solve the problem is of general applicability and can be straightforwardly particularised to any other structural behaviour without loss of generality. The above equations are intimately coupled by the fact that the velocity field of the structure and that of the fluid must be compatible at the fluid-structure interface Γ_{FS} , that is

$$\dot{\mathbf{d}}(t) = \mathbf{u}(t) \quad \text{on } \Gamma_{FS}(t) \quad (4.3.2)$$

where \mathbf{u} is the velocity of the fluid and $\dot{\mathbf{d}}$ that of the structure. For inviscid fluids, this classical non-slip condition can be replaced by the slip boundary condition

$$\dot{\mathbf{d}}(t) \cdot \mathbf{n}(t) = \mathbf{u}(t) \cdot \mathbf{n}(t) \quad \text{on } \Gamma_{FS}(t) \quad (4.3.3)$$

that is, in this case, the compatibility affects only to the normal component of the velocity fields. Whichever the case, the above equations reflect the fact that the position of the structure determines some boundaries of the fluid. In turn, as reflected in equation (4.3.1), the state of the fluid contributes to the external forces term that act over the structure by means of

$$\mathbf{f}_{FS}^{\text{ext}} = \oint_{\Gamma_{FS}} [p \mathbf{n} - \mathbf{T} \cdot \mathbf{n}] d\Gamma \quad (4.3.4)$$

where p is the pressure, \mathbf{T} is the deviatoric stress tensor and $\mathbf{f}_{FS}^{\text{ext}}$ is the contribution of the fluid-structure interaction to the external structural forces. Moreover, the structure and the dynamic ALE mesh are coupled by means of

$$\begin{aligned} \mathbf{d}(t) &= \mathbf{x}(t) \\ \dot{\mathbf{d}}(t) &= \dot{\mathbf{x}}(t) = \hat{\mathbf{u}}(t) \end{aligned} \quad \text{on } \Gamma_{FS} \quad (4.3.5)$$

where \mathbf{x} are the (spatial) coordinates of the mesh. The second condition in the above expression is imposed because a discontinuity between the velocity of the structure and that of the fluid mesh at the fluid-structure interface can perturb the energy exchange between the fluid and the structure. In summary, equations (4.3.2) to (4.3.5) must be taken into account when solving the system (4.3.1). This will impose some constraints on both the fluid-structure integrators and on the ALE mesh velocity.

In order to compute the fluid-structure interaction, the governing equations of the structure and the fluid should be solved simultaneously. Examples of implicit fully coupled algorithms applied to aeroelastic computations can be found, for instance, in [Alonso and Jameson, 1994; Melville et al., 1994; Morton et al., 1997]. Nevertheless, the solution of the coupled problem via a monolithic scheme is an expensive procedure and presents computational drawbacks since every component of the coupled problem has its own mathematical and numerical properties as well as its own software implementation requirements. An alternative

procedure is to use a *partitioned or staggered algorithm* in which the fluid and the structural equations are alternately integrated in time (in a sequential or parallel fashion) by using separate solvers. The interaction is then taken into account by means of the boundary conditions. This approach offers several computational advantages such as the solution of every problem within each own discipline, the preservation of software modularity or the simplification of the codes. Its major drawback is the inherent time lag between the integration of the fluid and the integration of the structure. If time steps are small the influence of this time lag can be neglected. However, this undesirable effect can be partially correct introducing some predictor/corrector iterations within each global cycle of the staggered scheme. In this case, the partitioned procedure becomes intimately coupled and its results tend to converge to those of the monolithic scheme as the number of iterations increases. The staggered method was firstly introduced by [Park *et al.*, 1977] and has been widely employed in many different fluid-structure interaction problems, specially in aeroelastic computations. Thus, for instance, [Rausch *et al.*, 1989; Farhat and Lin, 1993; Blom and Leyland, 1997] used this method to study the flutter of airfoils and [He, 1994] considered the cascade flutter problem. Other examples in aeroelasticity can be found in [Belytschko *et al.*, 1985; Farhat *et al.*, 1991; Farhat *et al.*, 1995; Piperno *et al.*, 1995; Farhat *et al.*, 1998] among many others.

The general procedure for the staggered method herein proposed is illustrated in figure 4.3.1. Given the fluid-structure states at $t = t^n$, the idea is to solve the next time step of the coupled system as follows

- ❶ Solve the structural equations to estimate the position of the structure (i.e. the domain of the fluid) at t^{n+1} .
- ❷ Transfer the motion of the boundary of the structure to the fluid dynamic mesh imposing the first condition of equation (4.3.5).
- ❸ Use the quasi-Laplacian method to compute the position of the ALE fluid mesh at t^{n+1} .
- ❹ Check if there is an unacceptable mesh distortion. In case of critical distortion perform a remeshing, transmit the nodal variables to the new mesh and go again to step ❶.
- ❺ Determine the mesh velocity $\hat{\mathbf{u}}$ and the boundary conditions at the fluid-structure interface in a manner compatible with the constrains imposed by equations (4.3.2), (4.3.3) and (4.3.5).
- ❻ Solve the equations of the fluid (and, if required, the convective transport equation) and compute the forces over the structure at t^{n+1} by means of equation (4.3.4). As previously stated, in problems with a high degree of coupling it can be necessary to introduce a predictor/corrector procedure. If this is the case, go again to step ❶ and repeat the procedure until the required convergence is achieved.

The algorithms proposed to solve the fluid and the convective transport equations (step ⑥) have been introduced and widely explained previously, in sections 4.1 and 4.2. The rest of steps will be explicitly discussed in the present section. Note also that the staggered procedure does not depend neither on the structural behaviour nor on the fluid solver. Thus, if one considers a structural behaviour different to that of the rigid solid (e.g. elastic, viscoelastic or whatever) the only change is the way to solve step ① but the rest of the procedure keeps unaltered. Analogously, if one wants to implement any other fluid solver it is sufficient to modify the solution of step ⑥. This is one of the major goals of the staggered procedure since keeps the simplicity, portability and modularity of the codes in the fluid-structure interaction problems.

4.3.2 A Structural Integrator for the Rigid Solid

The governing equations of the rigid solid are nothing but the general principles of linear and angular momentum. We will focus only on the equations that govern translation since the rotation of the rigid solid will not appear or will be negligible in all the fluid-structure interaction problems under consideration along the present work. The inclusion of rotational degrees of freedom does not affect substantially any of the procedures developed along this section. The reader is referred to [Childs and Reddy, 1999] for an extensive description of the solution of the fluid-structure interaction problems with both rotational and translational degrees of freedom in the rigid solid. The movement of the structure is then determined only by the well-known Newton's second law

$$M \ddot{\mathbf{d}} = \mathbf{f}^{\text{ext}} = \mathbf{f}_{\text{FS}}^{\text{ext}} + \mathbf{b} \quad (4.3.6)$$

where \mathbf{b} are the body forces per unit of mass and $\mathbf{f}_{\text{FS}}^{\text{ext}}$ is given by equation (4.3.4). Note that the above expression is nothing but a particular case of the more general structural behaviour defined in the equation (4.3.1). The structural equations (4.3.6) can be easily integrated in time to determine the position and velocity of the structure using, for instance, any Runge-Kutta method. However, it should be pointed out that in the fluid-structure interaction problems the order of the approximation is also limited by the fluid temporal integrator. In particular, for the algorithm proposed here to integrate in time the Navier-Stokes equations (see section 4.1) the approximation is, in the most favourable case, of order $O(\Delta t^2)$ and, moreover, the non-linearity of the convective term and the constitutive law(s) limit the critical time step able to ensure the stability of the scheme. In consequence, and for our general purposes, it is sufficient to consider

a simple lower-order structural integrator such as the constant average acceleration method [Blom, 1998] which is the optimal case of the Newmark method.

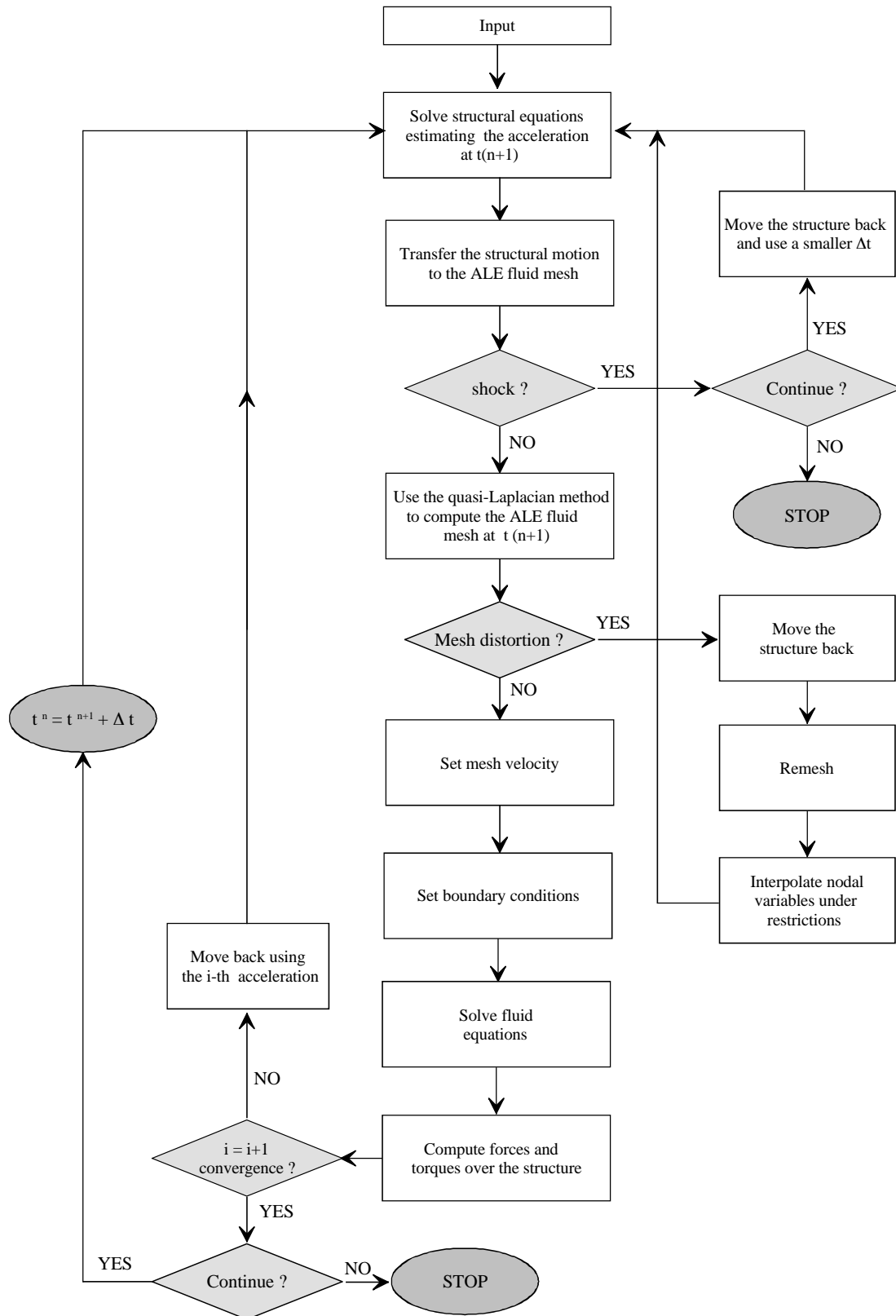


Figure 4.3.1. Cartoon showing the general procedure of the staggered algorithm.

The *constant average acceleration method* works as follows. Let \mathbf{d}^n , $\dot{\mathbf{d}}^n$, $\ddot{\mathbf{d}}^n$ and $\ddot{\mathbf{d}}^{n+1}$ be the given position, velocity and accelerations of the structure at the time instants $t = t^n$ and $t = t^{n+1}$ respectively. The objective is to find its position and velocity at $t = t^{n+1}$ assuming that

$$\begin{aligned}\dot{\mathbf{d}}^{n+1} &= \dot{\mathbf{d}}^n + \frac{\Delta t}{2} (\ddot{\mathbf{d}}^n + \ddot{\mathbf{d}}^{n+1}) \\ \mathbf{d}^{n+1} &= \mathbf{d}^n + \Delta t \dot{\mathbf{d}}^n + \frac{\Delta t^2}{4} (\ddot{\mathbf{d}}^n + \ddot{\mathbf{d}}^{n+1})\end{aligned}\quad (4.3.7)$$

where $\Delta t = t^{n+1} - t^n$. Rearranging terms one can easily obtain

$$\begin{aligned}\frac{4}{\Delta t^2} \mathbf{d}^{n+1} &= \frac{4}{\Delta t^2} \mathbf{d}^n + \frac{4}{\Delta t} \dot{\mathbf{d}}^n + \ddot{\mathbf{d}}^{n+1} + \ddot{\mathbf{d}}^n \\ -\frac{2}{\Delta t} \mathbf{d}^{n+1} + \dot{\mathbf{d}}^{n+1} &= -\frac{2}{\Delta t} \mathbf{d}^n - \dot{\mathbf{d}}^n\end{aligned}\quad (4.3.8)$$

or, in a matrix form

$$\begin{bmatrix} \frac{4}{\Delta t^2} \mathbf{I} & \mathbf{0} \\ -\frac{2}{\Delta t} \mathbf{I} & \mathbf{I} \end{bmatrix} \begin{bmatrix} \mathbf{d}^{n+1} \\ \dot{\mathbf{d}}^{n+1} \end{bmatrix} = \begin{bmatrix} \frac{4}{\Delta t^2} \mathbf{I} & \frac{4}{\Delta t} \mathbf{I} \\ -\frac{2}{\Delta t} \mathbf{I} & -\mathbf{I} \end{bmatrix} \begin{bmatrix} \mathbf{d}^n \\ \dot{\mathbf{d}}^n \end{bmatrix} + \begin{bmatrix} \ddot{\mathbf{d}}^{n+1} + \ddot{\mathbf{d}}^n \\ \mathbf{0} \end{bmatrix}\quad (4.3.9)$$

where \mathbf{I} is the identity matrix. The solution of (4.3.9) is trivial and allows to integrate the rigid solid equations in time. Once \mathbf{d}^{n+1} has been obtained, the continuity between the displacements of the structure and the ALE dynamic mesh (equation (4.3.5)) can be directly imposed setting $\mathbf{x} = \mathbf{d} \equiv \bar{\mathbf{x}}$ on Γ_{FS} .

Observation The solution of (4.3.6) by means of the average acceleration method (4.3.9) assumes that $\ddot{\mathbf{d}}^{n+1}$ (acceleration at $t = t^{n+1}$) is known, i.e. that $\mathbf{f}_{FS}^{\text{ext}}$ is known at $t = t^{n+1}$. However, note that in the case of the fluid-structure interaction problems this value is unknown. In consequence, it is necessary to do some structural prediction based, for instance, on some extrapolation from previous values of the acceleration. As previously discussed, if some predictor/corrector iterations are considered within each cycle of the staggered scheme, the prediction of $\ddot{\mathbf{d}}^{n+1}$ is successively refined and the results tend converge to those of the monolithic schemes.

Observation If $\ddot{\mathbf{d}}^{n+1}$ is exactly predicted, the constant average acceleration method would be unconditionally stable. However, the structural prediction imposes some critical time step on the stability of the scheme. The critical time step that ensures the stability of the global staggered scheme will be then the minimum between the structural and the fluid critical time steps.

In some problems such as, for instance, that of a rigid solid immersed in a fluid, it can be necessary to determine if the structure shocks against the walls of the fluid during the interval (t^n, t^{n+1}) under current consideration. This is verified at this stage of the staggered algorithm. The procedure employed for this purpose is to construct a fixed background mesh and check whether the points of the structure belong to some element of the background mesh or not. If some do, the problem is stopped. The associated computational cost will obviously depend on the number of elements of this fixed background mesh which, in principle, can be as coarse as desired (in fact in many practical applications is reduced to just one element) because it is only used to define the contour. Only problems with complex curved geometries will require a background mesh with an appreciable number of elements but, even in this case, the added relative time of CPU is not significantly high.

4.3.3 The Quasi-Laplacian Method

The solution of the fluid-structure interaction problem by means of an ALE formulation requires to compute the “arbitrary” fluid mesh movement at every time step. A common procedure for this purpose is to consider the ALE dynamic mesh as a discrete pseudo structural system in which the motion of the nodes is governed by structural equations (e.g. by the equations of linear elasticity) where the boundary conditions are given by the motion at the fluid-structure interface. This technique has been applied to many different problems with spatial domain variations such as, for instance, phase changes [Lynch, 1982], free surface problems [Tezduyar et al., 1992b; Johnson and Tezduyar, 1994] or fluid-structure interaction in both space-time [Tezduyar et al., 1992a; Aliabadi and Tezduyar, 1993] and ALE [Batina, 1989; Lesoinne and Farhat, 1993; Farhat et al., 1998] formulations. In general, these structural equations that govern the moving fluid grid can contain a fictitious mass, damping and stiffness matrices. A particular case is the Laplacian method, originally introduced as a mesh smoothing technique, in which neither the fictitious mass nor the damping terms are considered and, therefore, only a Laplacian term remains in the equations. Note that, as the ALE mesh movement is only limited by the equation (4.3.5), any field compatible with this constrain is, in principle, admissible. The Laplacian method has, however, an important drawback because in some domains can not prevent the inversion of the smaller elements of the mesh. In the present work, we use a

variation of the Laplacian method originally proposed by [Masud and Hughes, 1997] that not only conserves its main advantages but is also applicable to arbitrarily shaped domains and prevents the element inversion. In the context of this thesis, this method will be referred to the *quasi-Laplacian method*.

Let $\Omega \subset \mathbb{R}^n$ ($n=2,3$) be the spatial fluid domain at $t = t^n$ and $\Gamma = \Gamma_{FS} \cup \Gamma_0$ ($\Gamma_{FS} \cap \Gamma_0 = \emptyset$) its boundary, where Γ_{FS} is the fluid-structure interface (see figure 4.3.2). Given $\bar{\mathbf{x}}$, the prescribed ALE mesh displacements at Γ_{FS} , the displacement field of the fluid mesh $\hat{\mathbf{x}}$ during $t \in (t^n, t^{n+1})$ is determined solving

$$\left. \begin{aligned} \nabla \cdot [(1 + \mathbf{x}) \nabla \hat{\mathbf{x}}] &= \mathbf{0} && \text{in } \Omega \\ \hat{\mathbf{x}} &= \bar{\mathbf{x}} && \text{on } \Gamma_{FS} \\ \hat{\mathbf{x}} &= \mathbf{0} && \text{on } \Gamma_0 \end{aligned} \right\} \quad (4.3.10)$$

where \mathbf{x} is a bounded, non-dimensional function designed to prevent the element inversion. The above equation is numerically solved using a Finite Element Method. Following [Masud and Hughes, 1997] the function \mathbf{x} is defined for each element of the FEM mesh as

$$\mathbf{x}^e \equiv \frac{1 - A_{min}^e / A_{max}^e}{A^e / A_{max}^e} \quad (4.3.11)$$

where A_{min}^e and A_{max}^e are, respectively, the minimum and the maximum elemental areas (volumes) of the ALE mesh, and A^e is the area (volume) of the element under consideration.

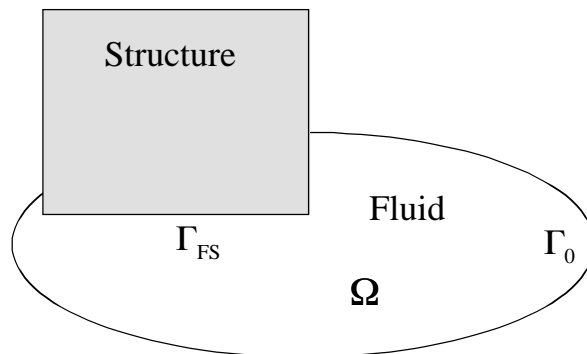


Figure 4.3.2. A fluid comprised in a domain Ω interacts with an structure. The boundary of this domain is $\Gamma = \Gamma_{FS} \cup \Gamma_0$ where Γ_{FS} is the fluid-structure interface and Γ_0 is its complementary.

The solution of equation (4.3.10) allows us to determine the fluid mesh displacement at every time step adding, as a computational cost, the solution of a linear system of algebraic equations. The variational weak form of (4.3.10) can be expressed as: find $\hat{\mathbf{x}} \in H^1(\Omega)^n$ such that

$$\int_{\Omega} (1 + \mathbf{x}) \nabla \mathbf{W}_x : \nabla \hat{\mathbf{x}} \, d\Omega = 0 \quad \forall \mathbf{W}_x \in H_0^1(\Omega)^n \quad (4.3.12)$$

Note that the above expression has been integrated by parts using the fact that the test functions \mathbf{W}_x vanish on the Dirichlet part of the boundary $\Gamma_D = \Gamma$. If the space is discretised by means of the standard Galerkin formulation (i.e. taking the test functions equal to the shape functions), the above expression reduces to a linear, symmetric and well-conditioned system of algebraic equations

$$\mathbf{K} \bar{\mathbf{x}} = 0 \quad (4.3.13)$$

where $\bar{\mathbf{x}}$ is the vector of nodal displacements. The Cartesian components of the matrix \mathbf{K} are given by

$$\mathbf{K}_{lk} = \sum_{e=1}^{ne} \int_{\Omega^e} \frac{\partial N^l}{\partial x^a} (1 + \mathbf{x}^e) \frac{\partial N^k}{\partial x^a} \, d\Omega \quad l, k = 1 \dots nnode \quad (4.3.14)$$

where $nnode$ and ne are, respectively, the elemental number of nodes and the number of elements of the ALE FEM mesh, N^i is the shape function associated with the i -th node of the mesh and \mathbf{x}^e is given by equation (4.3.11). Note also that the different spatial dimensions are uncoupled and, in consequence, it is only necessary to solve a symmetric system of $nnode \times nnode$ d.o.f. for each spatial dimension considered.

Observation For a uniform mesh (i.e. when $A_{min}^e = A_{max}^e = A^e$) it can be observed from equations (4.3.11) and (4.3.10) that the Laplacian method is recovered because $\mathbf{x}^e = 0 \, \forall e$. On the contrary, the smaller elements translate with less distortion while the larger ones absorb the motion. This prevents from element inversion and, moreover, keeps the shape and the proportion of the elements in the refined zones such as, for instance, the boundary layers.

Figure 4.3.3 illustrates the differences between the Laplacian and the quasi-Laplacian methods. A squared domain with an unstructured mesh refined through the edges is deformed

by displacing its upper edge by a certain amount. This could simulate, for instance, a structural effect. The induced mesh displacement is computed using both the Laplacian and the quasi-Laplacian methods. As shown in the figure, the quasi-Laplacian method produces a mesh of better quality and with much less distortion than that of the Laplacian method. This is an important point because despite the computational cost of both methods is nearly the same (they only differ in the computation of \mathbf{x}^e by means of equation (4.3.10)) the frequency of the remeshings (associated with the mesh distortion) is not. Since remeshing is a time consuming undesirable effect, the choice between both methods is clear.

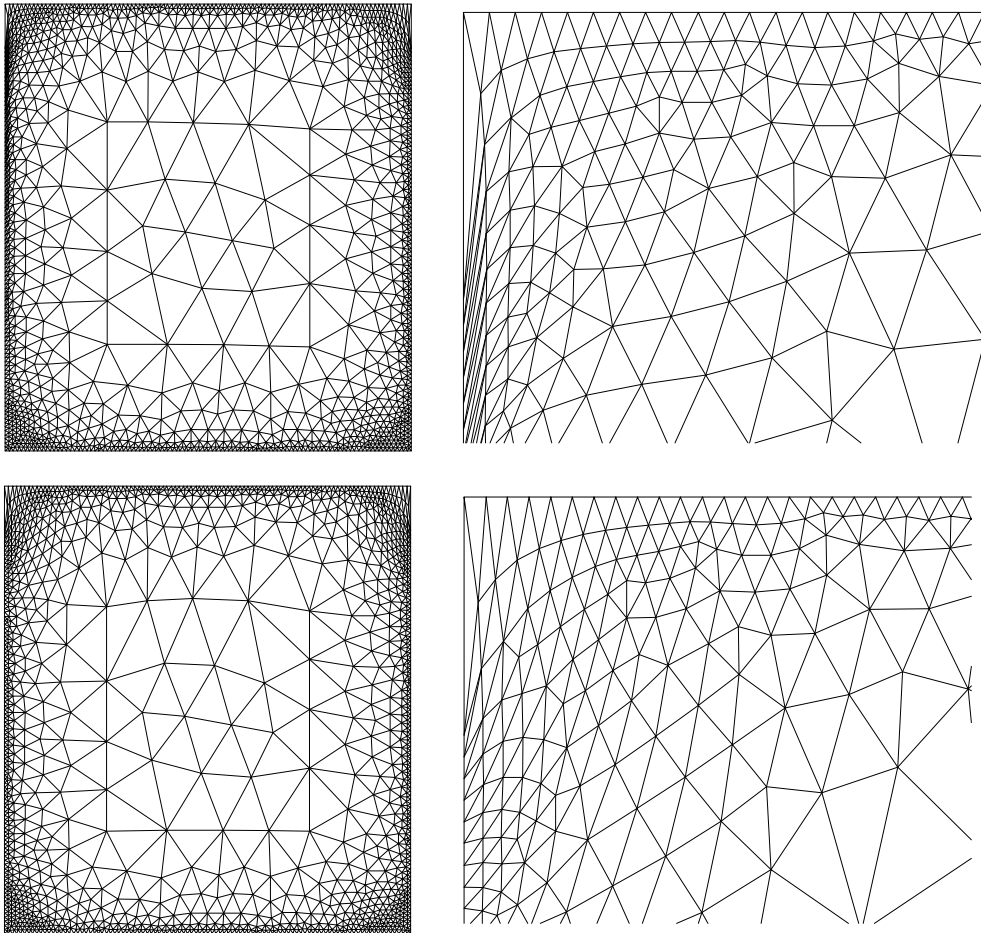


Figure 4.3.3. Example to illustrate the differences between the Laplacian (top) and the quasi-Laplacian (bottom) methods. Originally, a squared domain is meshed with an unstructured grid refined through the edges. The upper boundary is then shifted by a certain amount and the induced mesh displacement is computed using both the Laplacian and the quasi-Laplacian methods. Left figures show a general view of the derived meshes and right figures show a detail of the top left corners. Note how the quasi-Laplacian method (bottom right) produces a mesh of better quality because the smaller elements translate with less distortion while the larger ones absorb the motion. This allows to keep the quality of the mesh in the finer zones such the boundary layers and prevents from element distortion.

4.3.4 Mesh Velocity and Boundary Conditions

A key point in fluid-structure interaction problems is how to integrate the Navier-Stokes equations. Since the spatial configuration changes in time the choice of the appropriate time integration points becomes a crucial issue. In the context of the FEM, the normal procedure is first discretise in time the equations using Finite Differences and then obtain the weak form integrating over the spatial domain (obviously the FEM space-time formulations are not included here). In other words, once the equations are time-discretised, the use of a FEM leads to the evaluation of spatial integrals. It naturally raises the question of where to evaluate these integrals in the case of time-depending spatial domains: on the mesh configuration at (t^n, \mathbf{x}^n) , on the mesh configuration at $(t^{n+1}, \mathbf{x}^{n+1})$, or on a combination between these. A possible procedure could be to impose the weak form (i.e. evaluate all the spatial integrals) at the same time instant at which the continuous differential equation is verified when the time discretisation is performed via Finite Differences. Thus if a forward Euler time discretisation is considered, the mesh velocity and its configuration to evaluate the spatial integrals would be that of (t^n, \mathbf{x}^n) ; the configuration and velocity at $(t^{n+1}, \mathbf{x}^{n+1})$ would be employed in the case of a backward Euler discretisation and so on. Note that this introduces a time lag in some terms of the final resulting algebraic system between the geometry used to compute the integrals and the nodal variables. This effect is globally minimised in the case of a Crank-Nicholson scheme (i.e. when the continuous equation is verified at $t^{n+1/2}$) because in this case the time lag reduces to $\Delta t/2$ in both the LHS and the RHS terms of the resulting final system. It suggests that the best choice is to solve the Navier-Stokes equations using a Crank-Nicholson scheme to discretise in time and compute the spatial integrals with the mesh configuration and velocity evaluated at $t^{n+1/2}$. In particular, concerning the algorithm herein proposed for the Navier-Stokes equations it means that one must use $\vec{\mathbf{q}}_1 = \vec{\mathbf{q}}_2 = \vec{\mathbf{q}}_3 = (1/2, 1/2, 0)$ (see section 4.1). In summary, when solving the Navier-Stokes equations both the velocity and configuration of the ALE mesh are considered at $t^{n+1/2}$, that is using

$$\hat{\mathbf{u}}^{n+1/2} = \frac{\mathbf{x}^{n+1} - \mathbf{x}^n}{\Delta t} \quad (4.3.15)$$

and

$$\mathbf{x}^{n+1/2} = \frac{\mathbf{x}^{n+1} + \mathbf{x}^n}{2} \quad (4.3.16)$$

The same criteria is adopted to solve the convective transport equation (when required). Obviously, the above equations should be compatible with the constraints imposed by equation (4.3.5). The continuity between the structure and the dynamic ALE mesh at the fluid-structure interface at $t^{n+1/2}$ is trivially verified since we have imposed that $\mathbf{x}^n = \mathbf{d}^n$ and $\mathbf{x}^{n+1} = \mathbf{d}^{n+1}$ at this interface when solving equation (4.3.10). In consequence

$$\mathbf{x}^{n+1/2} = \frac{\mathbf{x}^{n+1} + \mathbf{x}^n}{2} = \frac{\mathbf{d}^{n+1} + \mathbf{d}^n}{2} = \mathbf{d}^{n+1/2} \quad (4.3.17)$$

The continuity between velocities at the interface is also verified. Using the second identity of equation (4.3.8) one gets

$$\hat{\mathbf{u}}^{n+1/2} = \frac{\mathbf{x}^{n+1} - \mathbf{x}^n}{\Delta t} = \frac{\mathbf{d}^{n+1} - \mathbf{d}^n}{\Delta t} = \frac{1}{2}(\dot{\mathbf{d}}^{n+1} + \dot{\mathbf{d}}^n) = \dot{\mathbf{d}}^{n+1/2} \quad (4.3.18)$$

It can be observed how the use of the constant average acceleration method (of the midpoint rule) for advancing the structure guarantees the accomplishment of the constraints expressed in equation (4.3.5). Note also that not all the structural integrators can, in general, satisfy the continuity between the velocity of the structure and that of the ALE dynamic mesh at Γ_{FS} if equation (4.3.15) is used to compute the mesh velocity. As previously pointed out in [Farhat *et al.*, 1995], this important result justifies the choice of the midpoint rule as the implicit time integrator for the low-frequency dominated structural equations.

A second important issue concerns the prescription of the fluid boundary conditions at the fluid-structure interface, that is, which value of \mathbf{u} must be prescribed at $t^{n+1/2}$ to verify the constraint imposed by equation (4.3.2). For the constant average acceleration method the structural velocity $\dot{\mathbf{d}}$ is linear in time so that its value at $t^{n+1/2}$ is directly given by the trapezoidal rule. In consequence, if one sets the velocity of the fluid as

$$\mathbf{u}^{n+1/2} = \frac{1}{2}(\dot{\mathbf{d}}^{n+1} + \dot{\mathbf{d}}^n) \quad (4.3.19)$$

verifies the required constraint because then

$$\mathbf{u}^{n+1/2} = \frac{1}{2}(\dot{\mathbf{d}}^{n+1} + \dot{\mathbf{d}}^n) = \dot{\mathbf{d}}^{n+1/2} \quad (4.3.20)$$

This prescription of the fluid boundary conditions when the constant average acceleration method is used as the structural integrator has been already proposed by [Blom, 1998].

Observation When the non-slip condition is considered, it can be observed from equations (4.3.18) and (4.3.20) how the particles of the structure, the particles of the fluid, and the nodes of the ALE dynamic mesh coincide at the fluid-structure interface, that is, the ALE formulation becomes Lagrangian at this part of the domain. This is not casual because one of the major goals of the ALE formulation is precisely to keep the properties of the Lagrangian description in zones such as moving boundaries of free surfaces.

Observation In the algorithm proposed here, all the spatial integrals of the weak form are evaluated using the same mesh configuration and, in consequence, some terms present a time lag between geometry and nodal variables¹. There are, however, other possible choices. Thus, in the algorithms proposed by [Farhat et al., 1995; Lesoinne and Farhat, 1996] and in successive works of these authors, the evaluation of the spatial integrals that come from the first term of equation (4.3.1) (the temporal derivative of \mathbf{V}) is done at (t^n, \mathbf{x}^n) and $(t^{n+1}, \mathbf{x}^{n+1})$, that is, considering different time instants and different spatial configurations². The advantage is that, in this case, these spatial integrals do not introduce any time lag between the spatial configuration and the nodal variables³. Nevertheless, there is an important drawback: the updating of the mesh velocity and the computation of the convective-diffusive terms can not be done arbitrarily if one wishes to verify the *Geometric Conservation Law* (GCL). The GCL dictates the consistency between the ALE mesh movement and the fluid solver and is deduced imposing that the solution of the ALE scheme conserves a uniform flow⁴. The most important implication of the GCL is that the ALE mesh velocity must be computed as done in equation (4.3.15) independently of the integration formula for the flow equations. Concerning to integration of the convective fluxes, the adequate spatial configuration is different for the two-dimensional and the three-dimensional cases. In the first case, the fluxes must be integrated on the mesh configuration at $t^{n+1/2}$, that is, using equation (4.3.17). In the second, it is necessary to evaluate the fluxes at two different time instants. Note that this duplicates the computational cost associated with the construction of the resulting FEM matrixes.

¹ As previously discussed, this time lag is globally minimised if one considers the configuration at $t^{n+1/2}$.

² A weak form with spatial integrals evaluated at different time instants can be obtained only if one considers first the spatial discretisation and then discretises in time the resulting weak form.

³ This time lag can be a “problem” in other disciplines such as aeroelasticity, where high frequency oscillations are susceptible to appear. However, this is not our case.

⁴ In fact, the verification of the GCL is not strictly necessary but is strongly recommended. It is also important to note that if one considers only one configuration (like us) the GCL is automatically verified.

4.3.5 Mesh Distortion and Remeshing

The solution of (4.3.10) determines a new configuration of the mesh of the fluid at every time step. At this point, some criteria to evaluate mesh distortion must be considered in order to guarantee the quality of the solution. This is done imposing a maximum and a minimum value for the angles of all the elements of the mesh. Whenever this condition is not attained (i.e. when one or more elements of the mesh are unacceptably stretched) it is necessary to perform a remeshing. For this purpose, a two dimensional generator of unstructured triangular meshes has been incorporated to the code¹. This generator uses Delaunay and constrained Delaunay triangulations combined with the Laplacian smoothing technique and produces a mesh of high quality in general domains.

Observation The remeshing procedure is an undesirable effect not only because its computational cost but also by its inherent associated projection errors. Fortunately, one of the advantages of the ALE formulation with an adequate mesh movement (such as the one induced by the quasi-Laplacian method) is that makes the remeshing necessary only in problems with large structural displacements and, even in this case, a few remeshing procedures are, in general, required.

Once a new mesh has been generated, it is necessary to interpolate all the variables from the old mesh to the new one. The simplest strategy for this purpose is the classical Lagrange interpolation, in which the nodal values of the new mesh are obtained using the Lagrange interpolation functions. The problem with this procedure is that is very diffusive (i.e. non conservative) when one interpolates from a fine grid to a coarse one. This phenomena is schematically illustrated in figure 4.3.4. In order to overcome this drawback, nodal variables can be transmitted with constrains that impose the conservation of any desired global quantity such as, for instance, mass, momentum or forces. Every global quantity introduces a constrain to the interpolation. This interpolation technique has been proposed and successfully applied by [Houzeaux and Codina, 1998] in the context of domain decomposition methods and allows a compromise between the continuity of the variable and the global information it carries.

Consider an initial distorted mesh 1 and a new generated mesh 2, both defined in the same domain Ω with boundary Γ . The number of nodal points of each mesh is $nnode1$ and $nnode2$, and let N_1^k and N_2^k be the shape functions associated with the k -th node of the first and the second mesh respectively. Let a_1 be given values of a generic variable, scalar for

¹ The original version of this generator was written by professor Borjan Niceno and it is freely available at <http://www-dinma.univ.trieste.it/~nirftc/research/easymesh/>

simplicity, in the original mesh 1 and let a_1 be its classical Lagrange interpolation to the new generated mesh 2 (that is, $a_1 = \mathbf{I}(a_1)$ where \mathbf{I} is the interpolation operator from one mesh to the other). The objective is to determine a new set of interpolated values, namely a_2 , imposing the conservation of a global quantity. This can be done by minimising the functional

$$\int_{\Omega} (a_2 - a_1)^2 d\Omega \quad (4.3.21)$$

under the constrain

$$\mathbf{R}(a_2) - \mathbf{f} = 0 \quad (4.3.22)$$

where \mathbf{R} is an operator. From a discrete point of view, the above condition can be expressed as

$$\begin{cases} \text{minimise } \int_{\Omega} (N_2^k a_2^k - N_2^k a_1^k)^2 d\Omega \\ \text{under the constrain } \mathbf{R}^{ik} a_2^k = f^i \end{cases} \quad (4.3.23)$$

In the above expression, indices k and i run from 1 to $nnode2$ and to the number of constrains ($ncons$) respectively. This problem can be solved by a classical Lagrange multiplier technique, in which the Lagrangian \mathbf{L} is given by

$$\mathbf{L}(a_2, \mathbf{I}) = \int_{\Omega} (N_2^k a_2^k - N_2^k a_1^k)^2 d\Omega - \mathbf{I}_i (\mathbf{R}^{ik} a_2^k - f^i) \quad (4.3.24)$$

where \mathbf{I}_i are the Lagrange multipliers. The minimisation of the Lagrangian imposing

$$\begin{aligned} \frac{\partial \mathbf{L}}{\partial a_2} &= \mathbf{0} \\ \frac{\partial \mathbf{L}}{\partial \mathbf{I}_i} &= 0 \end{aligned} \quad (4.3.25)$$

leads to the following linear system of equations

$$\begin{bmatrix} \mathbf{M} & -\mathbf{R}^T \\ \mathbf{R} & \mathbf{0} \end{bmatrix} \begin{bmatrix} \mathbf{a}_2 \\ \mathbf{I}/2 \end{bmatrix} = \begin{bmatrix} \mathbf{M} \mathbf{a}_1 \\ \mathbf{f} \end{bmatrix} \quad (4.3.26)$$

where \mathbf{M} is the mass matrix, \mathbf{R} the matrix of constrains and \mathbf{a}_2 and \mathbf{a}_1 the vectors of nodal variables. The solution of (4.3.26) for \mathbf{a}_2 is given by the following formal expression

$$\mathbf{a}_2 = \mathbf{a}_1 + \mathbf{M}^{-1} \mathbf{R}^T [\mathbf{R} \mathbf{M}^{-1} \mathbf{R}^T]^{-1} (\mathbf{f} - \mathbf{R} \mathbf{a}_1) \quad (4.3.27)$$

where, obviously, the matrix of constrains \mathbf{R} and the vector \mathbf{f} depend on the global quantity the conservation of which is imposed.

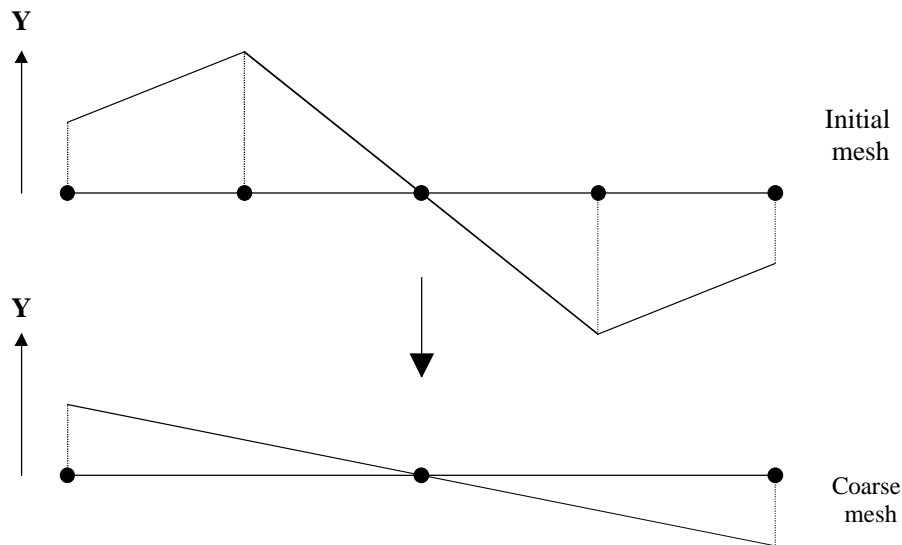


Figure 4.3.4. Example to illustrate how the interpolation from a fine mesh to a coarser one using the classical Lagrange interpolation can be very diffusive and non-conservative.

Observation Equation (4.3.27) becomes trivial if the lumped mass matrix is used. In this case, the computation of \mathbf{a}_2 is very economic because only matrix-vector products are required. Note that the inversion of the matrix $\mathbf{R} \mathbf{R}^T$ has a negligible computational cost since its dimension is only the number of constrains.

The procedure proposed here allows to conserve any global quantity of interest during the interpolation of one (or several) nodal variables. In general, the following restrictions are considered: mass conservation during the interpolation of the density, global linear momentum and mass flow rate during the interpolation of the momentum and forces over the boundary and over the fluid-structure interface during the interpolation of the pressure and the deviatoric stress tensor. Note that the conservation of the forces over the fluid-structure interface is a crucial point in order to avoid the introduction of numerical oscillations in the structural

behaviour as a consequence of the interpolation. The force exerted by the fluid over a generic boundary has two contributions

$$\mathbf{F} = \int_{\Gamma} p \mathbf{n} d\Gamma - \int_{\Gamma} \mathbf{T} \cdot \mathbf{n} d\Gamma \quad (4.3.28)$$

where p is pressure, \mathbf{T} is the deviatoric stress tensor and \mathbf{n} is the normal outward unit. The first contribution is conserved during the interpolation of the pressure, while the second is imposed during the interpolation of the deviatoric stress tensor. Whichever the case, forces are conserved not only over the fluid-structure interface but also over the whole boundary of the fluid.

All the above interpolations and its respective values for the matrix of constrains \mathbf{R} and the vector \mathbf{f} are explicitly outlined in this section because they are of general applicability. Moreover, in some particular problems the conservation of other additional global quantities can be also imposed. Thus, for instance, in the case of a magma with volatiles the total amount of volatiles must be conserved through the interpolation process. The derivation of \mathbf{R} and \mathbf{f} for these particular cases is straightforward and is not outlined here.

● **Density interpolation.** The interpolation of the density is done imposing mass conservation. Note that for incompressible flows this constrain is unnecessary because the areas (volumes) of both meshes are the same (provided, of course, the same geometrical interpolation in both meshes) and, in consequence, mass conservation is automatically ensured. For compressible flows the following system is solved

$$\left\{ \begin{array}{l} \text{minimise } \int_{\Omega} (N_2^k \mathbf{r}_2^k - N_1^k \mathbf{r}_1^k)^2 d\Omega \\ \text{under the constrain } M_1 = M_2 \end{array} \right. \quad (4.3.29)$$

where M is the total mass in the domain Ω . In this case, matrix of constrains \mathbf{R} and the vector \mathbf{f} in Cartesian coordinates are straightforwardly given by

$$\mathbf{f} = M_1 = \int_{\Omega} N_1^k \mathbf{r}_1^k d\Omega$$

$$\mathbf{R} = \left(\int_{\Omega} N_2^1 d\Omega \quad \dots \quad \int_{\Omega} N_2^{nnode2} d\Omega \right) \quad (4.3.30)$$

where k runs from 1 to $nnode1$.

② **Momentum interpolation.** The momentum is interpolated imposing the conservation of the mass flow rate and the global momentum in each space dimension, that is, one must

$$\left\{ \begin{array}{l} \text{minimise } \int_{\Omega} (N_2^k U_{2j}^k - N_2^k U_{1j}^k)^2 d\Omega \\ \text{under the constrains } \quad \left\{ \begin{array}{l} C_{1j} = C_{2j} \\ U_{1j} = U_{2j} \end{array} \right. \end{array} \right. \quad (4.3.31)$$

where C_j and U_j are the mass flow rate and the global momentum in the j direction (j runs from 1 to the space dimension). In this case, the matrix of constrains \mathbf{R} and the vector \mathbf{f} in Cartesian coordinates are (for each spatial dimension j)

$$\mathbf{f}_j = \begin{bmatrix} C_{1j} \\ U_{1j} \end{bmatrix} = \begin{bmatrix} \oint_{\Gamma} N_1^k U_{1j}^k n_j d\Gamma \\ \int_{\Omega} N_1^k U_{1j}^k d\Omega \end{bmatrix} \quad (4.3.32)$$

$$\mathbf{R}_j = \begin{bmatrix} \oint_{\Gamma} N_2^1 n_j d\Gamma & \dots & \oint_{\Gamma} N_2^{mode2} n_j d\Gamma \\ \int_{\Omega} N_2^1 d\Omega & \dots & \int_{\Omega} N_2^{mode2} d\Omega \end{bmatrix}$$

where n_j is the j -th component of the outward unit normal. In the above equation the repetition of the index j does not imply summation.

③ **Pressure interpolation.** Pressure is interpolated imposing the conservation of each component of the pressure load (first contribution in equation (4.3.28)) over the total boundary and over the interface fluid-structure. This leads to

$$\left\{ \begin{array}{l} \text{minimise } \int_{\Omega} (N_2^k p_2^k - N_2^k p_1^k)^2 d\Omega \\ \text{under the constrains } \quad \left\{ \begin{array}{l} \text{PL}_{1j} = \text{PL}_{2j} \\ \text{PL}_{1j}^{FS} = \text{PL}_{2j}^{FS} \end{array} \right. \end{array} \right. \quad (4.3.33)$$

where PL_j and PL_j^{FS} are the j -th component of the pressure load over the total boundary and over the fluid-structure interface respectively. In this case, the matrix of constrains \mathbf{R} and the vector \mathbf{f} are given, in Cartesian coordinates, by

$$\mathbf{f}_j = \begin{bmatrix} \text{PL}_{1j} \\ \text{PL}_{1j}^{FS} \end{bmatrix} = \begin{bmatrix} \oint_{\Gamma} N_1^k p^k n_j d\Gamma \\ \oint_{\Gamma_{FS}} N_1^k p^k n_j d\Gamma \end{bmatrix} \quad (4.3.34)$$

$$\mathbf{R}_j = \begin{bmatrix} \oint_{\Gamma} N_2^1 n_j d\Gamma & \cdots & \oint_{\Gamma} N_2^{node2} n_j d\Gamma \\ \oint_{\Gamma_{FS}} N_2^1 n_j d\Gamma & \cdots & \oint_{\Gamma_{FS}} N_2^{node2} n_j d\Gamma \end{bmatrix}$$

④ **Deviatoric stress interpolation.** As previously stated, each component of the deviatoric stress tensor is interpolated imposing the conservation of the stress load (second contribution in equation (4.3.28)) over the total boundary and over the interface fluid-structure, that is

$$\begin{cases} \text{minimise } \int_{\Omega} (N_2^k T_{2m}^k - N_2^k T_{1m}^k)^2 d\Omega \\ \text{under the constrains } \begin{cases} \text{SL}_{1j} = \text{SL}_{2j} \\ \text{SL}_{1j}^{FS} = \text{SL}_{2j}^{FS} \end{cases} \end{cases} \quad (4.3.35)$$

where SL_j and SL_j^{FS} are the j -th component of the stress load over the total boundary and over the fluid-structure interface respectively, and the index m runs from one to the number of tensorial components (assume that \mathbf{T} is organised as an array). In this case,

$$\mathbf{f}_j = \begin{bmatrix} \text{SL}_{1j} \\ \text{SL}_{1j}^{FS} \end{bmatrix} = \begin{bmatrix} \oint_{\Gamma} N_1^k T_{jm}^k n_m d\Gamma \\ \oint_{\Gamma_{FS}} N_1^k T_{jm}^k n_m d\Gamma \end{bmatrix} \quad (4.3.36)$$

$$\mathbf{R}_j = \begin{bmatrix} \oint_{\Gamma} N_2^1 n_j d\Gamma & \cdots & \oint_{\Gamma} N_2^{node2} n_j d\Gamma \\ \oint_{\Gamma_{FS}} N_2^1 n_j d\Gamma & \cdots & \oint_{\Gamma_{FS}} N_2^{node2} n_j d\Gamma \end{bmatrix}$$

Observation The matrixes in equations (4.3.34) and (4.3.36) contain only integrals over the boundaries and, in consequence, are filled with zeros except for those nodes that belong to the boundary. From a computational point of view it is recommended to store these matrixes using any sparse storage method such as, for instance, the compressed sparse row format.

4.4 Numerical Examples

An algorithm to numerically solve the Navier-Stokes equations with thermal and mechanical couplings has been proposed and widely discussed along this chapter. The flow equations are solved using a fractional step method (total or incremental) combined with a pressure gradient projection technique and within the frame of an ALE formulation. One of the major goals of the algorithm is its flexibility because it can be used to solve any kind of flow: viscous or inviscid, compressible or incompressible or both at the same time. Although the present work will mainly focus and constrain its applications to the context of volcanic processes, the algorithm can be also used to solve a huge spectra of problems that commonly appear in the context of engineering, physics or Earth's sciences.

In this section, some standard numerical benchmark tests are presented in order to verify the correctness of the proposed algorithm as well as to test its implementation. These tests are: ❶ the driven cavity flow, ❷ the flow past a circular cylinder, ❸ a fluid in a heated cavity, ❹ a perfect gas flowing over a NACA profile, ❺ the Stokes free fall problem, ❻ the simulation of the launching of a missile from a submarine and ❼ a mould filling simulation. The first two examples deal only with the Navier-Stokes equations for incompressible flows. The third involves also the energy equation by means of the Boussinesq hypothesis. The fourth is a typical problem of a thermally coupled flow. Examples fifth and sixth consider fluid-structure interaction. Finally, the seventh example considers the coupling with the convective transport equation. The results obtained are compared with some of those available in the literature.

4.4.1 The Driven Cavity Flow

The driven cavity flow is a classical benchmark test designed to evaluate the behaviour of algorithms that deal with incompressible viscous flows. Examples of this test can be found, among many others, in [Ghia *et al.*, 1982; Schreiber and Keller, 1983; Kim and Moin, 1985; Tanahashi *et al.*, 1990; Shen, 1991]. In this test, an incompressible viscous fluid is confined within a squared cavity in which only the upper edge is allowed to tangentially slide by prescribing the velocity on the edge, while the non-slip condition is imposed at the rest of the walls of the cavity. Pressure is prescribed to zero at the bottom left corner. Boundary conditions of the problem are sketched in Figure 4.4.1.

The transmission of momentum by means of viscosity produces, when the steady state is reached, a bigger central vortex and, eventually, smaller vortices at the corners. The

characteristics of the vortices (such as size and position) depend on the Reynolds number of the problem

$$R_e \equiv \frac{|\mathbf{u}|d}{\nu} \quad (4.4.1)$$

where d is the size of the edge, \mathbf{u} is the velocity and ν is the kinematic viscosity. Since in this problem $|\mathbf{u}|=1$ and $d=1$, the Reynolds number is directly the inverse of the kinematic viscosity. At $R_e \leq 1$ the flow is almost symmetric with respect to the central vertical line. As the Reynolds number increases, the position of the main central vortex moves towards the top right corner (towards the downstream corner) before it returns again to the centre of the cavity at higher Reynolds numbers. The bottom right and the bottom left vortices begin to develop at low Reynolds numbers and continuously increase its size and shift its position as the Reynolds number increases. Secondary vortices are also developed at the bottom corners at high Reynolds numbers. A secondary top left vortex is developed at $R_e = 3000$ approximately (this vortex is already well formed at $R_e = 5000$). Finally, at $R_e = 10000$ a new vortex (tertiary) is developed at the right bottom corner. Numerical results for Reynolds numbers of $R_e = 0.01$ (quasi-Stokes problem), 100, 1000, 5000 and 10000 are presented here. The last value can be considered as a limit for steady calculations since it seems that a Hopf bifurcation appears for $R_e > 10^4$ [Shen, 1991].

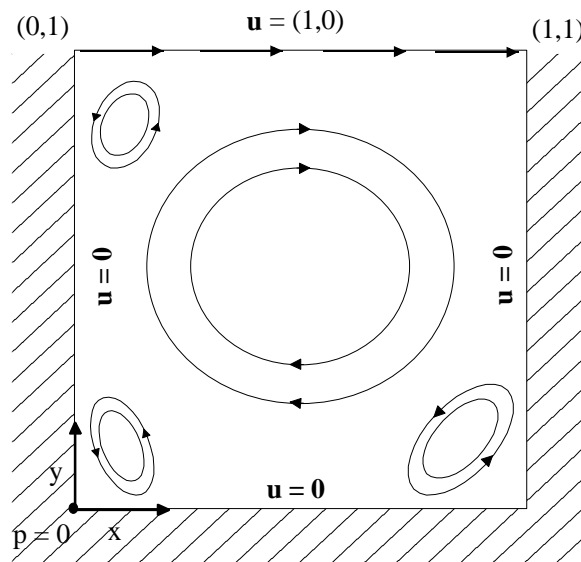


Figure 4.4.1. Boundary conditions for the driven cavity flow problem. The top of the wall moves with a uniform unit velocity on its own plane inducing a central vortex. Smaller secondary vortices can be also produced at the corners depending on the Reynolds number.

Whichever the case, numerical solutions have been obtained using both the incremental fractional step method (i.e. using $g = 1$ in equation 4.1.17) and the pressure gradient projection technique with $\mathbf{a} = \Delta t_c$. At high Reynolds numbers, the Galerkin formulation leads to numerical oscillations that are stabilised using the characteristic-Galerkin method. Two different spatial discretisations have been considered as shown in Figure 4.4.2. For $R_e \leq 5000$ the computational domain is discretised using a coarse mesh composed of 20×20 biquadratic elements (1681 nodal points) and refined through the edges in order to capture the properties of the flow. For $R_e = 10000$ a finer mesh composed of 30×30 biquadratic elements (3721 nodal points) has been used. Figures 4.4.3 to 4.4.7 show the pressure contours, the streamlines and the contours of velocity norm for different Reynolds numbers. Details of the streamlines and the velocity vectors at the corners at Reynolds numbers of 1000, 5000 and 10000 are also illustrated in figures 4.4.8 to 4.4.10. In these figures, it can be appreciated how the top left vortex is visible at $R_e = 5000$ but not at $R_e = 1000$, and also how the small tertiary vortex is visible at $R_e = 10000$. In general, the results obtained are in very good agreement with those found in literature.

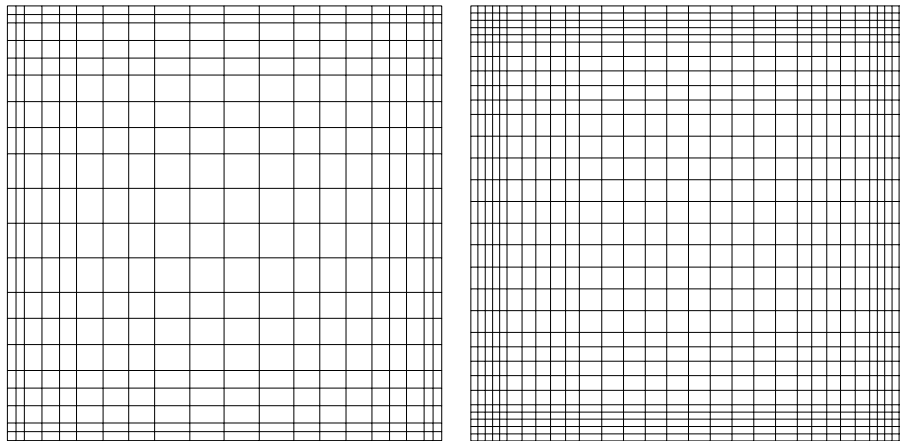


Figure 4.4.2. Spatial discretisations of the problem. Left: coarse mesh composed of 20×20 biquadratic elements (1681 nodal points). Right: finer mesh composed of 30×30 biquadratic elements (3721 nodal points). Both meshes are refined through the edges in order to reproduce the properties of the flow.

Figure 4.4.11 shows velocity profiles along vertical and horizontal lines through the geometric centre of the cavity. These results are compared with those of Ghia et al. [Ghia et al., 1982], who obtained very precise solutions of the problem using a finite-difference multigrid method based on the streamfunction-vorticity formulation. In this reference, meshes consisting of as many as 257×257 nodal points are considered. In general the results are in good agreement except for very high Reynolds numbers, where the roughness of the mesh can not capture well the strong velocity gradients.

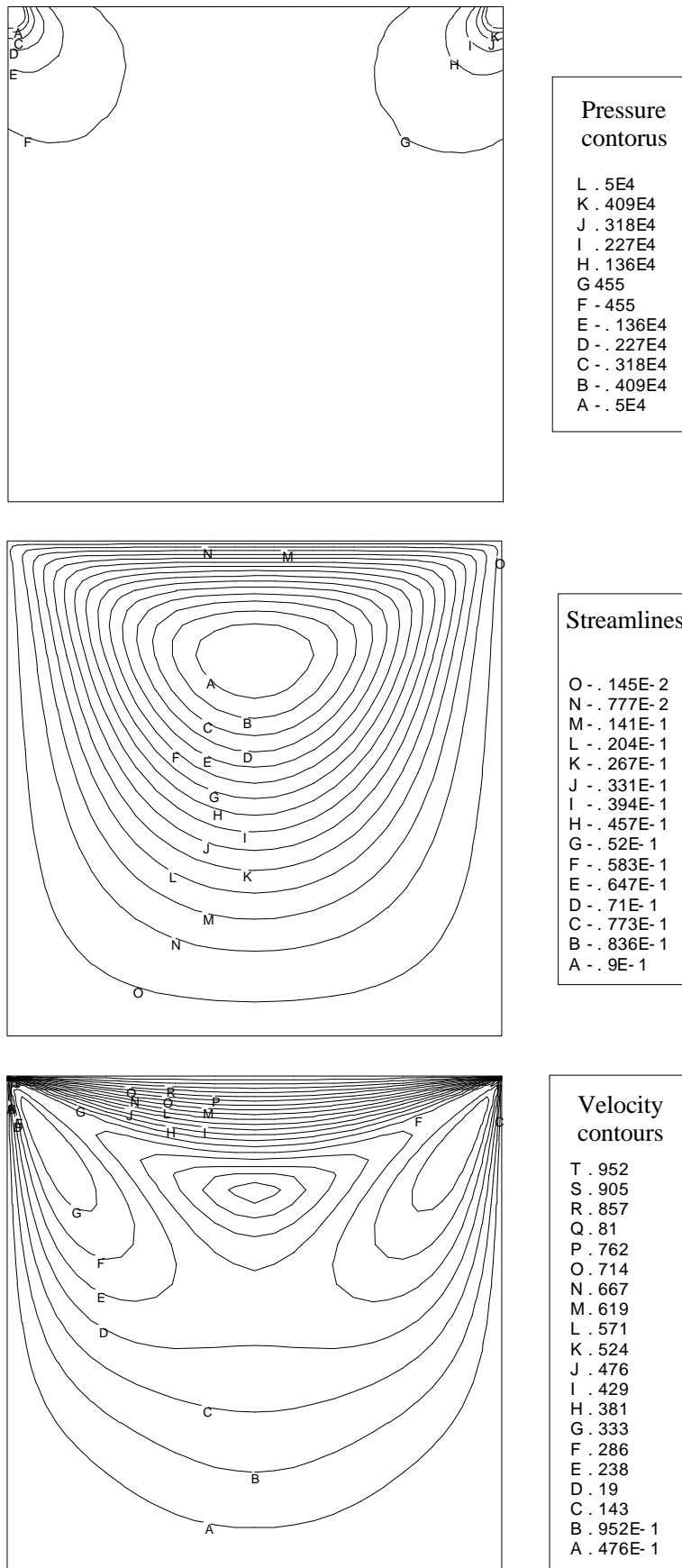


Figure 4.4.3. Numerical results at $Re = 0.01$ (quasi-Stokes problem). Top: pressure contours. Middle: streamlines. Bottom: contours of velocity norm.

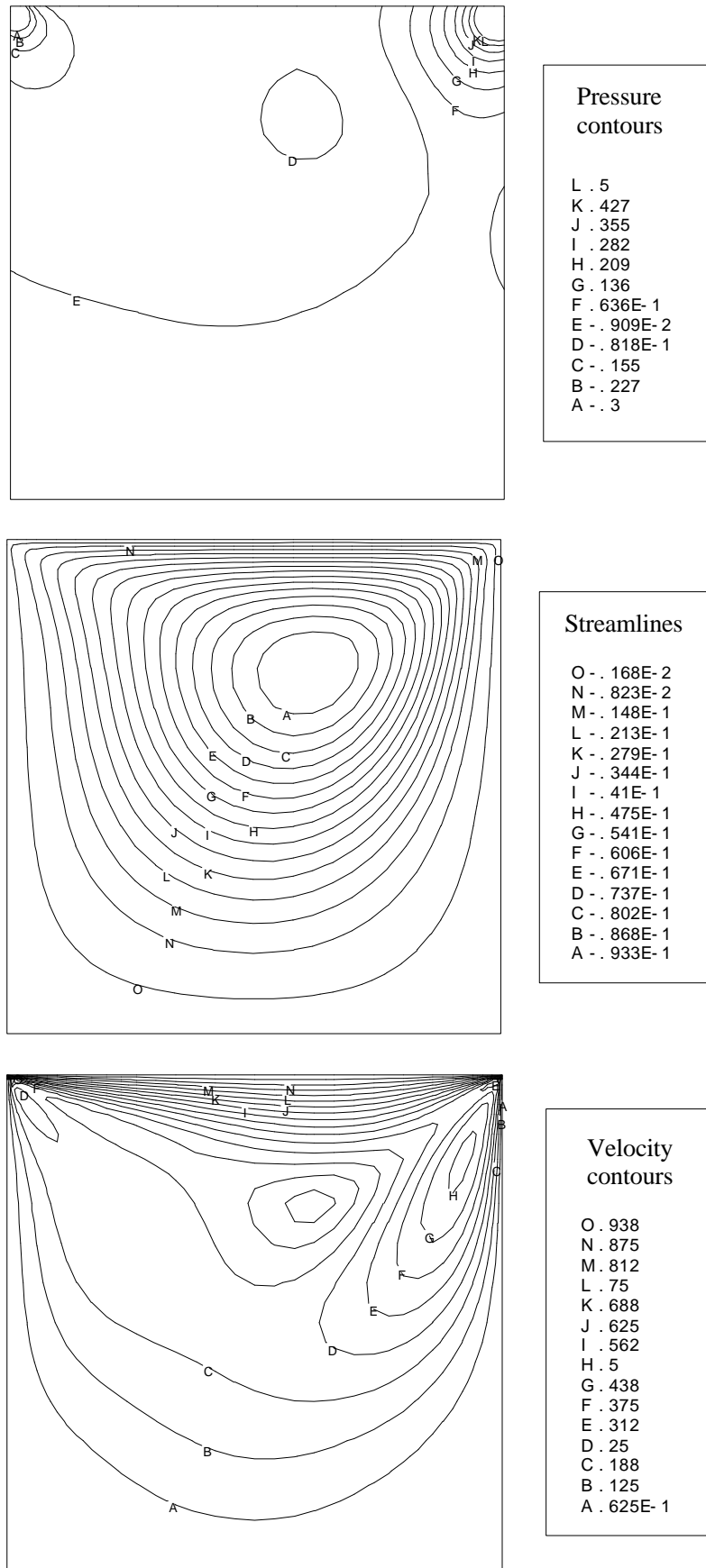


Figure 4.4.4. Numerical results at $Re = 100$. Top: pressure contours. Middle: streamlines. Bottom: contours of velocity norm.

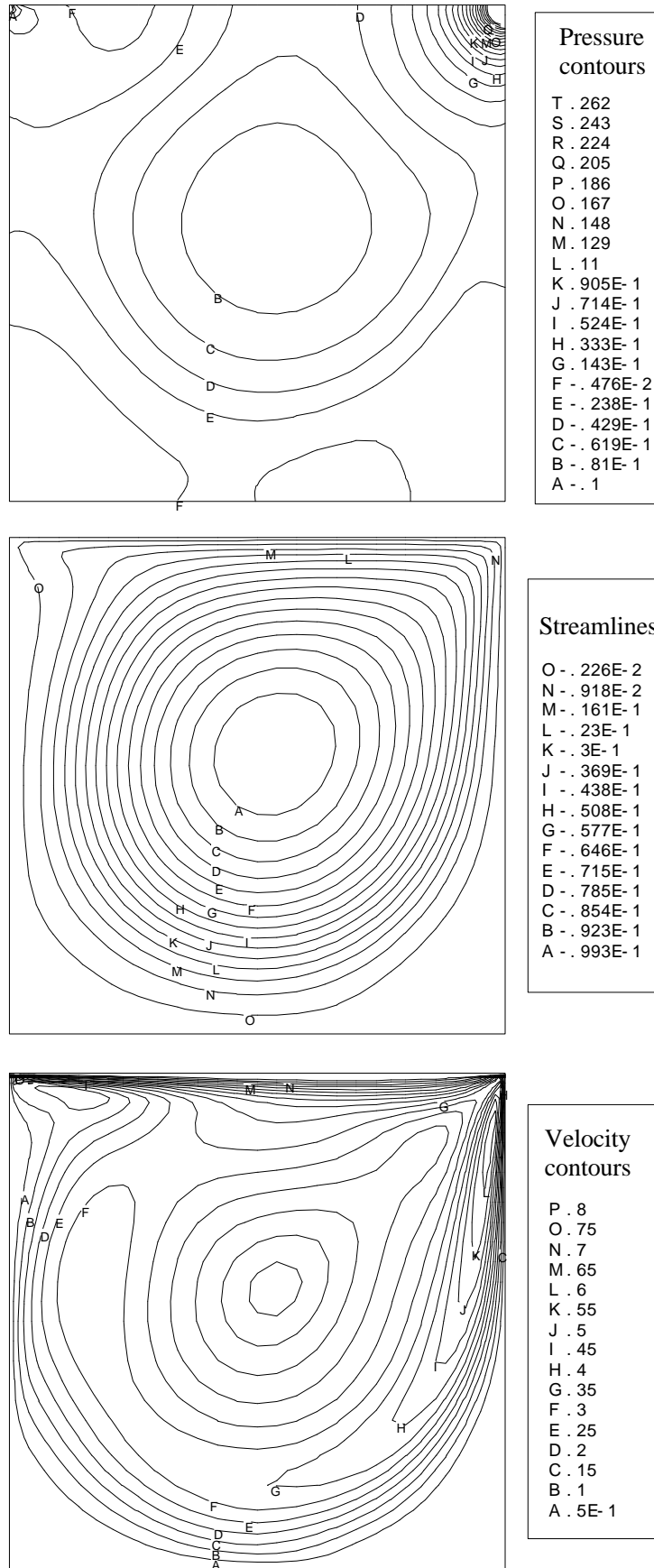


Figure 4.4.5. Numerical results at $Re = 1000$. Top: pressure contours. Middle: streamlines. Bottom: contours of velocity norm.

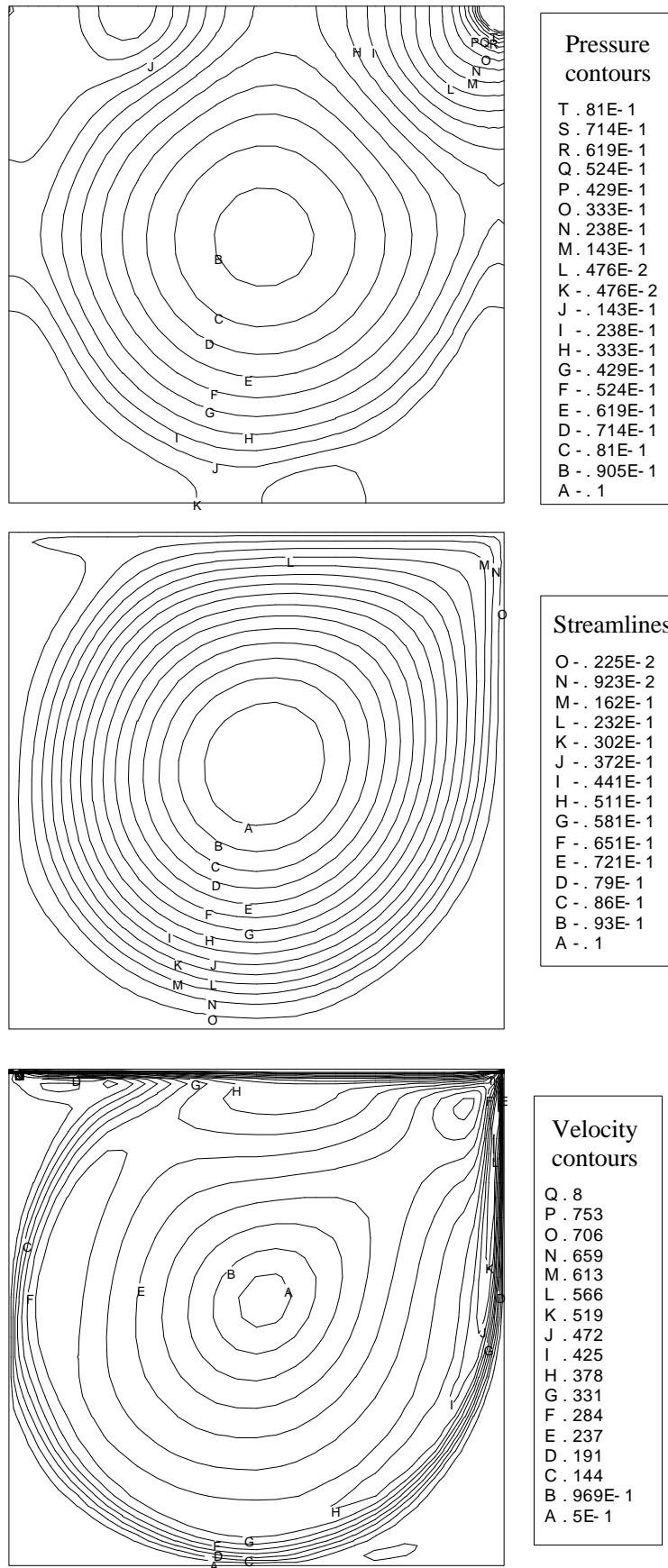


Figure 4.4.6. Numerical results at $Re = 5000$. Top: pressure contours. Middle: streamlines. Bottom: contours of velocity norm.

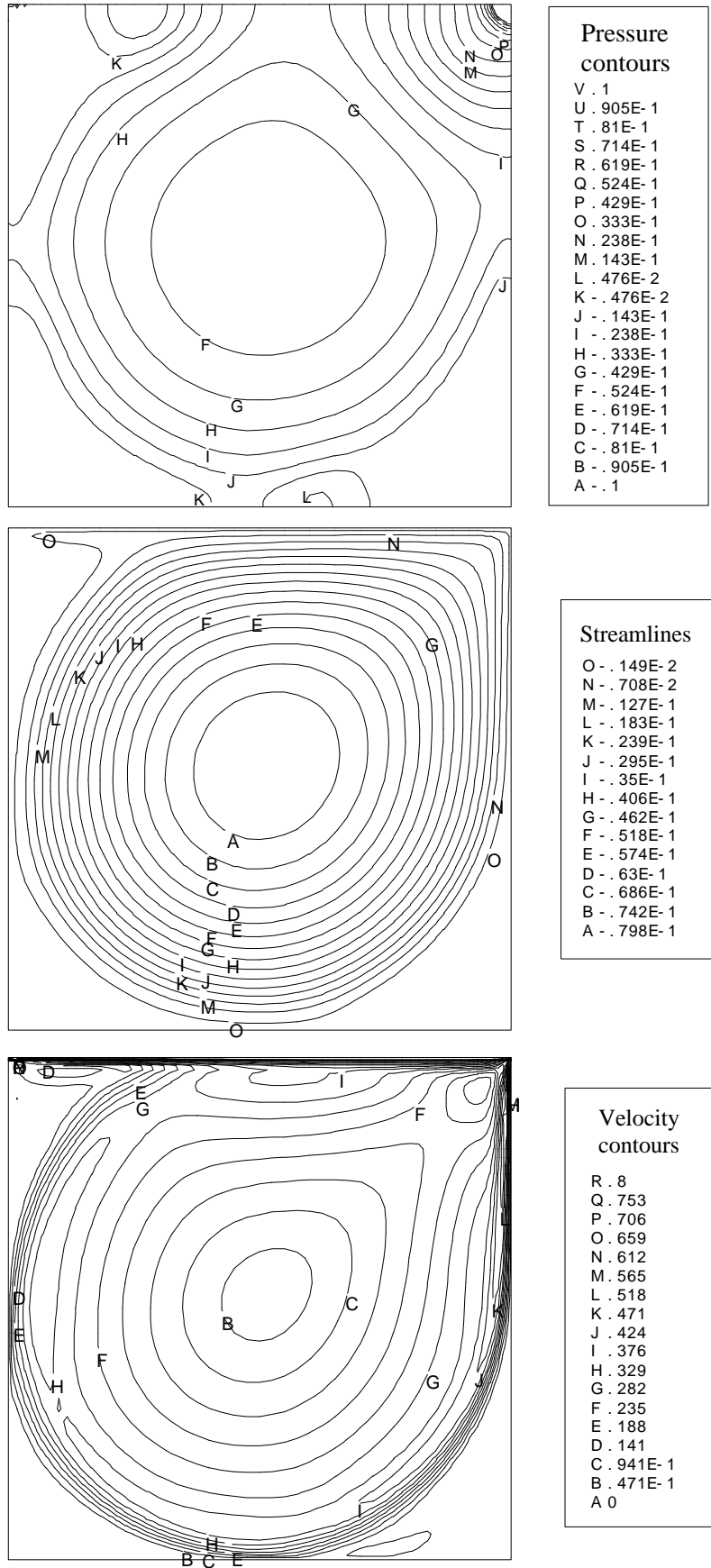


Figure 4.4.7. Numerical results at $Re = 10000$. Top: pressure contours. Middle: streamlines. Bottom: contours of velocity norm.

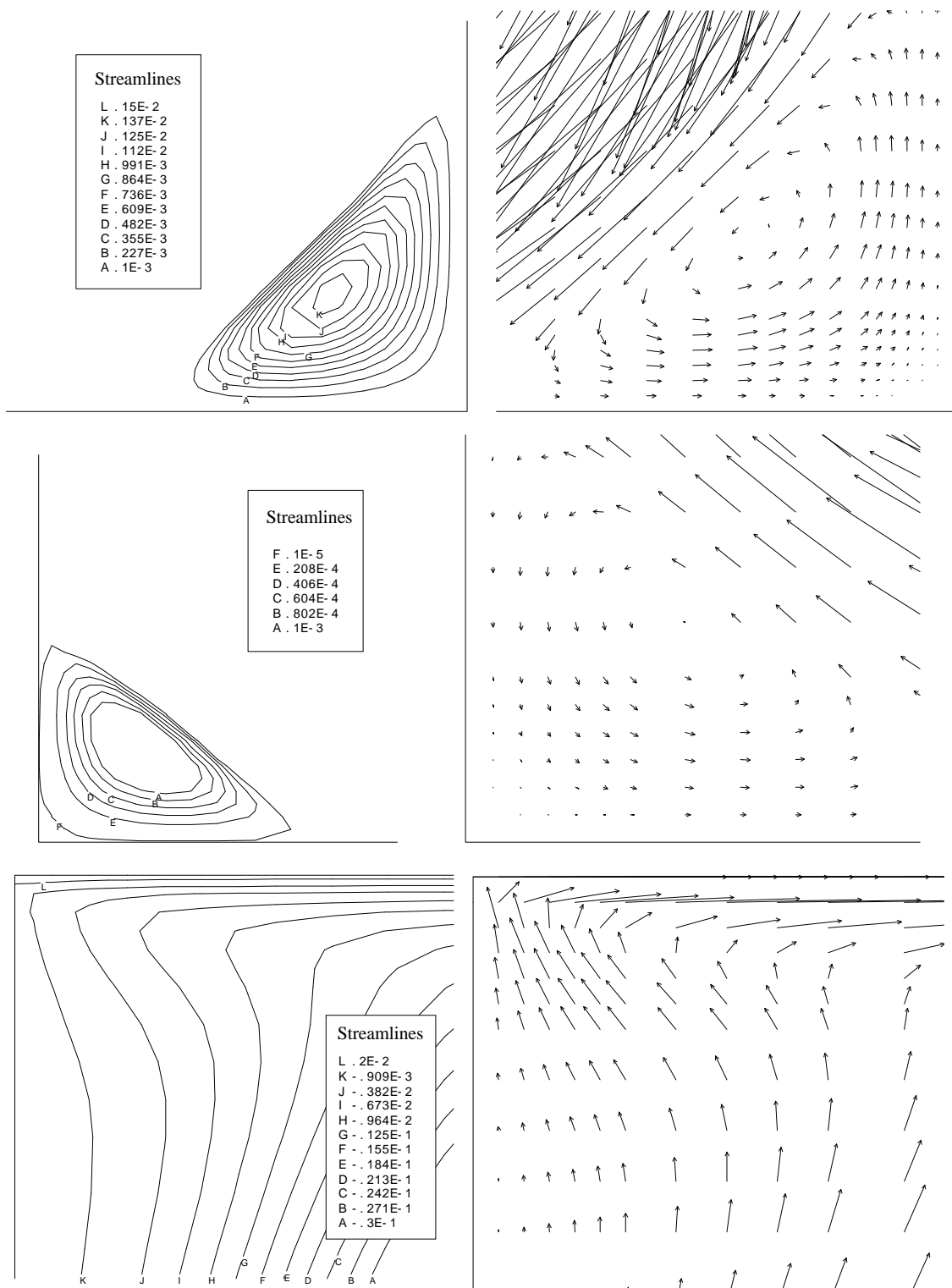


Figure 4.4.8. Numerical results at $Re = 1000$. Streamlines and velocity vectors detailed at three corners of the cavity. Top: bottom right corner. Middle: bottom left corner. Bottom: top left corner. Note how the vortex in this region is not yet developed at this Reynolds number.

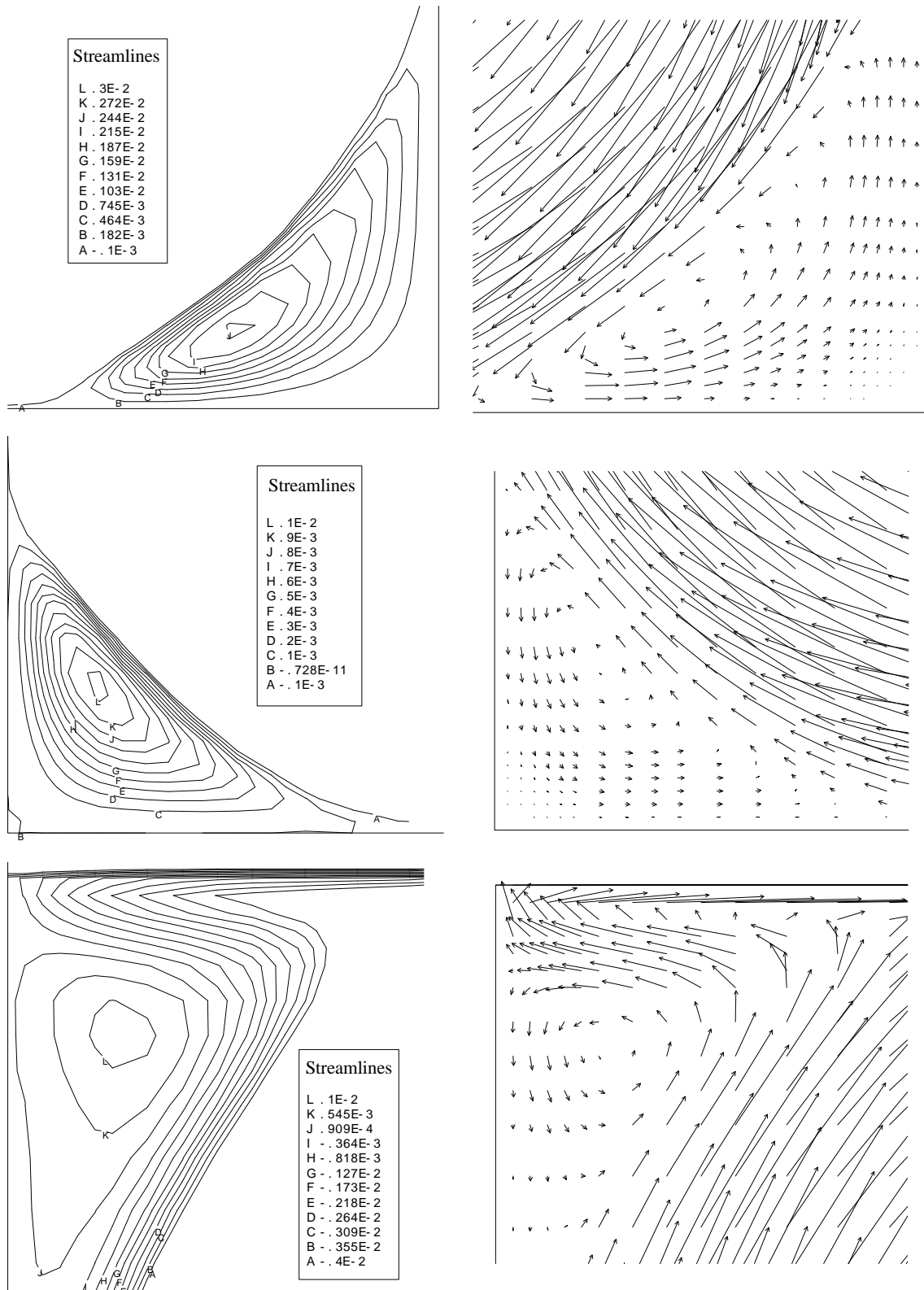


Figure 4.4.9. Numerical results at $Re = 5000$. Streamlines and velocity vectors detailed at three corners of the cavity. Top: bottom right corner. Middle: bottom left corner. Bottom: top left corner. Note how the vortex in this region is developed at this Reynolds number.

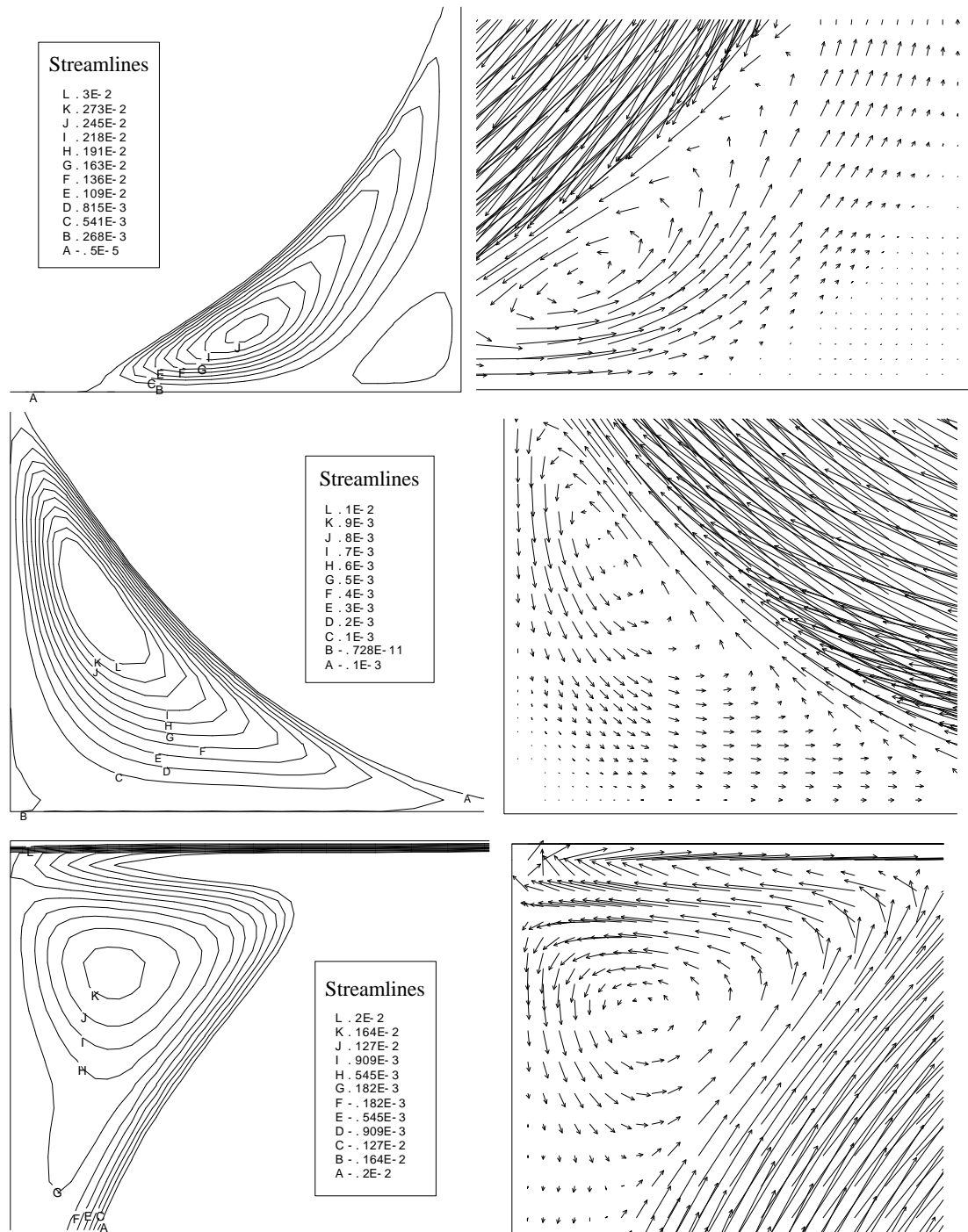


Figure 4.4.10. Numerical results at $Re = 10000$. Streamlines and velocity vectors detailed at three corners of the cavity. Top: bottom right corner. Middle: bottom left corner. Bottom: top left corner.

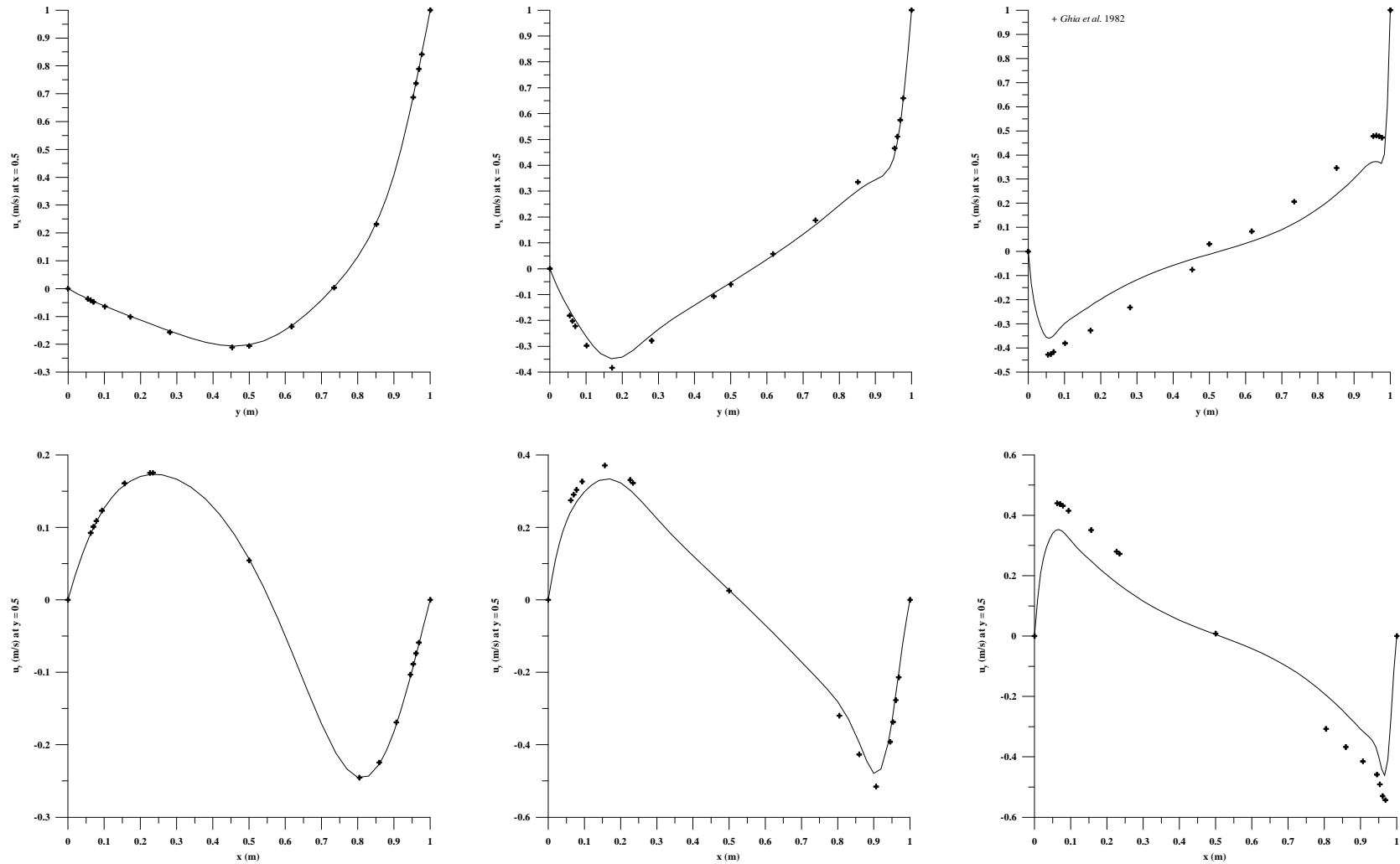


Figure 4.4.11. Velocity profiles along vertical (top) and horizontal (bottom) lines through the geometric centre of the cavity for Reynolds numbers of $R_c=100$ (left), $R_c=1000$ (middle) and $R_c=10000$ (right). The obtained results are compared with those of [Ghia et al., 1982]. Despite the differences between the meshes, the results agree reasonably well. The main differences appear at high Reynolds numbers and near the chamber walls (where high velocity gradients are not well captured due to the roughness of the mesh).

4.4.2 Flow Past a Circular Cylinder

The flow past a circular cylinder is a second widely considered benchmark problem for incompressible flows. Examples of results are given, for instance, in [Brooks and Hughes, 1982; Engelman and Jamnia, 1990; Codina, 1992b; Simo and Armero, 1994]. In this test, a circular cylinder of diameter d is immersed within an incompressible viscous fluid. The boundary conditions of the problem are schematically illustrated in Figure 4.4.12. Velocity is prescribed at the inflow (upstream), at the surface of the cylinder by means of the non-slip condition and at the top and bottom boundaries of the computational domain. Pressure is prescribed to zero at the computational outlet.

Again, the problem is characterised by the Reynolds number, based on the cylinder diameter and on the uniform inflow velocity. For R_e lower than 40 there is a stable stationary solution in which two symmetrical eddies develop behind the cylinder. As the Reynolds number increases the steady state becomes unstable and a periodic vortex shedding, known as the *von Karman vortex street*, develops behind the cylinder. The period of the vortex shedding depends on the Reynolds number, and can be evaluated by many different ways such as the evolution of a variable at a point behind the cylinder, the net force exerted over the cylinder or through the evolution of any norm. Numerical results for Reynolds numbers of $R_e=100$ and 200 are presented here. These different Reynolds numbers have been obtained using the same geometry and boundary conditions (i.e. modifying only the kinematic viscosity of the fluid). Results for $R_e=100$ are well established and are considered as the standard test for this problem. In this case, [Brooks and Hughes, 1982] give a period of the oscillations τ of 6.0 time units, while [Codina, 1992] and [Simo and Armero, 1994] found $\tau=5.7$. Finally, [Engelman and Jamnia, 1990] determined a period of $\tau=5.8$ employing a mixed formulation with a penalty function and a fine mesh (3436 Q_2/P_1 elements and 14000 nodal points).

The spatial discretisation has been performed using a mesh composed of 3200 bilinear elements and 3300 nodal points. This mesh is shown in figure 4.4.13. The mesh is refined towards the surroundings of the cylinder and behind it in order to capture the properties of the vortex shedding. The inflow, top and bottom boundaries are located at eight cylinder diameters in front of, above and below the centre of the cylinder respectively. Behind the cylinder, the mesh is extended up to 25 cylinder diameters. These extensions are done in order to minimise the effects of the boundary conditions on the flow. As in the previous example, numerical results have been obtained using an incremental fractional step method (i.e. using $\mathbf{g}=1$ in equation 4.1.17) and the pressure gradient projection technique. A first order implicit treatment for the convective and the viscous terms of the fractional momentum equation has been considered (i.e. $\vec{\mathbf{q}}_1 = \vec{\mathbf{q}}_2 = (1,0,0)$). Firstly, the stationary (unstable) solution has been obtained at

4.4 Numerical Examples

$R_e=100$. Some results are shown in Figures 4.4.14 and 4.4.15, where it can be observed how two symmetrical eddies develop behind the cylinder. After this, the von Karman vortex street have been obtained by slightly perturbing this unstable solution introducing an additional vertical velocity in some nodes located behind the cylinder.

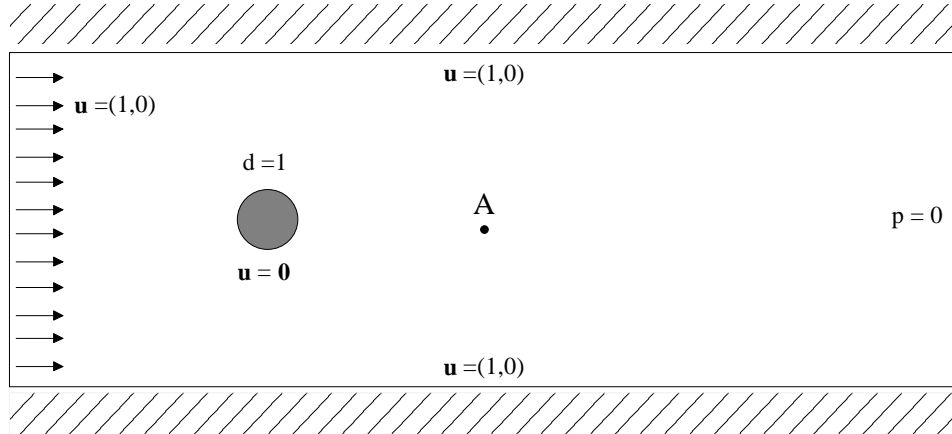


Figure 4.4.12. Boundary conditions for the flow past a circular cylinder.

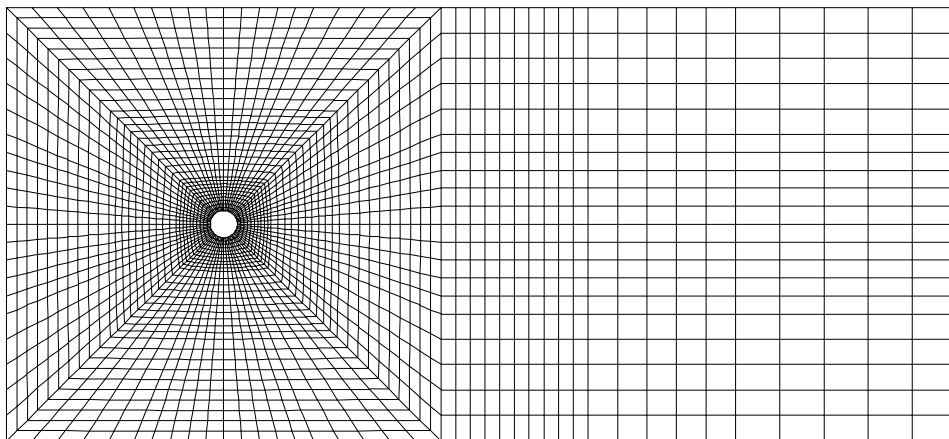


Figure 4.4.13. Spatial discretisation of the problem. The mesh is composed of 3200 bilinear elements (3300 nodal points) and has been refined toward the surroundings of the cylinder and behind it in order to reproduce the properties of the flow.

Figure 4.4.16 shows the temporal evolution for the L^2 norm of the difference between solutions at two consecutive time instants for both velocity and pressure fields. This norm has been computed as

$$L^2(f) = \sum_{n=1}^{mode} (f^{n+1} - f^n)^2 \quad (4.4.2)$$

and allows to determine when the vortex shedding is fully developed.

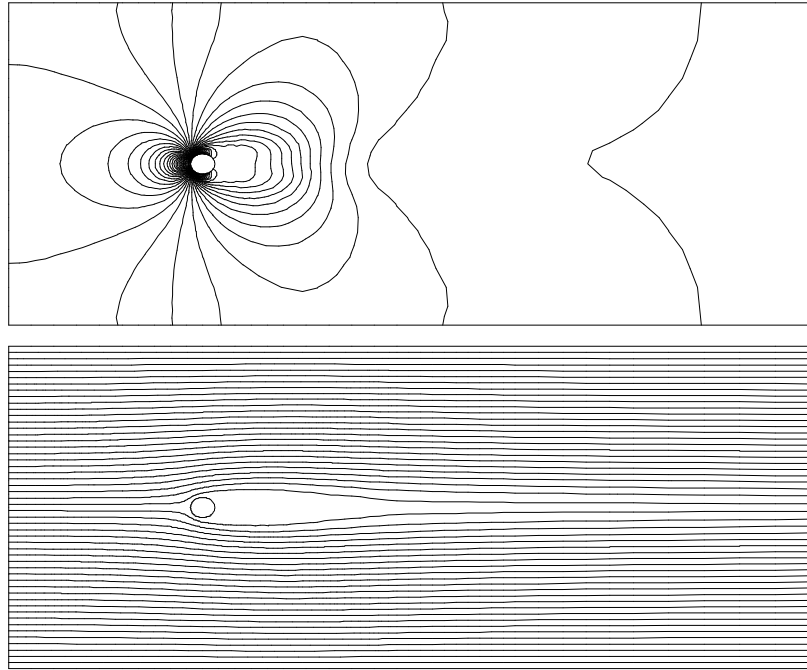


Figure 4.4.14. Steady (unstable) state for the flow past a circular cylinder at $R_e=100$. Note the symmetry of the problem along the horizontal axis. Top: pressure contours. Bottom: streamlines.

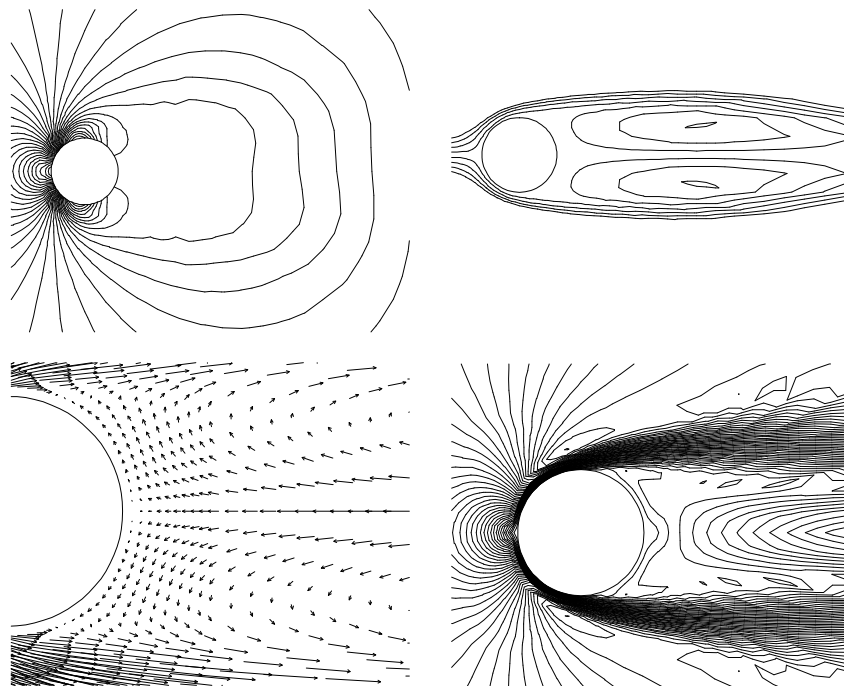


Figure 4.4.15. Steady (unstable) state for the flow past a circular cylinder at $R_e=100$. Results around the cylinder. Top left: pressure contours. Top right: streamlines. Bottom left: velocity vectors. Bottom right: contours of velocity norm.

In this oscillatory steady state, an arbitrary referential time instant t_{ref} can be considered in order to determine the period of the oscillations τ and to visualise the properties of the flow during a complete vortex shedding. This t_{ref} is, by definition, a time instant at which the vertical component of the velocity at A (see figure 4.4.12) is maximum. Figure 4.4.17 shows pressure contours and streamlines at $t = t_{ref}$. Note how the von Karman vortex are fully developed behind the cylinder. Figure 4.4.18 illustrates the temporal evolution of the vertical component of the velocity at A and the pressure force over half cylinder during three periods. This force has been computed as the surface integral over half cylinder

$$\oint_{0 \leq q \leq p} P ds \quad (4.4.3)$$

where P is pressure. The period of the oscillations has been found to be about 6 time units, value which agrees with those found in the literature. Some properties of the flow in the neighbourhood of the cylinder at $t=t_{ref}$ and $t=t_{ref}+\tau/2$ are shown in Figure 4.4.19. Finally, figure 4.4.20 details a complete cycle of vortex shedding around the cylinder.

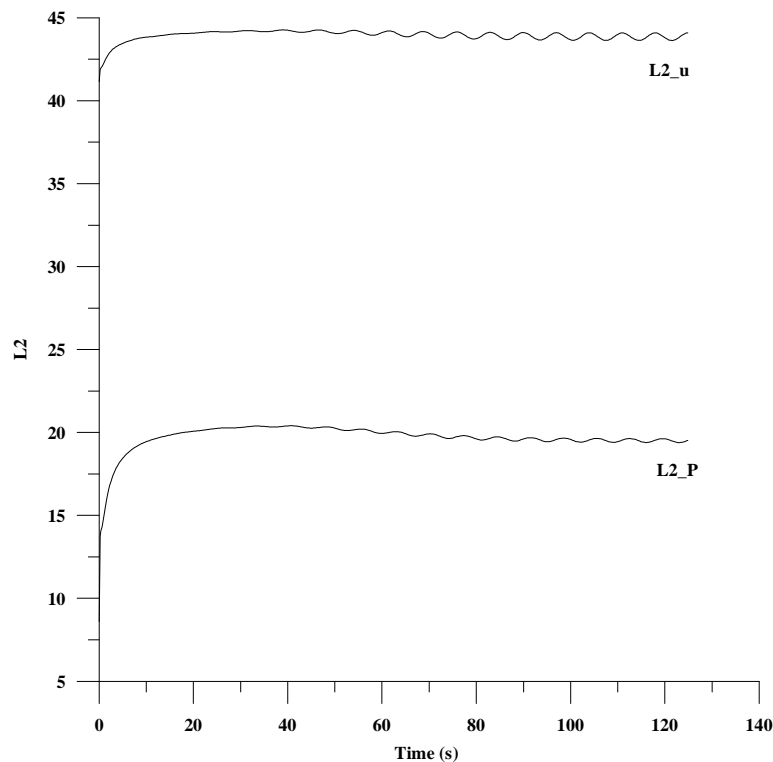


Figure 4.4.16. Pressure and velocity L^2 norms versus time. This norm has been computed as the norm of the difference at two time instants (without normalisation). The important point is the oscillatory behaviour once the vortex shedding is fully developed.

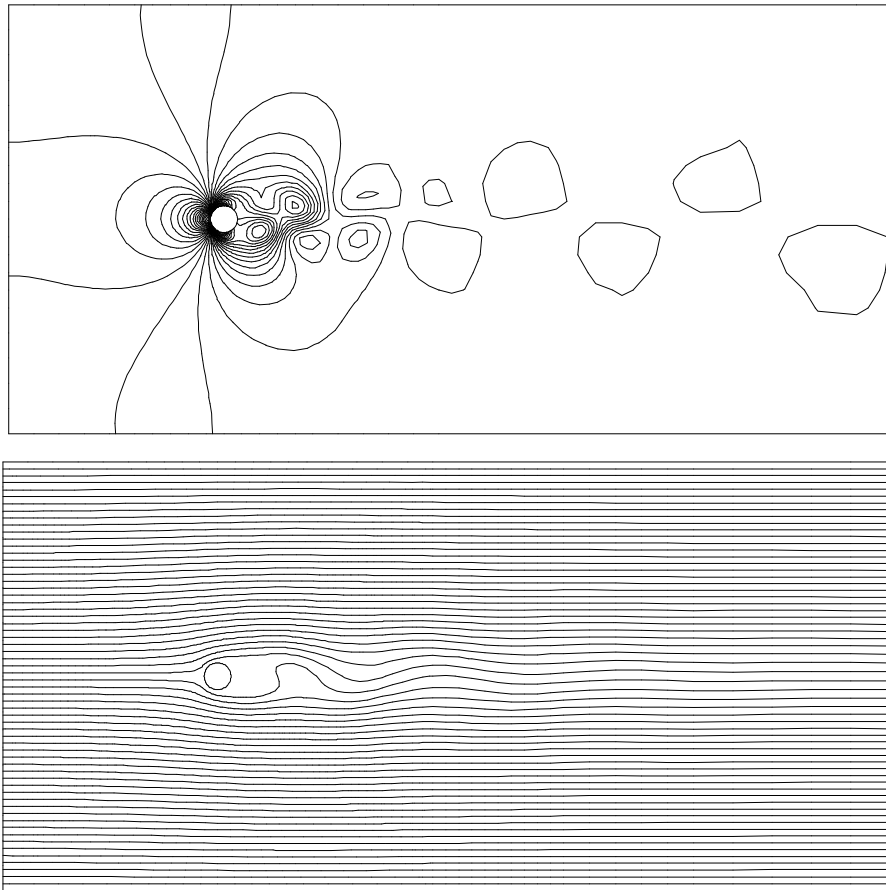


Figure 4.4.17. Flow past a circular cylinder at $Re=100$. Results at $t=t_{ref}$. Top: pressure contours. Bottom: streamlines.

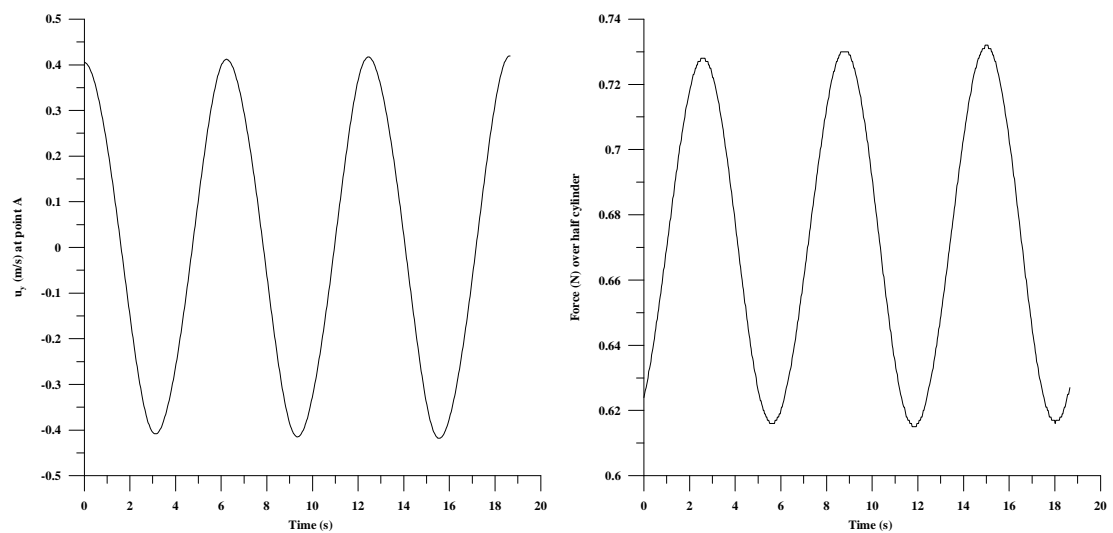


Figure 4.4.18. Illustration of the vortex shedding during three periods. Left: vertical component of the velocity at point A (see figure 4.4.12) versus time. Right: force over half cylinder versus time. In both cases the origin of the abscissa is at the time instant $t=t_{ref}$. The period found is about 6 time units.

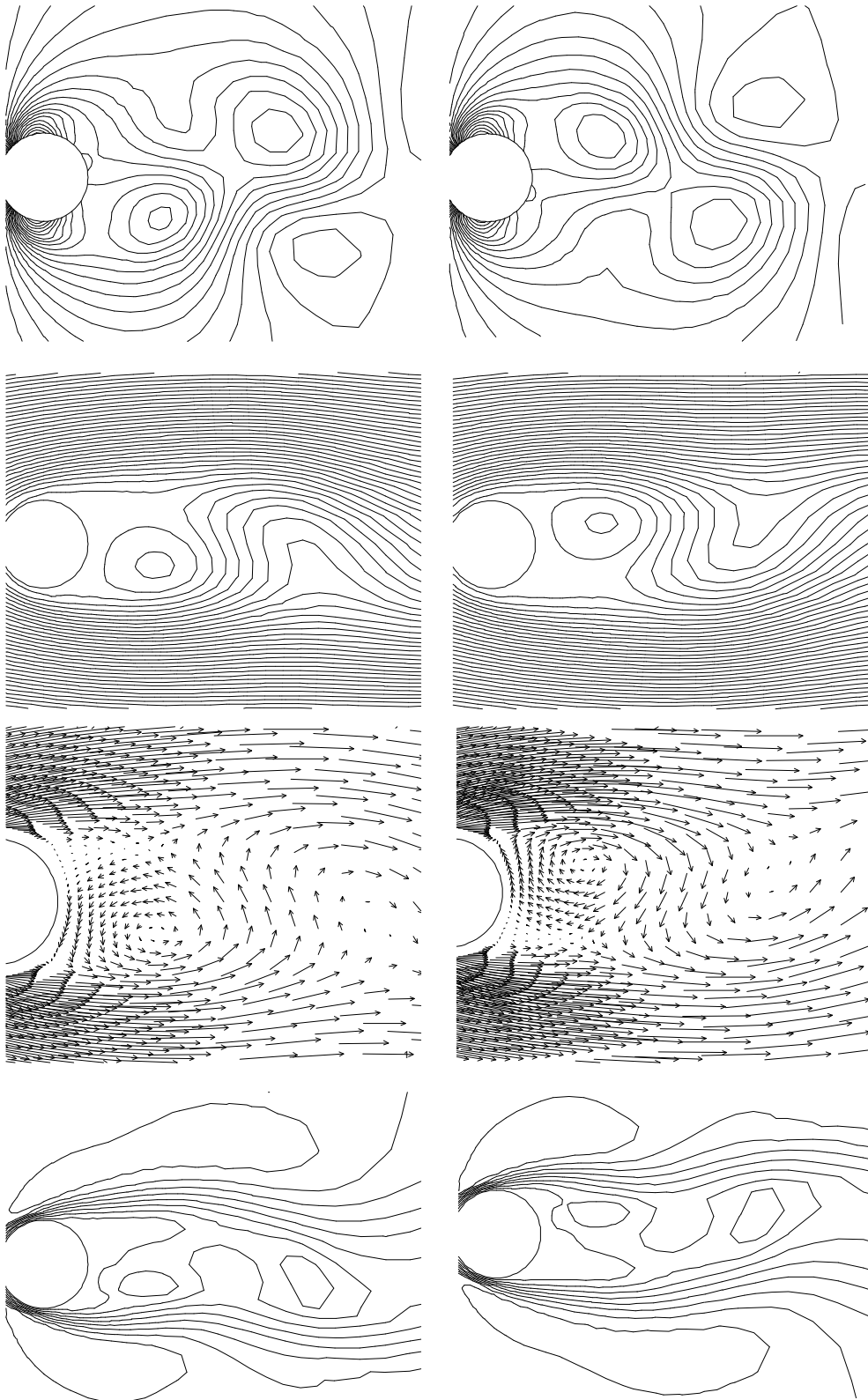


Figure 4.4.19. Detailed view of the vortex shedding around the cylinder at $Re=100$. Left column: results at $t=t_{ref}$. Right column: results at $t=t_{ref}+\tau/2$ (after half period). In both columns the results shown are, from top to bottom, pressure contours, streamlines, velocity vectors and contours of velocity norm respectively.

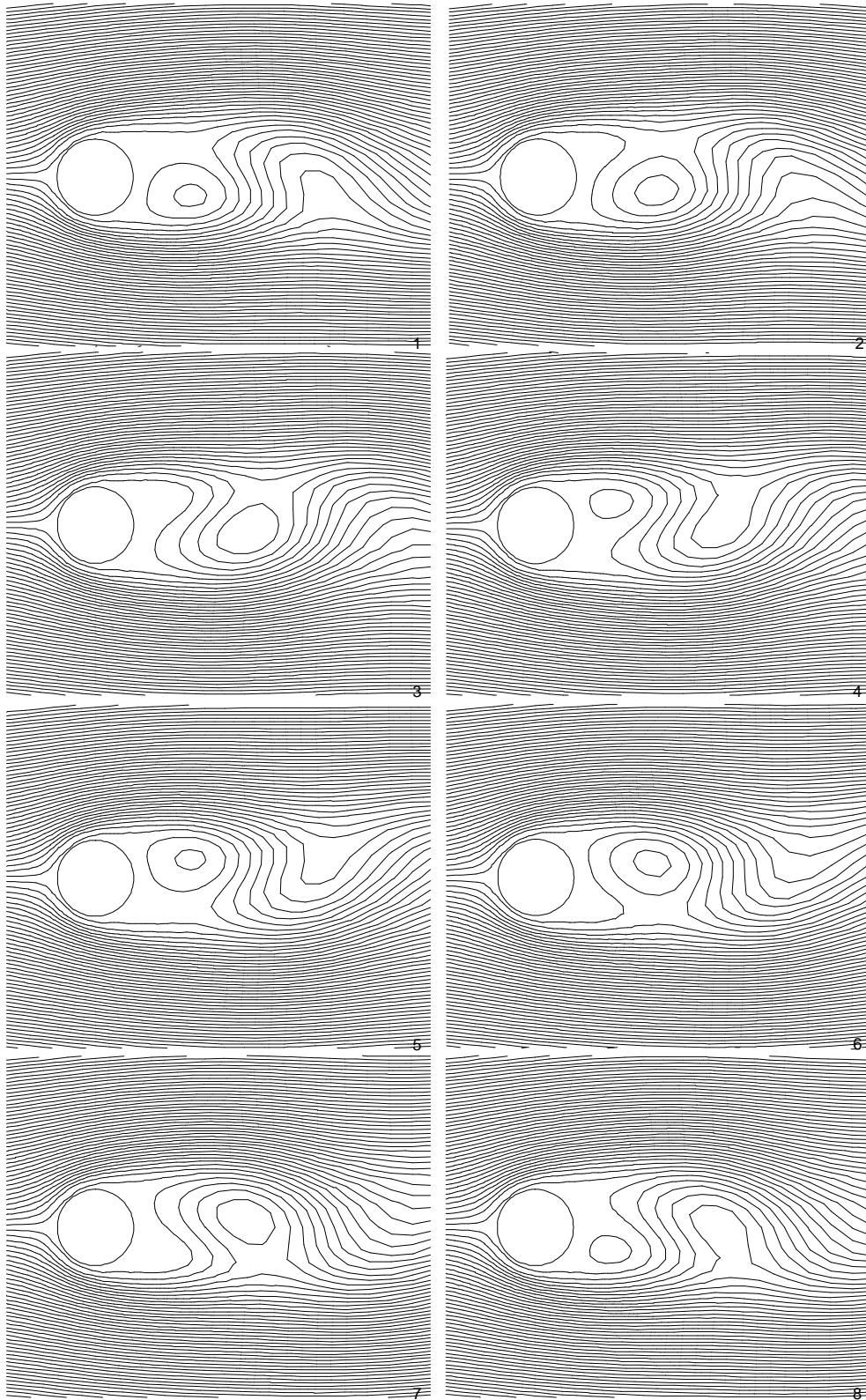


Figure 4.4.20. Detail of a full vortex shedding around the cylinder at $Re=100$. The results cover a full period, starting at $t=t_{ref}$ in (1). Each picture differs from the previous one in $\tau/8$ time units.

The solution of the problem at $R_e=200$ has been also considered. The results at this Reynolds number do not differ qualitatively from those found at $R_e=100$, being the only important difference the shortening of the period due to the decrease of the kinematic viscosity. Figure 4.4.21 plots the vertical component of the velocity at point A during three periods, starting at t_{ref} . In this case, the estimated period of the vortex shedding is about 4.8 time units. It should be remarked that the oscillatory behaviour at $R_e=200$ seems to be the result of two composed frequencies. Finally, the pressure contours and the streamlines around the cylinder at t_{ref} and $t_{ref}+\tau/2$ are detailed in Figure 4.4.22. The comparison of these results with those shown in Figure 4.4.19 illustrates how the behaviour of the flow is quite similar in both cases ($R_e=100$ and $R_e=200$).

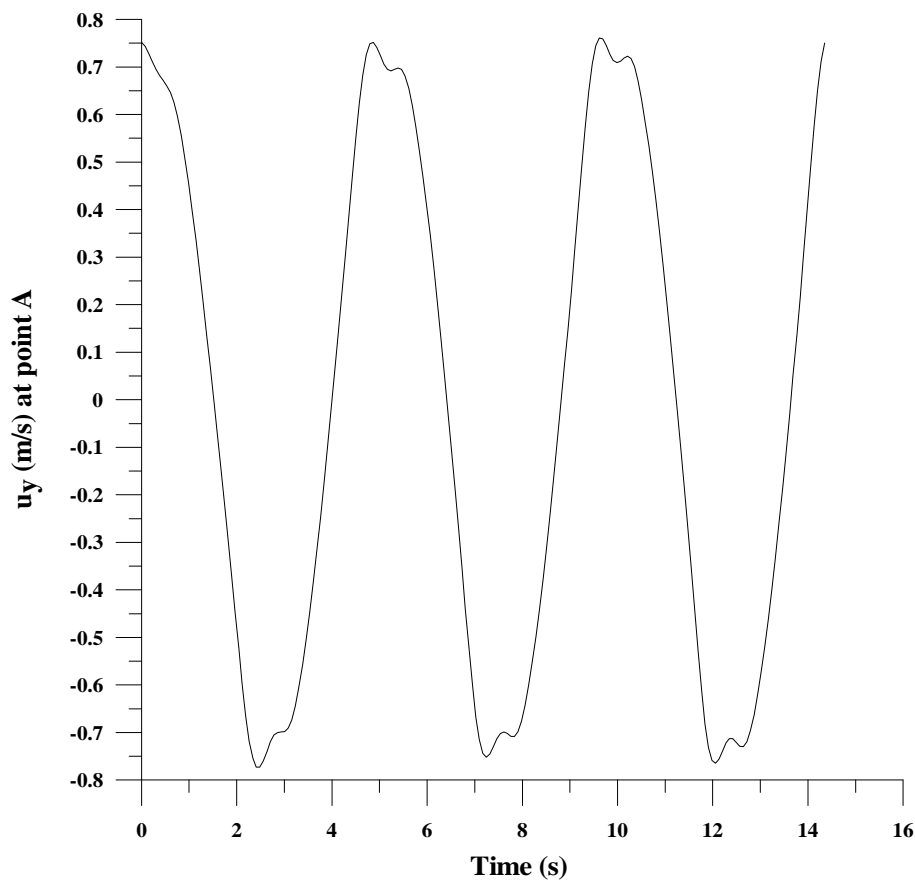


Figure 4.4.21. Results at $R_e=200$. Vertical component of the velocity at point A versus time during three periods. The origin of the abscissa is the time instant $t = t_{ref}$. The period found is about 4.8 time units. Note how the oscillatory behaviour seems to be the result of two composed frequencies.

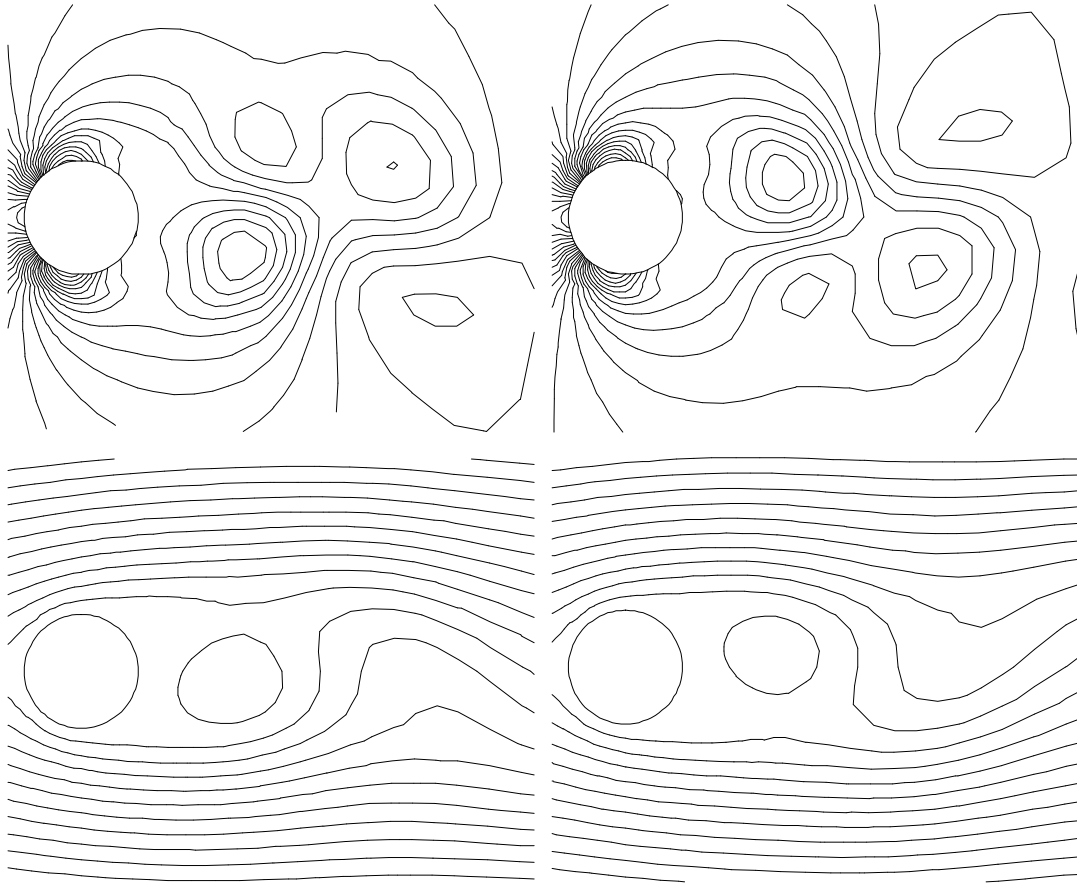


Figure 4.4.22. Detailed view of the vortex shedding around the cylinder at $R_c=200$. Left column: results at $t=t_{ref}$. Right column: results at $t=t_{ref}+\tau/2$. Top: pressure contours. Bottom: streamlines.

4.4.3 Fluid in a Heated Cavity

In this example, an homogeneous low-Prandtl-number fluid is enclosed within a square cavity $[0,1] \times [0,1]$. The vertical walls of the cavity are isothermal and are kept to different temperatures while the horizontal upper and lower walls are considered to be adiabatic. The fluid has constant viscosity and density except in the body forces term which couples the Navier-Stokes equations with the energy transport equation by means of the *Boussinesq hypothesis*¹. With this assumption, as soon as a thermal gradient is imposed between walls of the cavity, the buoyancy forces will tend to generate a convective motion. Boundary and initial conditions for this problem are schematically illustrated in figure 4.4.23. The whole fluid is initially at rest at the cold wall temperature $T = T_1$. One vertical wall is then suddenly heated to a higher temperature $T = T_2$ originating thus the convection. The non-slip condition is imposed at the walls of the chamber while pressure is set to zero at the top right corner of the cavity.

The characteristics of the problem depend on the *Prandtl* and the *Grashof* numbers, defined respectively as

$$\text{Pr} = \frac{\boldsymbol{n}}{k} \quad (4.4.4)$$

$$\text{Gr} = \frac{\boldsymbol{a} |\boldsymbol{g}| d^3 \Delta T}{\boldsymbol{n}^2} \quad (4.4.5)$$

where \boldsymbol{n} is the kinematic viscosity, k is the thermal conductivity, \boldsymbol{a} is the thermal expansion coefficient, \boldsymbol{g} is the gravity acceleration, d is a characteristic length (here the size of the cavity) and ΔT is the thermal gradient.

Observation The Prandtl number of a fluid determines the relation between mechanical and thermal diffusions. A low-Prandtl-number fluid (such the one considered in this example) diffuses heat more rapidly than momentum. The product between the Prandtl and the Grashof numbers is known as the *Rayleigh number*. In many problems involving natural convection, the Rayleigh number must exceed some threshold value in order to convection occur. This is the case, for instance, of the thermal convection in a layer of fluid heated from below, where the

¹ In this hypothesis it is assumed that the density is constant everywhere except in the body forces term of the momentum equation (4.1.3). In this term, the density is given by $\boldsymbol{r} = \boldsymbol{r}_o (1 + \boldsymbol{a} (T_o - T))$, where \boldsymbol{r}_o is the

critical Rayleigh number is 675 if the boundaries are stress free or 1707 in the case of the non-slip velocity boundary conditions [Turcotte and Schubert, 1982]. However, in the case of a fluid subjected to horizontal temperature gradients the convective motion is generated even for infinitesimally small temperature gradients, i.e. for any Rayleigh number.

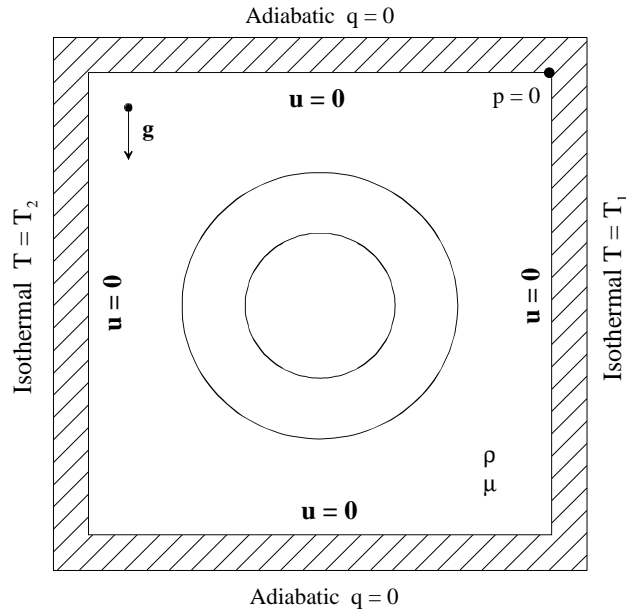


Figure 4.4.23. Boundary conditions of the problem. A fluid of density ρ and viscosity μ is initially at rest and at temperature $T=T_1$. A convective motion is induced by suddenly heating one vertical wall to a higher temperature $T=T_2$. The horizontal walls are adiabatic, i.e. there is not heat flux across them. The non-slip condition is imposed at the walls of the chamber while pressure is set to zero at the top right corner of the cavity.

The problem of transient natural convection of low-Prandtl-number fluids in a heated cavity for different combinations of the Prandtl and Grashof numbers is extensively discussed in [Mohamad and Viskanta, 1991]. In this paper, the authors solve the problem using finite differences in a fine mesh (up to 81×81 nodal points) and show that for some combinations of values there is a unique and steady solution of the Navier-Stokes equations coupled with the energy equation by means of the Boussinesq hypothesis while, in contrast, other combinations give rise to transient behaviours. In particular, one example of each case, corresponding respectively to $Pr = 0.005$, $Gr = 3 \times 10^6$ (example A) and $Pr = 0.01$, $Gr = 10^7$ (example B), are presented here. The results are compared with those of [Mohamad and Viskanta, 1991]. The correctness of the solution can be checked by means of the average *Nusselt number* at the vertical walls, computed as

density at the reference temperature T_0 and α is the thermal expansion coefficient. Obviously, this term couples the momentum equation with the energy equation.

$$N_u = - \int_0^1 \frac{\partial T}{\partial x} \Big|_{x=0,1} dy \quad (4.4.6)$$

Figure 4.4.24 shows the spatial discretisation of the problem, for which a uniform mesh composed of 1600 bilinear elements and 1681 nodal points is considered. The solutions have been obtained using the implicit second order in time scheme for both the mechanical and the energy equations (i.e. $\bar{\mathbf{q}}_1 = \bar{\mathbf{q}}_2 = \bar{\mathbf{q}}_3 = (1/2, 1/2, 0)$). The pressure gradient projection technique and the incremental fractional step method have been also employed.

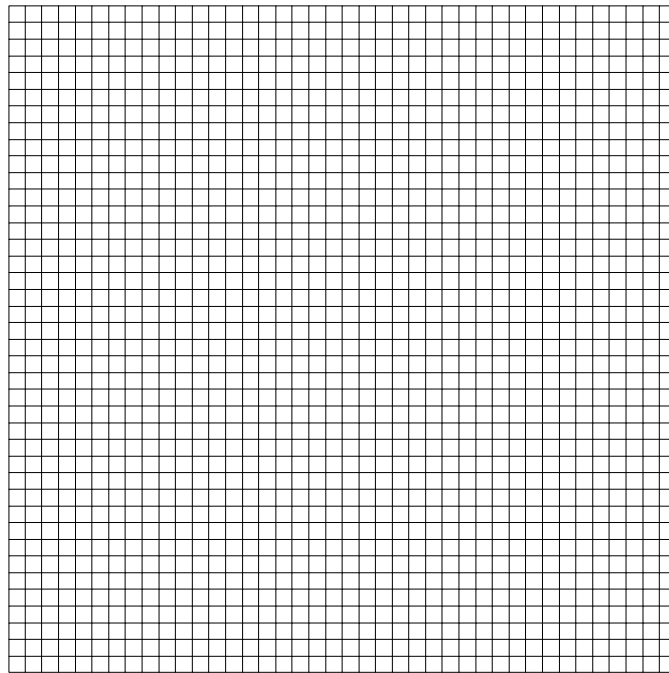


Figure 4.4.24. Spatial discretisation of the problem. Uniform mesh with 1600 (40×40) bilinear elements and 1681 nodal points.

Results for example A are shown in figures 4.4.25 and 4.4.26. Figure 4.4.25 illustrates how for this combination of Grashof and Prandtl numbers there is convergence to a steady state. This can be observed, for instance, by plotting the temporal evolution of the horizontal component of the velocity at the centre of the cavity. The steady temperature profile along a vertical line through the centre of the cavity is also shown in this figure. Figure 4.4.26 shows the steady results for example A. Some results to illustrate the oscillating flow of example B are given in Figure 4.4.27. For both examples, the temporal evolution of the Nusselt number at the isothermal vertical walls of the cavity is illustrated in figure 4.4.28. Finally, table 4.4.1 gives some results and its comparison with the values obtained by [Mohamad and Viskanta, 1991]

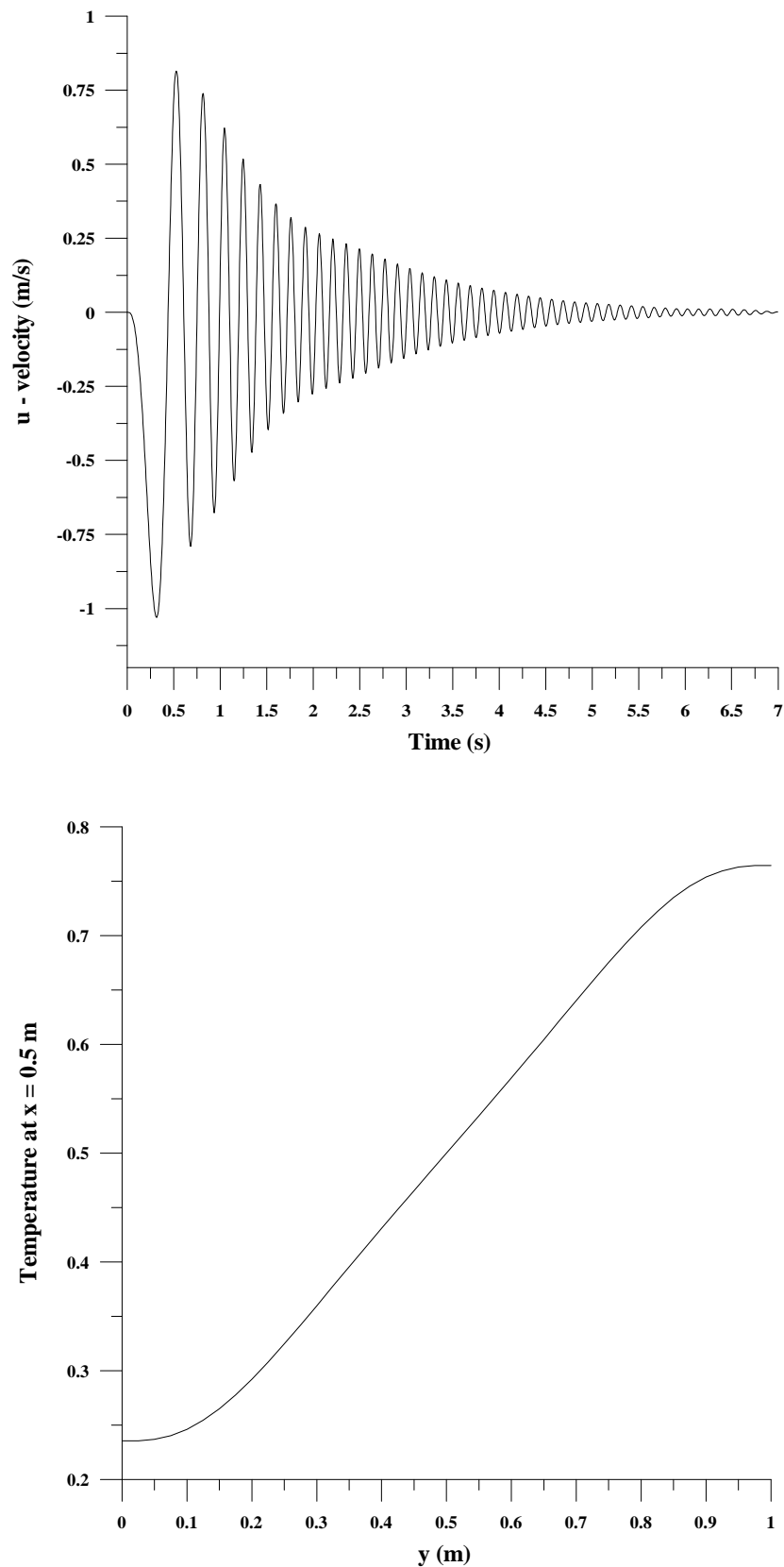


Figure 4.4.25. Results for example A. Top: u -velocity versus time at the centre of the cavity. Note how in this case the results converge to the steady solution. Bottom: temperature profile along a vertical line through the centre of the cavity once the steady state has been reached.

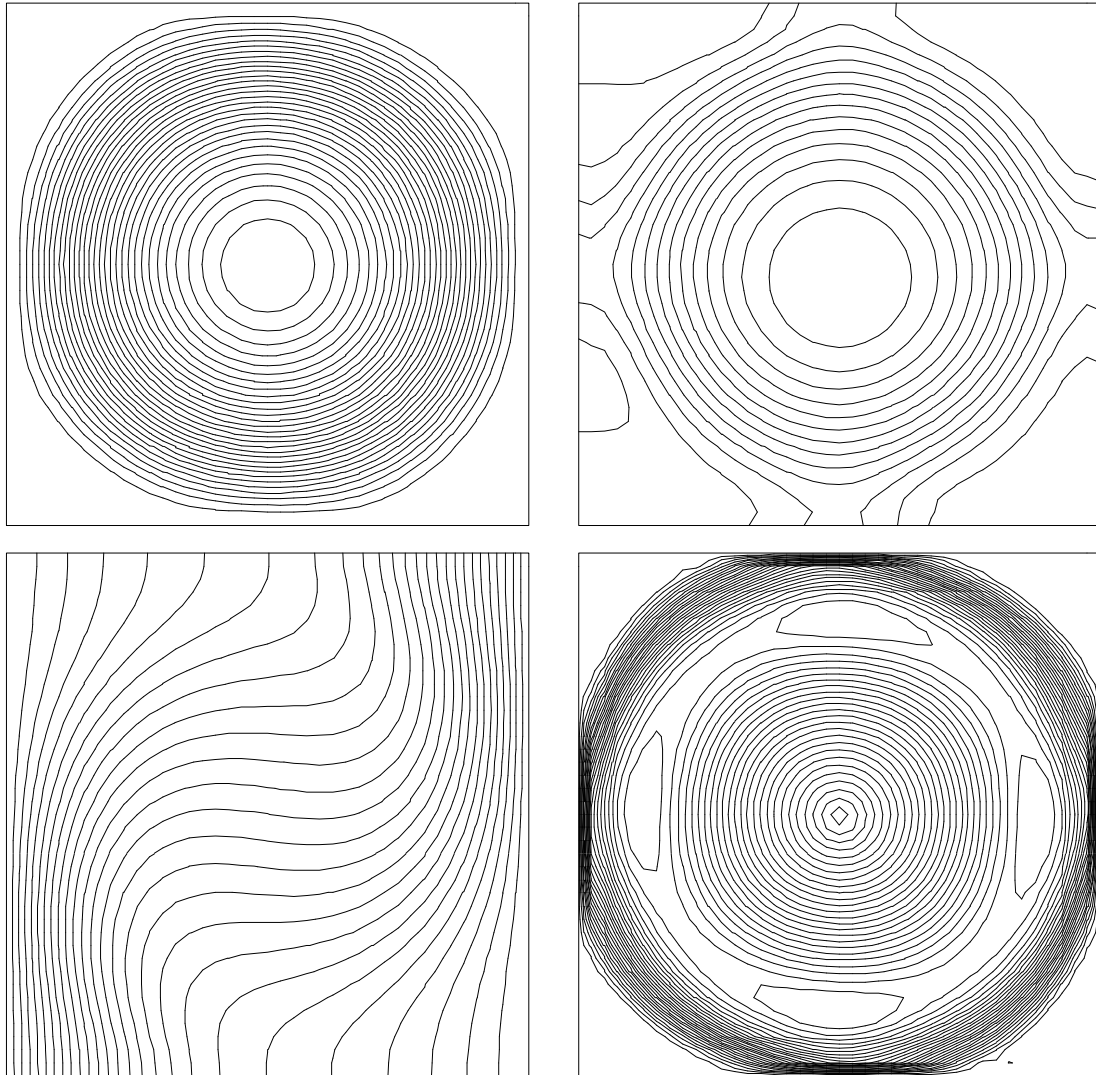


Figure 4.4.26. Steady results for example A. Top left: streamlines. Top right: pressure contours. Bottom left: temperature. Bottom right: contours of velocity norm.

	Nu	Ψ_{\max}	Ψ_{\min}
Example A			
Pr = 0.005	2.09	-5.24	0.02
Gr = 3×10^6	(2.10)	(-5.24)	(0.03)
Example B			
Pr = 0.01	3.35	-8.80	0.07
Gr = 10^7	(3.23)	(-7.89)	(0.09)

Table 4.4.1. Nusselt number and streamlines peaks for examples A and B. In the oscillatory case, values are averaged over time. Results of [Mohamad and Viskanta, 1991] are shown in parenthesis.

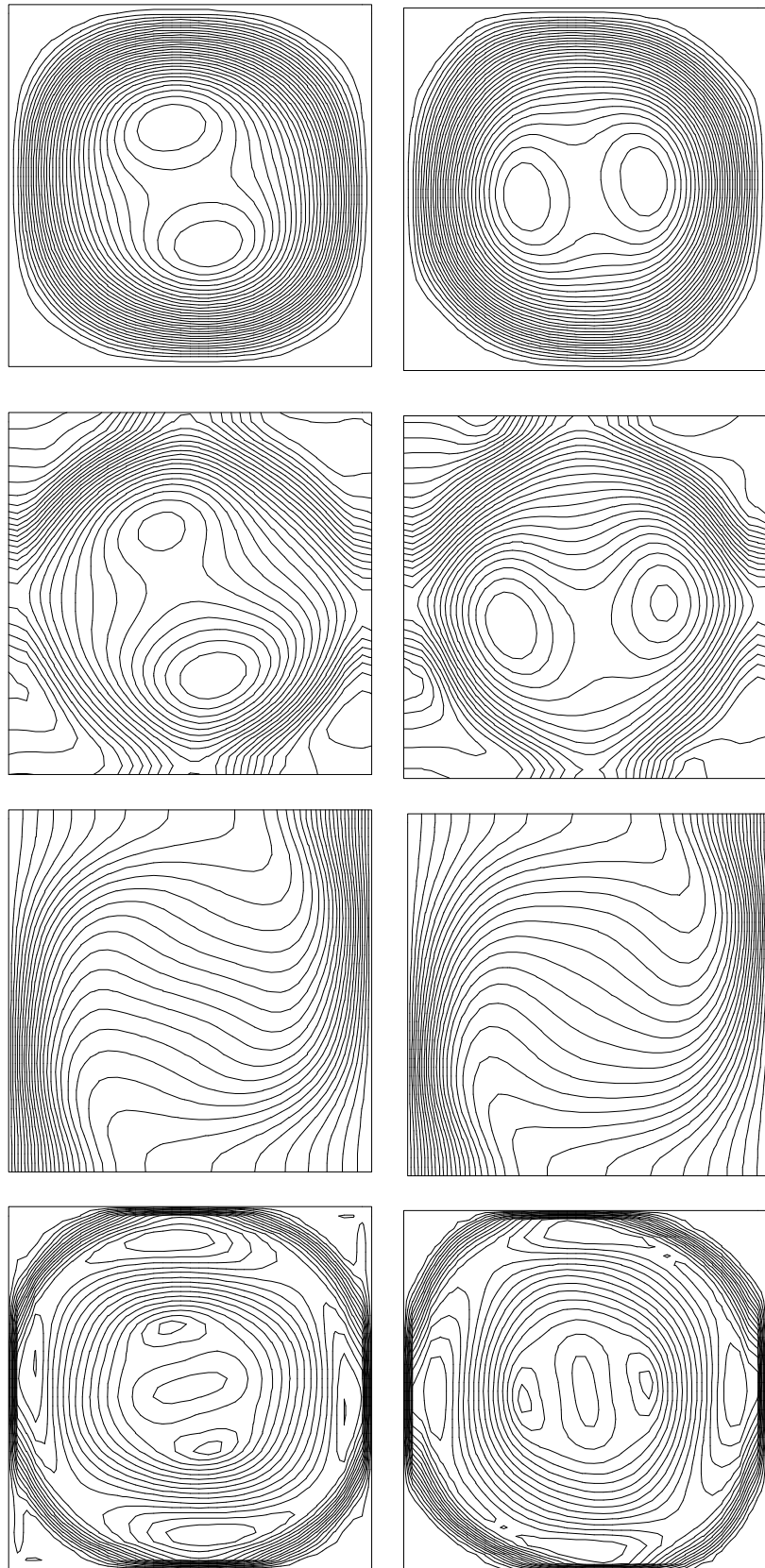


Figure 4.4.27. Results for example B (oscillating solution). Left and right results differ from a quarter of period. The results shown are, from top to bottom, streamlines, pressure contours, temperature and contours of velocity norm respectively.

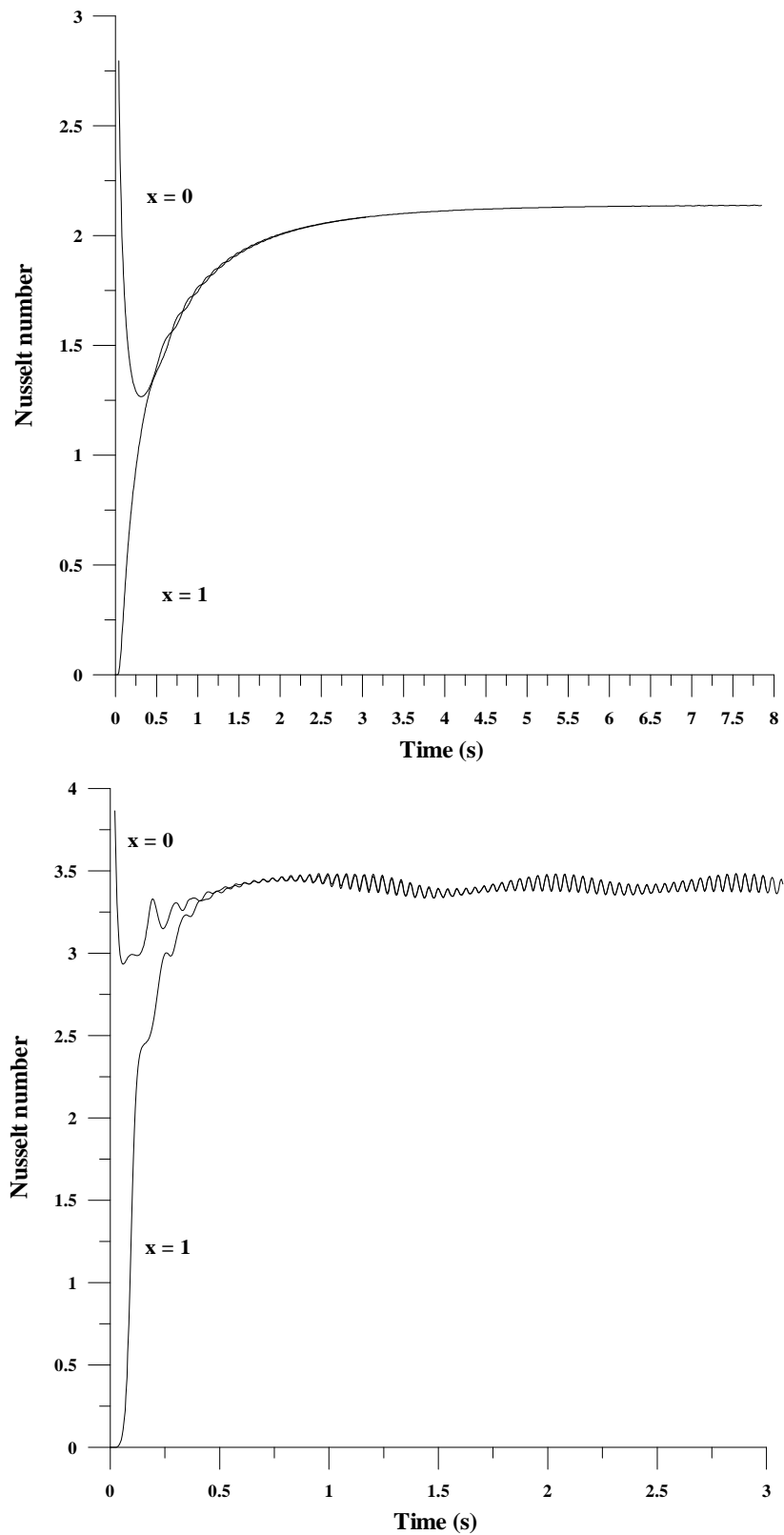


Figure 4.4.28. Temporal evolution of the Nusselt number at the vertical walls of the cavity (corresponding to $x=0$ and $x=1$). Top: example A. Bottom: example B. In the first case, the Nusselt number converges to 2.09, while in the second is oscillatory with an average value over time of 3.35.

4.4.4 Perfect Gas Flowing over a NACA Profile

This example illustrates the behaviour of the algorithm for compressible inviscid flows. A perfect gas at low Mach number flows over a NACA¹ profile. Boundary conditions for the problem are illustrated in figure 4.4.29. At the computational inlet velocity is prescribed to (1,0) and temperature is set to T_∞ , while at the computational outlet density (or pressure) is fixed to ρ_∞ (to P_∞). Since the flow is inviscid, the slip boundary condition is applied along the profile, that is, only the normal component of the velocity is set to zero. Figure 4.4.30 shows the spatial discretisation of the problem, for which a mesh composed of 4902 triangular elements (2556 nodal points) has been used.

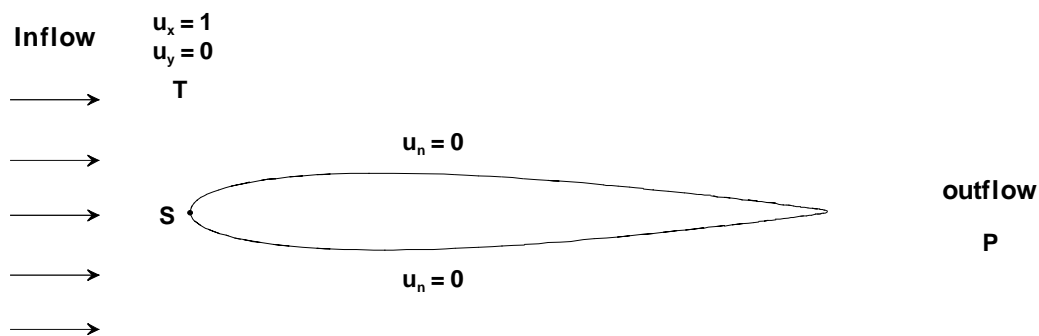


Figure 4.4.29. Boundary conditions of the problem. Properties are computed at the stagnation point S.

The properties of the flow are characterised by the *Mach number*, which for a perfect gas is given by

$$M_c \equiv \frac{|\mathbf{u}|}{c} = \frac{|\mathbf{u}|}{\sqrt{g R T}} \quad (4.4.7)$$

where \mathbf{u} is the velocity, g is the adiabatic exponent, R is the perfect gas constant and T is the temperature. In particular, when $T = T_\infty$ the above expression gives the Mach number at the inflow M_c^∞ . It can be shown that for Mach numbers equal or higher than $M_c^\infty = 0.5$ some additional shock capturing diffusion is needed due to the strong gradients present in the solution [Codina *et al.*, 1997]. Since the version of the algorithm used this work does not contemplate the possibility of shocks, the problem has been considered only at Mach number of

¹ NACA means National Advisory Committee for Aeronautics. NACA profiles are characterised by four numbers. In particular, the profile used here is the NACA0012. These profiles are available at <http://www.eng.mu.edu/~ses/solar/structures/foil/naca.html>.

4.4 Numerical Examples

$M_c^\infty = 0.3$. Considering this Mach number and using $g = 1.4$ and $R = 1.6$, the inflow temperature T_∞ is directly given by the above equation.

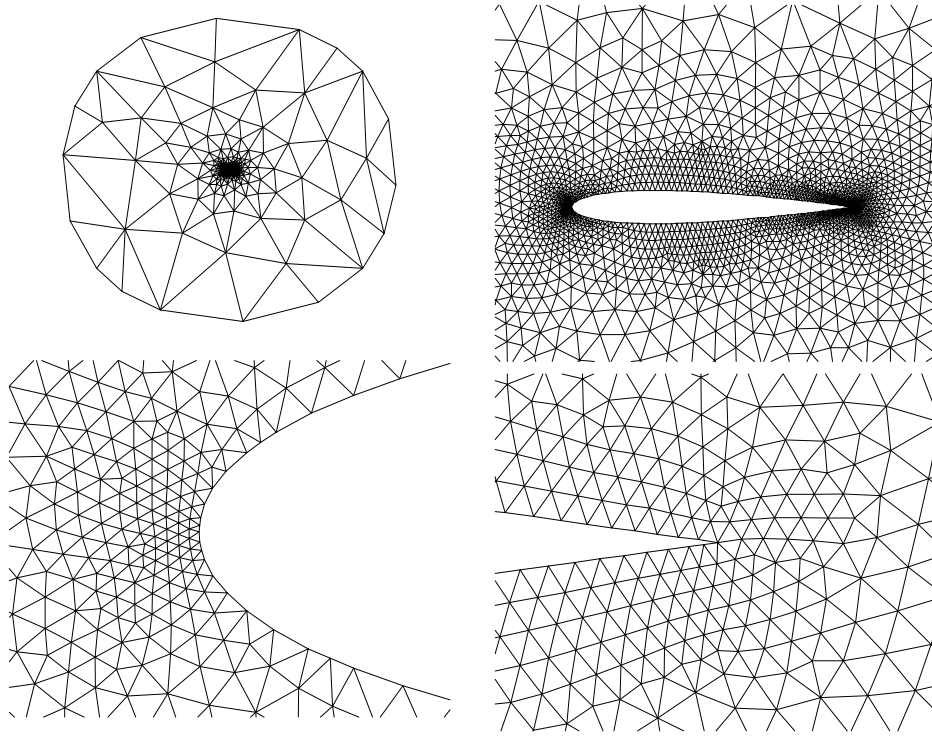


Figure 4.4.30. Spatial discretisation of the problem. The mesh is unstructured and composed of 4902 triangular elements (2556 nodal points). Top: general views of the mesh. Bottom: close up views of the front at the back of the wing.

The numerical solution has been obtained using the incremental fractional step method and the fully implicit scheme (first order). Figure 4.4.31 shows the pressure contours once the steady state has been reached. Figure 4.4.32 shows density and Mach number contours and the streamlines at the vicinity of the wing. A good test for the correctness of the solution is to compute the properties (pressure, temperature and density) at the stagnation point S (see figure 4.4.29). For the perfect gas, the analytical solution at the stagnation point is known and given by

$$r_s = r_\infty \left(1 + \frac{g-1}{2} M_c^{\infty 2} \right)^{\frac{1}{g-1}} \quad (4.4.8)$$

$$p_s = p_\infty \left(1 + \frac{g-1}{2} M_c^{\infty 2} \right)^{\frac{g}{g-1}} \quad (4.4.9)$$

$$T_s = T_\infty \left(1 + \frac{g-1}{2} M_c^{\infty 2} \right) \quad (4.4.10)$$

Table 4.4.2 compares the theoretical and the numerical results obtained. As observed from this table, the obtained results agree reasonably well with the theoretical values.

	Theoretical value	Obtained result
P_s	8.44	8.49
r_s	1.04	0.99
T_s	5.04	5.35

Table 4.4.2. Comparison between theoretical and numerical results at the stagnation point.

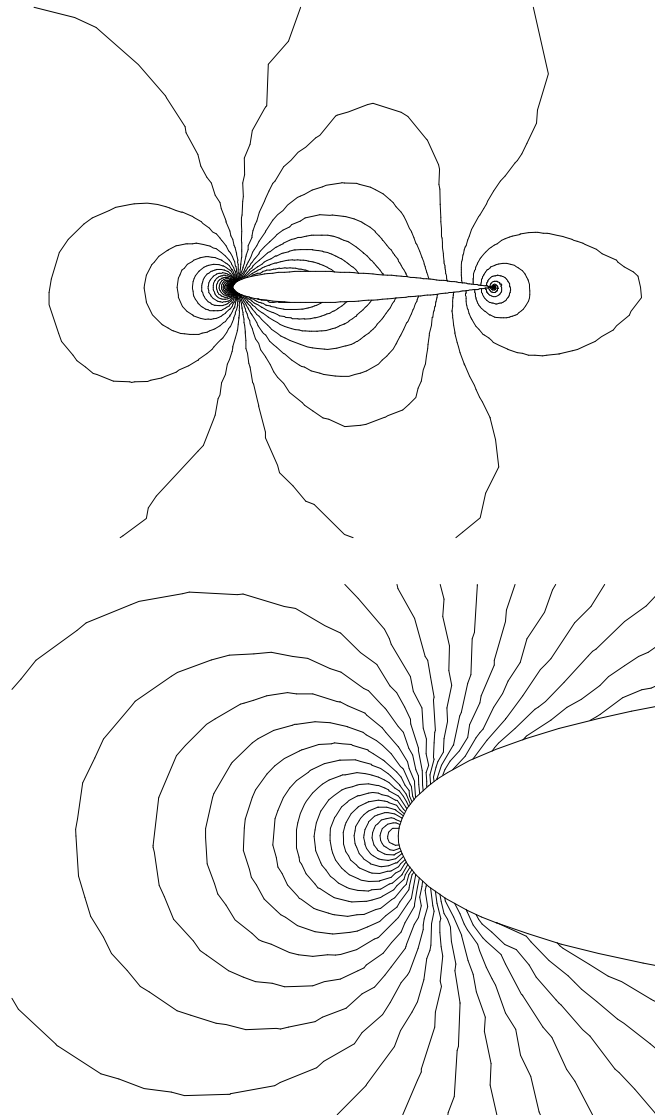


Figure 4.4.31. Pressure contours. Top: general view. Bottom: zoom around the front of the wing, at the stagnation point.

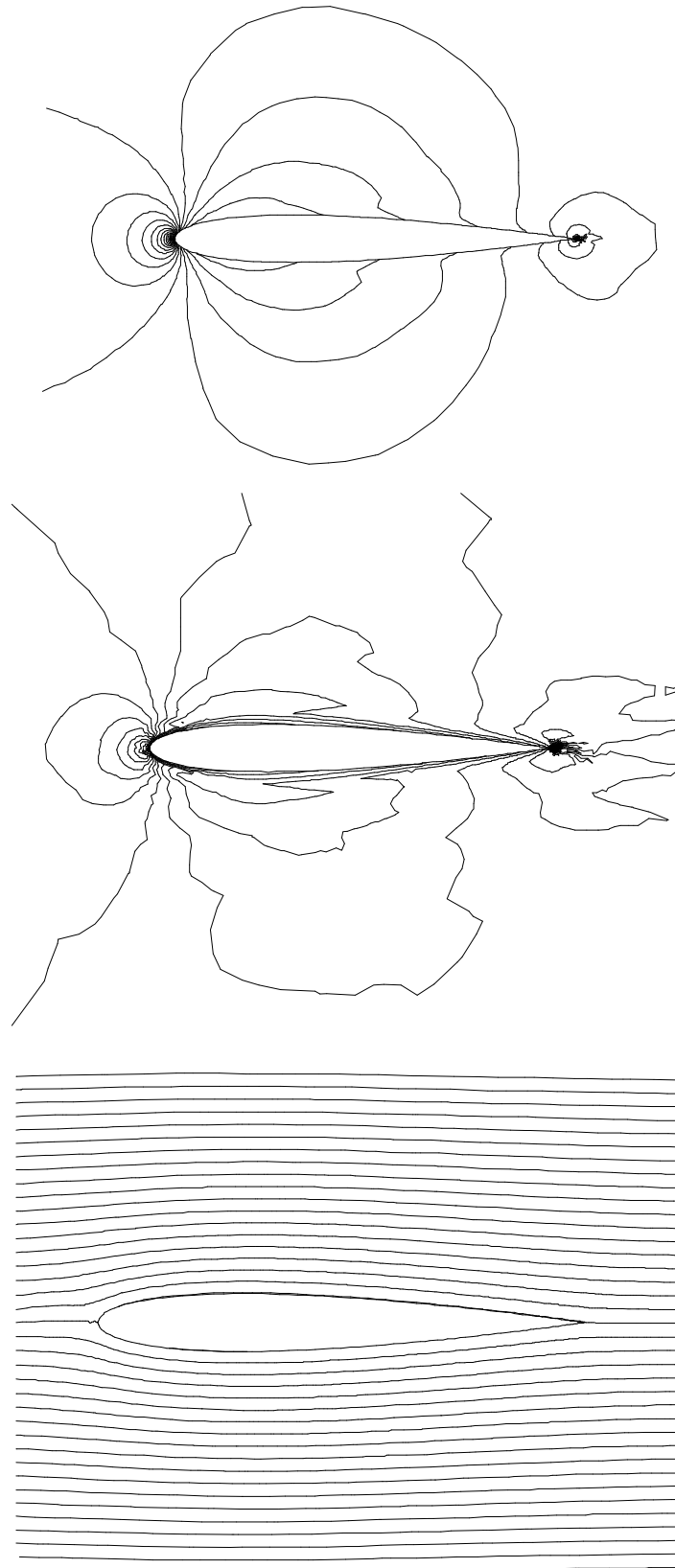


Figure 4.4.32. Results around the wing. Top: contours of density. Middle: Mach number contours. Bottom: Streamlines.

4.4.5 The Stokes Problem

This example illustrates the fluid-structure interaction. The physical framework is illustrated in Figure 4.4.33. A spherical body of radius a and density ρ_s is immersed within a viscous incompressible fluid of viscosity μ and density ρ_f . Initially the body is at rest, but as it is more dense than the fluid the buoyancy forces will cause it to fall downwards with an increasing velocity \mathbf{u} . In turn, the viscous and the pressure drag forces act against this movement and tend to compensate the buoyancy effects. Since buoyancy forces are constant and drag forces are proportional to the velocity of the body, a point of zero net force is reached after some time. The body moves then with a steady or terminal velocity \mathbf{u}_s known as the *Stokes terminal velocity*.

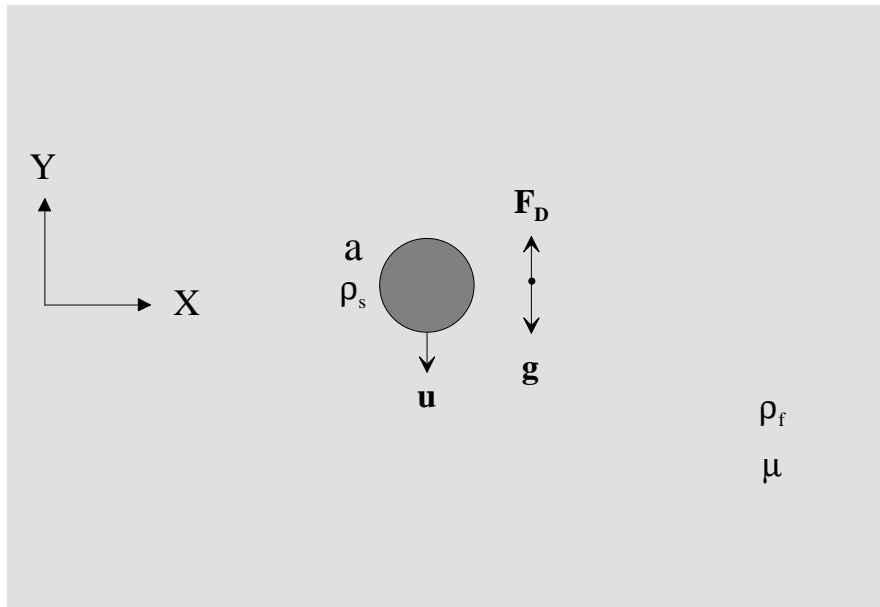


Figure 4.4.33. Sketch of the Stokes flow problem. A spherical rigid body of radius a and density ρ_s is immersed within a viscous fluid of viscosity μ and density ρ_f . Initially the body is at rest, but as it is more dense than the fluid it falls downwards with a velocity \mathbf{u} . When the drag forces \mathbf{F}_D compensate the gravitational effects \mathbf{g} the sphere reaches a steady or terminal velocity \mathbf{u}_s .

The characteristics of the problem depend on the Reynolds number, based on the radius of the sphere and on its fall velocity. At high Reynolds numbers the flow around the sphere is unsteady and complex because vortices are generated. However, at low Reynolds numbers (of the order one or smaller) the Stokes terminal velocity admits an analytical solution given by

$$\mathbf{u}_s = \frac{2(\mathbf{r}_s - \mathbf{r}_f)a^2}{9\mathbf{m}} \mathbf{g} \quad (4.4.11)$$

where \mathbf{g} is the gravity acceleration. The above equation allows to test the correctness of the numerical solution provided, of course, that this solution is obtained at low Reynolds numbers. In particular we have considered $\mathbf{r}_s = 2.0$, $\mathbf{r}_f = 1.0$, $\mathbf{m} = 10$, $\mathbf{g} = (0, -10)$ (the y-axis is positive upwards) and $a = 1.0$ so that the analytical solution predicts a terminal velocity of -0.2 in the vertical direction. Note that with this terminal velocity the Reynolds number of the problem is as low as $R_e = 0.02$ and, in consequence, the numerical terminal velocity should coincide with the analytical one.

Figure 4.4.34 shows the spatial discretisation of the problem. The axial symmetry allows to solve the three-dimensional problem as a two-dimensional one using cylindrical coordinates. Both velocity components are prescribed to zero at the top, bottom and outer computational boundaries, while only its horizontal component is set to zero along the symmetry axis. The non-slip condition is also imposed at the surface of the sphere. Pressure is set to zero at the top right corner. The computational domain has been extended up to several radius in order to minimise the effect of the boundary conditions on the final results. The coupled problem has been solved according to the methodology described in the previous section, that is, using a Crank-Nicholson scheme for the viscous and convective terms of the Navier-Stokes equations and integrating the equations of the rigid body by means of the constant average acceleration method. Figure 4.4.35 shows how the velocity of the sphere tends to converge to the analytical value. The computations have been stopped when the acceleration of the sphere is lower than 5×10^{-4} , that is, when the difference between the buoyancy and the drag forces is lower than this critical value. At this point the velocity of the sphere is 0.216, a value acceptably close to the predicted 0.222. Figure 4.4.36 shows some properties of the flow at this time instant. The velocity of the ALE dynamic mesh has been set to zero at the top, bottom and outer boundaries of the domain. At the rest of the nodal points it has been computed by means of the quasi-Laplacian method. It should be said that the total displacement of the sphere during the whole simulation is much lower than the length of the computational domain and as the external bigger elements absorb most of the deformation of the mesh, the condition of critical mesh distortion has not been achieved. Therefore, in this particular example it is not necessary to perform any remeshing. The correctness of the solution has been also tested by changing the frame of reference. Once the terminal velocity is achieved, a new velocity field can be obtained adding a negative velocity equal to that of the sphere. It has been checked that this solution is nearly equal to that of a fixed spherical body immersed in a fluid that moves with a velocity \mathbf{u}_s at the infinite.

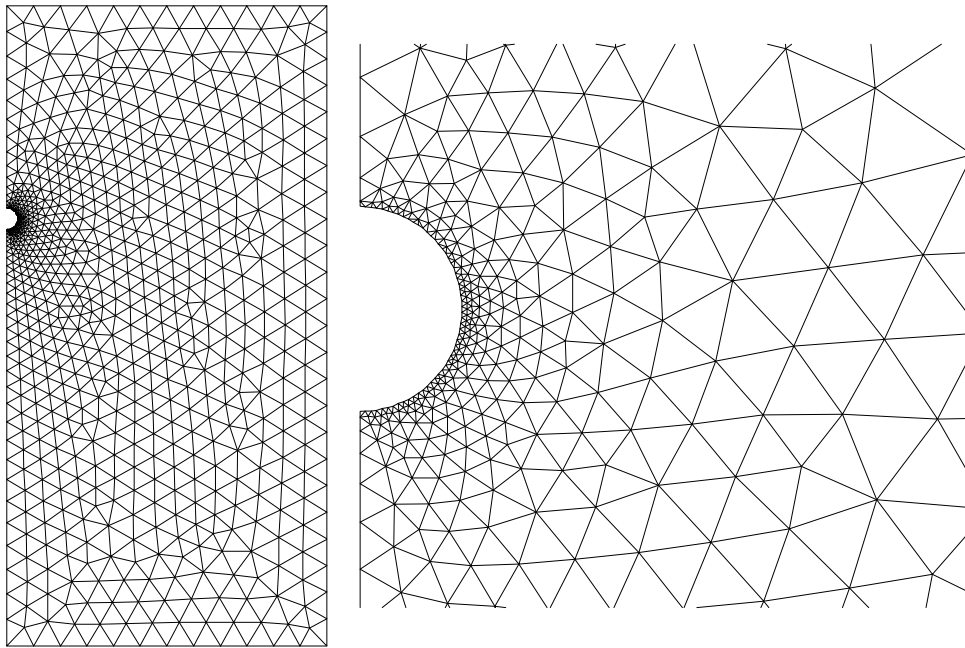


Figure 4.4.34. Spatial discretisation of the Stokes problem. View of the initial mesh (at $t=0$). The problem has axial symmetry, that is, the sphere falls immersed within a cylinder. The mesh is unstructured and composed of 1723 triangular elements. The lower part of the fluid domain has been extended up to 40 times the radius of the sphere, the upper up to 20 times and the lateral up to 30 times in order to make negligible the effect of the boundary conditions on the numerical solution. Left: general view of the mesh. Right: detail around the spherical body.

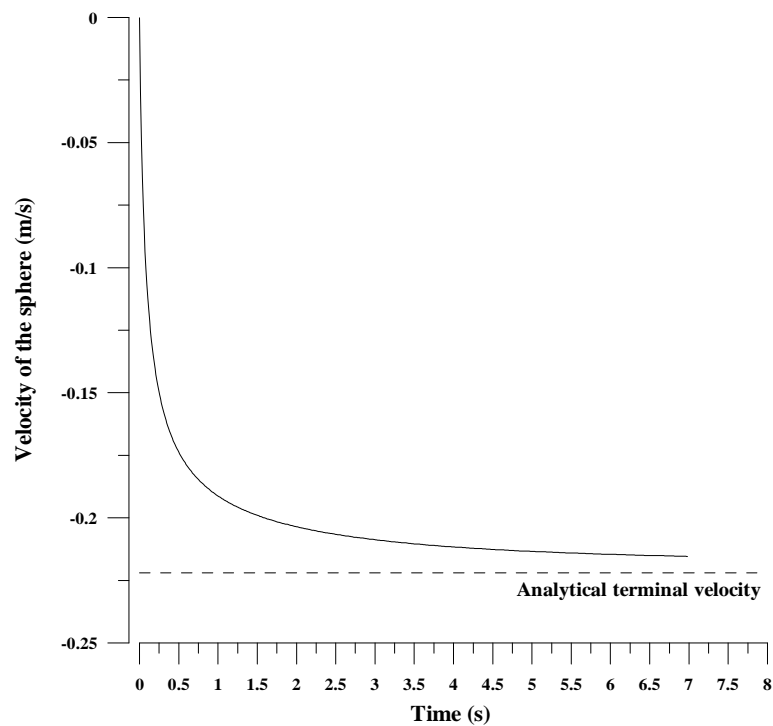


Figure 4.4.35. Fall velocity of the sphere as a function of time.

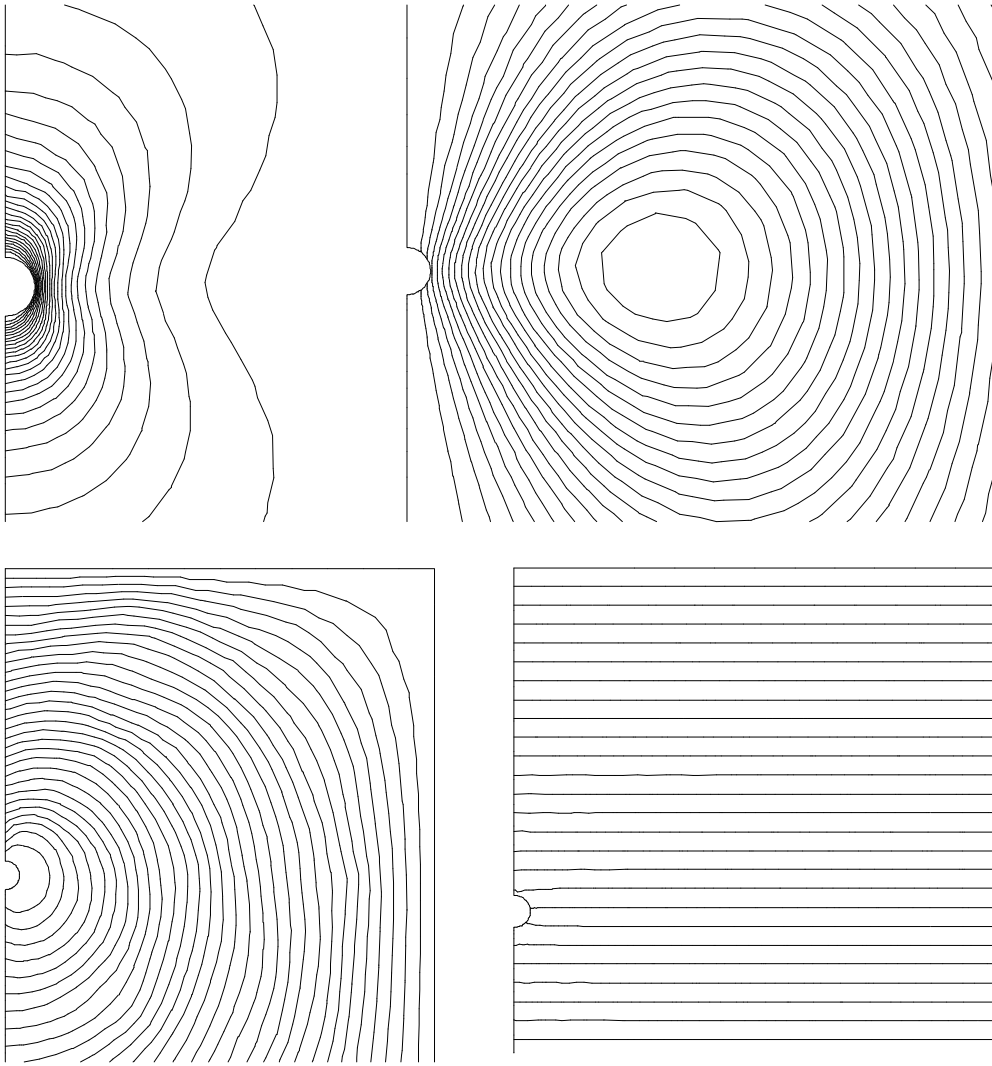


Figure 4.4.36. Numerical results once the Stokes terminal velocity has been achieved. Top left: contours of velocity norm around the sphere. Top right: stationary streamlines. Bottom left: contours of mesh velocity norm. Mesh velocity is set to zero only at the top, bottom and lateral margins of the computational domain. Bottom right: pressure contours.

4.4.6 Missile Launched from a Submarine

In this simulation, a missile with a constant unitary velocity in the vertical direction is launched from a submarine and moves within a viscous incompressible fluid (water). This example has been previously proposed by [Masud and Hughes, 1997] but considering the flow as slightly compressible. The problem involves fluid-structure interaction, but it is assumed that the properties of the flow do not affect the movement of the missile and, in consequence, the coupling is given only in one direction. As in [Masud and Hughes, 1997] the Reynolds number of the flow, based on the velocity and length of the missile, is 1000.

Figure 4.4.37 illustrates the boundary conditions of the problem. The computational domain has been extended up to 7 and 6 distance units in the horizontal and vertical directions respectively. Pressure is fixed to zero at the top of the domain, which represents the water-air interface. On all the outer boundaries, the velocity components are set to zero. The non-slip condition is also imposed at the missile and at the submarine surfaces. It means that the particles of the fluid in contact with the missile move with a velocity equal to that of the missile. Gravitational effects have been neglected.

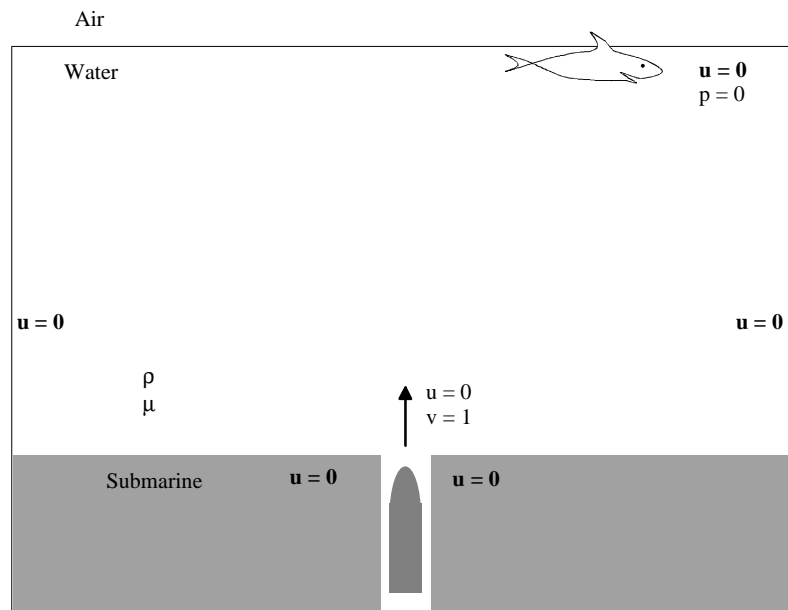


Figure 4.4.37. Schematic description of the problem. A missile with a constant velocity $(0,1)$ is launched from a submarine and moves within an incompressible fluid (water) of viscosity μ and density ρ . Velocity is set to zero at the computational boundaries, extended up to 7 and 6 distance units in the horizontal and vertical directions respectively. The non-slip condition is also imposed at the surfaces of the submarine and the missile (i.e. on the surface of the missile the velocity of the fluid particles is the same as that of the missile). Pressure is set to zero at the top of the domain, which simulates the water-air interface.

The problem has been solved according to the methodology described in the previous section, and simulates the first two seconds after the launching. Figure 4.4.38 shows a general and a detailed view of the initial mesh, composed of 20265 triangular elements and 10492 nodal points. The criteria for mesh distortion is based on the angles of the elements. A mesh is considered to be unacceptable when any of its elements has an angle lower than 10° or greater than 160° . Figure 4.4.39 illustrates this mesh criteria applied to the initial mesh (which becomes unacceptable at $t = 0.1$). When this condition is verified, a new mesh is generated and the interpolation with restrictions of the nodal variables onto the new mesh is performed. With this criteria, the whole simulation requires 15 remeshings. On average, the meshes are made of 16000 elements and 9000 nodal points. Some of these meshes are show in figure 4.4.40.

Figures 4.4.41 to 4.4.46 show respectively the pressure contours, the streamlines and the contours of mesh velocity at different time instants. It can be observed from these figures how two main vortices develop behind the tail of the missile during the early stages after the launching. These vortices become progressively elongated a break into a kind of vortex street once the missile has left the container in which is initially located.

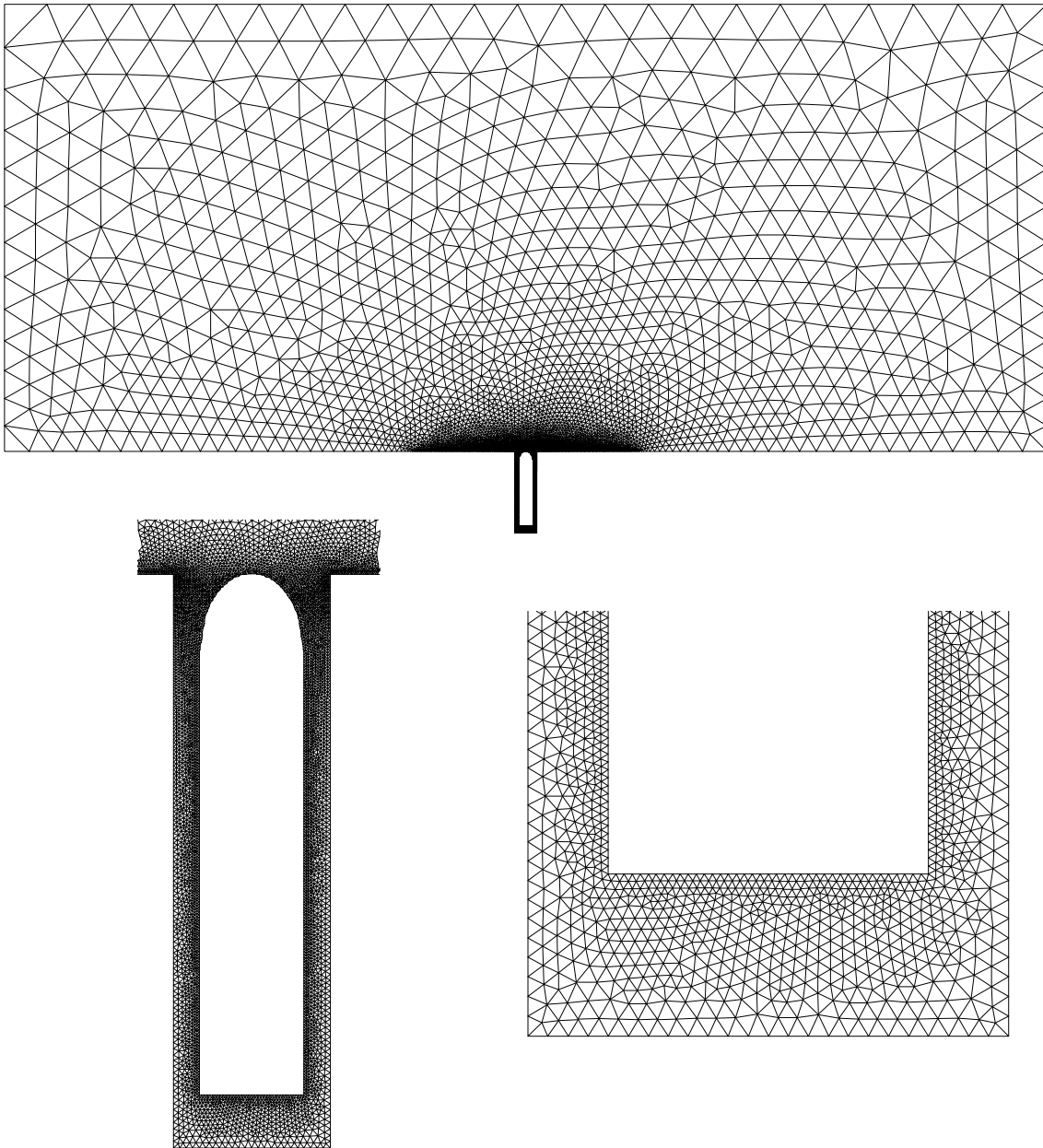


Figure 4.4.38. Views of the initial mesh, composed of 20265 triangular elements (10492 nodal points). Top: general view of the mesh. Bottom left: zoom around the missile. Bottom right: detail of the discretisation at the tail of the missile.

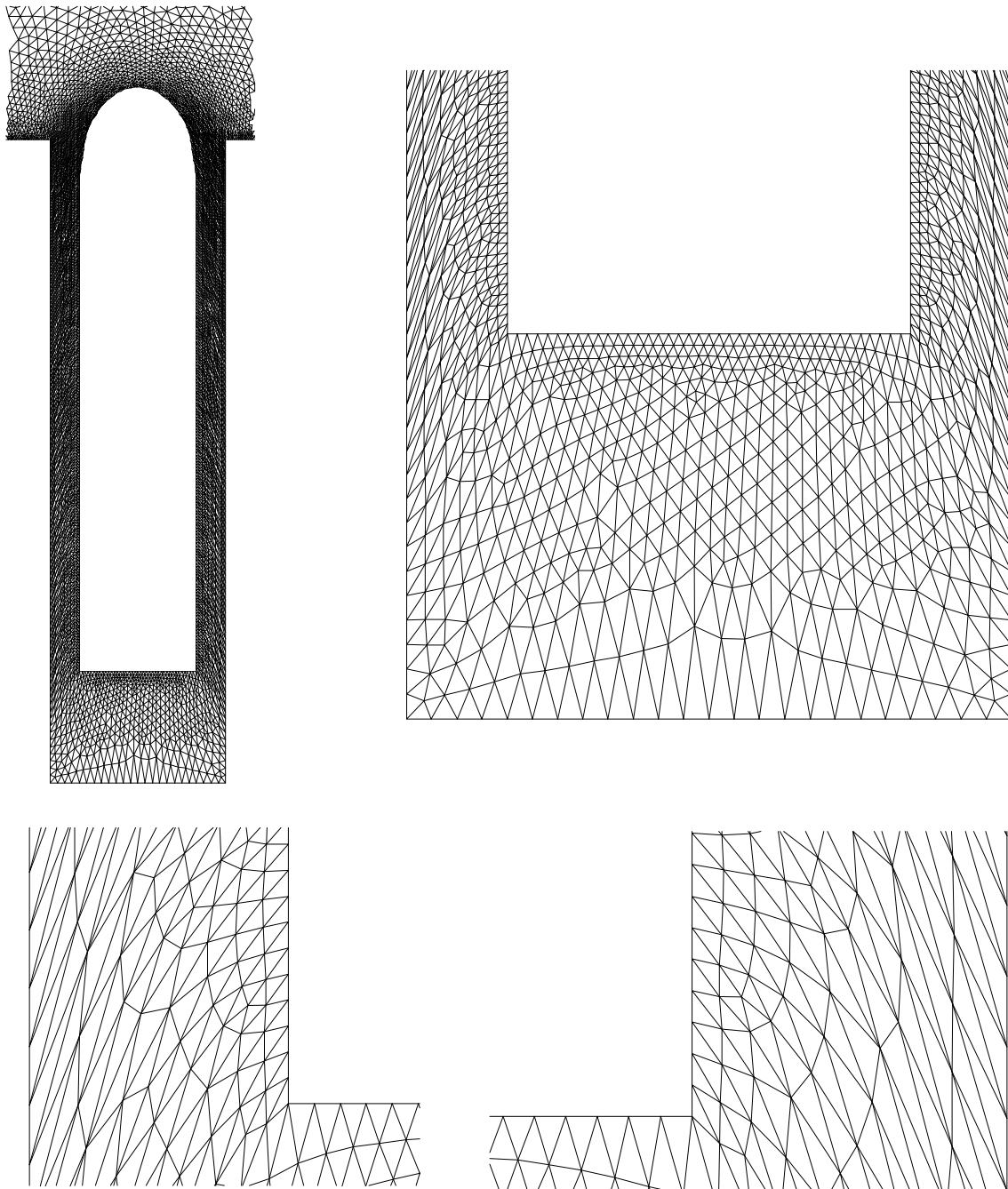


Figure 4.4.39. Final configuration of the initial mesh, at time $t = 0.1s$. Top right: general view around the missile. Top left: view of the tail. Bottom: zoom of the tail (left and right sides respectively). This figure illustrates the remeshing criteria. The most distorted elements are those near the walls of the submarine.

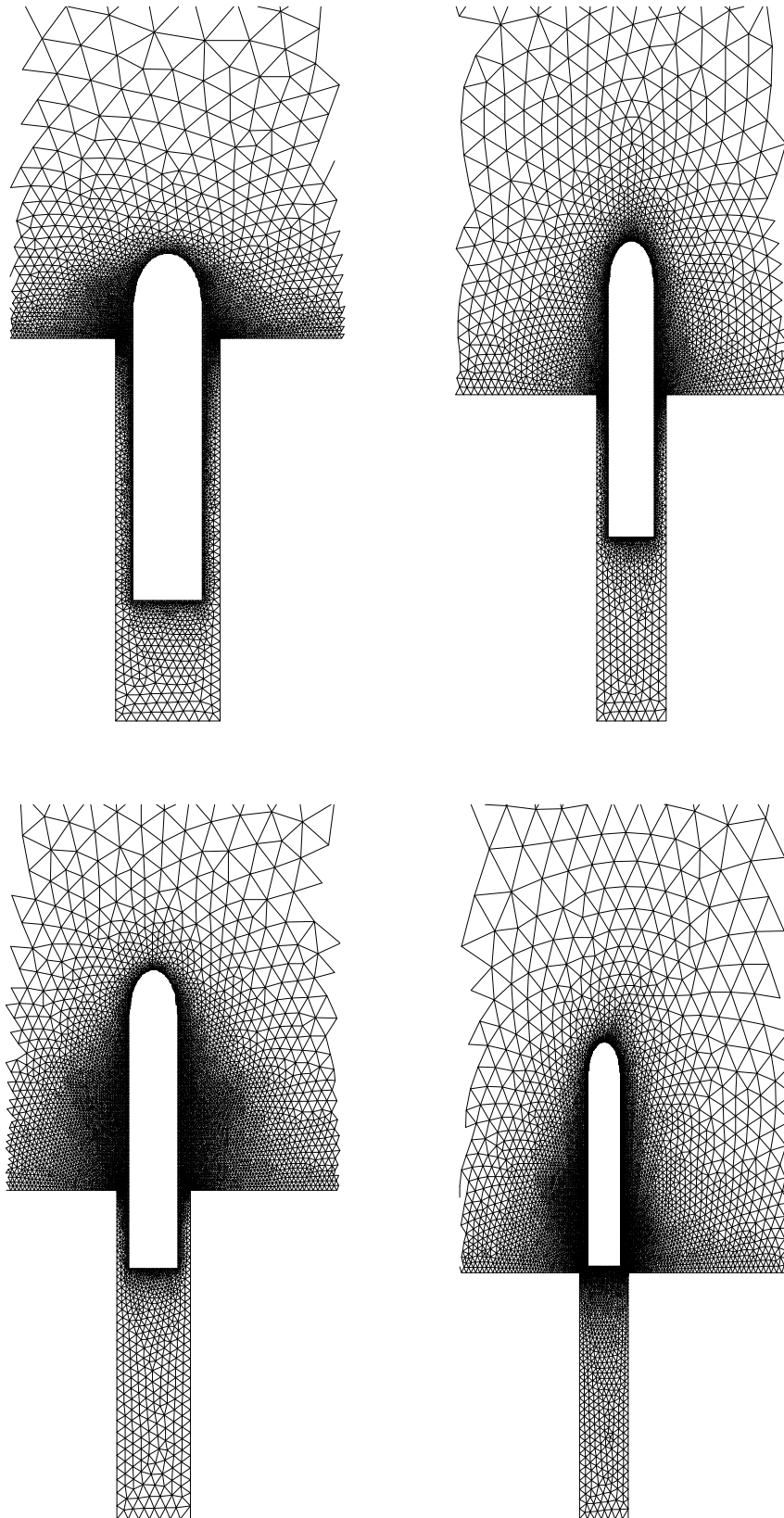


Figure 4.4.40. Partial views around the missile of the meshes 3, 7, 10 and 13. The corresponding time instants at which these meshes are generated are 0.24s, 0.52s, 0.74s and 1.03s respectively.

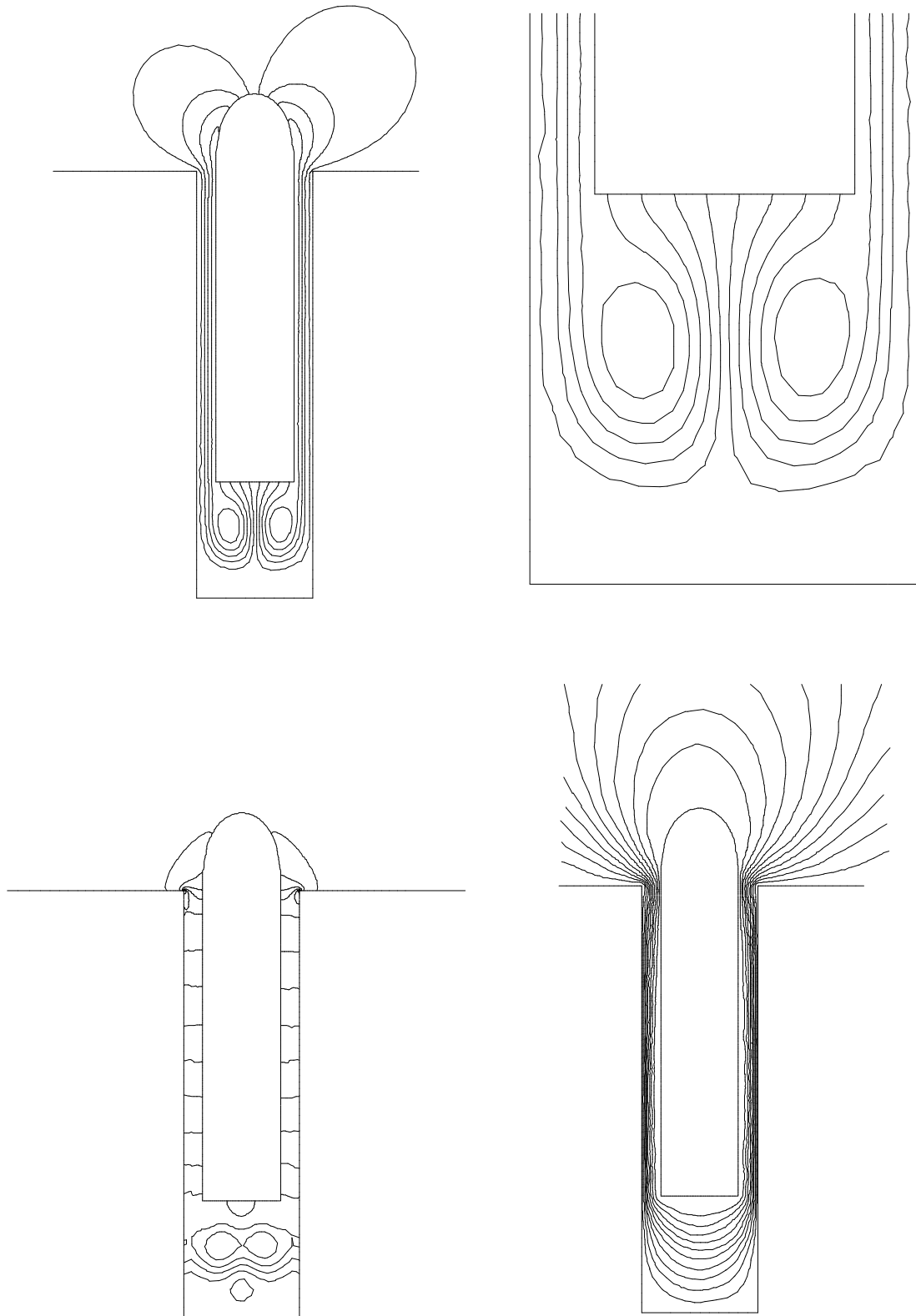


Figure 4.4.41. Numerical results at $t = 0.2s$. Top left: streamlines. Top right: zoom of the streamlines around the tail of the missile. Bottom left: pressure contours. Bottom right: contours of mesh velocity norm.

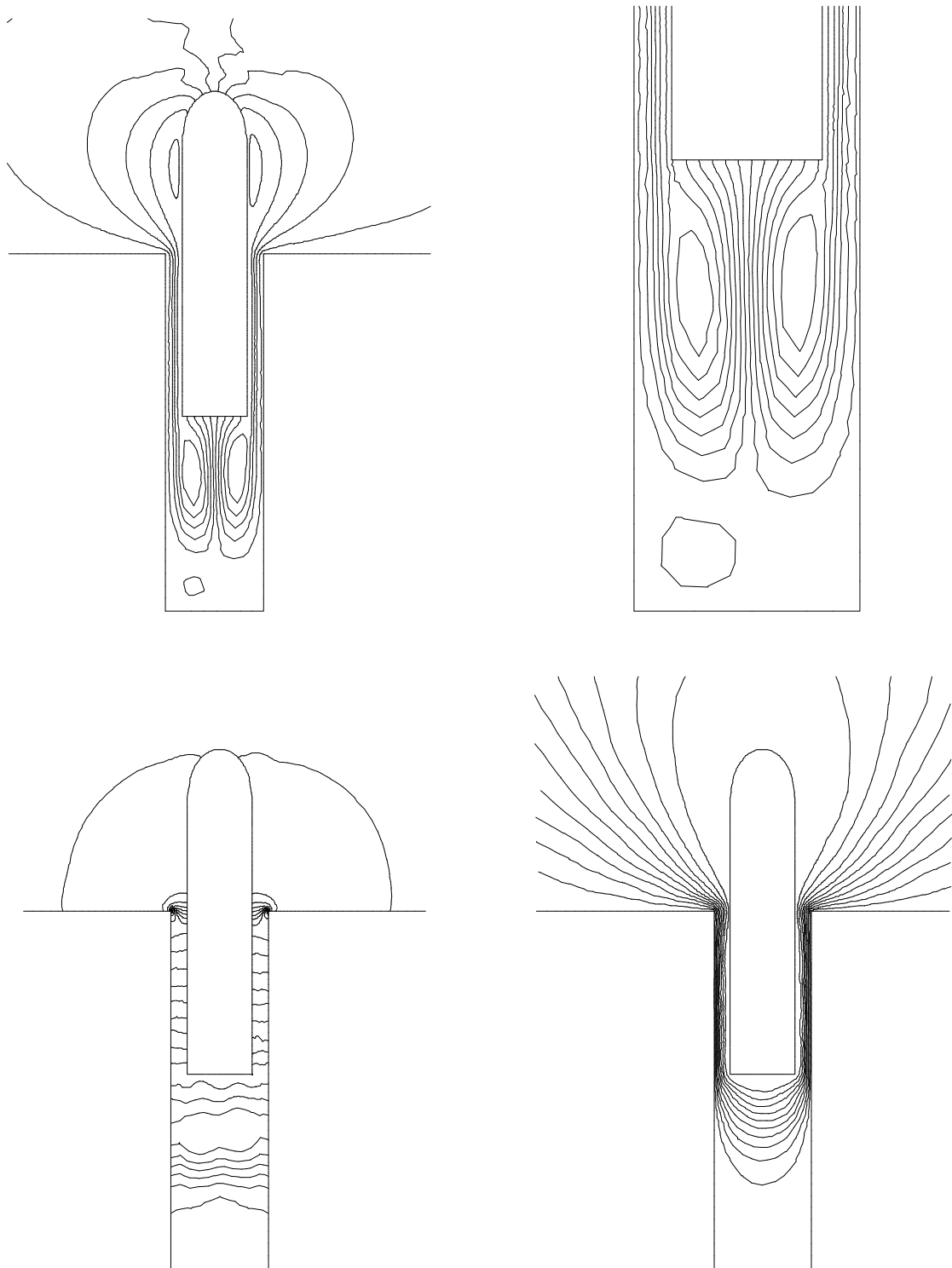


Figure 4.4.42. Numerical results at $t = 0.5$ s. Top left: streamlines. Top right: zoom of the streamlines around the tail of the missile. Bottom left: pressure contours. Bottom right: contours of mesh velocity norm.

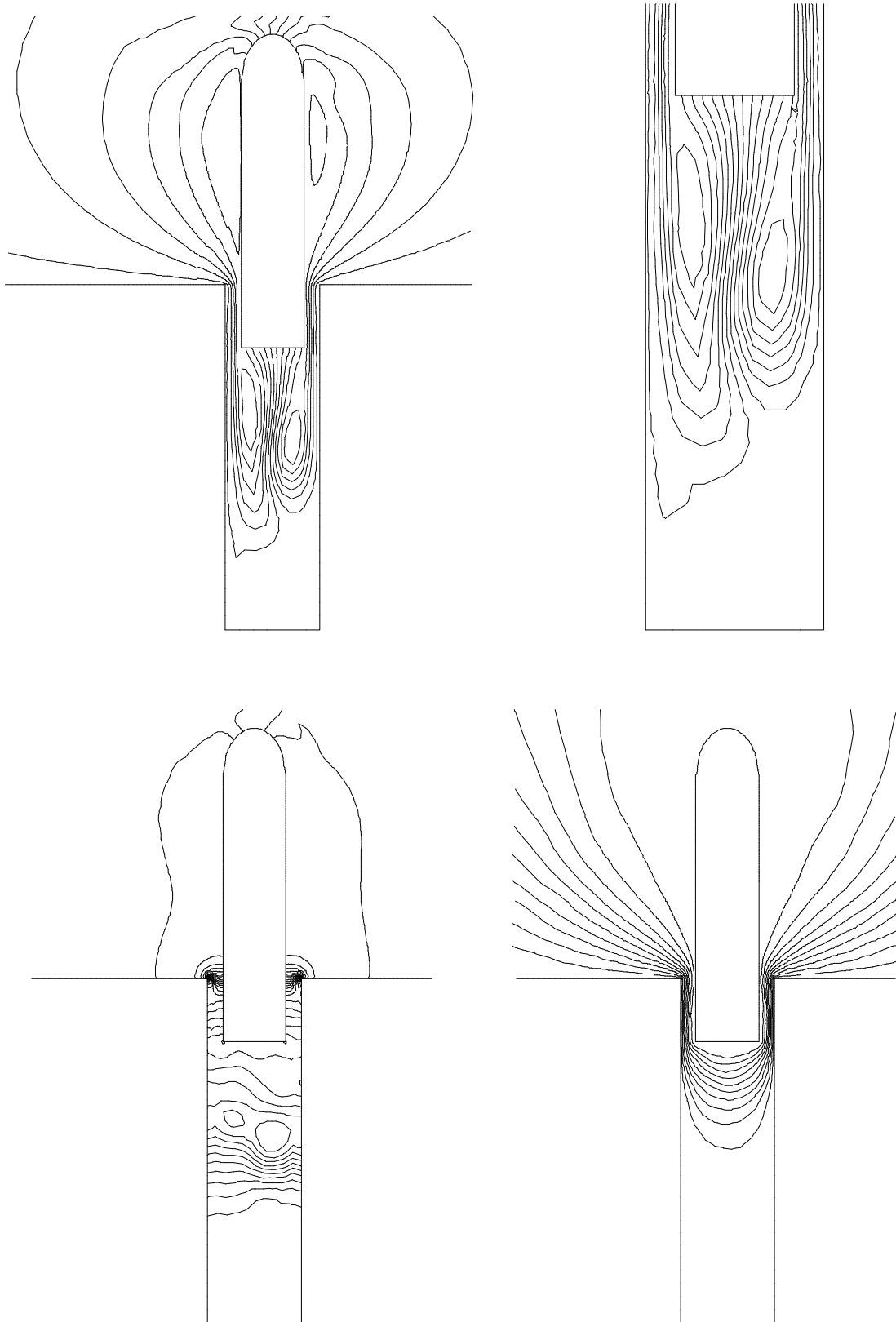


Figure 4.4.43. Numerical results at $t = 0.8$ s. Top left: streamlines. Top right: zoom of the streamlines around the tail of the missile. Bottom left: pressure contours. Bottom right: contours of mesh velocity norm.

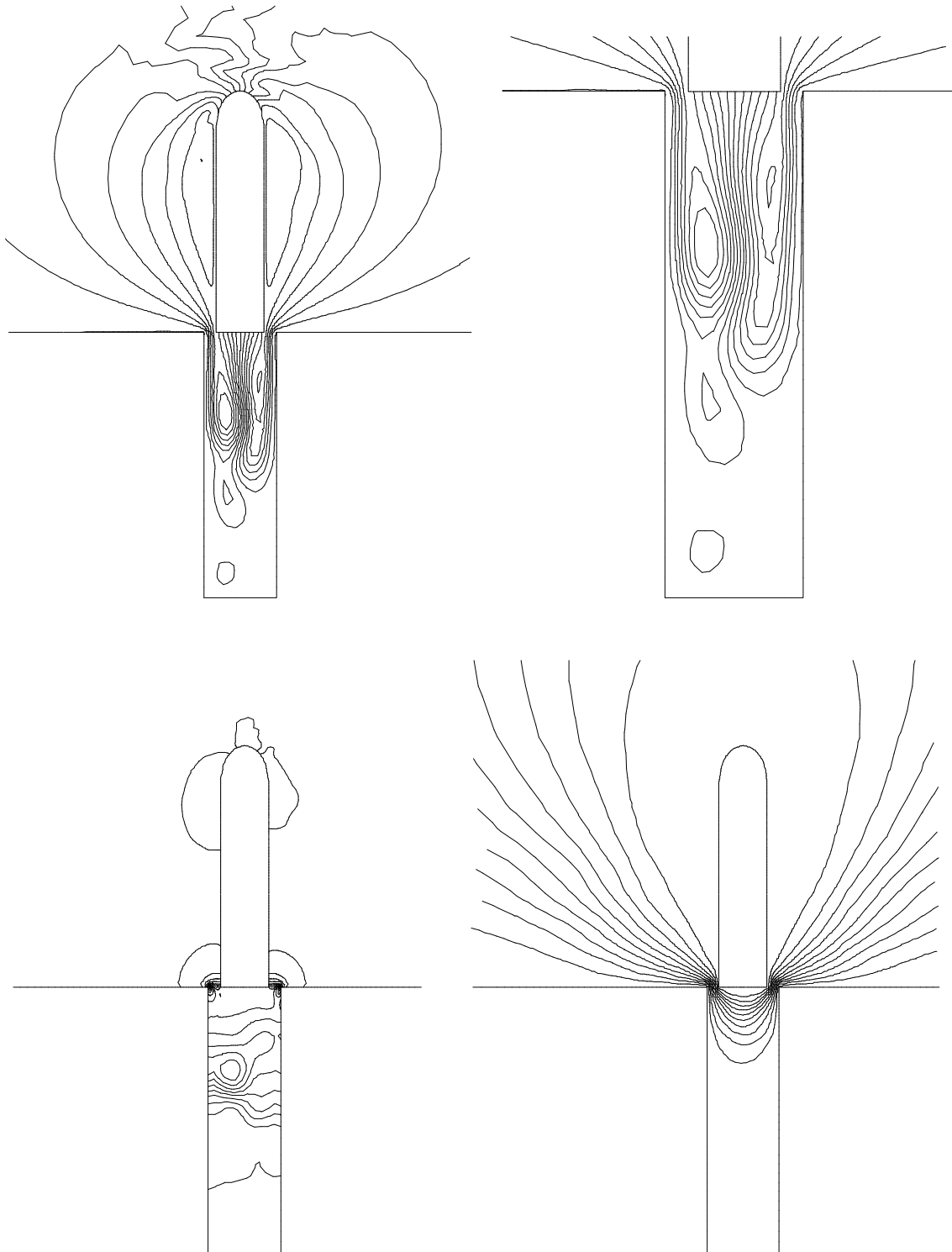


Figure 4.4.44. Numerical results at $t = 1.0$ s. Top left: streamlines. Top right: zoom of the streamlines around the tail of the missile. Bottom left: pressure contours. Bottom right: contours of mesh velocity norm.

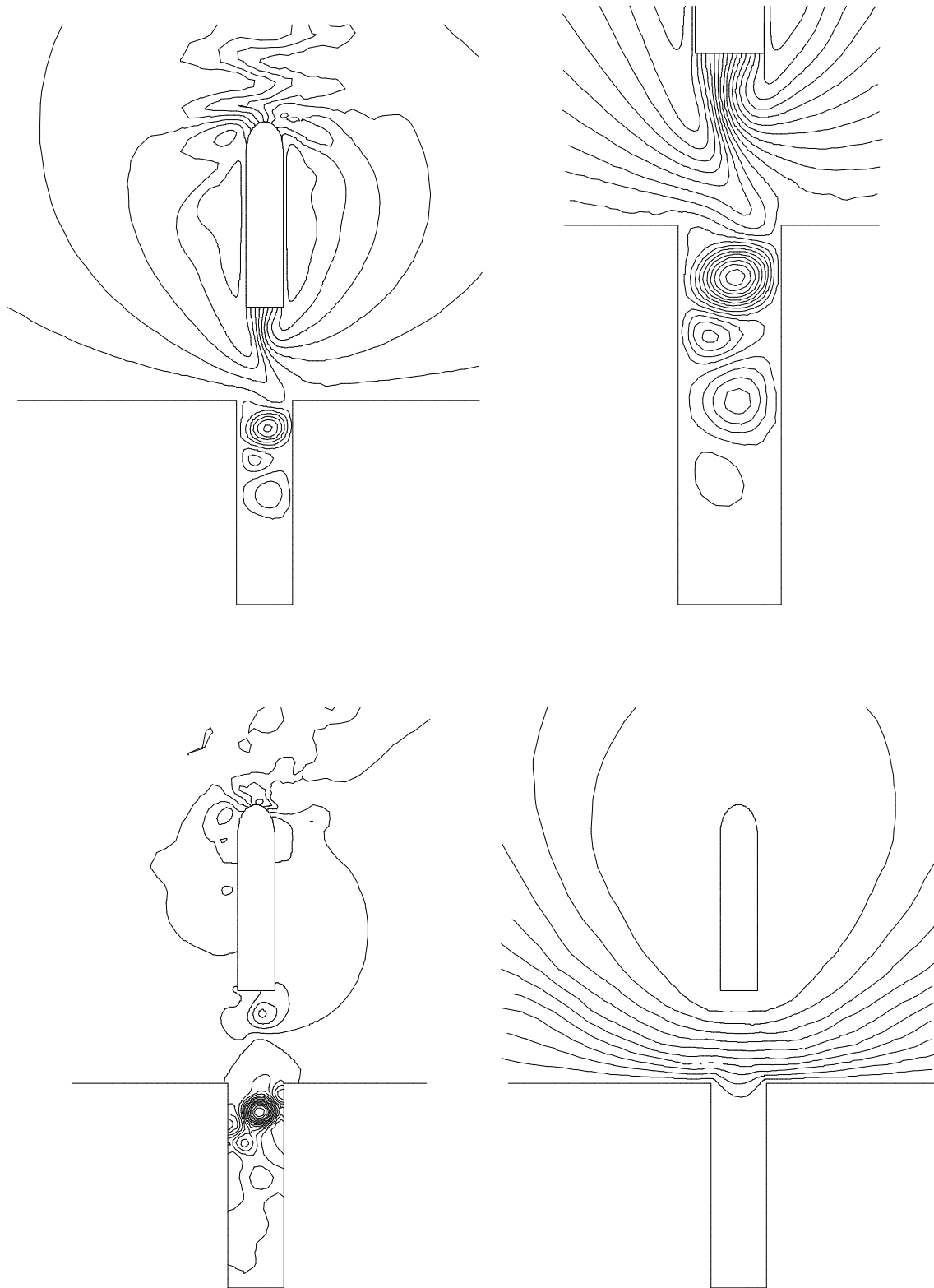


Figure 4.4.45. Numerical results at $t = 1.5s$. Top left: streamlines. Top right: zoom of the streamlines around the tail of the missile. Bottom left: pressure contours. Bottom right: contours of mesh velocity norm.

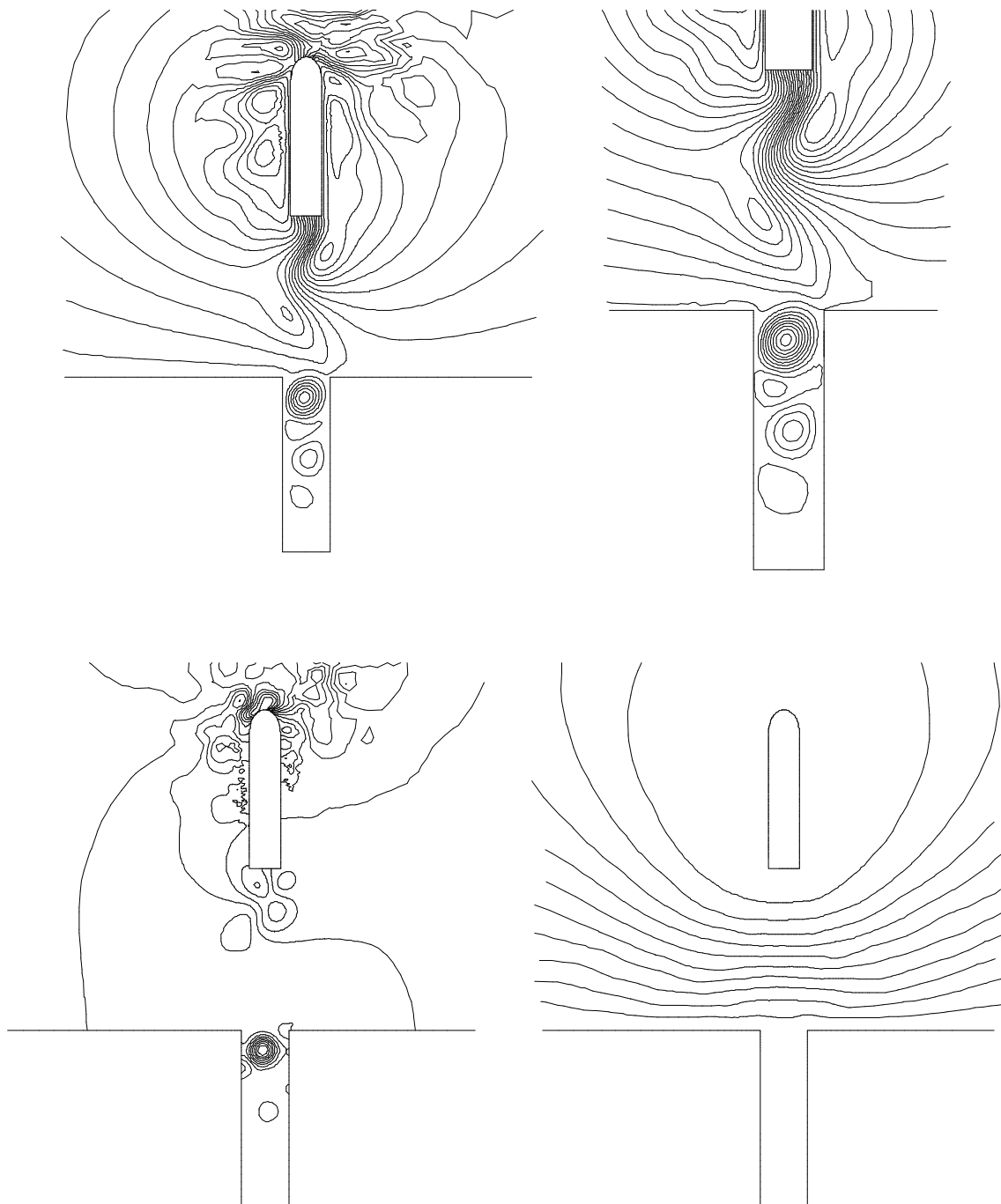


Figure 4.4.46. Numerical results at $t = 2.0$ s. Top left: streamlines. Top right: zoom of the streamlines around the tail of the missile. Bottom left: pressure contours. Bottom right: contours of mesh velocity norm.

4.4.7 Mould Filling Simulation

This example simulates the filling of the mould shown in figure 4.4.47. The mould is initially filled with a resident material A with physical properties (SI units) $\mathbf{r}_a = 1.0$ and $\mathbf{m}_a = 10^{-3}$. At $t \geq 0$ a new material B with $\mathbf{r}_b = 100.0$ and $\mathbf{m}_b = 10^{-1}$ enters through the left side of the mould with a constant inflow velocity \mathbf{u}_i , simulating thus the filling with a molten metal. Both materials are assumed to be incompressible. In order to allow the evacuation of the resident material, the mould contains a couple of holes at its uppermost face. The horizontal component of \mathbf{u}_i is $u_x = 31 \text{ cm/s}$ while the vertical component is accommodated to the slope of the entering region. Under these conditions, the Reynolds number, based on the horizontal injection velocity and on the length of the entering wall (2 cm), is $R_e = 6.2$. In addition to the inflow velocity, the slip condition $\mathbf{u} \cdot \mathbf{n} = 0$ is imposed, as boundary condition, at the walls of the mould. Pressure is set to zero at the outflows (holes). Spatial discretisation of the problem is done considering a mesh composed with 550 bilinear elements (617 nodal points).

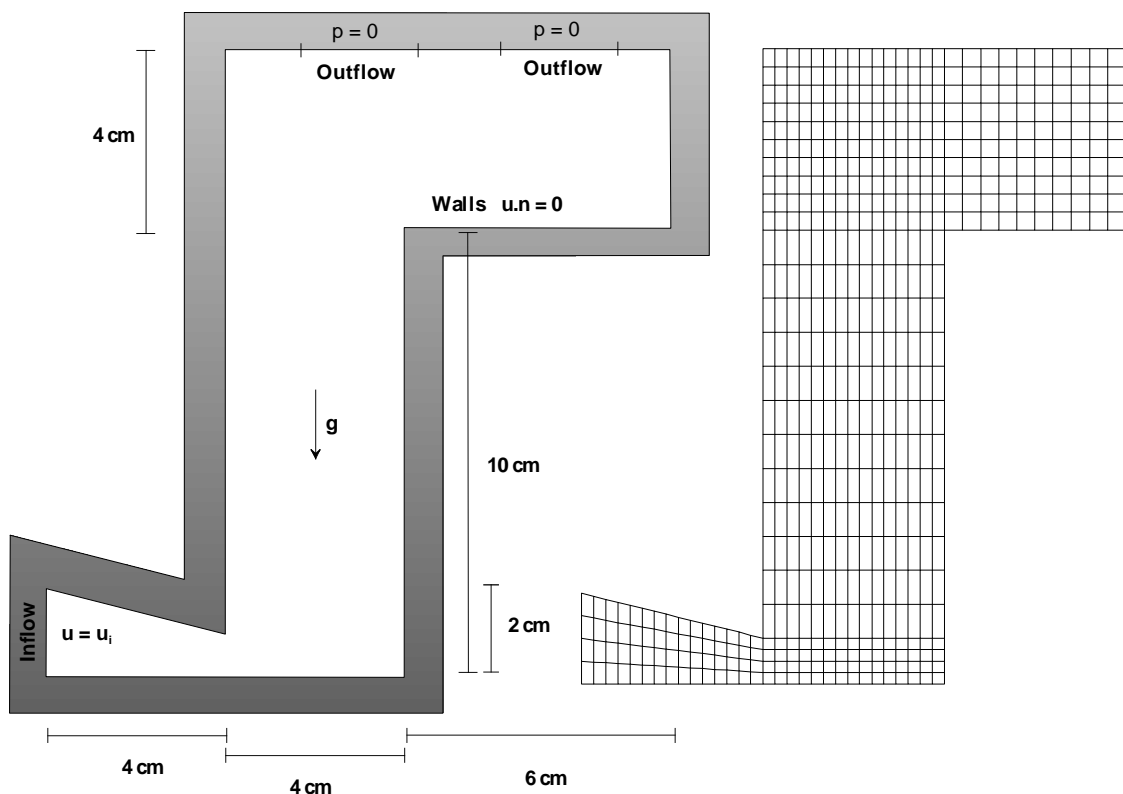


Figure 4.4.47. Geometry of the mould and space discretisation. The mesh is made up with 550 bilinear elements (617 nodal points).

The problem is solved by means of the *pseudo-concentration method*, in which the convective transport equation

$$\begin{aligned} \frac{\partial C}{\partial t} + \mathbf{u} \cdot \nabla C &= 0 \text{ on } \Omega; t \in (0, T) \\ C &= 1 \text{ on } \Gamma_i \\ C(t=0) &= 0 \text{ on } \Omega/\Gamma_i \end{aligned} \tag{4.4.12}$$

is solved to obtain the *pseudo-concentration function* C ($0 \leq C \leq 1 \forall (\mathbf{x}, t) \in (\Omega, T)$). Γ_i is the inflow part of the boundary. In this method, a generic property of the flow \mathbf{p} , such as density or viscosity, depends on the value of the pseudo-concentration function as

$$\mathbf{p} = \begin{cases} \mathbf{p}_a & \text{if } C \leq 0.5 \\ \mathbf{p}_b & \text{if } C > 0.5 \end{cases} \tag{4.4.13}$$

The position of the fluid front (i.e. the free surface) is given by the condition $C = 0.5$. The rest of variables are evaluated, at each Gauss point, according to the above expression. Note that the convective transport equation is coupled with the Navier-Stokes problem but, in order to uncouple both problems, one can consider a staggered procedure in which the transport equation is solved at the end of each time step. Obviously it introduces a time lag Δt between the fluid front and the properties of the flow. The temporal evolution of the front is illustrated in figures 4.4.48 and 4.4.49. Other relevant properties at different time instants are plotted in figures 4.4.50 to 4.4.51.

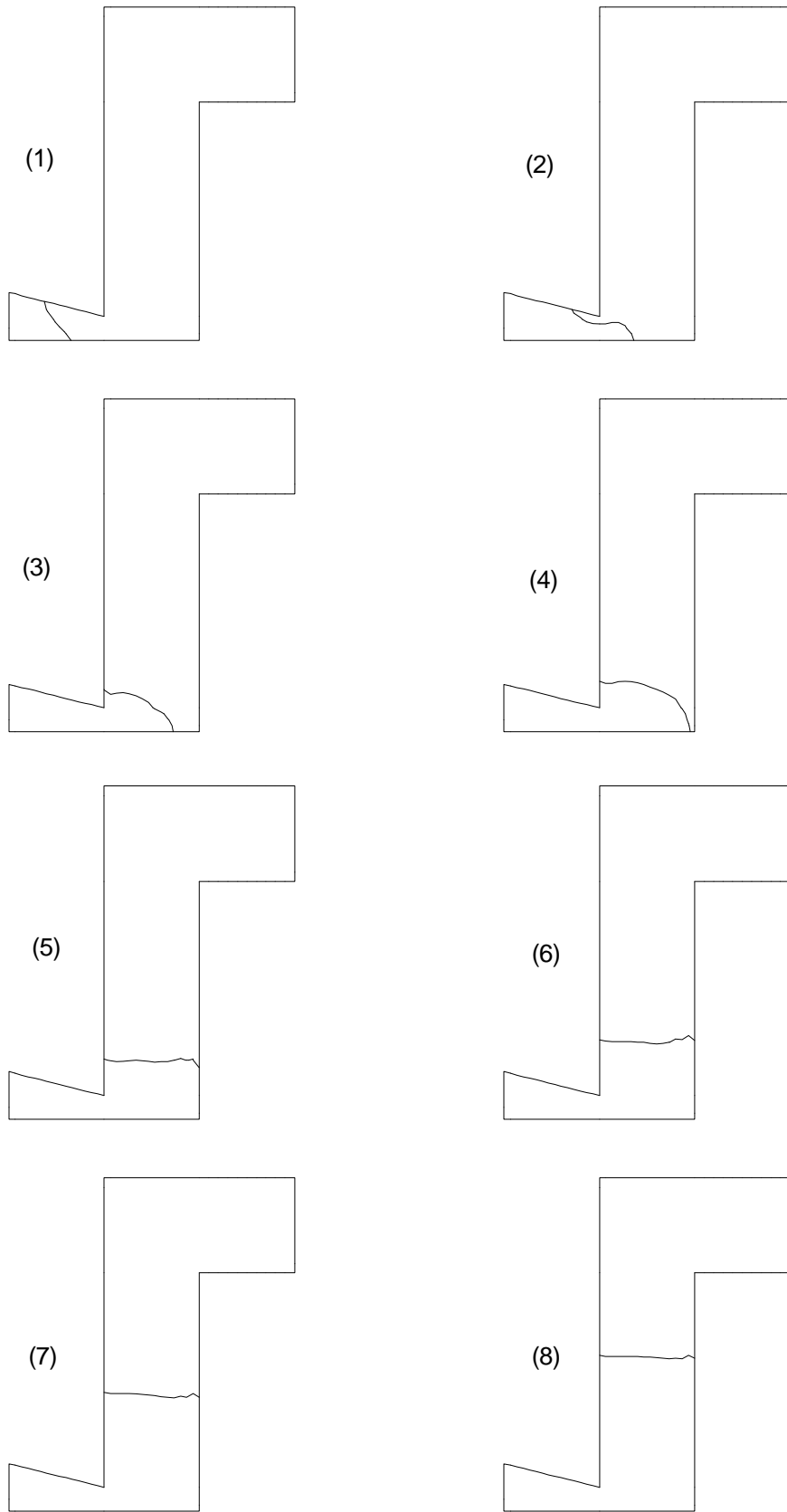


Figure 4.4.48. Position of the front at different time instants: (1) 0.05s, (2) 0.1s, (3) 0.15s, (4) 0.2s, (5) 0.25s, (6) 0.3s, (7) 0.4s, (8) 0.5s.

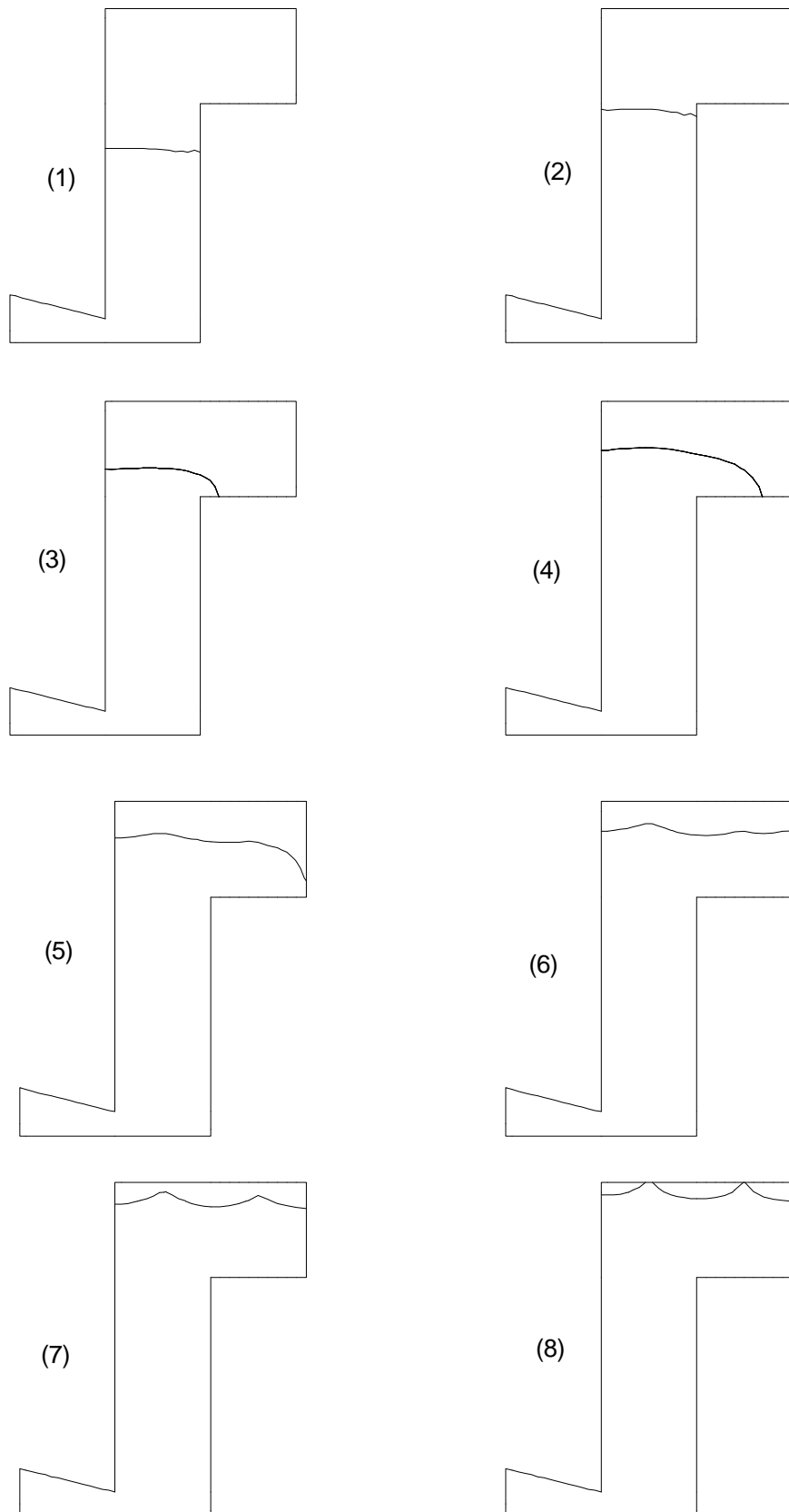


Figure 4.4.49. Position of the front at different time instants: (1) 0.6s, (2) 0.7s, (3) 0.8s, (4) 0.9s, (5) 1.0s, (6) 1.05s, (7) 1.1s, (8) 1.15s.

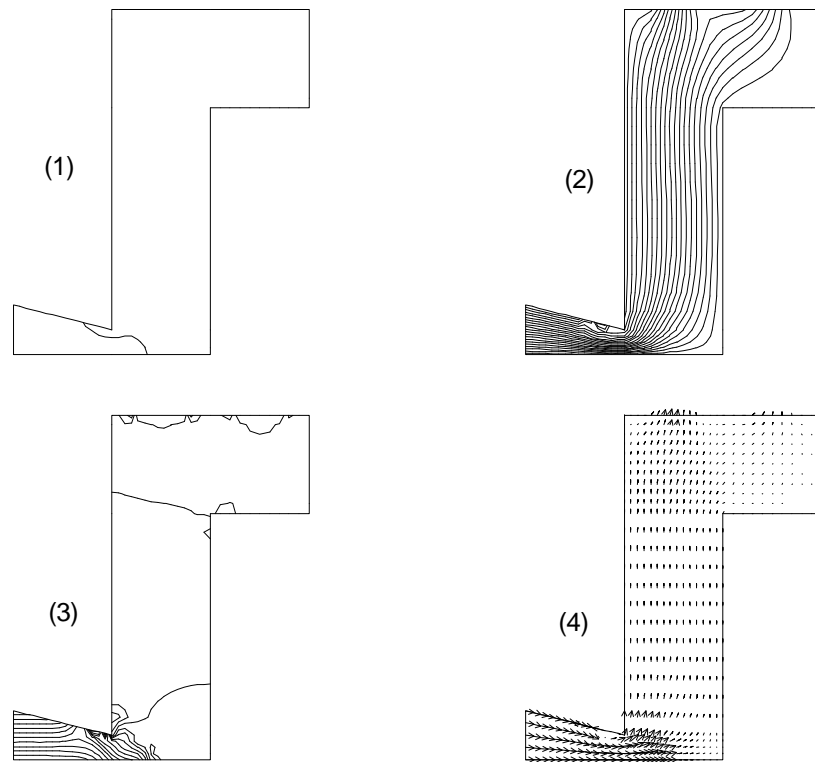


Figure 4.4.50. Results at $t = 0.1$ s. (1) position of the front, (2) streamlines, (3) pressure, (4) velocity vectors.

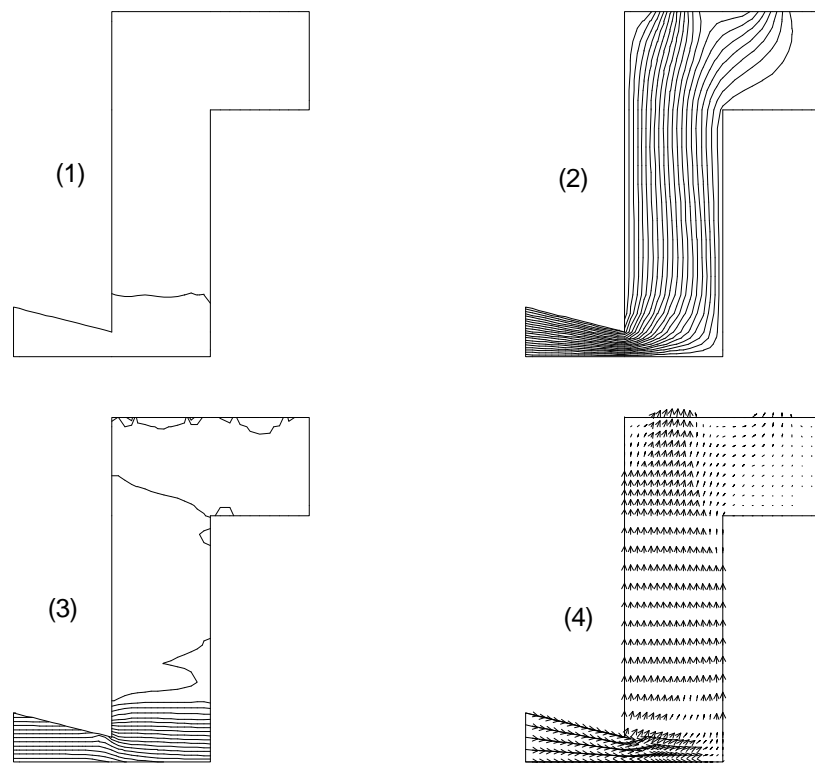


Figure 4.4.51. Results at $t = 0.25$ s. (1) position of the front, (2) streamlines, (3) pressure, (4) velocity vectors.

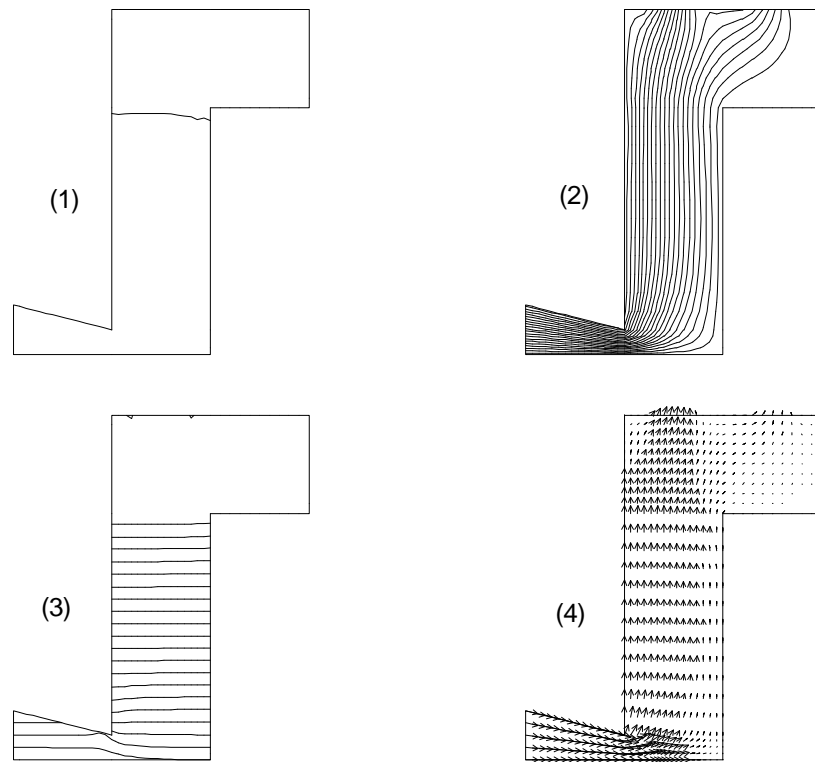


Figure 4.4.52. Results at $t = 0.7$ s. (1) position of the front, (2) streamlines, (3) pressure, (4) velocity vectors.

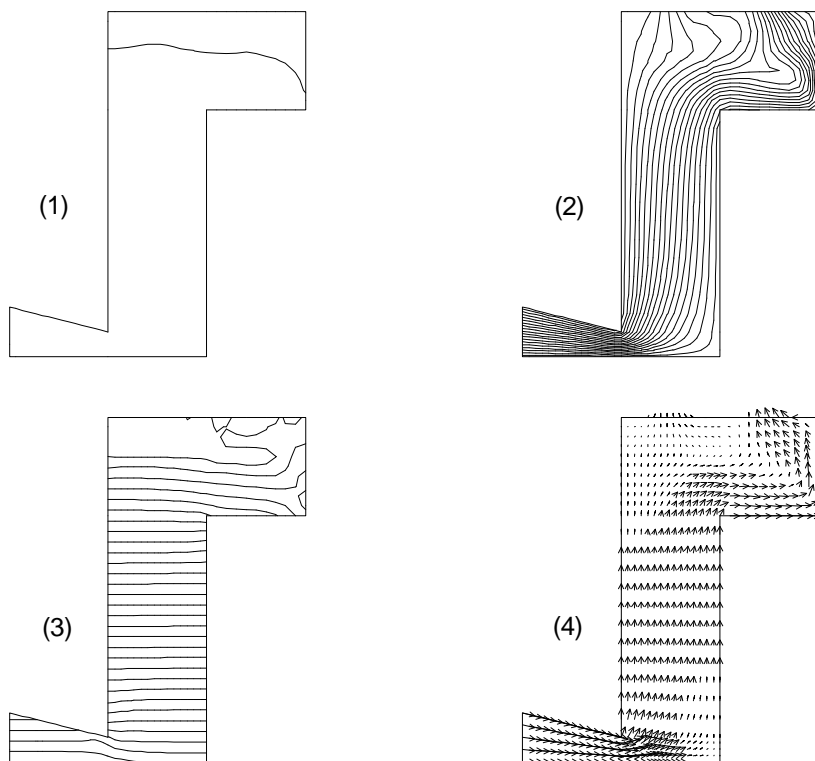


Figure 4.4.53. Results at $t = 1.0$ s. (1) position of the front, (2) streamlines, (3) pressure, (4) velocity vectors.

4.5 The Mechanical Equations

One of the objectives of this thesis is to develop an algorithm to compute ground deformations in volcanic areas considering viscoelastic properties for the crust. Up to date, all the viscoelastic models available within this context admit analytical solutions¹. Commonly, these analytical solutions are obtained by means of the *correspondence principle* in combination with some method to compute inverse Laplace transforms (e.g. [Rundle, 1982; Bonafede et al., 1986; Dragoni and Magnanensi, 1989; Folch et al., 2000] among many others). The “numerical version” of these methods, based also on the correspondence principle and on the Laplace inversion performed by means of the Prony series method, is presented here for the first time².

This section is organised as follows. Firstly, the solution of the standard linear elastic problem using the Galerkin finite element method is explained. This is necessary because the use of the correspondence principle in viscoelastic problems requires the solution of elastic problems. Secondly, the numerical method to obtain viscoelastic solutions is presented.

Observation It should be remarked again that, in the context of this thesis, neither the elastic nor the viscoelastic solutions have anything to do with the fluid-structure interaction problem, in which it is considered that the structure behaves as rigid solid. The reasons for this are exposed in section 3.1. Two different programs have been written: one to solve the “flow problem” and another for the “structural problem”. However, the algorithm implemented in the fluid/fluid-structure program permits the incorporation of any other structural behaviour changing just one subroutine in the source code (see section 4.3.1). In other words, if elastic/viscoelastic behaviours are required in future applications, the “structural program” can become a “slave” of the fluid/fluid-structure program adding very few modifications to the source code.

4.5.1 Elastic Problem

Consider the Navier equation³ (see section 3.5.1 for the meaning of each variable)

¹ Analytical solutions can be obtained under certain restrictive assumptions such as, for instance, the point source hypothesis. See section 2.4.2 for major details.

² Obviously, numerical solutions are not restricted and allow to consider important effects such as, for instance, extended sources, topography or discontinuities.

³ We do not consider the coupling between elasticity and gravitation and, in consequence, the body forces term that appears in (4.5.1) is constant. If one wishes to solve elastic-gravitational problems a new term which accounts for gravity variations due to deformation must be added to this equation [Rundle, 1980].

$$\nabla \cdot [\mathbf{m}(\nabla \mathbf{u} + \mathbf{u}\nabla)] + \nabla [I (\nabla \cdot \mathbf{u})] + \mathbf{r} \mathbf{g} = \mathbf{r} \frac{\partial^2 \mathbf{u}}{\partial t^2} \quad (4.5.1)$$

to be solved in $\Omega \times (0, T)$ together with a given set of boundary and initial conditions

$$\left. \begin{array}{l} \mathbf{u} = \bar{\mathbf{u}} \quad \text{in } \Gamma_D \\ \mathbf{S} \cdot \mathbf{n} = \bar{\mathbf{t}} \quad \text{in } \Gamma_N \end{array} \right\} \quad (4.5.2)$$

$$\left. \begin{array}{l} \mathbf{u} = \mathbf{u}^0 \quad \text{at } t = 0 \\ \dot{\mathbf{u}} = \dot{\mathbf{u}}^0 \quad \text{at } t = 0 \end{array} \right\} \quad (4.5.3)$$

where Γ_D and Γ_N are, respectively, the Dirichlet and the Neumann parts of the boundary Γ ($\Gamma = \Gamma_D \cup \Gamma_N$, $\Gamma_D \cap \Gamma_N = \emptyset$) and \mathbf{S} is given by (3.5.6). For simplicity, boundary conditions are assumed to be time independent. In many practical cases, the elastic problem can be considered in its *quasi-static approach*, in which the inertial term is neglected. Under these circumstances, the Navier equation is time independent and reduces to

$$\nabla \cdot [\mathbf{m}(\nabla \mathbf{u} + \mathbf{u}\nabla)] + \nabla [I (\nabla \cdot \mathbf{u})] + \mathbf{r} \mathbf{g} = \mathbf{0} \quad (4.5.4)$$

where, obviously, only boundary conditions are required in this case. The aim is to solve the general Navier equation (4.5.1) using the standard Galerkin finite element method.

4.5.1.1 Weak Form and Boundary Conditions

Multiplying (4.5.1) by the test function \mathbf{W} ($\mathbf{W} = \mathbf{0}$ at Γ_D) and integrating over the domain Ω one has

$$\begin{aligned} & \int_{\Omega} \mathbf{W} \cdot [\nabla \cdot [\mathbf{m}(\nabla \mathbf{u} + \mathbf{u}\nabla)]] d\Omega + \int_{\Omega} \mathbf{W} \cdot [\nabla [I (\nabla \cdot \mathbf{u})]] d\Omega + \int_{\Omega} \mathbf{r} \mathbf{W} \cdot \mathbf{g} d\Omega = \\ & \int_{\Omega} \mathbf{W} \cdot \mathbf{r} \frac{\partial^2 \mathbf{u}}{\partial t^2} d\Omega \end{aligned} \quad (4.5.5)$$

Integrating by parts the first and the second terms of the above expression and using the Gauss theorem to transform the volume integral into a surface integral, one obtains

$$\begin{aligned}
 & - \int_{\Omega} \mathbf{m}(\nabla \mathbf{W} : \nabla \mathbf{u} + \nabla \mathbf{W} \cdot \nabla \mathbf{u}) d\Omega - \int_{\Omega} I (\nabla \cdot \mathbf{W})(\nabla \cdot \mathbf{u}) d\Omega + \int_{\Omega} \mathbf{r} \mathbf{W} \cdot \mathbf{g} d\Omega \\
 & + \int_{\Gamma} \mathbf{m} \mathbf{W} \cdot (\nabla \mathbf{u} + \mathbf{u} \nabla) \cdot \mathbf{n} d\Gamma + \int_{\Gamma} I (\nabla \cdot \mathbf{u}) \mathbf{W} \cdot \mathbf{n} d\Gamma = \int_{\Omega} \mathbf{W} \cdot \mathbf{r} \frac{\mathcal{I}^2 \mathbf{u}}{\mathcal{I} t^2} d\Omega
 \end{aligned} \tag{4.5.6}$$

where \mathbf{n} is the unit outward vector normal to the boundary Γ . Finally, the use of the expression of the traction vector \mathbf{t} yields

$$\begin{aligned}
 & \int_{\Omega} \mathbf{W} \cdot \mathbf{r} \frac{\mathcal{I}^2 \mathbf{u}}{\mathcal{I} t^2} d\Omega + \int_{\Omega} \mathbf{m}(\nabla \mathbf{W} : \nabla \mathbf{u} + \nabla \mathbf{W} \cdot \nabla \mathbf{u}) d\Omega + \int_{\Omega} I (\nabla \cdot \mathbf{W})(\nabla \cdot \mathbf{u}) d\Omega = \\
 & \int_{\Omega} \mathbf{r} \mathbf{W} \cdot \mathbf{g} d\Omega + \int_{\Gamma} \mathbf{W} \cdot \mathbf{t} d\Gamma
 \end{aligned} \tag{4.5.7}$$

• **Boundary Conditions.** The integration by parts of the weak form leads to a boundary integral in which the traction vector \mathbf{t} is multiplied by the test function. It allows to impose the Neumann boundary conditions in Γ_N by prescribing \mathbf{t} to $\bar{\mathbf{t}}$, that is

$$\int_{\Gamma} \mathbf{W} \cdot \mathbf{t} d\Gamma = \int_{\Gamma_N} \mathbf{W} \cdot \bar{\mathbf{t}} d\Gamma \tag{4.5.8}$$

($\mathbf{W} = \mathbf{0}$ at Γ_D). Dirichlet boundary conditions for the displacement are implemented in a straight forward way on the weak form (4.5.7). It is also possible to prescribe pressure instead of traction as a Neumann boundary condition. In this case, it is assumed that

$$\bar{\mathbf{t}} = -p \mathbf{n} \tag{4.5.9}$$

4.5.1.2 Space Discretisation

Once the weak form is established, the space can be discretised considering the standard Galerkin formulation, that is, one imposes that the test functions \mathbf{W} coincide with the shape functions. The result is a system of ordinary differential equations (second-order in time) which, written in a matricial form, is

$$\mathbf{M} \ddot{\mathbf{u}} + \mathbf{K} \mathbf{u} = \bar{\mathbf{F}} \tag{4.5.10}$$

where \mathbf{M} and \mathbf{K} are the standard mass and stiffness matrices and $\ddot{\mathbf{u}}$, \mathbf{u} , and $\bar{\mathbf{F}}$ are nodal vectors. Equation (4.5.10) does not allow to uncouple spatial components so that the dimension of these vectors is $n_{dime} \times n_{node}$, being n_{dime} the space dimension and n_{node} the number of

nodes in the finite element mesh. This system must be now solved in time together with the initial conditions (4.5.3) using, for instance, a finite difference procedure. Note that in the quasi-static approach, the space discretisation leads to an algebraic system

$$\mathbf{K} \bar{\mathbf{u}} = \bar{\mathbf{F}} \quad (4.5.11)$$

which can be directly solved to obtain the displacements.

4.5.1.3 The Newmark Method

In the context of this work, the elastic problem will be always considered to be time-independent (i.e. only the solution of (4.5.11) will be required in practise). However, the more general time-dependent behaviour (i.e. the solution of (4.5.10)) has been also implemented in the “structural program”. Equation (4.5.10) –complemented with the Rayleigh hypothesis– is solved by means of the Newmark method.

Firstly, it should be noted that this equation is that of a “free harmonic oscillator” and, in consequence, the steady state presents periodic temporal oscillations. In real materials, this oscillations are damped by internal frictional effects which are not included in (4.5.10) because are not taken into account in the constitutive equation. To reflect this real behaviour, a common procedure is to add a damping term which is proportional to the velocity. Then, the system to solve is

$$\mathbf{M} \ddot{\bar{\mathbf{u}}} + \mathbf{C} \dot{\bar{\mathbf{u}}} + \mathbf{K} \bar{\mathbf{u}} = \bar{\mathbf{F}} \quad (4.5.12)$$

From a physical point of view, the term added *a posteriori* includes a frictional effect which is not reflected in the constitutive equation, that is, reflects that tensions are not only proportional to the displacements but also depend on the velocity of the particles¹. Thus, different values of \mathbf{C} can be considered to reflect different behaviours of the elastic materials during its transient stages. Note that, if \mathbf{C} is not zero, the steady state is always the same that in the quasi-static approach (i.e. verifies $\mathbf{K} \bar{\mathbf{u}}^{\text{STD}} = \bar{\mathbf{F}}$), but the transient solutions differ from one material to another. In the *Rayleigh hypothesis*, the damping matrix \mathbf{C} is assumed to be

$$\mathbf{C} \equiv a \mathbf{M} + b \mathbf{K} \quad (4.5.13)$$

¹ In fact, the inclusion of damping can be interpreted as the use of a viscoelastic model.

where a and b are constants that depend on the material and are known as the *Rayleigh damping parameters*.

The *Newmark method* is a procedure to solve (4.5.12) using finite differences and works as follows. Consider first the following system of second-order in time ordinary differential equations

$$\mathbf{M} \mathbf{a} + \mathbf{C} \mathbf{v} + \mathbf{K} \mathbf{u} = \mathbf{F} \quad (4.5.14)$$

where $\mathbf{a} \equiv \ddot{\mathbf{u}}$ and $\mathbf{v} \equiv \dot{\mathbf{u}}$. Note that the above expression does not necessarily come from a spatial discretisation and, in consequence, the arrow above the vectors can be, in general, omitted. Note also that (4.5.10) is nothing but a particular case of (4.5.14) in which the damping matrix \mathbf{C} vanishes. Obviously, equation (4.5.14) must be verified at any time instant. In particular

$$\mathbf{M} \mathbf{a}^{n+1} + \mathbf{C} \mathbf{v}^{n+1} + \mathbf{K} \mathbf{u}^{n+1} = \mathbf{F}^{n+1} \quad (4.5.15)$$

The idea behind the Newmark method is solve for \mathbf{a}^{n+1} approximating \mathbf{u}^{n+1} and \mathbf{v}^{n+1} by

$$\begin{aligned} \mathbf{u}^{n+1} &= \mathbf{u}^n + \Delta t \mathbf{v}^n + \frac{\Delta t^2}{2} \mathbf{a}^{n+q_1} = \mathbf{u}^n + \Delta t \mathbf{v}^n + \frac{\Delta t^2}{2} [\mathbf{q}_1 \mathbf{a}^{n+1} + (1-\mathbf{q}_1) \mathbf{a}^n] \\ \mathbf{v}^{n+1} &= \mathbf{v}^n + \Delta t \mathbf{a}^{n+q_2} = \mathbf{v}^n + \Delta t [\mathbf{q}_2 \mathbf{a}^{n+1} + (1-\mathbf{q}_2) \mathbf{a}^n] \end{aligned} \quad (4.5.16)$$

where $\mathbf{q}_1, \mathbf{q}_2 \in [0,1]$ are parameters. Particular cases of interest are the forward Euler (when $\mathbf{q}_1 = \mathbf{q}_2 = 0$), the backward Euler (when $\mathbf{q}_1 = \mathbf{q}_2 = 1$) and the Crank-Nicholson (when $\mathbf{q}_1 = \mathbf{q}_2 = 1/2$). The above expressions can be split between explicit and implicit contributions, known, respectively, as *predictors* and *correctors*

$$\bar{\mathbf{u}}^{n+1} \equiv \mathbf{u}^n + \Delta t \mathbf{v}^n + \frac{\Delta t^2}{2} (1-\mathbf{q}_1) \mathbf{a}^n \quad (\text{Predictors}) \quad (4.5.17)$$

$$\bar{\mathbf{v}}^{n+1} \equiv \mathbf{v}^n + \Delta t (1-\mathbf{q}_2) \mathbf{a}^n$$

$$\mathbf{u}^{n+1} = \bar{\mathbf{u}}^{n+1} + \frac{\Delta t^2}{2} \mathbf{q}_1 \mathbf{a}^{n+1} \quad (\text{Correctors}) \quad (4.5.18)$$

$$\mathbf{v}^{n+1} = \bar{\mathbf{v}}^{n+1} + \Delta t \mathbf{q}_2 \mathbf{a}^{n+1}$$

Finally, substituting (4.5.18) into (4.5.15) one gets

$$\left[\mathbf{M} + \mathbf{q}_2 \Delta t \mathbf{C} + \mathbf{q}_1 \frac{\Delta t^2}{2} \mathbf{K} \right] \mathbf{a}^{n+1} = \mathbf{F}^{n+1} - \mathbf{C} \bar{\mathbf{v}}^{n+1} - \mathbf{K} \bar{\mathbf{u}}^{n+1} \quad (4.5.19)$$

which allows to find \mathbf{a}^{n+1} .

In summary: consider that \mathbf{u}^n , \mathbf{v}^n and \mathbf{a}^n are known at $t = t^n$. The solution at t^{n+1} is the determined as follows:

- ❶ Compute the predictors $\bar{\mathbf{u}}^{n+1}$ and $\bar{\mathbf{v}}^{n+1}$ using (4.5.17).
- ❷ Solve (4.5.19) to obtain \mathbf{a}^{n+1} .
- ❸ Use the correctors (4.5.18) to get \mathbf{u}^{n+1} and \mathbf{v}^{n+1} .

Obviously, the initial condition (4.5.3) is used to compute the first time step, in which

$$\left[\mathbf{M} + \mathbf{q}_2 \Delta t \mathbf{C} + \mathbf{q}_1 \frac{\Delta t^2}{2} \mathbf{K} \right] \mathbf{a}^0 = \mathbf{F}^0 - \mathbf{C} \mathbf{v}^0 - \mathbf{K} \mathbf{u}^0 \quad (4.5.20)$$

The Newmark algorithm is unconditionally stable if $\mathbf{q}_1 \geq \mathbf{q}_2 \geq 1/2$. In any other case, the algorithm is conditionally stable, that is, there exists a maximum time step able to ensure stability of the scheme. In the particular case of (4.5.10) (i.e. if \mathbf{C} vanishes), the critical time step Δt_c is

$$\Delta t_c = \sqrt{\frac{h_{min}^2 \mathbf{r}}{2(\mathbf{I} + 2\mathbf{m})}} \quad (4.5.21)$$

where h_{min} is the minimum element length.

4.5.2 Viscoelastic Problem. The Prony Series Method

For a linear isotropic viscoelastic material, the solution of the governing equations can be obtained from the elastic one employing the correspondence principle [Fung, 1965]. The idea behind this principle is to replace -in the elastic solution- the Lamé parameters \mathbf{I} and \mathbf{m} by two functions $\tilde{\mathbf{I}}(s)$ and $\tilde{\mathbf{m}}(s)$. If this is done, it can be shown that the resulting expression is the Laplace transform of the viscoelastic solution¹. Hence, if the obtained expression is now

¹ It has been exposed previously (see section 3.5.2) how the rheology of isotropic linear viscoelastic materials depends only on two relaxation functions. The Laplace transforms of these functions are precisely $\tilde{\mathbf{I}}(s)$ and $\tilde{\mathbf{m}}(s)$.

inverted, one gets the viscoelastic solution in the time domain. Obviously, the specific values for the functions $\tilde{I}(s)$ and $\tilde{m}(s)$ will depend on the particular rheology under consideration. However, only the three different possibilities, formed by combinations of the simplest 1D viscoelastic rheologies (the Maxwell solid and the Standard Linear Solid), are usually considered when modelling the behaviour of the crust¹. From now on, these rheologies or relaxation types will be referred as relaxation 1, relaxation 2 and relaxation 3. Its properties are summarised in table 4.5.1.

- **Relaxation 1** (e.g. [Rundle, 1982; Dragoni and Magnanensi, 1989]) assumes that the crust deforms as a Maxwell viscoelastic solid with respect to the deviatoric stresses but behaves elastically with respect to the normal stresses. In this case

$$\begin{aligned}\tilde{I}(s) &= I \\ \tilde{m}(s) &= \frac{s \mathbf{m} t}{s t + 2} \\ t &= \frac{2h}{m}\end{aligned}\tag{4.5.22}$$

where t is the characteristic time of the of the Maxwell rheological model and h is the viscosity of the material (crust). Note that only the Lamé parameter m is replaced with $\tilde{m}(s)$, while I is left as in the elastic case because this behaviour corresponds to a situation in which the material only relaxes its deviatoric stresses.

- **Relaxation 2** (e.g. [Bonafede et al., 1986]) assumes that the crust deforms as a Maxwell viscoelastic solid in both the deviatoric and the normal stresses (keeping constant the coefficient of Poisson). In this case

$$\begin{aligned}\tilde{I}(s) &= \frac{s I t}{s t + 2} \\ \tilde{m}(s) &= \frac{s \mathbf{m} t}{s t + 2} \\ t &= \frac{2h}{m}\end{aligned}\tag{4.5.23}$$

¹ The method herein exposed is, nevertheless, completely general. The consideration of any other behaviour different from the Maxwell solid or the SLS would affect only to the definitions of the functions $\tilde{I}(s)$ and $\tilde{m}(s)$.

• **Relaxation 3** (e.g. [Rundle, 1982; Bonafede et al., 1986]) assumes that the crust deforms as a Maxwell viscoelastic solid with respect to the deviatoric stresses and as a standard linear solid (SLS) with respect the normal stresses (i.e. keeping constant the bulk modulus). In this case

$$\begin{aligned}\tilde{m}(s) &= \frac{s \mathbf{m} \mathbf{t}}{s \mathbf{t} + 2} \\ \tilde{I}(s) &= \mathbf{I} + \frac{2}{3} \mathbf{m} - \frac{2}{3} \tilde{m}(s) \\ \mathbf{t} &= \frac{2\mathbf{h}}{\mathbf{m}}\end{aligned}\quad (4.5.24)$$

Once the above expressions are introduced in the elastic solution, any method of inversion (analytical in the simplest cases, numerical on the contrary) is, in principle, valid. The specific method proposed here to perform this inversion is the *Prony series method* [Schapery, 1961; Cost, 1964]. The objective is to determine the function $f(t)$ given its Laplace transform $\tilde{f}(s)$. In the Prony series method, the searched scalar function $f(t)$ is approximated by a series of decaying exponentials

$$f(t) \cong \sum_{i=1}^N a_i \mathbf{t}_i (1 - e^{-t/\mathbf{t}_i}) \quad (4.5.25)$$

where \cong means “approximately equal in the least square sense”, \mathbf{t}_i is a set of N known relaxation times and a_i is a set of unknown constants that can be determined by least squares methods. [Rundle, 1982] showed that good results for the inversion can be obtained by choosing the set of relaxation times as

$$\{\mathbf{t}_i\} = \{0.1\mathbf{t}, 0.5\mathbf{t}, \mathbf{t}, 5\mathbf{t}, 10\mathbf{t}, 50\mathbf{t}, 100\mathbf{t}\} \quad (\text{i.e. } N = 7) \quad (4.5.26)$$

where \mathbf{t} is the relaxation time defined in equation (4.5.22). The application of the Laplace transform to (4.5.25) leads to

$$s \tilde{f}(s) = \sum_{i=1}^N a_i \mathbf{t}_i \frac{1}{1 + s \mathbf{t}_i} \quad (4.5.27)$$

The above expression must be verified for any value of s and, in particular, for the N values $s_j = 1/\mathbf{t}_j$. Then, providing that the Laplace transform $\tilde{f}(s)$ is known, this equation can be

transformed into an algebraic system of N equations with N unknowns (the interpolation constants a_i)

$$\mathbf{F} = \mathbf{K} \cdot \mathbf{a} \quad (4.5.28)$$

where

$$\mathbf{K}_{ij} = \frac{\mathbf{t}_i \mathbf{t}_j}{\mathbf{t}_i + \mathbf{t}_j} \quad (4.5.29)$$

$$\mathbf{F}_i = \frac{1}{\mathbf{t}_i} \tilde{f} \left(\frac{1}{\mathbf{t}_i} \right) \quad (4.5.30)$$

$$(\mathbf{a})_j = a_j \quad (4.5.31)$$

It the expression above, the indexes i and j run from 1 to N . The solution of the system determines the constants a_i and, in consequence, determines the inverse Laplace transform (4.5.25). In summary, one must proceed as follows:

- ❶ Solve the quasi-static elastic problem (4.5.11) as usual. It gives the elastic solution which, at $t = 0$, coincides with the viscoelastic.
- ❷ Solve N additional quasi-static elastic problems (one for each value of \mathbf{t}_i) replacing the Lamé parameters \mathbf{I} and \mathbf{m} by $\tilde{\mathbf{I}}(1/\mathbf{t}_i)$ and $\tilde{\mathbf{m}}(1/\mathbf{t}_i)$ respectively. It gives the N functions $\tilde{\mathbf{u}}(1/\mathbf{t}_i)$. The specific values of $\tilde{\mathbf{I}}$ and $\tilde{\mathbf{m}}$ depend on the rheological model and, for the rheologies under consideration are given by (4.5.22) to (4.5.24) (see also table 4.5.1). Both Dirichlet and Neumann boundary conditions must also be Laplace-transformed. Note that this constrains the procedure to viscoelastic problems in which boundary conditions are known *a priori* such as, for instance, the case of time-independent boundary conditions.
- ❸ Solve a system analogous to (4.5.28) to obtain the coefficients a_i . It should be pointed out that these coefficients are different for each scalar unknown (such as, for instance, the components of the displacement vector or the components of the stress tensor) and for each material point (for each point of the mesh). In other words, the system must be solved at each node of the mesh and for each component of the unknowns. Nevertheless, note that the algebraic system is only $N \times N$ (7×7 if (4.5.26) is used) and the matrix \mathbf{K} is always the same. In consequence, one can easily compute the inverse matrix \mathbf{K}^{-1} at the beginning of the calculations and solve the system as a vector-matrix multiplication without appreciable additional computational cost.
- ❹ Once the coefficients a_i are determined, equation (4.5.25) applied to displacements and stresses is used to determine the viscoelastic solution at any time instant.

From a numerical point of view, the combination between the correspondence principle and the Prony series method provides an efficient, extremely cost-effective method to solve these viscoelastic problems in which the only requirement is to modify slightly the source code of an elastic program.

Rheological Model	Normal stresses	Deviatoric stresses
Relaxation 1	$\tilde{\mathbf{I}}(s) = \mathbf{I}$ (Elastic)	$\tilde{\mathbf{m}}(s) = \frac{s \mathbf{m} \mathbf{t}}{s \mathbf{t} + 2}$ (Maxwell)
Relaxation 2	$\tilde{\mathbf{I}}(s) = \frac{s \mathbf{I} \mathbf{t}}{s \mathbf{t} + 2}$ (Maxwell)	$\tilde{\mathbf{m}}(s) = \frac{s \mathbf{m} \mathbf{t}}{s \mathbf{t} + 2}$ (Maxwell)
Relaxation 3	$\tilde{\mathbf{I}}(s) = \mathbf{I} + \frac{2}{3} \mathbf{m} - \frac{2}{3} \tilde{\mathbf{m}}(s)$ (SLS)	$\tilde{\mathbf{m}}(s) = \frac{s \mathbf{m} \mathbf{t}}{s \mathbf{t} + 2}$ (Maxwell)

Table 4.5.1. Summary of the viscoelastic rheologies commonly assumed for the crust.

4.6 References

- Aliabadi, S. K., and T. E. Tezduyar, Space-time finite element computation of compressible flows involving moving boundaries and interfaces, *Comput. Meth. Appl. Mech. Engrg.*, 107, 209-223, 1993.
- Alonso, J. J., and A. Jameson, Fully-implicit time-marching aeroelastic solutions, *AIAA Paper*, 94-0056, 1994.
- Batina, J. T., Unsteady Euler airfoil solutions using unstructured dynamic meshes, *AIAA Paper*, 89-0115, AIAA 27th Aerospace Sciences Meeting, Reno, Nevada, 1989.
- Belytschko, T., P. Smolenski, and W. K. Liu, Stability of multi-time step partitioned integrators for first-order finite element systems, *Comput. Meth. Appl. Mech. Engrg.*, 49, 281-297, 1985.
- Blom, F. J., and P. Leyland, Analysis of fluid-structure interaction on moving airfoils by means of an improved ALE-method, *AIAA J.*, 97, 1997.
- Blom, F. J., A monolithical fluid-structure interaction algorithm applied to the piston problem, *Comput. Meth. Appl. Mech. Engrg.*, 167, 369-391, 1998.
- Bonafede, M., M. Dragoni, and M. Quareni, Displacement and stress fields produced by a centre of dilation and by a pressure source in a viscoelastic half-space: application to the study of ground deformation and seismic activity at Campi Flegrei, Italy, *Geophys. J. Royal Astr. Soc.*, 87, 455-485, 1986.
- Brezzi, F., and M. Fortin, Mixed and hybrid finite element methods, *Springer-Verlag*, 1991.
- Brooks, A. N., and T. J. R. Hughes, Streamline Upwind/Petrov-Galerkin formulations for convective dominated flows with particular emphasis on the incompressible Navier-Stokes equations, *Comput. Meth. Appl. Mech. Engrg.*, 32, 199-259, 1982.
- Childs, S. J., and B. D. Reddy, Finite element simulation of the motion of a rigid body in a fluid with free surface, *Comput. Meth. Appl. Mech. Engrg.*, 175, 99-120, 1999.
- Chorin, A. J., A numerical method for solving incompressible viscous problems, *J. Comput. Phys.*, 2, 12-26, 1967.
- Chorin, A. J., On the convergence of discrete approximation to the Navier-Stokes equations, *Math. Comput.*, 23, 1969.
- Codina, R., E. Oñate, and M. Cervera, The intrinsic time for the streamline-upwind/Petrov-Galerkin formulation using quadratic elements, *Comput. Meth. Appl. Mech. Engrg.*, 94, 239-262, 1992a.
- Codina, R., A finite element model for incompressible flow problems, *PhD Thesis*, UPC, Barcelona, 1992b.
- Codina, R., A finite element formulation for the numerical solution of the convection-diffusion equation, *CIMNE Monograph*, 14, 1993.

-
- Codina, R., and J. Blasco, A finite element formulation for the Stokes problem allowing equal velocity-pressure interpolation, *Comput. Meth. Appl. Mech. Engrg.*, 143, 373-391, 1997.
- Codina, R., M. Vázquez, and O. C. Zienkiewicz, A general algorithm for compressible and incompressible flows. The semi-implicit form, *CIMNE Publication*, 108, 1997.
- Codina, R., A comparison of some finite element methods for solving the diffusion-convection-reaction equation, *Comput. Meth. Appl. Mech. Engrg.*, 156, 185-210, 1998a.
- Codina, R., M. Vázquez, and O. C. Zienkiewicz, A general algorithm for compressible and incompressible flows. Part III : the semi-implicit form, *Inter. J. Numer. Meth. Fluids*, 27, 13-32, 1998b.
- Codina, R., and J. Blasco, Stabilized finite element method for the transient Navier-Stokes equations based on a pressure gradient projection, *Comput. Meth. Appl. Mech. Engrg.*, 182, 277-300, 2000.
- Cost, T. L., Approximate Laplace transform inversions in viscoelastic stress analysis, *AIAA J.*, 2, 2157-2166, 1964.
- Donéa, J., A Taylor-Galerkin method for convection transport equations, *Inter. J. Numer. Meth. Fluids*, 20, 101-119, 1984.
- Douglas, J., and T. F. Russell, Numerical methods for convection dominated problems based on combining the method of characteristics with finite element or finite differences procedures, *J. Numer. Analysis*, 19, 871-885, 1982.
- Dragoni, M., and C. Magnanensi, Displacement and stress produced by a pressurized, spherical magma chamber, surrounded by a viscoelastic shell, *Phys. Earth Plan. Interiors*, 56, 316-328, 1989.
- Engelman, M. S., and M. Jamnia, Transient flow past a circular cylinder: a benchmark solution, *Int. J. Numer. Meth. Fluids*, 11, 985-1000, 1990.
- Farhat, C., and T. Y. Lin, transient aeroelastic computations using multiple moving frames of reference, *AIAA Paper*, 90-3053, 1990.
- Farhat, C., K. C. Perk, and Y. D. Pelerin, An unconditionally stable staggered algorithm for transient finite element analysis of coupled thermoelastic problems, *Comput. Meth. Appl. Mech. Engrg.*, 85, 349-365, 1991.
- Farhat, C., and T. Y. Lin, A structure attached corotational fluid grid for transient aeroelastic computations, *AIAA J.*, 31, 597-599, 1993.
- Farhat, C., M. Lesoinne, and N. Maman, Mixed explicit/implicit time integration of coupled aerolastic problems: three-field formulation, geometric conservation and distributed solution, *Int. J. Numer. Meth. Fluids*, 21, 807-835, 1995.
- Farhat, C., M. Lesoinne, and P. Le Tallec, Load and motion transfer algorithms for fluid/structure interaction problems with non-matching discrete interfaces: Momentum and energy conservation, optimal discretization and application to aeroelasticity, *Comput. Meth. Appl. Mech. Engrg.*, 157, 95-114, 1998.

-
- Fernández, J., and J. B. Rundle, Gravity changes and deformation due to a magmatic intrusion in a two-layered crustal model, *J. Geophys. Res.*, 99, 2737-2746, 1994.
- Folch, A., J. Fernández, J. B. Rundle, and J. Martí, Ground deformation in a viscoelastic medium composed of a layer overlaying a half-space. A comparison between point and extended sources, *Geophys. J. Int.*, 140, 37-50, 2000.
- Franca, L. P., and R. Stenberg, Error analysis of some Galerkin least-squares methods for the elasticity equations, *J. Numer. Analysis*, 28, 1680-1697, 1991.
- Fung, Y. C., Foundations of solid mechanics, New Jersey, 1965.
- Ghia, U., K. N. Ghia, and C. T. Shin, High-Re solutions for incompressible flow using the Navier-Stokes equations and a multigrid method, *J. Comput. Phys.*, 48, 387-411, 1982.
- He, L., Integration of 2-D fluid/structure coupled system for calculations of turbomachinery aerodynamic/aeroelastic instabilities, *Int. J. Comput. Fluid Dyn.*, 3, 217-231, 1994.
- Hindmarsh, A. C., P. M. Gresho, and D. F. Griffiths, The stability of explicit Euler time-integration for certain finite-difference approximation of the multidimensional advection-diffusion equations, *Int. J. Numer. Meth. Fluids*, 4, 853-897, 1984.
- Hirsch, C., Numerical Computation of Internal and External Flows, *John Wiley & Sons*, 1991.
- Houzeaux, G., and R. Codina, Transmission conditions with constraints in domain decomposition methods for the incompressible Navier-Stokes equations, in Computational Fluid dynamics '98. Proceedings of the Fourth European Fluid Dynamics Conference, Athens(Greece), 194-199, 1998.
- Hughes, T. J. R., and A. Brooks, A multi-dimensional upwind scheme with no crosswind diffusion, *ASME*, New York, 1979.
- Hughes, T. J. R., and A. Brooks, A theoretical framework for Petrov-Galerkin methods, with discontinuous weighting functions: applications to the streamline procedure, *Finite Elements in Fluids*, *Wiley & Sons*, London, 1982.
- Hughes, T. J. R., and L. P. Franca, A new finite element formulation for computational fluid dynamics: VII. The Stokes problem with various well-posed boundary conditions: symmetric formulations that converge for all velocity/pressure spaces, *Comput. Meth. Appl. Mech. Engrg.*, 65, 85-96, 1987.
- Hughes, T. J. R., L. P. Franca, and G. M. Hulbert, A new finite element formulation for computational fluid dynamics: VIII. The Galerkin/least-squares method for advective-diffusion equations, *Comput. Meth. Appl. Mech. Engrg.*, 73, 173-198, 1989.
- Hughes, T. J. R., Multiscale phenomena: Green's function, the Dirichlet to Neumann formulation, subgrid scale models, bubbles and the origins of stabilized formulations, *Comput. Meth. Appl. Mech. Engrg.*, 127, 387-401, 1995.
- Johnson, A. A., and T. E. Tezduyar, Mesh update strategies in parallel finite element computations of flow problems with moving boundaries and interfaces, *Comput. Meth. Appl. Mech. Engrg.*, 119, 73-94, 1994.

-
- Kandil, O. A., and H. A. Chuang, Unsteady vortex-dominated flows around manoeuvring wings over a wide range of Mach numbers, *AIAA Paper*, 88-0317, 1988.
- Kelly, D. W., S. Nakazawa, O. C. Zienkiewicz, and J. C. Heinrich, A note on upwinding and anisotropic balancing dissipation in finite element approximations to convective diffusion problems, *Inter. J. Numer. Meth. Engrg.*, 15, 1705-1711, 1980.
- Kim, J., and P. Moin, Application of a fractional-step method to incompressible Navier-Stokes equations, *J. Comput. Phys.*, 59, 308-323, 1985.
- Lesoinne, M., and C. Farhat, Stability analysis of dynamic meshes for transient aeroelastic computations, *AIAA Paper*, 93-3325, 1993.
- Lesoinne, M., and C. Farhat, Geometric conservation laws for flow problems with moving boundaries and deformable meshes, and their impact on aeroelastic computations, *Comput. Meth.. Appl. Mech. Engrg.*, 134, 71-90, 1996.
- Lönher, R., K. Morgan, and O. C. Zienkiewicz, The solution of non-linear hyperbolic equation systems by the finite element method, *Int. J. Numer. Meth. Fluids*, 4, 1043-1063, 1984.
- Lynch, D. R., Unified approach to simulation on deforming elements with applications to phase change problems, *J. Comput. Phys.*, 47, 187-411, 1982.
- Masud, A., A space-time finite element method for fluid structure interaction, *Ph. D. Thesis*, Stanford University, 1993.
- Masud, A., and T. J. R. Hughes, A space-time Galerkin/least-squares finite element formulation of the Navier-Stokes equations for moving domain problems, *Comput. Meth. Appl. Mech. Engrg.*, 146, 91-126, 1997.
- Melville, R. B., S. A. Morton, and D. P. Rizzetta, Implementation of a fully-implicit aeroelastic Navier-Stokes solver, *AIAA Paper*, 94-0056, 1994.
- Mohamad, A. A., and R. Viskanta, Transient natural convection of low-Prandtl-number fluids in a differentially heated cavity, *Int. J. Numer. Meth. Fluids*, 13, 61-81, 1991.
- Morton, S. A., R. B. Melville, and M. R. Visbal, Accuracy and coupling issues of aeroelastic Navier-Stokes solutions on deforming meshes, *AIAA Paper*, 97-1085, 1997.
- Papanastasiou, T. C., N. Malamataris, and K. Ellwood, A new outflow boundary condition, *Inter. J. Numer. Meth. Fluids*, 14, 587-608, 1992.
- Park, K. C., C. A. Felippa, and J. A. De Runtz, Stabilisation of staggered solution procedures for fluid-structure interaction analysis, *Comput. Meth. Fluid-Structure Interaction Problems*, 26, 1977.
- Piperno, S., C. Farhat, and B. Larrouturou, Partitioned procedures for the transient solution of coupled aeroelastic problems, *Comput. Meth. Appl. Mech. Engrg.*, 124, 79-111, 1995.
- Pironneau, O., On the transport-diffusion algorithm and its applications to the Navier-Stokes equations, *Numer. Math.*, 38, 309-332, 1982.
- Rausch, R. D., J. T. Batina, and H. T. Y. Yang, Euler flutter analysis of airfoils using unstructured dynamic meshes, *AIAA Paper*, 89-1384, 1989.

-
- Rundle, J. B., Static elastic-gravitational deformation of a layered half space by point couple sources, *J. Geophys. Res.*, 85, 5355-5363, 1980.
- Rundle, J. B., Viscoelastic-gravitational deformation by a rectangular thrust fault in a layered Earth, *J. Geophys. Res.*, 87, 7787-7796, 1982.
- Schapery, R. A., Approximate methods of transform inversion for viscoelastic stress analysis, *Proc. Fourth U. S. Natl. Congr. Appl. Mech.*, 1075-1085, 1961.
- Schreiber, R., and H. B. Keller, Driven cavity flows by efficient numerical techniques, *J. Comput. Phys.*, 49, 310-333, 1983.
- Shen, J., Hopf bifurcation of the unsteady regularized driven cavity-flow, *J. Comput. Phys.*, 95, 228-245, 1991.
- Simo, J., and F. Armero, Unconditional stability and long behaviour of transient algorithms for the incompressible Navier-Stokes equations, *Comput. Meth. Appl. Mech. Engrg.*, 111, 111-154, 1994.
- Tanahashi, T., H. Okanaga, and T. Saito, GSMAC finite element method for the unsteady incompressible Navier-Stokes equations at high Reynolds numbers, *Int. J. Numer. Meth. Fluids*, 11, 479-499, 1990.
- Temam, R., Sur l'approximation de la solution des équations de Navier-Stokes par la méthode des pas fractionnaires (I), *Arch. Rat. Mech. Anal.*, 32, 135-153, 1969.
- Tezduyar, T., M. Behr, and J. Liou, A new strategy for finite element computations involving moving boundaries and interfaces-The deforming spatial domain/space-time procedure: I. The concept and the preliminary numerical tests, *Comput. Meth. Appl. Mech. Engrg.*, 94, 339-351, 1992a.
- Tezduyar, T., M. Behr, S. Mittal, and J. Liou, A new strategy for finite element computations involving moving boundaries and surfaces-the deformable-spatial-domain/space-time procedure: II. Computation of free-surface flows, two-liquid flows and flows with drifting cylinders, *Comput. Meth. Appl. Mech. Engrg.*, 94, 353-371, 1992b.
- von Neumann, J., and R. D. Richtmeyer, A method for the numerical calculation of hydrodynamical shocks, *J. Appl. Phys.*, 21, 232, 1950.
- Turcotte, D. L., and G. Schubert, *Geodynamics*, 1982.

Appendix 4A. Weak Forms

This appendix compiles the final expressions for the weak forms of the Navier-Stokes equations (section 4.1) and for the convective transport equation (section 4.2).

Fractional momentum equation

The weak form is obtained substituting equations (4.1.38), (4.1.40), (4.1.43) (or 4.1.44), and (4.1.49) (or 4.1.50) into equation (4.1.30). An additional stabilisation term must be added in convective dominated flows (see section 4.1.6 and Appendix 4B).

$$\begin{aligned}
\text{LHS} = & \int_{\Omega} \tilde{\mathbf{W}} \cdot \tilde{\mathbf{U}}^{n+1} d\Omega \\
& + \Delta t q_1^1 \int_{\Omega} \tilde{\mathbf{W}} \cdot \nabla \cdot (\mathbf{u}^n \otimes \tilde{\mathbf{U}}^{n+1}) d\Omega && \text{(convective term)}^1 \\
& - \Delta t q_1^1 \int_{\Omega} \tilde{\mathbf{W}} \cdot (\hat{\mathbf{u}} \cdot (\nabla \tilde{\mathbf{U}})^{n+1}) d\Omega && \text{(mesh motion term)}^2 \\
& + \Delta t q_2^1 \int_{\Omega} \left[\frac{\mathbf{m}}{\mathbf{r}^n} \nabla \tilde{\mathbf{W}} : \nabla \tilde{\mathbf{U}}^{n+1} - \frac{\mathbf{m}}{(\mathbf{r}^n)^2} \nabla \tilde{\mathbf{W}} : (\nabla \mathbf{r}^n \otimes \tilde{\mathbf{U}}^{n+1}) \right] d\Omega && \text{(viscous term)}^3 \\
& - \Delta t q_2^1 \int_{\Gamma} \left[\frac{\mathbf{m}}{\mathbf{r}^n} \tilde{\mathbf{W}} \cdot (\tilde{\mathbf{U}} \nabla)^{n+1} \cdot \mathbf{n} - \frac{\mathbf{m}}{(\mathbf{r}^n)^2} \tilde{\mathbf{W}} \cdot (\tilde{\mathbf{U}}^{n+1} \otimes \nabla \mathbf{r}^n) \cdot \mathbf{n} \right] d\Gamma && \text{(boundary viscous term)}
\end{aligned}$$

$$\begin{aligned}
\text{RHS} = & \int_{\Omega} \tilde{\mathbf{W}} \cdot \mathbf{U}^n d\Omega \\
& - \Delta t q_1^2 \int_{\Omega} \tilde{\mathbf{W}} \cdot \nabla \cdot (\mathbf{u}^n \otimes \mathbf{U}^n) d\Omega - \Delta t q_1^3 \int_{\Omega} \tilde{\mathbf{W}} \cdot \nabla \cdot (\mathbf{u}^{n-1} \otimes \mathbf{U}^{n-1}) d\Omega && \text{(convective terms)} \\
& - \Delta t^2 (1-g) q_1^1 \int_{\Omega} \nabla \tilde{\mathbf{W}} : (\mathbf{u}^n \otimes \nabla p^n) d\Omega && \text{(splitting correction of the convective term)} \\
& + \Delta t^2 (1-g) q_1^1 \int_{\Gamma} \tilde{\mathbf{W}} \cdot (\nabla p^n \otimes \mathbf{u}^n) \cdot \mathbf{n} d\Gamma \\
& + \Delta t q_1^2 \int_{\Omega} \tilde{\mathbf{W}} \cdot [\hat{\mathbf{u}} \cdot (\nabla \mathbf{U})^n] d\Omega + \Delta t q_1^3 \int_{\Omega} \tilde{\mathbf{W}} \cdot [\hat{\mathbf{u}} \cdot (\nabla \mathbf{U})^{n-1}] d\Omega && \text{(mesh motion terms)} \\
& + \Delta t^2 q_1^1 (1-g) \int_{\Omega} \nabla \cdot (\tilde{\mathbf{W}} \otimes \hat{\mathbf{u}}) \cdot \nabla p d\Omega && \text{(splitting correction of the mesh motion terms)} \\
& - \Delta t^2 q_1^1 (1-g) \int_{\Gamma} \tilde{\mathbf{W}} \cdot (\nabla p \otimes \hat{\mathbf{u}}) \cdot \mathbf{n} d\Gamma
\end{aligned}$$

¹ For the second order implicit scheme the advective velocity is evaluated as $3/2\mathbf{u}^n - 1/2\mathbf{u}^{n-1}$. See observation in page 4-12.

² The mesh velocity is evaluated at $t^{n+1/2}$ as indicated in equation (4.3.15).

³ When $g=1$ and for compressible flows, density must be evaluated as $3/2\mathbf{r}^n - 1/2\mathbf{r}^{n-1}$. See observation in page 4-14.

$$\begin{aligned}
 & -\mathbf{g} \Delta t \int_{\Omega} \tilde{\mathbf{W}} \cdot \nabla p^n d\Omega && \text{(incremental fractional step term)} \\
 & + \Delta t \int_{\Omega} \mathbf{r}^n \tilde{\mathbf{W}} \cdot \mathbf{g} d\Omega && \text{(body forces term)}^1 \\
 & - \Delta t \mathbf{q}_2^2 \int_{\Omega} \nabla \tilde{\mathbf{W}} \cdot \cdot \mathbf{T}^n d\Omega - \Delta t \mathbf{q}_2^3 \int_{\Omega} \nabla \tilde{\mathbf{W}} \cdot \cdot \mathbf{T}^{n-1} d\Omega && \text{(viscous terms)} \\
 & + \Delta t \mathbf{q}_2^2 \int_{\Gamma} \tilde{\mathbf{W}} \cdot \mathbf{T}^n \cdot \mathbf{n} d\Gamma + \Delta t \mathbf{q}_2^3 \int_{\Gamma} \tilde{\mathbf{W}} \cdot \mathbf{T}^{n-1} \cdot \mathbf{n} d\Gamma && \text{(boundary viscous terms)} \\
 & - \Delta t \int_{\Omega} \mathbf{m} \left[\nabla \tilde{\mathbf{W}} \cdot \cdot \nabla \mathbf{u}^n - \frac{2}{3} (\nabla \cdot \tilde{\mathbf{W}}) (\nabla \cdot \mathbf{u})^n \right] d\Omega && \text{(uncoupling of the implicit viscous term)}^2 \\
 & + \Delta t \int_{\Gamma} \mathbf{m} \left[\tilde{\mathbf{W}} \cdot \nabla \mathbf{u}^n \cdot \mathbf{n} - \frac{2}{3} (\tilde{\mathbf{W}} \cdot \mathbf{n}) (\nabla \cdot \mathbf{u})^n \right] d\Gamma && \text{(uncoupling of the implicit boundary viscous} \\
 & \text{term)}^3
 \end{aligned}$$

Continuity equation

Weak form given by equation (4.1.54)

$$\begin{aligned}
 & \int_{\Omega} W_p A p^{n+1} d\Omega + \Delta t^2 \left(1 + \frac{\mathbf{a}}{\Delta t} \right) \int_{\Omega} \nabla W_p \cdot \nabla p^{n+1} d\Omega = \\
 & \int_{\Omega} W_p B \mathbf{r}^n d\Omega + \Delta t \int_{\Omega} W_p \hat{\mathbf{u}} \cdot \nabla \mathbf{r}^n d\Omega - \Delta t \int_{\Omega} W_p (\nabla \cdot \mathbf{U})^n d\Omega + \Delta t \int_{\Omega} \nabla W_p \cdot \Delta \tilde{\mathbf{U}}^n d\Omega + \\
 & \mathbf{g} \Delta t^2 \int_{\Omega} \nabla W_p \cdot \nabla p^n d\Omega + \mathbf{a} \Delta t \int_{\Omega} \nabla W_p \cdot \xi^n d\Omega - \Delta t \int_{\Gamma} W_p \mathbf{n} \cdot \Delta \mathbf{U}^n d\Gamma
 \end{aligned}$$

Pressure gradient projection equation

Weak form given by equation (4.1.55)

$$\int_{\Omega} \mathbf{W}_G \cdot \xi^{n+1} d\Omega = \int_{\Omega} \mathbf{W}_G \cdot \nabla p^{n+1} d\Omega$$

Momentum equation

Weak form given by equation (4.1.56)

$$\int_{\Omega} \mathbf{W} \cdot \mathbf{U}^{n+1} d\Omega = \int_{\Omega} \mathbf{W} \cdot \tilde{\mathbf{U}}^{n+1} d\Omega - \Delta t \int_{\Omega} \mathbf{W} \cdot \nabla p^{n+1} d\Omega + \mathbf{g} \Delta t \int_{\Omega} \mathbf{W} \cdot \nabla p^n d\Omega$$

¹ For compressible flows and second order schemes $3/2 \mathbf{r}^n - 1/2 \mathbf{r}^{n-1}$. See observation in page 4-6.

² Using equation (4.1.43), that is, considering $\mathbf{q}_2^1 = 1$.

³ Using equation (4.1.49), that is, considering $\mathbf{q}_2^1 = 1$.

Energy equation

Weak form given by equation (4.1.57). As in the fractional momentum equation, an additional stabilisation term must be added in those convective dominated flows (see section 4.1.6 and Appendix 4B).

$$\begin{aligned}
 \text{LHS} &= \int_{\Omega} W_T T^{n+1} d\Omega \\
 &- \Delta t q_3^1 \int_{\Omega} W_T [(\hat{\mathbf{u}} - \mathbf{u}) \cdot \nabla T]^{n+1} d\Omega && \text{(convective term)} \\
 &+ \Delta t q_3^1 \int_{\Omega} \frac{k}{c_v} \nabla W_T \cdot \left(\frac{1}{\mathbf{r}} \nabla T \right)^{n+1} d\Omega - \Delta t q_3^1 \int_{\Omega} \frac{k}{c_v} W_T \left(\frac{1}{\mathbf{r}^2} \nabla \mathbf{r} \cdot \nabla T \right)^{n+1} d\Omega \\
 &- \Delta t q_3^1 \int_{\Gamma} \frac{k}{c_v} W_T \mathbf{n} \cdot \left(\frac{1}{\mathbf{r}} \nabla T \right)^{n+1} d\Gamma && \text{(diffusive terms)} \\
 \\
 \text{RHS} &= \int_{\Omega} W_T T^n d\Omega \\
 &+ \Delta t q_3^2 \int_{\Omega} W_T [(\hat{\mathbf{u}} - \mathbf{u}) \cdot \nabla T]^n d\Omega + \Delta t q_3^3 \int_{\Omega} W_T [(\hat{\mathbf{u}} - \mathbf{u}) \cdot \nabla T]^{n-1} d\Omega && \text{(convective terms)} \\
 &- \Delta t q_3^2 \int_{\Omega} \frac{k}{c_v} \nabla W_T \cdot \left(\frac{1}{\mathbf{r}} \nabla T \right)^n d\Omega - \Delta t q_3^3 \int_{\Omega} \frac{k}{c_v} \nabla W_T \cdot \left(\frac{1}{\mathbf{r}} \nabla T \right)^{n-1} d\Omega \\
 &+ \Delta t q_3^2 \int_{\Omega} \frac{k}{c_v} W_T \left(\frac{1}{\mathbf{r}^2} \nabla \mathbf{r} \cdot \nabla T \right)^n d\Omega + \Delta t q_3^3 \int_{\Omega} \frac{k}{c_v} W_T \left(\frac{1}{\mathbf{r}^2} \nabla \mathbf{r} \cdot \nabla T \right)^{n-1} d\Omega && \text{(diffusive terms)} \\
 &+ \Delta t q_3^2 \int_{\Gamma} \frac{k}{c_v} W_T \mathbf{n} \cdot \left(\frac{1}{\mathbf{r}} \nabla T \right)^n d\Gamma + \Delta t q_3^3 \int_{\Gamma} \frac{k}{c_v} W_T \mathbf{n} \cdot \left(\frac{1}{\mathbf{r}} \nabla T \right)^{n-1} d\Gamma \\
 &+ \Delta t \int_{\Omega} \frac{1}{c_v} W_T \left[\frac{1}{\mathbf{r}} \mathbf{S} \cdot \nabla \mathbf{u} \right]^{n+q_3^-} d\Omega && \text{(Joule effect terms)} \\
 &+ \Delta t \int_{\Omega} \frac{1}{c_v} W_T \mathbf{g} \cdot \mathbf{u}^{n+q_3^-} d\Omega && \text{(gravitational terms)}
 \end{aligned}$$

Convective transport equation

Weak form given by equation (4.2.4)

$$\begin{aligned}
 \int_{\Omega} W C^{n+1} d\Omega + \Delta t q_c \int_{\Omega} W (\mathbf{u}^{n+1} - \hat{\mathbf{u}}) \cdot \nabla C^{n+1} d\Omega = \\
 \int_{\Omega} W C^n d\Omega - \Delta t (1 - q_c) \int_{\Omega} W (\mathbf{u}^n - \hat{\mathbf{u}}) \cdot \nabla C^n d\Omega
 \end{aligned}$$

Appendix 4B. Discretised Algebraic Systems

Once the space has been discretised using the standard Galerkin formulation, the weak forms become algebraic systems. This appendix compiles the final expressions of these algebraic systems for the Navier-Stokes equations (section 4.1) and the convective transport equation (section 4.2). The resultant vectors and matrixes are expressed in Cartesian coordinates. Cylindrical coordinates (r, \mathbf{q}, z) are used in axially symmetric problems¹. If this is the case, some of the expressions given here must be slightly modified taking into account that

$$\nabla \cdot \mathbf{u} = \frac{\partial u_r}{\partial r} + \frac{\partial u_z}{\partial z} + \frac{u_r}{r} \quad (4B.1)$$

$$\nabla \mathbf{u} = \begin{bmatrix} \frac{\partial u_r}{\partial r} & 0 & \frac{\partial u_z}{\partial r} \\ 0 & \frac{u_r}{r} & 0 \\ \frac{\partial u_r}{\partial z} & 0 & \frac{\partial u_z}{\partial z} \end{bmatrix} \quad (4B.2)$$

$$\nabla \cdot \mathbf{T} = \begin{bmatrix} \frac{\partial T_{rr}}{\partial r} + \frac{\partial T_{zr}}{\partial z} + \frac{1}{r}(T_{rr} - T_{qq}) \\ 0 \\ \frac{\partial T_{zz}}{\partial z} + \frac{\partial T_{rz}}{\partial r} + \frac{T_{rz}}{r} \end{bmatrix} \quad (4B.3)$$

Notation A vector of nodal unknowns is designed by an arrow above the vector. The index m runs from 1 to $ndime$, where $ndime$ is the space dimension. The indexes i and j run from 1 to $nnode$, where $nnode$ is the number of nodes of the finite element mesh (obviously, when there is assembly, $nnode$ is the elemental number of nodes n_e). The shape function associated with the i -th node of the finite element mesh is denoted by N^i .

Fractional momentum equation

$$\mathbf{F} \cdot \tilde{\mathbf{U}}_m^{n+1} = \bar{\mathbf{F}}_m \quad (4B.4)$$

where

¹ In these problems there is no \mathbf{q} dependence and, in consequence, can be solved as a two-dimensional Cartesian case identifying r with x and z with y .

$$\mathbf{F} \equiv \mathbf{M} + \Delta t \mathbf{q}_1^1 [\mathbf{K}(\mathbf{u}^n) - \hat{\mathbf{K}}(\hat{\mathbf{u}})] + \Delta t \mathbf{q}_2^1 [\mathbf{V}(\mathbf{r}^n) - \mathbf{V}^{\mathbf{B}}(\mathbf{r}^n)] + \Delta t \mathbf{S}^{\mathbf{F}}(\mathbf{u}^n, \hat{\mathbf{u}}) \quad (4B.5)$$

$$\begin{aligned} \bar{\mathbf{F}}_m &\equiv \bar{\mathbf{M}}_m(\mathbf{U}^n) \\ &- \Delta t [\mathbf{q}_1^2 \bar{\mathbf{K}}_m(\mathbf{u}^n, \mathbf{U}^n) + \mathbf{q}_1^3 \bar{\mathbf{K}}_m(\mathbf{u}^{n-1}, \mathbf{U}^{n-1}) + \mathbf{q}_1^1 \Delta t (1 - \mathbf{g}) \bar{\mathbf{K}}_m^{\text{co}}(\mathbf{u}^n, p^n)] \\ &+ \Delta t [\mathbf{q}_1^2 \bar{\tilde{\mathbf{K}}}_m(\hat{\mathbf{u}}, \mathbf{U}^n) + \mathbf{q}_1^3 \bar{\tilde{\mathbf{K}}}_m(\hat{\mathbf{u}}, \mathbf{U}^{n-1})] - \mathbf{g} \Delta t \bar{\mathbf{G}}_m(p^n) + \Delta t \bar{\mathbf{B}}_m(\mathbf{r}^n) \\ &- \Delta t [\bar{\mathbf{V}}_m^{\text{dec}}(\mathbf{q}_2^1, \mathbf{u}^n) + \mathbf{q}_2^2 \bar{\mathbf{V}}_m(\mathbf{T}^n) + \mathbf{q}_2^3 \bar{\mathbf{V}}_m(\mathbf{T}^{n-1})] \\ &+ \Delta t \bar{\mathbf{S}}_m^{\mathbf{F}}(\mathbf{u}^n, \mathbf{u}^{n-1}, \hat{\mathbf{u}}, \mathbf{U}^n, \mathbf{U}^{n-1}, p^n, \mathbf{r}^n, \mathbf{T}^{n+\bar{q}_2}) \end{aligned} \quad (4B.6)$$

Note that the contributions of the stabilisation term have been also included in the LHS ($\mathbf{S}^{\mathbf{F}}$) and in the RHS ($\bar{\mathbf{S}}_m^{\mathbf{F}}$) of equation (4B.4). Both the matrix $\mathbf{S}^{\mathbf{F}}$ and the vector $\bar{\mathbf{S}}_m^{\mathbf{F}}$ will obviously depend on the method of stabilisation chosen. See table 4.1.3 for the definitions of the intrinsic times. Note also that, if the methods of stabilisation are applied as proposed in the section 4.1.6, the implicit contribution of the viscous term in the residual does not allow to uncouple the components of the fractional momentum. Moreover, when the GLS, the TG or the SGS methods are applied, the operator \mathbf{P} contains also a diffusive contribution that does not allow the uncoupling. The first inconvenience can be solved treating the viscous contribution of the residual explicitly. In the second case, the diffusive contribution of \mathbf{P} that does not allow the uncoupling is neglected. In Cartesian coordinates, the matrixes and the vectors introduced above are

Matrixes

$$\mathbf{M}_{ij} = \int_{\Omega} N^i N^j d\Omega \quad (4B.7)$$

$$\mathbf{K}(\mathbf{u}^n)_{ij} = \int_{\Omega} N^i \left[(\nabla \cdot \mathbf{u})^n N^j + u_k^n \frac{\mathcal{I} N^j}{\mathcal{I} x_k} \right] d\Omega \quad (4B.8)$$

$$\hat{\mathbf{K}}(\hat{\mathbf{u}})_{ij} = \int_{\Omega} N^i \hat{u}_k \frac{\mathcal{I} N^j}{\mathcal{I} x_k} d\Omega \quad (4B.9)$$

$$\mathbf{V}(\mathbf{r}^n)_{ij} = \int_{\Omega} \frac{\mathbf{m}}{\mathbf{r}^n} \left(\frac{\mathcal{I} N^i}{\mathcal{I} x_k} \frac{\mathcal{I} N^j}{\mathcal{I} x_k} - \frac{1}{\mathbf{r}^n} \frac{\mathcal{I} N^i}{\mathcal{I} x_k} \frac{\mathcal{I} \mathbf{r}^n}{\mathcal{I} x_k} N^j \right) d\Omega \quad (4B.10)$$

$$\mathbf{V}^{\mathbf{B}}(\mathbf{r}^n)_{ij} = \int_{\Gamma} \frac{\mathbf{m}}{\mathbf{r}^n} \left(N^i \frac{\mathcal{I} N^j}{\mathcal{I} x_k} n_k - \frac{1}{\mathbf{r}^n} N^i \frac{\mathcal{I} \mathbf{r}^n}{\mathcal{I} x_k} n_k N^j \right) d\Omega \quad (4B.11)$$

Vectors

$$\bar{\mathbf{M}}_m(\mathbf{U}^n)_j = \int_{\Omega} N^j U_m^n d\Omega \quad (4B.12)$$

$$\bar{\mathbf{K}}_m(\mathbf{u}^n, \mathbf{U}^n)_j = \int_{\Omega} N^j \frac{\mathcal{I}}{\mathcal{I} x_k} (u_k^n U_m^n) d\Omega \quad (4B.13)$$

$$\bar{\mathbf{K}}_m^{\text{co}}(\mathbf{u}^n, p^n)_j = \int_{\Omega} \frac{\mathcal{I} N^j}{\mathcal{I} x_k} u_k^n \frac{\mathcal{I} p^n}{\mathcal{I} x_m} d\Omega - \int_{\Gamma} N^j \frac{\mathcal{I} p^n}{\mathcal{I} x_m} u_k^n n_k d\Gamma \quad (4B.14)$$

$$\bar{\tilde{\mathbf{K}}}_m(\hat{\mathbf{u}}, \mathbf{U}^n)_j = \int_{\Omega} N^j \hat{u}_k \frac{\mathcal{I} U_m^n}{\mathcal{I} x_k} d\Omega \quad (4B.15)$$

$$\bar{\mathbf{G}}_m(p^n)_j = \int_{\Omega} N^j \frac{\mathcal{I} p^n}{\mathcal{I} x_m} d\Omega \quad (4B.16)$$

$$\bar{\mathbf{B}}_m(\mathbf{r}^n)_j = \int_{\Omega} N^j \mathbf{r}^n g_m d\Omega \quad (4B.17)$$

$$\bar{\mathbf{V}}_m(\mathbf{T}^n)_j = \int_{\Omega} \frac{\mathcal{I} N^j}{\mathcal{I} x_k} \mathbf{T}_{mk}^n d\Omega - \int_{\Gamma} N^j \mathbf{T}_{mk}^n n_k d\Gamma \quad (4B.18)$$

$$\bar{\mathbf{V}}_m^{\text{dec}}(\mathbf{q}_2^1 = 0, \mathbf{u}^n)_j = 0 \quad (4B.19)$$

$$\begin{aligned} \bar{\mathbf{V}}_m^{\text{dec}}(\mathbf{q}_2^1 = 1, \mathbf{u}^n)_j &= \int_{\Omega} \mathbf{m} \left[\frac{\mathcal{I} N^j}{\mathcal{I} x_k} \frac{\mathcal{I} u_k^n}{\mathcal{I} x_m} - \frac{2}{3} (\nabla \cdot \mathbf{u})^n \frac{\mathcal{I} N^j}{\mathcal{I} x_m} \right] d\Omega \\ &\quad - \int_{\Gamma} \mathbf{m} \left[N^j \frac{\mathcal{I} u_k^n}{\mathcal{I} x_m} n_k - \frac{2}{3} (\nabla \cdot \mathbf{u})^n N^j n_m \right] d\Gamma \end{aligned} \quad (4B.20)$$

$$\begin{aligned} \bar{\mathbf{V}}_m^{\text{dec}}\left(\mathbf{q}_2^1 = \frac{1}{2}, \mathbf{u}^n\right)_j &= \frac{3}{4} \int_{\Omega} \mathbf{m} \left[\frac{\mathcal{I} N^j}{\mathcal{I} x_k} \frac{\mathcal{I} u_k^n}{\mathcal{I} x_m} - \frac{2}{3} (\nabla \cdot \mathbf{u})^n \frac{\mathcal{I} N^j}{\mathcal{I} x_m} \right] d\Omega \\ &\quad - \frac{1}{4} \int_{\Omega} \mathbf{m} \left[\frac{\mathcal{I} N^j}{\mathcal{I} x_k} \frac{\mathcal{I} u_k^{n-1}}{\mathcal{I} x_m} - \frac{2}{3} (\nabla \cdot \mathbf{u})^{n-1} \frac{\mathcal{I} N^j}{\mathcal{I} x_m} \right] d\Omega \\ &\quad - \frac{3}{4} \int_{\Gamma} \mathbf{m} \left[N^j \frac{\mathcal{I} u_k^n}{\mathcal{I} x_m} n_k - \frac{2}{3} (\nabla \cdot \mathbf{u})^n N^j n_m \right] d\Gamma \\ &\quad + \frac{1}{4} \int_{\Gamma} \mathbf{m} \left[N^j \frac{\mathcal{I} u_k^{n-1}}{\mathcal{I} x_m} n_k - \frac{2}{3} (\nabla \cdot \mathbf{u})^{n-1} N^j n_m \right] d\Gamma \end{aligned} \quad (4B.21)$$

Stabilisation terms

$$\mathbf{s}^{\mathbf{F}}(\mathbf{u}^n, \hat{\mathbf{u}})_{ij} = \sum_{e=1}^{ne} \int_{\Omega^e} \mathbf{t}_{\text{SUPG}}^e u_k^n \frac{\mathcal{J}}{\mathcal{J} x_k} N^i \mathbf{R}_j^{\text{IMPL}} d\Omega \quad (4\text{B.22})$$

$$(\bar{\mathbf{S}}_m^{\mathbf{F}})_j = \sum_{e=1}^{ne} \int_{\Omega^e} \mathbf{t}_{\text{SUPG}}^e u_k^n \frac{\mathcal{J}}{\mathcal{J} x_k} N^j \bar{\mathbf{R}}_m^{\text{EXPL}} d\Omega \quad (\text{SUPG})$$

$$\mathbf{s}^{\mathbf{F}}(\mathbf{u}^n, \hat{\mathbf{u}})_{ij} = \sum_{e=1}^{ne} \int_{\Omega^e} \mathbf{t}_{\text{CG}}^e \frac{\mathcal{J}}{\mathcal{J} x_k} (u_k^n N^i) \bar{\mathbf{R}}_j^{\text{IMPL}} d\Omega \quad (4\text{B.23})$$

$$(\bar{\mathbf{S}}_m^{\mathbf{F}})_j = \sum_{e=1}^{ne} \int_{\Omega^e} \mathbf{t}_{\text{CG}}^e \frac{\mathcal{J}}{\mathcal{J} x_k} (u_k^n N^j) \bar{\mathbf{R}}_m^{\text{EXPL}} d\Omega \quad (\text{CG})$$

$$\mathbf{s}^{\mathbf{F}}(\mathbf{u}^n, \hat{\mathbf{u}})_{ij} = \sum_{e=1}^{ne} \int_{\Omega^e} \mathbf{t}_{\text{GLS}}^e \left[u_k^n \frac{\mathcal{J}}{\mathcal{J} x_k} N^i - m \frac{\mathcal{J}^2 N^i}{\mathcal{J} x_k^2} \right] \mathbf{R}_j^{\text{IMPL}} d\Omega \quad (4\text{B.24})$$

$$(\bar{\mathbf{S}}_m^{\mathbf{F}})_j = \sum_{e=1}^{ne} \int_{\Omega^e} \mathbf{t}_{\text{GLS}}^e \left[u_k^n \frac{\mathcal{J}}{\mathcal{J} x_k} N^j - m \frac{\mathcal{J}^2 N^j}{\mathcal{J} x_k^2} \right] \bar{\mathbf{R}}_m^{\text{EXPL}} d\Omega \quad (\text{GLS})$$

$$\mathbf{s}^{\mathbf{F}}(\mathbf{u}^n, \hat{\mathbf{u}})_{ij} = \sum_{e=1}^{ne} \int_{\Omega^e} \mathbf{t}_{\text{TG}}^e \left[\frac{\mathcal{J}}{\mathcal{J} x_k} (u_k^n N^i) + m \frac{\mathcal{J}^2 N^i}{\mathcal{J} x_k^2} \right] \mathbf{R}_j^{\text{IMPL}} d\Omega \quad (4\text{B.25})$$

$$(\bar{\mathbf{S}}_m^{\mathbf{F}})_j = \sum_{e=1}^{ne} \int_{\Omega^e} \mathbf{t}_{\text{TG}}^e \left[\frac{\mathcal{J}}{\mathcal{J} x_k} (u_k^n N^j) + m \frac{\mathcal{J}^2 N^j}{\mathcal{J} x_k^2} \right] \bar{\mathbf{R}}_m^{\text{EXPL}} d\Omega \quad (\text{TG})$$

$$\mathbf{s}^{\mathbf{F}}(\mathbf{u}^n, \hat{\mathbf{u}})_{ij} = \sum_{e=1}^{ne} \int_{\Omega^e} \mathbf{t}_{\text{SGS}}^e \left[\frac{\mathcal{J}}{\mathcal{J} x_k} (u_k^n N^i) + m \frac{\mathcal{J}^2 N^i}{\mathcal{J} x_k^2} \right] \mathbf{R}_j^{\text{IMPL}} d\Omega \quad (4\text{B.26})$$

$$(\bar{\mathbf{S}}_m^{\mathbf{F}})_j = \sum_{e=1}^{ne} \int_{\Omega^e} \mathbf{t}_{\text{SGS}}^e \left[\frac{\mathcal{J}}{\mathcal{J} x_k} (u_k^n N^j) + m \frac{\mathcal{J}^2 N^j}{\mathcal{J} x_k^2} \right] \bar{\mathbf{R}}_m^{\text{EXPL}} d\Omega \quad (\text{TG})$$

$$\mathbf{R}_j^{\text{IMPL}} = \frac{N^j}{\Delta t} + \mathbf{q}_1^1 \left[\frac{\mathcal{J}}{\mathcal{J} x_k} (u_k^n N^j) - \hat{u}_k \frac{\mathcal{J}}{\mathcal{J} x_k} N^j \right] \quad (4\text{B.27})$$

$$\bar{\mathbf{R}}_m^{\text{EXPL}} = \frac{U_m^n}{\Delta t} - \mathbf{q}_1^2 \frac{\mathcal{J}}{\mathcal{J} x_k} (u_k^n U_m^n) - \mathbf{q}_1^3 \frac{\mathcal{J}}{\mathcal{J} x_k} (u_k^{n-1} U_m^{n-1}) \quad (\text{SUPG})$$

$$+ \mathbf{q}_1^2 \hat{u}_k \frac{\mathcal{J}}{\mathcal{J} x_k} U_m^n + \mathbf{q}_1^3 \hat{u}_k \frac{\mathcal{J}}{\mathcal{J} x_k} U_m^{n-1} - \mathbf{g} \frac{\mathcal{J}}{\mathcal{J} x_m} p^n + \frac{\mathcal{J}}{\mathcal{J} x_k} \mathbf{T}_{km}^{n+\bar{q}_2} + \mathbf{r}^n g_m \quad (\text{GLS})$$

$$\mathbf{R}_j^{\text{IMPL}} = \mathbf{q}_1^1 \left[\frac{\mathcal{J}}{\mathcal{J} x_k} (u_k^n N^j) - \hat{u}_k \frac{\mathcal{J}}{\mathcal{J} x_k} N^j \right] \quad (4\text{B.28})$$

$$\bar{\mathbf{R}}_m^{\text{EXPL}} = -\mathbf{q}_1^2 \frac{\mathcal{J}}{\mathcal{J} x_k} (u_k^n U_m^n) - \mathbf{q}_1^3 \frac{\mathcal{J}}{\mathcal{J} x_k} (u_k^{n-1} U_m^{n-1}) \quad (\text{CG})$$

$$+ \mathbf{q}_1^2 \hat{u}_k \frac{\mathcal{J}}{\mathcal{J} x_k} U_m^n + \mathbf{q}_1^3 \hat{u}_k \frac{\mathcal{J}}{\mathcal{J} x_k} U_m^{n-1} - \mathbf{g} \frac{\mathcal{J}}{\mathcal{J} x_m} p^n + \frac{\mathcal{J}}{\mathcal{J} x_k} \mathbf{T}_{km}^{n+\bar{q}_2} + \mathbf{r}^n g_m \quad (\text{TG})$$

Continuity equation

$$\mathbf{C} \cdot \bar{\mathbf{p}}^{n+1} = \bar{\mathbf{C}} \quad (4B.29)$$

where (see table 4.1.2 for the definitions of A and B)

$$\mathbf{C} = \mathbf{M}(A) + \Delta t^2 \mathbf{L} \quad (4B.30)$$

$$\bar{\mathbf{C}} = \bar{\mathbf{M}}(B, \mathbf{r}^n) + \Delta t \bar{\mathbf{K}}(\hat{\mathbf{u}}, \mathbf{r}^n) - \Delta t \bar{\mathbf{D}}(\mathbf{U}^n) + \Delta t^2 \bar{\mathbf{g}}(\mathbf{p}^n) + \Delta t \bar{\mathbf{F}}(\tilde{\mathbf{U}}^{n+1}, \mathbf{U}^n, \xi^n) \quad (4B.31)$$

In Cartesian coordinates, the above matrixes and vectors by

Matrixes

$$\mathbf{M}(A)_{ij} = \int_{\Omega} N^i A N^j d\Omega \quad (4B.32)$$

$$\mathbf{L}_{ij} = \sum_{e=1}^{ne} \int_{\Omega^e} \left(1 + \frac{\mathbf{a}^e}{\Delta t} \right) \frac{\int N^i}{\int x_k} \frac{\int N^j}{\int x_k} d\Omega \quad (4B.33)$$

Vectors

$$\bar{\mathbf{M}}(B, \mathbf{r}^n)_j = \int_{\Omega} N^j B \mathbf{r}^n d\Omega \quad (4B.34)$$

$$\bar{\mathbf{K}}(\hat{\mathbf{u}}, \mathbf{r}^n)_j = \int_{\Omega} N^j \hat{u}_k \frac{\int \mathbf{r}^n}{\int x_k} d\Omega \quad (4B.35)$$

$$\bar{\mathbf{D}}(\mathbf{U}^n)_j = \int_{\Omega} N^j (\nabla \cdot \mathbf{U})^n d\Omega \quad (4B.36)$$

$$\bar{\mathbf{G}}(\mathbf{p}^n)_j = \int_{\Omega} \frac{\int N^j}{\int x_k} \frac{\int p^n}{\int x_k} d\Omega \quad (4B.37)$$

$$\bar{\mathbf{F}}(\tilde{\mathbf{U}}^{n+1}, \mathbf{U}^n, \xi^n)_j = \sum_{e=1}^{ne} \int_{\Omega} \frac{\int N^j}{\int x_k} (\tilde{U}_k^{n+1} - U_k^n + \mathbf{a}^e \mathbf{x}_k^n) d\Omega \quad (4B.38)$$

Pressure gradient projection equation

$$\mathbf{M} \cdot \tilde{\xi}_m^{n+1} = \tilde{\mathbf{G}}_m \quad (4B.39)$$

where, in Cartesian coordinates

$$\mathbf{M}_{ij} = \int_{\Omega} N^i N^j d\Omega \quad (4B.40)$$

$$\tilde{\mathbf{G}}_m(p^{n+1})_j = \int_{\Omega} N^j \frac{\mathcal{I} p^{n+1}}{\mathcal{I} x_m} d\Omega \quad (4B.41)$$

Momentum equation

$$\mathbf{M} \cdot \tilde{\mathbf{U}}_m^{n+1} = \tilde{\mathbf{M}}_m(\tilde{\mathbf{U}}^{n+1}) - \Delta t \tilde{\mathbf{G}}_m(p^{n+1}) + \Delta t \mathbf{g} \tilde{\mathbf{G}}_m(p^n) \quad (4B.42)$$

where, in Cartesian coordinates

$$\mathbf{M}_{ij} = \int_{\Omega} N^i N^j d\Omega \quad (4B.43)$$

$$\tilde{\mathbf{M}}_m(\tilde{\mathbf{U}}^{n+1})_j = \int_{\Omega} N^j \tilde{U}_m^{n+1} d\Omega \quad (4B.44)$$

$$\tilde{\mathbf{G}}_m(p^{n+1})_j = \int_{\Omega} N^j \frac{\mathcal{I} p^{n+1}}{\mathcal{I} x_m} d\Omega \quad (4B.45)$$

Energy equation

$$\mathbf{E} \cdot \tilde{\mathbf{T}}^{n+1} = \tilde{\mathbf{E}} \quad (4B.46)$$

where

$$\mathbf{E} = \mathbf{M} + \Delta t \mathbf{q}_3^1 [\mathbf{D}(\mathbf{r}^{n+1}) - \mathbf{K}(\mathbf{u}^{n+1}, \hat{\mathbf{u}})] + \Delta t \mathbf{S}^T(\mathbf{u}^{n+1}, \mathbf{u}^n, \hat{\mathbf{u}}, \mathbf{r}^{n+1}) \quad (4B.47)$$

$$\begin{aligned}
\bar{\mathbf{E}} &= \bar{\mathbf{M}}(T^n) \\
&+ \Delta t \left[q_3^2 \bar{\mathbf{K}}(\mathbf{u}^n, \hat{\mathbf{u}}, T^n) + q_3^3 \bar{\mathbf{K}}(\mathbf{u}^{n-1}, \hat{\mathbf{u}}, T^{n-1}) \right] \\
&- \Delta t \left[q_3^2 \bar{\mathbf{D}}(\mathbf{r}^n, T^n) + q_3^3 \bar{\mathbf{D}}(\mathbf{r}^{n-1}, T^{n-1}) \right] \\
&+ \Delta t \left[q_3^1 \bar{\mathbf{F}}(\mathbf{S}^{n+1}, \mathbf{u}^{n+1}) + q_3^2 \bar{\mathbf{F}}(\mathbf{S}^n, \mathbf{u}^n) + q_3^3 \bar{\mathbf{F}}(\mathbf{S}^{n-1}, \mathbf{u}^{n-1}) \right] \\
&+ \Delta t \left[q_3^1 \bar{\mathbf{b}}(\mathbf{u}^{n+1}) + q_3^2 \bar{\mathbf{b}}(\mathbf{u}^n) + q_3^3 \bar{\mathbf{b}}(\mathbf{u}^{n-1}) \right] \\
&+ \Delta t \bar{\mathbf{S}}^T(\mathbf{u}, \hat{\mathbf{u}}, \mathbf{r}, \mathbf{S}, T^n, T^{n-1})
\end{aligned} \tag{4B.48}$$

Note that, as in the fractional momentum equation, the contributions of the stabilisation term have been also included in the LHS (\mathbf{S}^T) and in the RHS ($\bar{\mathbf{S}}^T$) of the above expressions because the energy equation contains a convective term. In Cartesian coordinates

Matrixes

$$\mathbf{M}_{ij} = \int_{\Omega} N^i N^j d\Omega \tag{4B.49}$$

$$\begin{aligned}
\mathbf{D}(\mathbf{r}^{n+1})_{ij} &= \int_{\Omega} \frac{k}{c_v \mathbf{r}^{n+1}} \frac{\int N^i}{\int x_k} \frac{\int N^j}{\int x_k} d\Omega - \int_{\Omega} \frac{k}{c_v (\mathbf{r}^{n+1})^2} N^i \frac{\int \mathbf{r}^{n+1}}{\int x_k} \frac{\int N^j}{\int x_k} d\Omega \\
&- \int_{\Gamma} \frac{k}{c_v \mathbf{r}^{n+1}} N^i \frac{\int N^j}{\int x_k} n_k d\Gamma
\end{aligned} \tag{4B.50}$$

$$\mathbf{K}(\mathbf{u}^{n+1}, \hat{\mathbf{u}})_{ij} = \int_{\Omega} N^i (\hat{u}_k - u_k^{n+1}) \frac{\int N^j}{\int x_k} d\Omega \tag{4B.51}$$

Vectors

$$\bar{\mathbf{M}}(T^n)_j = \int_{\Omega} N^j T^n d\Omega \tag{4B.52}$$

$$\bar{\mathbf{K}}(\mathbf{u}^n, \hat{\mathbf{u}}, T^n)_j = \int_{\Omega} N^j (\hat{u}_k - u_k^n) \frac{\int T^n}{\int x_k} d\Omega \tag{4B.53}$$

$$\begin{aligned}
\bar{\mathbf{D}}(\mathbf{r}^n, T^n)_j &= \int_{\Omega} \frac{k}{c_v \mathbf{r}^n} \frac{\int N^j}{\int x_k} \frac{\int T^n}{\int x_k} d\Omega - \int_{\Omega} \frac{k}{c_v (\mathbf{r}^n)^2} N^j \frac{\int \mathbf{r}^n}{\int x_k} \frac{\int T^n}{\int x_k} d\Omega \\
&- \int_{\Gamma} \frac{k}{c_v \mathbf{r}^n} N^j \frac{\int T^n}{\int x_k} n_k d\Gamma
\end{aligned} \tag{4B.54}$$

$$\bar{\mathbf{F}}(\mathbf{S}^n, \mathbf{u}^n)_j = \int_{\Omega} \frac{1}{c_v \mathbf{r}^n} N^j S_{kl}^n \frac{\int u_k}{\int x_l} d\Omega \tag{4B.55}$$

$$\bar{\mathbf{b}}(\mathbf{u}^n)_j = \int_{\Omega} \frac{1}{c_v} N^j g_k u_k^n d\Omega \tag{4B.56}$$

Stabilisation terms

$$\mathbf{S}^T(\mathbf{u}^n, \hat{\mathbf{u}})_{ij} = \sum_{e=1}^{ne} \int_{\Omega^e} \mathbf{t}_{\text{SUPG}}^e u_k^n \frac{\mathcal{J} N^i}{\mathcal{J} x_k} \mathbf{R}_j^{\text{IMPL}} d\Omega \quad (4B.57)$$

$$(\tilde{\mathbf{S}}^T)_j = \sum_{e=1}^{ne} \int_{\Omega^e} \mathbf{t}_{\text{SUPG}}^e u_k^n \frac{\mathcal{J} N^j}{\mathcal{J} x_k} \bar{\mathbf{R}}^{\text{EXPL}} d\Omega \quad (\text{SUPG})$$

$$\mathbf{S}^T(\mathbf{u}^n, \hat{\mathbf{u}})_{ij} = \sum_{e=1}^{ne} \int_{\Omega^e} \mathbf{t}_{\text{CG}}^e \frac{\mathcal{J}}{\mathcal{J} x_k} (u_k^n N^i) \mathbf{R}_j^{\text{IMPL}} d\Omega \quad (4B.58)$$

$$(\tilde{\mathbf{S}}^T)_j = \sum_{e=1}^{ne} \int_{\Omega^e} \mathbf{t}_{\text{CG}}^e \frac{\mathcal{J}}{\mathcal{J} x_k} (u_k^n N^j) \bar{\mathbf{R}}^{\text{EXPL}} d\Omega \quad (\text{CG})$$

$$\mathbf{S}^T(\mathbf{u}^n, \hat{\mathbf{u}})_{ij} = \sum_{e=1}^{ne} \int_{\Omega^e} \mathbf{t}_{\text{GLS}}^e \left[u_k^n \frac{\mathcal{J} N^i}{\mathcal{J} x_k} - \frac{k}{c_v \mathbf{r}^{n+1}} \frac{\mathcal{J}^2 N^i}{\mathcal{J} x_k^2} \right] \mathbf{R}_j^{\text{IMPL}} d\Omega \quad (4B.59)$$

$$(\tilde{\mathbf{S}}^T)_j = \sum_{e=1}^{ne} \int_{\Omega^e} \mathbf{t}_{\text{GLS}}^e \left[u_k^n \frac{\mathcal{J} N^j}{\mathcal{J} x_k} - \frac{k}{c_v \mathbf{r}^{n+1}} \frac{\mathcal{J}^2 N^j}{\mathcal{J} x_k^2} \right] \bar{\mathbf{R}}^{\text{EXPL}} d\Omega \quad (\text{GLS})$$

$$\mathbf{S}^T(\mathbf{u}^n, \hat{\mathbf{u}})_{ij} = \sum_{e=1}^{ne} \int_{\Omega^e} \mathbf{t}_{\text{TG}}^e \left[\frac{\mathcal{J}}{\mathcal{J} x_k} (u_k^n N^i) + \frac{k}{c_v \mathbf{r}^{n+1}} \frac{\mathcal{J}^2 N^i}{\mathcal{J} x_k^2} \right] \mathbf{R}_j^{\text{IMPL}} d\Omega \quad (4B.60)$$

$$(\tilde{\mathbf{S}}^T)_j = \sum_{e=1}^{ne} \int_{\Omega^e} \mathbf{t}_{\text{TG}}^e \left[\frac{\mathcal{J}}{\mathcal{J} x_k} (u_k^n N^j) + \frac{k}{c_v \mathbf{r}^{n+1}} \frac{\mathcal{J}^2 N^j}{\mathcal{J} x_k^2} \right] \bar{\mathbf{R}}^{\text{EXPL}} d\Omega \quad (\text{TG})$$

$$\mathbf{S}^T(\mathbf{u}^n, \hat{\mathbf{u}})_{ij} = \sum_{e=1}^{ne} \int_{\Omega^e} \mathbf{t}_{\text{SGS}}^e \left[\frac{\mathcal{J}}{\mathcal{J} x_k} (u_k^n N^i) + \frac{k}{c_v \mathbf{r}^{n+1}} \frac{\mathcal{J}^2 N^i}{\mathcal{J} x_k^2} \right] \mathbf{R}_j^{\text{IMPL}} d\Omega \quad (4B.61)$$

$$(\tilde{\mathbf{S}}^T)_j = \sum_{e=1}^{ne} \int_{\Omega^e} \mathbf{t}_{\text{SGS}}^e \left[\frac{\mathcal{J}}{\mathcal{J} x_k} (u_k^n N^j) + \frac{k}{c_v \mathbf{r}^{n+1}} \frac{\mathcal{J}^2 N^j}{\mathcal{J} x_k^2} \right] \bar{\mathbf{R}}^{\text{EXPL}} d\Omega \quad (\text{SGS})$$

$$\bar{\mathbf{R}}_j^{\text{IMPL}} = \frac{N^j}{\Delta t} + \mathbf{q}_3^1 \left[(u_k^{n+1} - \hat{u}_k) \frac{\mathcal{J} N^j}{\mathcal{J} x_k} - \frac{k}{c_v \mathbf{r}^{n+1}} \frac{\mathcal{J}^2 N^j}{\mathcal{J} x_k^2} \right] \quad (4B.62)$$

$$\bar{\mathbf{R}}^{\text{EXPL}} = \frac{T^n}{\Delta t} + \mathbf{q}_3^2 (\hat{\mathbf{u}} - \mathbf{u}^n) \cdot \nabla T^n + \mathbf{q}_3^3 (\hat{\mathbf{u}} - \mathbf{u}^{n-1}) \cdot \nabla T^{n-1} \quad (\text{SUPG})$$

$$+ \mathbf{q}_3^2 \frac{k}{c_v \mathbf{r}^n} \nabla^2 T^n + \mathbf{q}_3^2 \frac{k}{c_v \mathbf{r}^{n-1}} \nabla^2 T^{n-1} \quad (\text{GLS})$$

$$+ \left(\frac{1}{c_v \mathbf{r}} \mathbf{S} \cdot \nabla \mathbf{u} \right)^{n+\bar{\mathbf{q}}_3} + \frac{1}{c_v} \mathbf{g} \cdot \mathbf{u}^{n+\bar{\mathbf{q}}_3} \quad (\text{SGS})$$

$$\bar{\mathbf{R}}_j^{\text{IMPL}} = \mathbf{q}_3^1 \left[(u_k^{n+1} - \hat{u}_k) \frac{\mathcal{J} N^j}{\mathcal{J} x_k} - \frac{k}{c_v \mathbf{r}^{n+1}} \frac{\mathcal{J}^2 N^j}{\mathcal{J} x_k^2} \right] \quad (4B.63)$$

$$\bar{\mathbf{R}}^{\text{EXPL}} = \mathbf{q}_3^2 (\hat{\mathbf{u}} - \mathbf{u}^n) \cdot \nabla T^n + \mathbf{q}_3^3 (\hat{\mathbf{u}} - \mathbf{u}^{n-1}) \cdot \nabla T^{n-1} \quad (\text{CG})$$

$$+ \mathbf{q}_3^2 \frac{k}{c_v \mathbf{r}^n} \nabla^2 T^n + \mathbf{q}_3^2 \frac{k}{c_v \mathbf{r}^{n-1}} \nabla^2 T^{n-1} \quad (\text{TG})$$

$$+ \left(\frac{1}{c_v \mathbf{r}} \mathbf{S} \cdot \nabla \mathbf{u} \right)^{n+\bar{\mathbf{q}}_3} + \frac{1}{c_v} \mathbf{g} \cdot \mathbf{u}^{n+\bar{\mathbf{q}}_3}$$

Convective transport equation

$$\mathbf{T} \cdot \bar{\mathbf{c}}^{n+1} = \bar{\mathbf{T}} \quad (4B.64)$$

where

$$\mathbf{T} = \mathbf{M} + q_c \Delta t \mathbf{K}(\mathbf{u}^{n+1}, \hat{\mathbf{u}}) + \Delta t \mathbf{S}^c(\mathbf{u}^{n+1}, \hat{\mathbf{u}}) \quad (4B.65)$$

$$\bar{\mathbf{T}} = \bar{\mathbf{M}} - \Delta t (1 - q_c) \bar{\mathbf{K}}(\mathbf{u}^n, \hat{\mathbf{u}}) + \Delta t \bar{\mathbf{S}}^c(\mathbf{u}^{n+1}, \hat{\mathbf{u}}) \quad (4B.66)$$

Again, the contributions of the stabilisation term have been also included in the LHS (\mathbf{S}^c) and in the RHS. In Cartesian coordinates

Matrixes

$$\mathbf{M}_{ij} = \int_{\Omega} N^i N^j d\Omega \quad (4B.67)$$

$$\mathbf{K}(\mathbf{u}^{n+1}, \hat{\mathbf{u}})_{ij} = \int_{\Omega} N^i (u_k^{n+1} - \hat{u}_k) \frac{\int N^j}{\int x_k} d\Omega \quad (4B.68)$$

Vectors

$$\bar{\mathbf{M}}(C^n)_j = \int_{\Omega} N^j C^n d\Omega \quad (4B.69)$$

$$\bar{\mathbf{K}}(\mathbf{u}^n, \hat{\mathbf{u}})_j = \int_{\Omega} N^j (u_k^n - \hat{u}_k) \frac{\int C^n}{\int x_k} d\Omega \quad (4B.70)$$

Stabilisation terms¹

$$\mathbf{s}^c(\mathbf{u}^{n+1}, \hat{\mathbf{u}})_{ij} = \sum_{e=1}^{ne} \int_{\Omega^e} \mathbf{t}^e u_k^{n+1} \frac{\mathcal{I} N^i}{\mathcal{I} x_k} \mathbf{R}_j^{\text{IMPL}} d\Omega \quad (4B.71)$$

(SUPG)

$$(\bar{\mathbf{S}}^c)_j = \sum_{e=1}^{ne} \int_{\Omega^e} \mathbf{t}^e u_k^n \frac{\mathcal{I} N^j}{\mathcal{I} x_k} \bar{\mathbf{R}}^{\text{EXPL}} d\Omega \quad (\text{GLS})$$

(GLS)

$$\mathbf{s}^c(\mathbf{u}^{n+1}, \hat{\mathbf{u}})_{ij} = \sum_{e=1}^{ne} \int_{\Omega^e} \mathbf{t}^e \frac{\mathcal{I}}{\mathcal{I} x_k} (u_k^{n+1} N^i) \mathbf{R}_j^{\text{IMPL}} d\Omega \quad (4B.72)$$

(CG)

$$(\bar{\mathbf{S}}^c)_j = \sum_{e=1}^{ne} \int_{\Omega^e} \mathbf{t}^e \frac{\mathcal{I}}{\mathcal{I} x_k} (u_k^n N^j) \bar{\mathbf{R}}^{\text{EXPL}} d\Omega \quad (\text{TG})$$

(SGS)

$$\bar{\mathbf{R}}_j^{\text{IMPL}} = \frac{N^j}{\Delta t} + \mathbf{q} (u_k^{n+1} - \hat{u}_k) \frac{\mathcal{I} N^j}{\mathcal{I} x_k} \quad (4B.73)$$

(SUPG)

$$\bar{\mathbf{R}}^{\text{EXPL}} = \frac{C^n}{\Delta t} + (1 - \mathbf{q}) (\hat{\mathbf{u}} - \mathbf{u}^n) \cdot \nabla C^n \quad (\text{GLS})$$

(GLS)

(SGS)

$$\bar{\mathbf{R}}_j^{\text{IMPL}} = \mathbf{q} (u_k^{n+1} - \hat{u}_k) \frac{\mathcal{I} N^j}{\mathcal{I} x_k} \quad (4B.74)$$

(CG)

$$\bar{\mathbf{R}}^{\text{EXPL}} = (1 - \mathbf{q}) (\hat{\mathbf{u}} - \mathbf{u}^n) \cdot \nabla C^n \quad (\text{TG})$$

(TG)

¹ In this case, SUPG method practically coincides with the GLS method (the only -minimum- difference is the definition of the intrinsic time) and the CG and the TG methods are the same.

Appendix 4C. Programming Notes

Two programs have been written: *Rigel* and *Sirius*. *Rigel* solves fluid/fluid-structure problems for both compressible and incompressible flows. The structural response is, by now, constrained to a rigid solid. However, if other structural behaviours are required in future applications, only few lines of the source code must be modified because the staggered algorithm facilitates modularity. *Sirius* solves structural problems considering elastic (static or transient) and some simple viscoelastic rheologies.


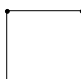
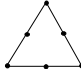
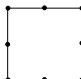
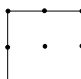

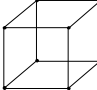

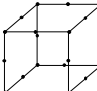
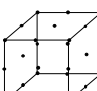
Space dimension	$nnode$	$nnode_b$	Element
2	3	2	
	4	2	
	6	3	
	8	3	
	9	3	
3	4	3	
	8	4	
	10	6	
	20	8	
	27	9	

Table 4C.1. Set of elements implemented in the programs. $nnode$ and $nnode_b$ are the number of elemental nodes and the number of elemental boundary nodes respectively.

The set of elements available is shown in table 4C.1. Both programs are written in Fortran and use, as solver, the MatMan library¹. A summary of the flow diagrams is shown in figures 4C.1 and 4C.2.

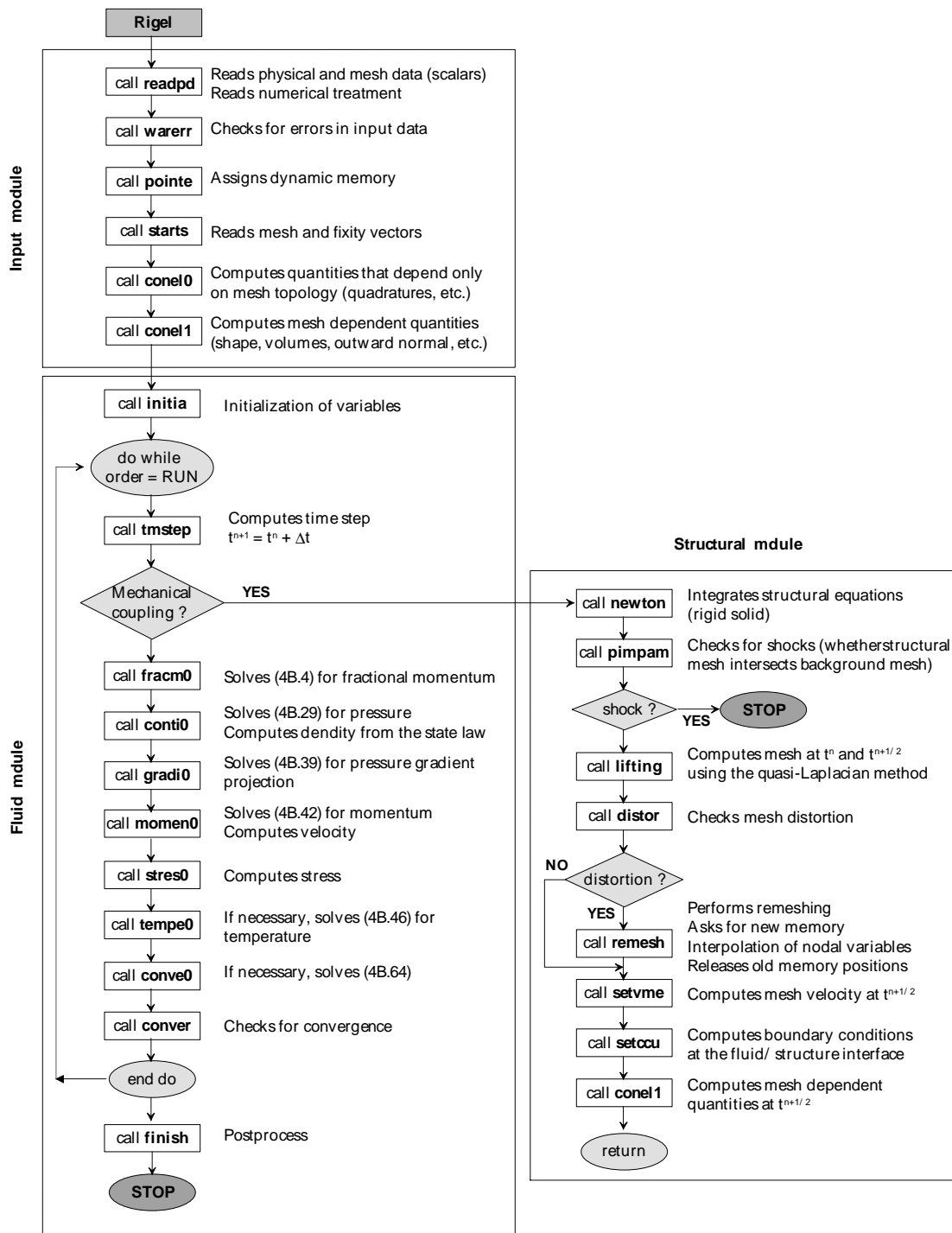


Figure 4C.1. Flow diagram of Rigel. Structural behaviours different from rigid solid can be easily incorporated by changing only the call to subroutine newton.

¹ See <http://www.rmee.upc.es/homes/codina/software.html>.

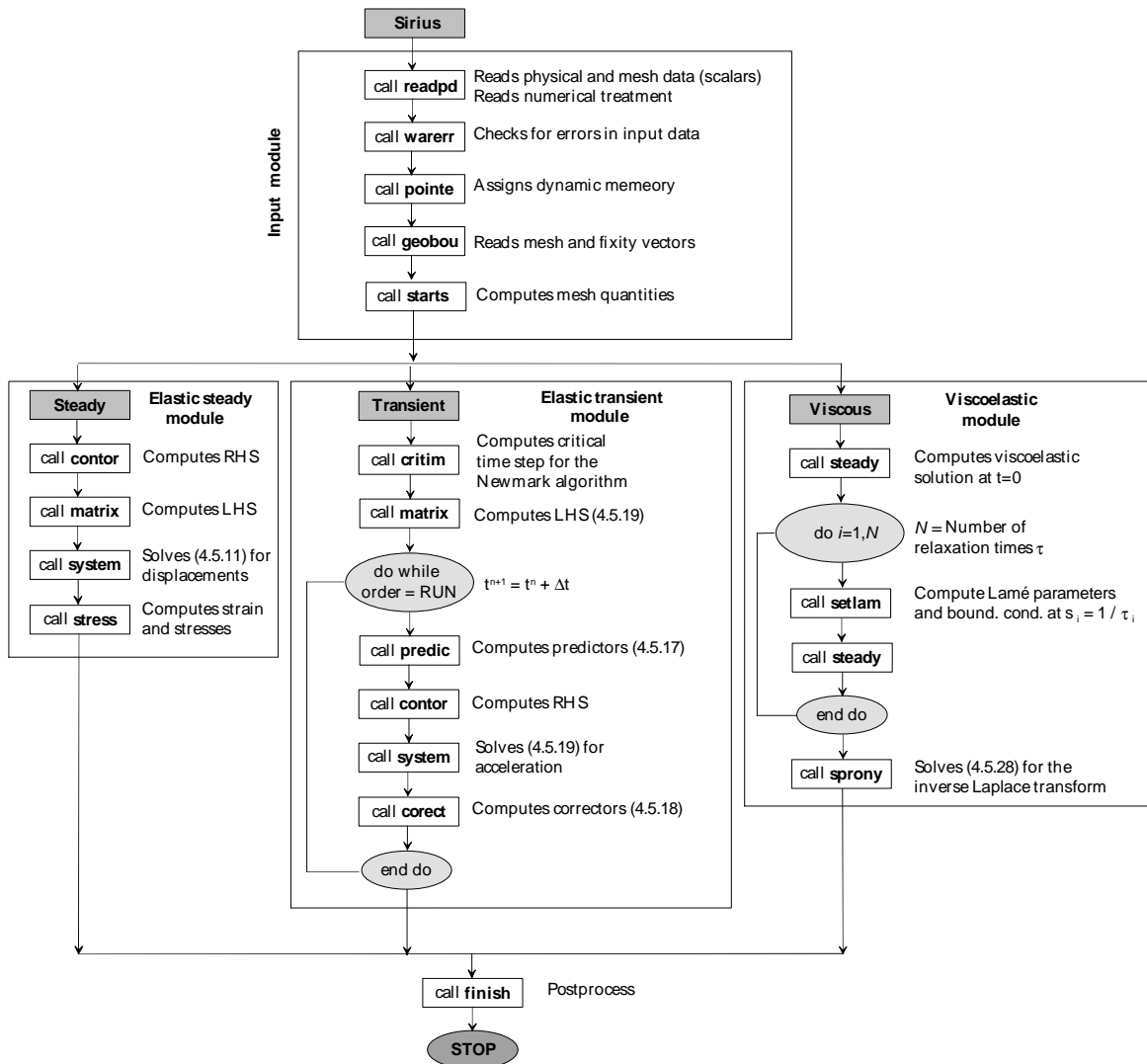


Figure 4C.2. Flow diagram of Sirius. Three different possibilities: steady elastic, transient elastic (solved by means of the Newmark method) and some simple viscoelastic rheologies (solved using the correspondence principle combined with the Prony series method to obtain the inverse Laplace transform).